The deformation mechanisms and formation of non-basal texture in Rare Earth micro-alloyed Mg alloys

By

Yang Liu

Department of Mining and Materials Engineering

McGill University, Montreal

August 2021

A Thesis Submitted to the Faculty of Graduate Studies and Research in Partial Fulfillment of the Requirement for the Degree of Doctor of Philosophy

Abstract

The texture modification in magnesium (Mg) alloys brought by the diluted neodymium (Nd) addition was characterized, investigated, and explained in the current study.

The formation of non-basal texture was validated through the investigation of Mg-1Zn-xNd (noted as ZE alloys, x=0.1, 0.2, and 0.5). Different cooling paths were applied to the specimens before hot rolling and subsequent annealing. Stronger suppression of dynamic and static recrystallization (DRX and SRX) and weaker texture intensities were acquired with the decreasing of precipitation volume fraction. Eventually, non-basal texture featuring (0002) poles tilting towards the rolling direction (RD-split) and transverse direction (TD-split) was obtained in ZE-05 alloy with 0.5 wt.% Nd addition and a faster cooling rate. Therefore, the mechanism of texture weakening effect was related to the Nd in solid solution.

To explain the effect of Nd solute, precipitated ZE alloys were subjected to various solutionizing treatments to control the Nd content in solid solution. The textural transition from the intensified basal type to a dramatically weakened TD-split pattern was acquired upon post deformation annealing. This process was tracked by quasi-in-situ electron backscatter diffraction (EBSD). A broader distribution of orientations was associated with shear-band induced nucleation and the TD-split orientation stood out in the competition through preferential grain growth. Consequently, the ZE-02 exhibited the best combination of weakened TD-split texture, limited Nd usage (0.2 wt.%), and enhanced ductility (23% elongation to fracture). The scanning transmission electron microscope (STEM)

observation indicated that more Nd dissolved in the matrix in ZE-02 featuring TD-split texture. In addition, prompted activation of prismatic <a> slip was validated by the intragranular misorientation axis (IGMA) analysis and slip trace analysis. The first-principal calculation and molecular dynamic simulation revealed that the enhanced activity of prismatic slip is attributed to the lower stacking fault energy (SFE) and critical resolved shear stress (CRSS) brought by Nd solute. Considering the dominance of basal <a> slip during deformation, a parameter based on the ratio of prismatic to basal geometrically necessary dislocation densities (rGNDp/b) was originally proposed. The textural transition was explained as the evolution of rGNDp/b distribution upon deformation and annealing.

To further reduce the usage of Nd, calcium (Ca) was introduced, an Mg-1Zn-0.1Nd-0.2Ca (ZEX-0102) alloy and an Mg-1Zn-0.2Ca (ZX-02) alloy were designed based on the concept of promoting prismatic <a> slip with the increased solute of alloying elements. Upon multi-pass rolling and annealing, the basal to TD-split texture transition was gradually enhanced in ZEX-0102 which can also be explained as the evolution of rGNDp/b distribution. However, the TD-split texture formed in ZX-02 experienced noticeable retardation under the same treatment, which could be due to the effect of diluted Nd on stabilizing Ca solute. The critical contents of Nd and Ca solute to trigger the formation of TD-split texture were also measured by electron probe micro-analysis (EPMA) in ZEX-0102. Eventually, the texture modification performance of ZEX-0102 was examined at lower elevated temperatures. The resulting non-basal ring texture was presumably attributed to the activation of prismatic and pyramidal slip along with deformation twins.

Résumé

La modification de la texture des alliages de magnésium (Mg) apportée par l'addition de néodyme (Nd) dilué a été caractérisée, évaluée et expliquée dans cette étude.

La formation d'une texture non basale a été validée par l'étude de Mg-1Zn-xNd (noté comme alliages ZE, x=0.1, 0.2, et 0.5). Différentes voies de refroidissement ont été appliquées aux échantillons, avant d'être laminés à chaud, puis recuits. Une suppression plus forte de la recristallisation dynamique et statique (DRX et SRX) et des intensités de texture plus faibles ont été acquises avec la diminution de la fraction volumique de précipitation. Finalement, une texture non basale présentant des pôles (0002) inclinés dans la direction du laminage (RD-split) et dans la direction transversale (TD-split) a été obtenue dans l'alliage ZE-05 avec un ajout de 0,5% en poids de Nd et une vitesse de refroidissement plus rapide. Par conséquent, le mécanisme de l'effet d'affaiblissement de la texture était lié au Nd en solution solide.

Pour expliquer l'effet du soluté Nd, les alliages ZE précipités ont été soumis à divers traitements de mise en solution pour contrôler la teneur en Nd dans la solution solide. La transition texturale du type basal intensifié à un motif de division TD considérablement affaiblie a été acquise lors du recuit de post-déformation, via la diffraction des électrons rétrodiffusés (EBSD) quasi in situ. Une distribution plus large d'orientations a été associée avec une nucléation induite par la bande de cisaillement et que l'orientation TD-split s'est distinguée dans la compétition par la croissance préférentielle des grains. Par conséquent, le ZE-02 présente la meilleure combinaison de texture TD-split affaiblie, d'utilisation limitée de Nd (0,2% en poids) et de ductilité accrue (23% d'allongement à la rupture).

L'observation au microscope électronique à transmission à balayage (STEM) a indiqué qu'une plus grande quantité de Nd s'est dissoute dans la matrice dans le ZE-02 présentant une texture de fissure TD. En outre, l'activation incitée du glissement prismatique <a> a été validée par l'analyse de l'axe de désorientation intragranulaire (IGMA) et l'analyse des traces de glissement. Le calcul de premier principe et la simulation de dynamique moléculaire ont révélé que l'activité accrue du glissement prismatique est attribuée à la baisse de l'énergie de défaut d'empilement (SFE) et de la contrainte de cisaillement résolue critique (CRSS) apportée par le soluté Nd. En considérant la dominance du glissement basal <a> pendant la déformation, un paramètre basé sur le rapport entre les densités de dislocation prismatiques et basales géométriquement nécessaires (rGNDp/b) a été proposé pour la première fois. La transition texturale a été expliquée comme l'évolution de la distribution rGNDp/b lors de la déformation et du recuit.

Pour réduire davantage l'utilisation du Nd, le calcium (Ca) a été introduit et un alliage Mg-1Zn-0.1Nd-0.2Ca (ZEX-0102) et un alliage Mg-1Zn-0.2Ca (ZX-02) ont été conçus sur la base du concept de promotion du glissement prismatique <a> avec l'augmentation de la soluté des éléments d'alliage. Après laminage et recuit, la transition de la texture basale à la texture TD-split a été progressivement améliorée dans le ZEX-0102, ce qui peut également être expliqué comme l'évolution de la distribution rGNDp/b. Cependant, la texture TD-split formée dans ZX-02 a connu un retard notable de formation sous le même traitement, qui pourrait être dû à l'effet du Nd dilué sur la stabilisation du soluté de Ca. Les teneurs critiques en soluté de Nd et de Ca pour déclencher la formation de la texture TD-split ont également été mesurées par micro-analyse à sonde électronique (EPMA) dans ZEX-0102. Enfin, la performance de modification de texture du ZEX-0102

a été examinée à des températures élevées plus basses. La texture annulaire non basale résultante serait à attribuer à l'activation du glissement prismatique et pyramidal avec les jumeaux de déformation.

Acknowledgement

Foremost, I would like to express my sincere gratitude to my supervisor, Professor Stephen Yue, for the rigorous, liberal, and mutual respectful academic atmosphere he established and implemented throughout my entire Ph.D. project. Prof. Yue shared his immense knowledge while providing patient guidance, constant encouragement, and selfless support. I have benefited a lot in terms of scientific knowledge and attitude towards life.

I would like to thank Professor Jun Song for his helpful guidance and insightful discussions. I was deeply inspired by his knowledge, sincerity, and vision. I am grateful for the tremendous help I have received from Dr. Jing Su. She has always provided prompt responses, invaluable suggestions, and genuine friendship. It has been an honor to work and collaborate with her.

Working with members of the Hot Deformation Lab has made my life in McGill joyful and memorable. I thank Dr. Binhan Sun, Dr. Baoqi Guo, Dr. Hanqing Che, Dr. Abu Syed H. Kabir, and Dr. Xin Chu for their help and assistance. I sincerely thank all my current and former colleagues, especially Dr. Elizabeth Guerra López, Dr. Marianna Uceda, Yiwen Chen, Bo Wang, Zewei Chen, Huicong Chen, Qiwen Qiu, Rui Gao, Xun Zeng, Xu Zheng.

I am grateful for the financial support provided by the Natural Sciences and Engineering Research Council (NSERC) Strategic Project Grant, the China Scholarship Council (CSC), the McGill Engineering Doctoral Award (MEDA). Special thanks to

CanmetMATERIALS, Dr. Amjad Javid, and Mr. Tim Skszek for their help with my Ph.D. project.

Finally, my deepest gratitude to my wife Lei, my daughter Shumeng, my parents, and all family members. Thank you all for your care, love, and understanding.

Contribution of Authors

This thesis was prepared following the guidelines for a manuscript-based thesis. These guidelines are published by the Graduate and Postdoctoral Studies office of McGill University (https://www.mcgill.ca/gps/thesis/thesis-guidelines). The present thesis is comprised of the following four manuscripts; one of which is published and three are ready for submission:

1.2.1 **Y. Liu**, J. Su, R. Gao, H. Geng, A. Javaid, T. Skszek, S. Yue, Effect of Cooling Path on Precipitation Behavior, Microstructure, and Texture Evolution of Micro-alloyed Magnesium Alloy, J. Mater. Eng. Perform. (2020) 1–8. https://doi.org/10.1007/s11665-020-04718-9. (Chapter 3).

2.2.1 **Y. Liu**, J. Su, H. Chen, Q. Qiu, R. Gao, N. Brodusch, A, Javaid, T. Skszek, J. Song, S. Yue, The underlying deformation mechanisms and texture evolution in micro-alloyed Mg-Zn-Nd alloys, Ready for submission (Chapter 4).

3.2.1 **Y. Liu**, J. Su, H. Chen, Q. Qiu, R. Gao, A, Javaid, T. Skszek, J. Song, S. Yue, Tailoring texture in micro-alloyed Mg-Zn alloys with diluted Nd and Ca, Ready for submission (Chapter 5).

4.2.1 **Y. Liu**, J. Su, B. Guo, R. Gao, N. Brodusch, A, Javaid, T. Skszek, S. Yue, The textural transition from basal to TD-split upon annealing in rolled micro-alloyed Mg-Zn-Nd-Ca alloy, Ready for submission (Chapter 6).

All the manuscripts were co-authored by Prof. Stephen Yue, who supervised the research projects, provided guidance, and edited the manuscripts. The manuscripts were authored by the candidate who planned and conducted all the experiments. The majority of

characterizations and related data analysis, including SEM, EBSD, XRD, mechanical test, etc., were also performed by the candidate. Throughout this project, Professor Jun Song provided guidance on atomic simulations, made insightful suggestions, and edited the manuscripts. Dr. Jing Su guided rolling experiments, EBSD characterizations, manuscript editing, and engaged in a significant constructive discussion. Huicong Chen and Qiwen Qiu conducted simulation calculations and drafted the relevant parts in our collaborated manuscripts. Rui Gao generated phase diagrams based on thermodynamic calculations. Huiwen Geng performed part of data analysis in chapter 3. Dr. Nicolas Brodusch conducted characterization of solute and precipitates using STEM. Dr. Baoqi Guo engaged in discussing and drafting our collaborated manuscript. Dr. Amjad Javid at CanmetMATERIALS provided help on casting and primary rolling of various alloys. Mr. Tim Skszek from Magna International provided insightful advice from an industrial user perspective.

Table of Contents

List of Figures

List of Tables

Chapter 1.Introduction

The quest for improved fuel efficiency, less environmental impact, and lower cost have led to a demand for weight reduction in automotive manufacturing [1]. Magnesium (Mg) alloys, which have high specific strength and stiffness, are promising candidates as the lightest structural materials [2]. However, Mg alloys remain minimally utilized in commercial vehicles (less than 0.5% of the weight of an average vehicle [3]). This is attributed to the insufficient formability of Mg alloy sheets at lower elevated temperatures and the increased cost due to manufacturing at higher temperatures [1,4]. Part of the limited formability is ascribed to the shortage of independent slip systems owing to the hexagonal closed packed (HCP) structure of Mg [5]. Moreover, the strain accommodated by twinning is not enough [6] and the pyramidal <c+a> slip, which is the only slip system that provides accommodation of deformation along c-axis and five independent slip systems, has the highest critical decomposition shear stress (CRSS) at ambient temperature [7]. On the other hand, the preferred crystallographic orientation featuring the [0001] axis (c-axis) of most grains is parallel to the normal direction (ND) of the rolled sheet and further restricts the performance of wrought Mg sheets [8]. The strong basal texture is related to the excessive activation of basal slip owing to the low CRSS [9]. Therefore, as the consequence of orientation randomization [10,11] and activation of multiple deformation mechanisms [12,13], better formability is expected in the texture-modified alloy [14,15].

Alloying with rare earth (RE) elements is considered to be an effective way to activate non-basal slip systems [16,17] as well as to generate non-basal texture [18,19]. However, most previous studies have favored a relatively high amount of RE addition (usually $\geqslant$1 wt.%) in a binary system [20], which is inconsistent with the goal of weight

reduction and cost control. This is associated with the controversy over the underlying mechanisms for the various beneficial effects of RE addition. Some researchers attribute the formation of "RE-texture" to the consequence of static recrystallization (SRX) [18,21,22], while a change of deformation mechanism is emphasized in other investigations [12,16]. Nonetheless, the effect of different RE element and their contents on texture modification has rarely been revealed. Recently, it has been reported that the improved effect of RE on texture modification can be achieved by Zn addition [19] or enhancement of RE dissolution in the Mg matrix [23]. In addition, the notable "RE texture" has been observed in Mg-Zn-Ca alloys, implying that Ca be a potential substitute for the expensive RE [24,25].

Based on the aforementioned issues on texture modification in RE-containing Mg alloys, a better alloying strategy that aims to reduce the usage of RE needs to be developed based on thorough investigation of deformation mechanism and texture evolution. Therefore, the overall objective of the current study is to understand the effect of Nd additions on the formation of non-basal texture in micro-alloyed Mg-Zn-Nd(-Ca) upon rolling and subsequent annealing by following the evolution of the microstructure from reheating to deformation and finally annealing. This information can then be used to design alloys and processes to maximize ductility by texture control.

A literature review focusing on the deformation mechanism, recrystallization, texture modification of wrought Mg alloy is presented in chapter 2. In chapter 3, the texture modification of micro-alloyed Mg-Zn-Nd alloy is achieved by controlling the precipitation processing after homogenization. The formation mechanism of the TD-split texture in micro-alloyed Mg-Zn-Nd alloy is thoroughly investigated in chapter 4. In chapter 5, it is

revealed that a combined addition of Ca and Nd can further reduce the usage of RE while maintaining the TD-split texture. In chapter 6, critical contents of Nd and Ca to trigger texture transition are determined and the effect of low temperature rolling on these compositions is investigated. The conclusions resulting from this study, the contributions to original knowledge as well as future work are stated in chapters 7, 8, and 9, respectively.

1.1. Reference

[1]W.J. Joost, P.E. Krajewski, Towards magnesium alloys for high-volume automotive applications, Scr. Mater. 128 (2017) 107–112. https://doi.org/10.1016/j.scriptamat.2016.07.035.

[2]B.L. Mordike, K.U. Kainer, Magnesium Alloys and their application, in: 2000.

[3]S.C. Davis, S.W. Diegel, R.G. Boundy, Transportation Energy Data Book 34, Oak Ridge Natl. Lab. (2016).

[4]M. Gupta, N.M.L. Sharon, Magnesium, magnesium alloys and magnesium composites, 2011.

[5]M.O. Pekguleryuz, Current developments in wrought magnesium alloys, in: M. Barnett (Ed.), Adv. Wrought Magnes. Alloy., Woodhead Publishing, 2012: pp. 3–62. https://doi.org/http://dx.doi.org/10.1533/9780857093844.1.3.

[6]D.W. Brown, S.R. Agnew, M.A.M. Bourke, T.M. Holden, S.C. Vogel, C.N. Tomé, Internal strain and texture evolution during deformation twinning in magnesium, Mater. Sci. Eng. A. 399 (2005) 1–12.

[7]J.F. Nie, K.S. Shin, Z.R. Zeng, Microstructure, Deformation, and Property of Wrought Magnesium Alloys, Springer US, 2020. https://doi.org/10.1007/s11661-020-05974-z.

[8]Y.N. Wang, J.C. Huang, Texture analysis in hexagonal materials, Mater. Chem. Phys. 81 (2003) 11–26. https://doi.org/10.1016/s0254-0584(03)00168-8.

[9]Q. Jin, S.-Y. Shim, S.-G. Lim, Correlation of microstructural evolution and formation of basal texture in a coarse grained Mg–Al alloy during hot rolling, Scr. Mater. 55 (2006) 843–846. https://doi.org/10.1016/j.scriptamat.2006.05.040.

[10]J.D. Robson, D.T. Henry, B. Davis, Particle effects on recrystallization in magnesium-manganese alloys: Particle-stimulated nucleation, Acta Mater. 57 (2009) 2739–2747. https://doi.org/10.1016/j.actamat.2009.02.032.

[11]L.Y. Zhao, H. Yan, R.S. Chen, E.H. Han, Study on the evolution pattern of grain orientation and misorientation during the static recrystallization of cold-rolled Mg-Zn-Gd alloy, Mater. Charact. 150 (2019) 252–266. https://doi.org/10.1016/j.matchar.2019.02.023.

[12]Y.M. Kim, C. Mendis, T. Sasaski, D. Letzig, F. Pyczak, K. Hono, S. Yi, Static recrystallization behaviour of cold rolled Mg-Zn-Y alloy and role of solute segregation in microstructure evolution, Scr. Mater. 136 (2017) 41–45. https://doi.org/10.1016/j.scriptamat.2017.04.001.

[13]J. Victoria-Hernandez, S. Yi, J. Bohlen, G. Kurz, D. Letzig, The influence of the recrystallization mechanisms and grain growth on the texture of a hot rolled AZ31 sheet during subsequent isochronal annealing, J. Alloys Compd. 616 (2014) 189–197. https://doi.org/10.1016/j.jallcom.2014.07.083.

[14]J. Hirsch, T. Al-Samman, Superior light metals by texture engineering: Optimized aluminum and magnesium alloys for automotive applications, Acta Mater. 61 (2013) 818–843. https://doi.org/10.1016/j.actamat.2012.10.044.

[15]T. Al-Samman, X. Li, Sheet texture modification in magnesium-based alloys by selective rare earth alloying, Mater. Sci. Eng. A. 528 (2011) 3809–3822. https://doi.org/10.1016/j.msea.2011.01.080.

[16]X. Zeng, P. Minárik, P. Dobroň, D. Letzig, K.U. Kainer, S. Yi, Role of deformation mechanisms and grain growth in microstructure evolution during recrystallization of Mg-Nd based alloys, Scr. Mater. 166 (2019) 53–57. https://doi.org/10.1016/j.scriptamat.2019.02.045.

[17]Y. Chino, X. Huang, K. Suzuki, K. Sassa, M. Mabuchi, Influence of Zn concentration on stretch formability at room temperature of Mg-Zn-Ce alloy, Mater. Sci. Eng. A. 528 (2010) 566–572. https://doi.org/10.1016/j.msea.2010.09.081.

[18]L.Y. Zhao, H. Yan, R.S. Chen, E.H. Han, Oriented nucleation causing unusual texture transition during static recrystallization annealing in cold-rolled Mg–Zn–Gd alloys, Scr. Mater. 188 (2020) 200–205. https://doi.org/10.1016/j.scriptamat.2020.07.037.

[19]I. Basu, T. Al-Samman, Triggering rare earth texture modification in magnesium alloys by addition of zinc and zirconium, Acta Mater. 67 (2014) 116–133. https://doi.org/10.1016/j.actamat.2013.12.015.

[20]A. Imandoust, C.D. Barrett, T. Al-Samman, K.A. Inal, H. El Kadiri, A review on the effect of rare-earth elements on texture evolution during processing of magnesium alloys, J. Mater. Sci. 52 (2017) 1–29. https://doi.org/10.1007/s10853-016-0371-0.

[21]L.Y. Zhao, H. Yan, R.S. Chen, E.H. Han, Orientations of nuclei during static recrystallization in a cold-rolled Mg-Zn-Gd alloy, J. Mater. Sci. Technol. 60 (2021) 162–167. https://doi.org/10.1016/j.jmst.2020.05.027.

[22]D. Guan, W.M. Rainforth, J. Gao, L. Ma, B. Wynne, Individual effect of recrystallisation nucleation sites on texture weakening in a magnesium alloy: Part 2- shear bands, Acta Mater. 145 (2018) 399–412. https://doi.org/10.1016/j.actamat.2017.12.019.

[23]I.-H. Jung, M. Sanjari, J. Kim, S. Yue, Role of RE in the deformation and recrystallization of Mg alloy and a new alloy design concept for Mg–RE alloys, Scr. Mater. 102 (2015) 1–6. https://doi.org/10.1016/j.scriptamat.2014.12.010.

[24]M. Yuasa, M. Hayashi, M. Mabuchi, Y. Chino, Improved plastic anisotropy of Mg-Zn-Ca alloys exhibiting high-stretch formability: A first-principles study, Acta Mater. 65 (2014) 207–214. https://doi.org/10.1016/j.actamat.2013.10.063.

[25]L.Q. Zhao, C. Wang, J.C. Chen, H. Ning, Z.Z. Yang, J. Xu, H.Y. Wang, Development of weak-textured and high-performance Mg–Zn–Ca alloy sheets based on Zn content optimization, J. Alloys Compd. 849 (2020) 156640. https://doi.org/10.1016/j.jallcom.2020.156640.

Chapter 2.Literature review

Magnesium, which is the seventh most abundant element in the earth's crust [1], is the lightest structural metal [2]. As a promising choice for weight reduction, Mg and its alloys attract attention from the automotive manufacturing industry [3,4]. However, the formability of Mg alloys is restricted at ambient temperature due to insufficient independent slip systems owing to the hexagonal close-packed (HCP) structure [5] as well as the strong crystallographic texture related to the manufacturing procedure [6].

2.1. Deformation mechanisms in Mg

The lattice parameter of Mg is a = b = 2r = 0.32092 nm, c = 0.52105 nm, and c/a= 1.6236, which is close to the ideal c/a ratio of HCP structure (1.633) [7]. The stacking of Mg atoms in a unit cell is shown in Figure 2.1.

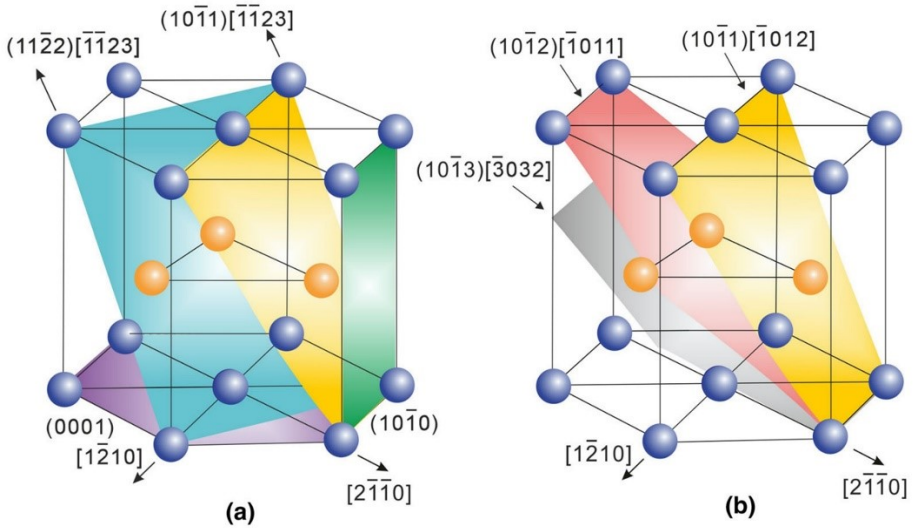

Figure 2.1 Schematic diagrams of a unit cell of Mg showing (a) basal, prismatic, and pyramidal slip systems, (b) extension and contraction deformation twinning systems [8].

2.1.1.Slip

Slip is the movement of dislocations and is described as the combination of specific crystallographic planes (slip plane) and glide direction (slip direction) [5]. Information of various slip systems for Mg, including the critical resolved shear stress (CRSS), is listed in Table 2.1.1 and shown schematically in Figure 2.1.

Table 2.1.1 Crystallographic characteristics of slip systems for Mg.

Slip modes	Crystallographic planes and directions	Number of independent slip systems	CRSS/ MPa*
Basal <a>	{0001} <11$\bar{2}$0>	2	0.52 [9], 0.76 [10], 0.81 [11]
Prismatic <a>	{10$\bar{1}$0} <11$\bar{2}$0>	2	39 [12], 50 [13]
Pyramidal I <a>	{10$\bar{1}$1} <11$\bar{2}$0>	4	40 [14], 44 [14], 54 [15]
Pyramidal II <c+a>	{11$\bar{2}$2} <11$\bar{2}$3>	5	80 [16]

* The CRSS values are measured at ambient temperature.

As the result of the symmetry of the HCP structure, the independent slip systems for basal, prismatic, and pyramidal I slip are less than 5. Thus, those slip modes fail to meet the requirement of the Von Mises law, which requires at least 5 independent slip systems to achieve homogenous deformation [17]. Moreover, the Pyramidal II <c+a> is the only slip system that provides enough independent slip systems as well as accommodates deformation along the <c> direction [7].

To activate a specific slip system, the strain applied on this slip plane along its slip direction must exceed a threshold value which is known as the CRSS [18]. At room temperature, the basal slip is the preferentially activated slip because it has the lowest CRSS. On the contrary, the Pyramidal II slip processes the highest CRSS, which restricts the activation of slip mode and, therefore, leads to the poor performance of Mg on formability. Consequently, one approach to improve the formability for Mg is to active more slip modes by lowering the CRSS, especially for the pyramidal II slip. For CRSS reduction, the most common methods are increasing processing temperature and adding alloying elements.

It is well acknowledged that the CRSS generally decreases with increasing deformation temperature for the various deformation modes in Mg, especially for the non-basal slip [8], as seen in Figure 2.2.

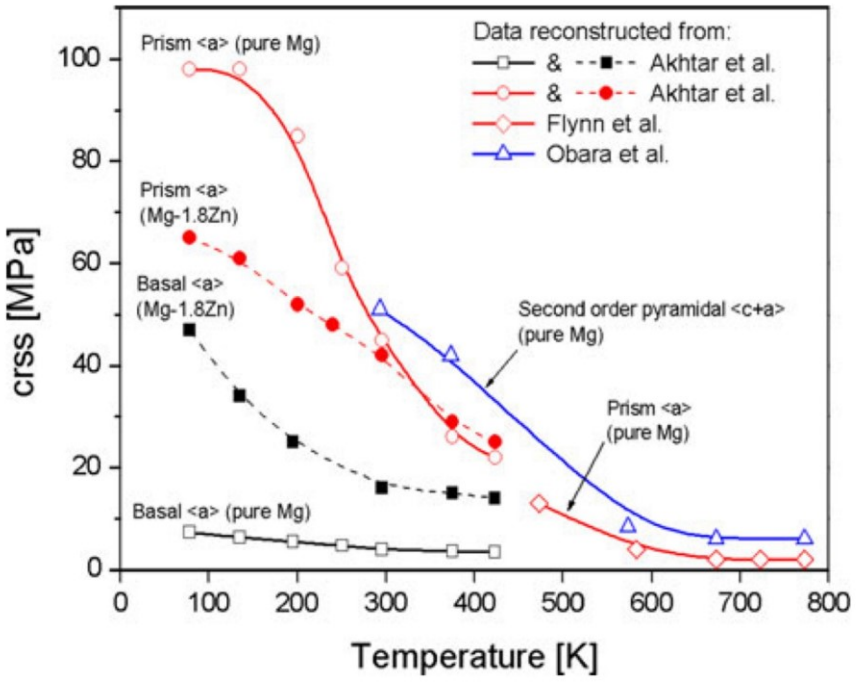

Figure 2.2 The CRSS evolution of Mg single crystal with temperature [19].

Starting from 225℃, the CRSS of prismatic <a> and pyramidal <c+a> sharply drop and thus, leads to the activation of those slip systems [8,19]. The reduced CRSS at elevated temperature contributes to the better formability for Mg alloys. Therefore, to compensate for the insufficient independent slip system, the wrought Mg alloys are commonly thermo-processed at an elevated temperature ranging from 300°C to 500°C [8].

For the Mg alloys, the choice of the alloying element also affects the CRSS values. The CRSS for various slip systems generally rises with the addition of alloying elements [21,22], as seen in Figure 2.2, for the addition of 1.8 wt.% Zn. Furthermore, the difference between CRSSes of basal and non-basal slips (prismatic <a> and pyramidal <c+a>) have been reduced through alloying with calcium (Ca) [22], and rare earth (RE) elements such as yttrium (Y) [23], neodymium (Nd) [24], cerium (Ce) [25].

2.1.2.Twinning

In magnesium and its alloys, twinning plays a critical role to effect plastic deformation along the c-axis [26]. Deformation twinning is a process in which a portion of the crystal taking up an orientation that is a mirror image of the untwinned region [27]. Similar to deformation slip, twinning takes place on a certain crystal plane (twin plane) in a certain direction (twin shear direction), known as the twinning system [27] (as shown in Figure 2.1). The commonly reported twinning system and corresponding crystallographic details are listed in Table 2.1.2. Deformation twins are divided into primary and secondary twinning based on their twinning mechanism. The former commences with twin nucleation at the grain boundary and twin interfaces of the primary twin serve as the nucleation site for the latter [26]. In terms of the deformation along the c-axis brought by twinning, the twins are categorized as contraction (compression) and extension (tension) twins [28,29].

Table 2.1.2 Twinning modes commonly observed in magnesium alloys.

Twin mode	Twin plane	Twin shear direction	Theoretical Misorientation
Tension – I [27]	$\{10\bar{1}2\}$	$\langle\bar{1}011\rangle$	$86.3°\langle11\bar{2}0\rangle$
Compression – I [27]	$\{10\bar{1}1\}$	$\langle10\bar{1}\bar{2}\rangle$	$56.2°\langle11\bar{2}0\rangle$
Compression – II [27]	$\{10\bar{1}3\}$	$\langle30\bar{3}\bar{2}\rangle$	$64°\langle11\bar{2}0\rangle$
Tension – II [24]	$\{11\bar{2}1\}$	$\langle11\bar{2}\bar{6}\rangle$	$34.2°\langle10\bar{1}0\rangle$
Compression-tension – I [27]	$\{10\bar{1}1\}-\{10\bar{1}2\}$	$37.5°\langle11\bar{2}0\rangle$; $30.1°\langle11\bar{2}0\rangle$; $66.5°\langle11\bar{2}0\rangle$; $69.9°\langle11\bar{2}0\rangle$ [30]	
Compression-tension – II [27]	$\{10\bar{1}3\}-\{10\bar{1}2\}$	$29.7°\langle11\bar{2}0\rangle$; $22.3°\langle11\bar{2}0\rangle$; $63.6°\langle3\bar{9}62\rangle$; $66.3°\langle3\bar{7}41\rangle$ [30]	
Tension-tension [31]	$\{10\bar{1}2\}-\{10\bar{1}2\}$	$7.4°\langle11\bar{2}0\rangle$; $60.0°\langle10\bar{1}0\rangle$; $60.4°\langle8\bar{1}\bar{7}0\rangle$ [32]	

The contraction twinning initiates by subjecting a strain of contraction along the c-axis or a tension perpendicular to the c-axis. The contraction twins reorient the basal plane by 56° or 64° about the $\langle11\bar{2}0\rangle$ axis, which is reported as the $\{10\bar{1}1\}$ and $\{10\bar{1}3\}$ twins, respectively [27]. Similarly, the extension twinning initiates under a strain of tension along the c-axis or a contraction perpendicular to the c-axis [26]. The extension twins include the $\{10\bar{1}2\}$ and $\{11\bar{2}1\}$ twins which rotate the basal plane by 86° about the $\langle11\bar{2}0\rangle$ axis and

34° about the $\langle 10\bar{1}0 \rangle$ axis, respectively. The secondary twin, also known as the double twin, is the extension twin generated in a pre-existing twin (contraction or extension). Three secondary twinning systems have been commonly reported, which are also listed in Table 2.1.2.

The most commonly reported are the $\{10\bar{1}2\}$ extension, $\{10\bar{1}1\}$ contraction, and $\{10\bar{1}1\} - \{10\bar{1}2\}$ double twin. This is usually attributed to the smaller shear and simpler atomic shuffle [27] as well as a lower CRSS [33] for those twinning modes. Furthermore, the $\{10\bar{1}1\}$ contraction and $\{10\bar{1}1\} - \{10\bar{1}2\}$ double twins are reported as favorable nucleation sites during recrystallization owing to the less mobile twin boundary and higher localized strain compared with $\{10\bar{1}2\}$ extension twins [34,35].

Because of the symmetry of the HCP structure, each twinning mode has six theoretical variants, which represent six possible twinning systems with equivalent crystallographic characteristics [34]. To further identify the twin variants, the Schmid Factor (SF) of each variant needs to be considered. The most possible twin variant is formed by higher resolved shear stress which means the corresponding SF is also higher.

2.1.3.Shear banding

Shear bands correspond to narrow regions of intense shear that occur independently of the grain structure and normal crystallographic considerations [36]. The shear banding is usually characterized as deformation bands about 35 degrees to the rolling direction [36] although the interior structure (various deformation twins) is hard to be defined owing to the residual stress. The formation of shear bands in Mg alloys is ascribed to the formation and build-up of fine contraction and secondary twins owing to the high shear stress brought

by localized high activity of basal slip [37,38], as seen in Figure 2.3. However, shear bands have been reported as the source of crack initiation during rolling owing to the strong strain concentrated in the shear bands [37]. A reduced severity and increased number of shear bands can lead to better rollability for the Mg alloy sheet [39].

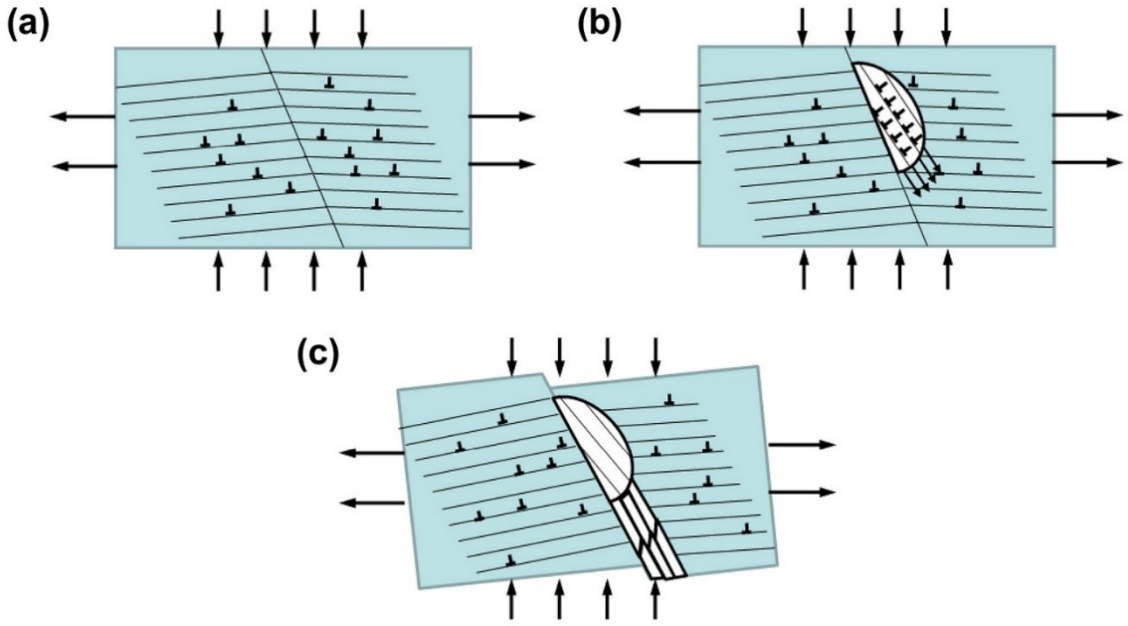

Figure 2.3 Proposed model for shear band formation in pure Mg and Mg-Y alloy [37]

2.1.4.Deformation modes during rolling of polycrystalline Mg alloys

Upon rolling, various deformation mechanisms have been observed in polycrystalline Mg alloys, especially twinning and shear banding owing to their distinct morphology. Both optical microscope (OM) and electron backscattered diffraction (EBSD) can perform this characterization. To observe the slip activation in deformed Mg alloys, Transmission Electron Microscope (TEM) is usually indispensable. Yet the limited survey area prevents the TEM characterization from providing statistical results of activated slips. There are approaches developed to reveal the activation of the slip system in Mg alloy, which will be introduced in the following section.

2.1.4.1.Generalized Schmid Factor (GSF)

The Schmid law (or SF rule) has been widely used to evaluate deformation under single-axis stress. A higher SF indicates higher resolved shear stress for certain deformation mechanism which is more likely to be activated [40]. To explain the slip system activation and twinning variants selection upon rolling, researchers have adopted various adjusted SFs by modifying the applied stress. Luo et al. [41] defined an effective SF based on the biaxial stress state, which allows a more direct physical interpretation of the observed twin variant selection. Barnett et al. [42] also calculated SF by hypothesizing the strain state as $\sigma_1 = 0, \sigma_3 = 2\sigma_2$ (or $\sigma_{RD} = 0, \sigma_{Nd} = \sigma, \sigma_{TD} = 0.5\sigma$). Similar stress states have also been proposed by Molodov et al. [43], Basu et al. [35], and Wang et al. [44] with σ_{TD} ranging from $0.29\sigma \sim 0.5\sigma$ for SF calculation in rolled Mg. The Generalized Schmid Factor (GSF) was proposed and developed by Guo et al. [45] based on the assumption of replacing stress state in three-dimensional space by a stress tensor matrix:

$$\sigma = \begin{pmatrix} \sigma_{xx} & \sigma_{xy} & \sigma_{xz} \\ \sigma_{yx} & \sigma_{yy} & \sigma_{yz} \\ \sigma_{zx} & \sigma_{zy} & \sigma_{zz} \end{pmatrix} = \begin{pmatrix} 0 & 0 & 0 \\ 0 & -0.5 & 0 \\ 0 & 0 & -1 \end{pmatrix} \quad \textit{Equation 2.1.1}$$

where x, y, and z correspond to rolling direction (RD), transverse direction (TD), and normal direction (ND) of the rolled specimen, respectively. σ_{zz} is determined as -1 since the material is subjected to compressive stresses along the ND during rolling [45]. Given the assumption that rolling has the same stress state with plane strain compression (PSC) [46], σ_{zz} is determined as -0.5 [45]. The rest components in σ are zero for rolling condition [45]. Thus, the GSF can be calculated by:

$$GSF = b \cdot g \cdot \sigma \cdot g^T \cdot n \quad \textit{Equation 2.1.2}$$

Where b and n are the slip/twinning direction and slip/twinning plane normal, respectively. The g and g^T are the orientation matrix and its transpose, which are defined based on the Euler angles measured by EBSD. An example of the application of GSF is shown in Figure 2.4 [47].

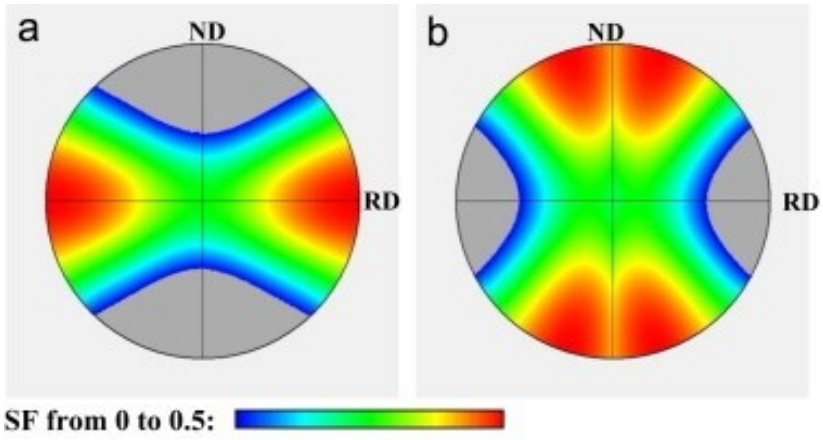

Figure 2.4 Calculated GSFs for twins as a function of (0001) pole for this applied rolling deformation: (a) {10−12} twin; (b) {10−11} twin [47].

With GSF evaluation, the slip traces analysis is possible for rolled Mg alloys. After crystallographic features, especially the orientation of grains and slip traces, are acquired by EBSD measurement, the theoretical traces of the different slip systems for the given orientation can be calculated and visualized. By comparing the observed and calculated slip trace, the activation of the slip system is thus determined.

2.1.4.2.Intragranular misorientation axis (IGMA) distribution

The IGMA analysis was originally proposed by Chun et al. and exclusively focuses on the slip activation in HCP materials [19,48]. Deformation was interpreted as the bending of a crystal lattice around the axis called the “Taylor axis” and thus, the net rotation is generated by activation of various slip systems. The IGMA is defined as the axis of the misorientation between two points inside a grain due to slip-induced lattice rotation. The

dominant slip system in a single grain is determined by matching the Taylor axis for a given slip mode to the measured IGMA [48]. The details of the Taylor axis and corresponding slip modes are listed in Table 2.1.3. The IGMA distribution map was built using the Aztec Crystal. For current alloys, the misorientation angle within 1~3° was evaluated and a maximum intensity higher than 2 mrd indicates the dominant activation of certain slip system [49]. Although the IGMA is theoretically capable of determining the slip activation, the application of IGMA is limited to investigate the prismatic <a> slip system owing to the Taylor axis of basal and pyramidal is the same [48]. Thus, derived from the misorientation profile, the IGMA can only be used to determine whether prismatic slip is the dominant deformation mechanism upon deformation.

Table 2.1.3 The Taylor axes and corresponding slip systems for HCP materials [19]

Slip modes	**Crystallographic planes and directions**	**Taylor axes**
Basal <a>	{0001} <11$\bar{2}$0>	<0$\bar{1}$10>
Prismatic <a>	{10$\bar{1}$0} <11$\bar{2}$0>	<0001>
Pyramidal II <c+a>	{11$\bar{2}$2} <11$\bar{2}$3>	<1$\bar{1}$00>

2.1.4.3.Geometrically necessary dislocations (GND) distribution

Geometrically necessary dislocations (GND) distribution provides not only a quantitative understanding of slip activation, but also, more importantly, the distribution of resolved or total GND of various slip systems, as seen in Figure 2.5. Therefore, the connection between microstructural characteristics and dislocation movement can be established.

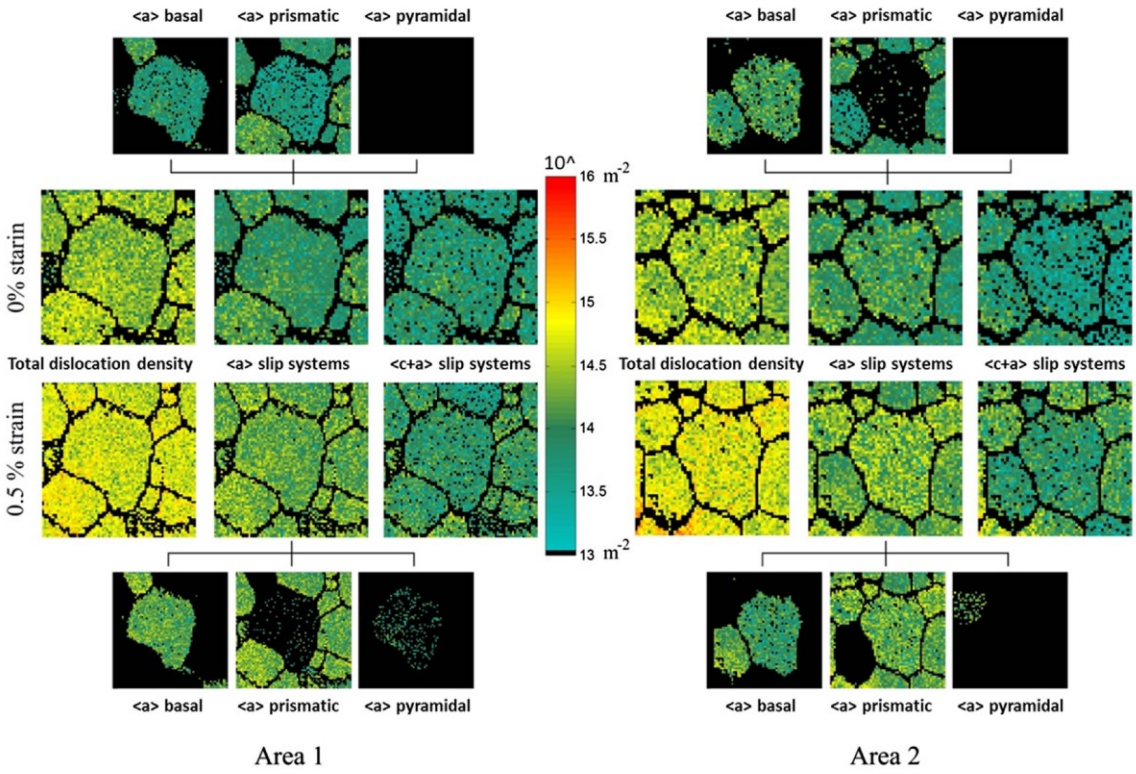

Figure 2.5 An example of GND distribution derived from EBSD test of AZ31 Mg alloy: total dislocation density and resolved slip systems maps of area 1and 2 for 0% and 0.5% strain [50].

The concept of GND has been proposed by Nye et al. [51] since 1953, yet the practical use of GND analysis was possible almost 50 years later with the development of high-resolution EBSD [52]. However, despite the development of better calculation algorithms [53,54], the GND evaluation is not widely performed by EBSD users owing to the shortage of commercial software support. Nonetheless, encouraging applications of GND distribution have been reported in HCP metals. Littlewood et al. [55] and Britton et al. [56] examined the GND distribution of Ti-6Al-4V (Ti64) subjecting to tensile deformation and hot rolling, respectively. The quantitative GND results of various dislocation systems were related to the corresponding microstructures. Chaoyi et al. [57] investigated the role of GND in the dislocation generation of pure nickel and found that GNDs are the more important for the strength of polycrystalline metals in the early stages

of work hardening. Khosravani et al. [50] explained the nucleation and propagation of tensile twins in Mg-3Al-1Zn (AZ31). It was inferred from the GND distribution that the twinning occurs in grains that cannot accommodate necessary contraction via <a>-type slip [50].

Although the GND density of a specific slip system can be quantified over large regions of interest, the GND density distribution map and the GND density data still suffer from three crucial limitations that prevent GND analysis from being correlated with the evolution of microstructure and texture. The first limitation is the error introduced to the average GND density data due to the nature of the EBSD test. The EBSD data consists of a series of data points containing misorientation and position information. Even though the order of magnitude of total indexed points is usually around 10^5~10^7 (depends on the surveyed area and the scanning step size), this magnitude is still insignificant compared to that of GND density in deformed material, which could reach 10^{15}~10^{20} m^{-2} [36]. Thus, the deviation of the average GND density will be affected by this large difference of magnitudes between the indexed points and the GND density value. The second limitation results from the nature of the mapping method of GND density. Normally, the slip systems are calculated and described individually. Although this expression method is convenient when analyzing a specific slip system (as seen in Figure 2.5), the individually presented data diminishes the comprehensive effect brought by multiple slip systems on the structural and textural evolution. The last limitation is related to the interference brought by various microstructures, especially the recrystallized grains and substructures. In general, the dislocation density increases at local stress concentrations during deformation and decreases with recrystallization when annealed [50]. Therefore, the substructures,

including LABs, low angle twin boundaries, and slip traces would be highlighted on the GND map with higher intensity, while the recrystallized grains would be characterized as low GND regions. Even though other alternative approaches, such as Kernel Average Misorientation (KAM) distribution, are also capable of revealing the substructures and recrystallized grains. The intensity difference between deformed and recrystallized structures, which could reach ~10^5 m^{-2}, would lead to attenuation on the impact of the low GND region. Finally, the GND distribution can only provide 2D analysis since the data is surveyed at the surface of the specimen.

2.2. Recrystallization of deformed Mg alloys

Defects, such as dislocations, twins, and shear bands are introduced as the consequence of plastic deformation in Mg and its alloys, as discussed in 2.1. Thus, the free energy is raised owing to the presence of those defects [36]. This deformation-induced energy increase is also known as the stored energy [58]. Upon annealing, driven by the stored energy, recrystallization occurs to lower the total free energy and restore the deformed structure [36]. Together with deformation, the recrystallization process controls the microstructure, texture, and mechanical properties [6,34,59].

The recrystallization process can be described as the formation of strain-free nuclei within the deformed or recovered structure and the replacement of deformed structure by the growth of recrystallized grains [36]. It can also be divided into dynamic recrystallization (DRX) and static recrystallization (SRX). The former takes place during deformation at elevated temperatures and the latter occurs after deformation [60].

2.2.1.Dynamic recrystallization

Dynamic recrystallization has been observed to be active during hot, warm, and even cold deformation in Mg alloys [60]. Three main mechanisms are proposed to explain DRX in Mg and its alloys by various studies and categorized as: (i) continuous, which occurs at an intermediate temperature ranging from 200° C to 300° C [61–66], (ii) discontinuous [67–70], which takes place at elevated temperature around 300° C to 450° C, and (iii) twinning induced, which has been observed at a wide temperature range between 150° C to 450° C [35,71,72].

2.2.1.1.Continuous dynamic recrystallization (CDRX)

In CDRX, recrystallization occurs through a continuous increase in misorientation across deformation-induced boundaries [61,62]. The CDRX process involves the formation of three-dimensional arrays of low angle boundaries (LABs), and the transformation from LABs to high angle boundaries (HABs) [60]. Therefore, the <c+a> slip, which can contribute the additional Burgers vectors other than the commonly observed <a> slip, is needed for the formation of LABs [36]. Moreover, the ratio between the contributions of basal and non-basal slip may also affect the CDRX process. When basal slip is dominant, CDRX features the formation of lamellar microbands that are subsequently subdivided by transverse LABs [63,64]. LABs convert to HABs owing to the contribution of mobile dislocation trapped within the subgrains [66], as shown in Figure 2.6 (a) [60]. When non-basal dislocation contributes similarly to the basal ones, subgrains formation takes place initially. Except for the misorientation contribution from the interaction of LABs and mobile dislocations, the CDRX is also facilitated by the

progressive lattice rotation with strain [65,66], the schematic is also shown in Figure 2.6 (b) [60].

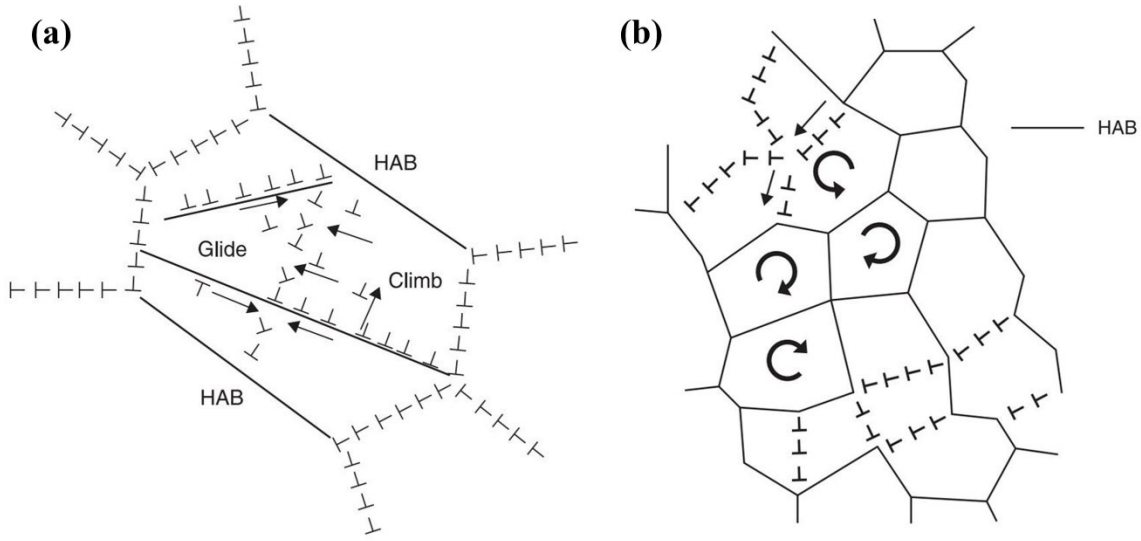

Figure 2.6 (a) interaction of low-angle boundaries with lattice dislocations resulting in progressive increase in their misorientation. (b) Rotation of (sub)grains facilitates the transformation of low-angle boundaries into high-angle boundaries. [60]

2.2.1.2.Discontinuous dynamic recrystallization (DDRX)

DDRX is associated with the strain-induced local migration of initial HABs, which is also reported as the bulging mechanism, and the subsequent grain growth through the consumption of deformed structure [67,68]. The driving force for the grain boundary migration includes the stored energy (dislocation density) difference over the boundary [36] and the stress field formed owing to the lattice dislocations interact with a grain boundary [60], as shown in Figure 2.7 (a). The nucleation is complete once the bulged region is divided by the formation of strain-induced LAB, as observed by Yang et al. [69] and Sun et al. [70], the schematic is shown in Figure 2.7 (b). In addition, the DDRX commonly

creates a necklace microstructure featuring large parent grains surrounded by fine recrystallized grains [60,65].

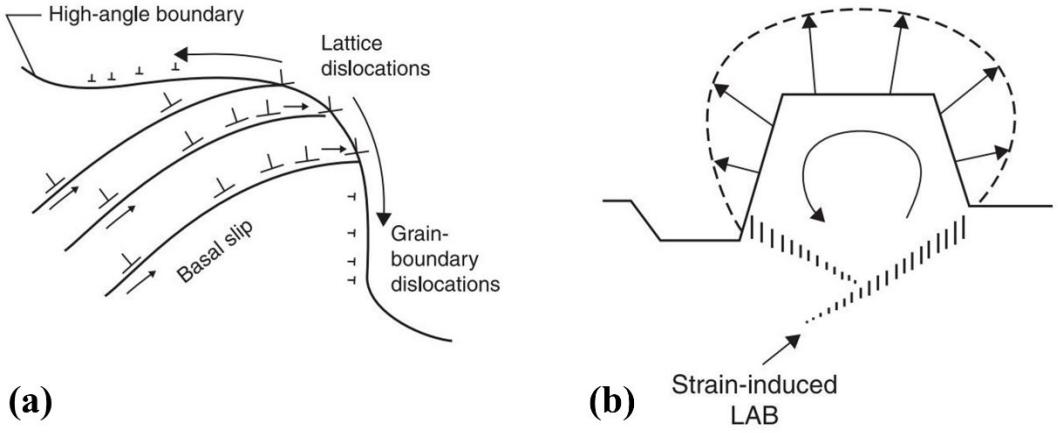

Figure 2.7 (a) The formation of dislocation pileups within bulging interiors promotes local migration toward decreased dislocation density. Dissociation of leading lattice dislocations trapped by the grain boundary interact with grain boundary dislocations. (b) Grain boundary sliding facilitates the formation of a LAB subdivided bulged area from a parent grain. [60]

2.2.1.3.Twinning induced dynamic recrystallization (TDRX)

Since twinning is commonly observed in Mg alloys, the corresponding TDRX has also been widely recognized during deformation [35,71,72]. The nucleation mechanism of TDRX can be concluded as nucleation at the mutual intersection of primary-secondary twins [35] or secondary-secondary twins [71] (as shown in schematics in Figure 2.8 (a)), subdivision of twin lamellas by fine secondary twins [60] (as seen in Figure 2.8 (b)) or rearrangement of lattice dislocations [72] (LABs, as seen in Figure 2.8 (c)). Then, the nuclei transform into recrystallized grains due to the transformation of special twin boundaries into random HABs [60]. Finally, the recrystallized grains gain the equiaxed shape owing to the energy raised by the increased dislocation density [60,72]. It is worth noting that the CDRX is reported as a strong recovery process without size change in sub-

grains, while the DDRX is classified as a recrystallization process for the migrating HABs, and the TDRX exists as a transition between two extreme cases [60].

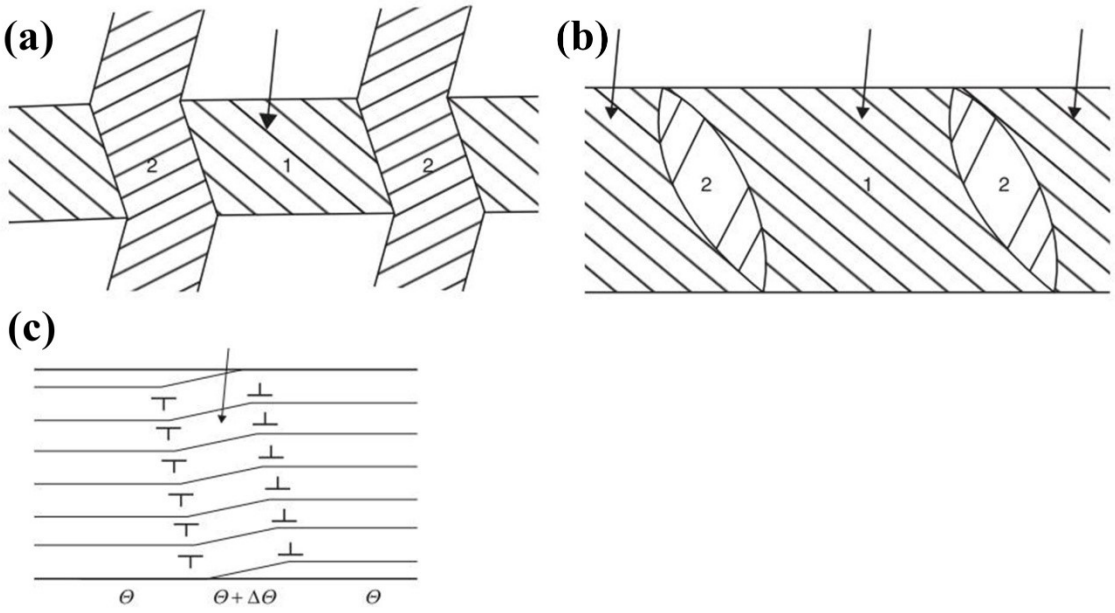

Figure 2.8 Schematic representation of TDRX nucleation mechanism: (a) nucleation by mutual intersection by primary twins, (b) nucleation by subdivision of coarse lamellae (1) of primary twins by fine secondary twins (2), and (c) Nucleation by subdivision of coarse lamellae of primary twins by transverse low-angle boundaries. [60]

2.2.2.Static recrystallization

The SRX usually occurs in Mg alloys when the deformed material is subsequently annealed [36]. Since the driving force is the stored energy resulting from plastic deformation, SRX is generally affected by temperature, strain, strain rate, solutes, and the second-phase particles [8]. Continuous SRX (CSRX) and discontinuous SRX (DSRX) mechanisms have been proposed in the literature [36]. The former is ascribed to the transition from subgrains to recrystallized grains, while the latter is related to the nucleation and grain growth in the vicinity of grain boundaries, twin boundaries, shear bands, and second-phase particles [35,73]. The schematics of continuous and discontinuous SRX are shown in Figure 2.9.

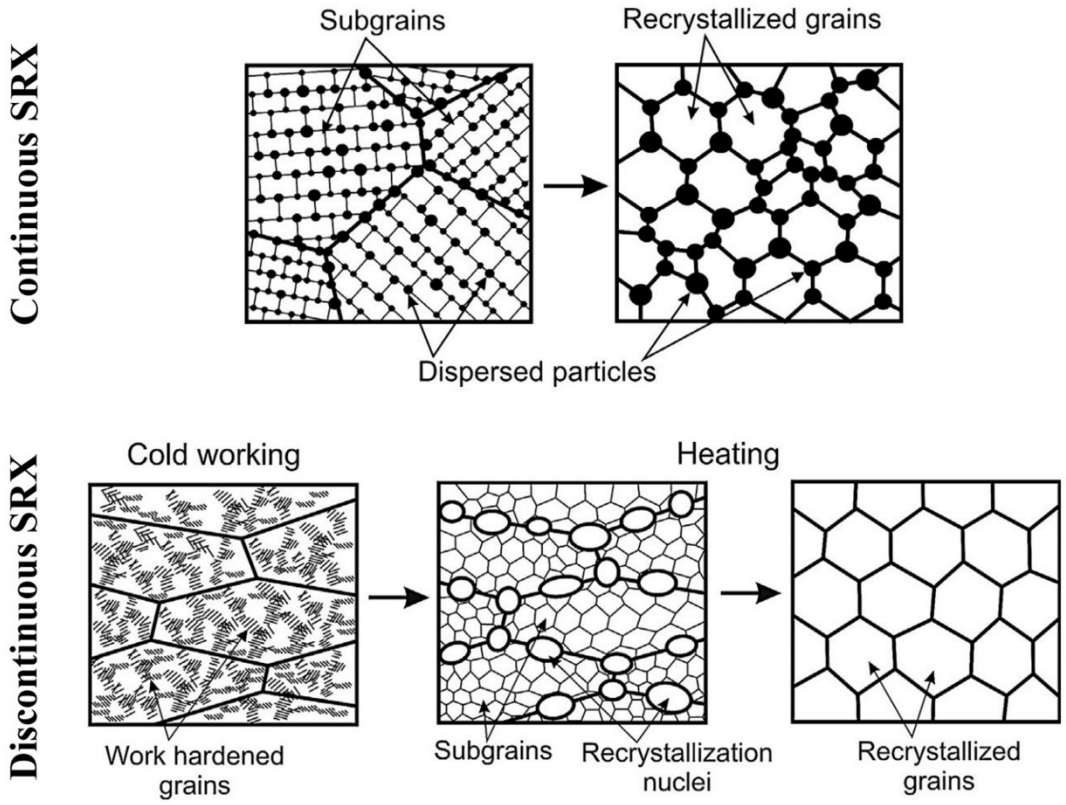

Figure 2.9 Schematic representation of the CSRX and DSRX taking place during the annealing of strain hardened materials [75].

In addition to CSRX and DSRX, depending on the nucleation site, various studies have proposed other mechanisms of SRX nucleation:

i. Grain boundary nucleation: The higher stored energy near the grain boundaries is due to the activated non-basal slip, which subsequently leads to nucleation of recrystallized grains adjacent to the original grain boundaries [75].

ii. Subgrain coalescence: The HABs are formed through the subgrain boundary motion, which is ascribed to the coalescence of subgrains [76]. This mechanism is also described as the rotation of zones in deformed parent grain after the development of orientation gradients [75].

iii. Shear band-induced nucleation (SBIN): Nucleation is favored in shear bands not only because of the high extensive plastic strain but also due to the large spread of orientations provided [36]. In particular, SBIN in RE-containing Mg alloys is reported to promote the formation of non-basal texture [77].

iv. Deformation twinning induced nucleation (DTIN): Similar to shear bands, twins are also the potential nucleation sites during the SRX process of Mg alloys. Contraction twins serve as a better choice for SRX, as discussed in 2.1.2. It has also been reported that nucleation is preferentially initiated at the twin–twin intersections, the twin–grain boundary intersections, and within twins [78,79].

v. Particle-stimulated nucleation (PSN): To facilitate nucleation, evenly distributed secondary-phase particles with a size larger than 1 um is the prerequisite [36]. Otherwise, recrystallization is retarded owing to the pinning effect of fine precipitates on boundaries [80]. The PSN has been reported to provide more randomly oriented nuclei even though the PSN competes with other nucleation mechanisms [81].

2.3. Texture in wrought Mg sheets

In polycrystal materials, the orientation distribution of the grains can favor certain orientations due to processing [82]. This is known as preferred orientation or crystallographic texture [82]. For Mg alloy sheets, the texture is closely related to the inferior formability due to the sharp texture developed during deformation [83]. The concentrated texture, which aligns grains along the same orientation, limits the accommodation of deformation along the <c>-axis and amplifies the independent slip

system shortage for Mg alloys [84]. Therefore, it is crucial to understand the formation mechanism of various textures in Mg alloy sheets.

2.3.1.Representation and measurement of texture

2.3.1.1.Representation of texture

To describe the texture or orientations of grains, it is necessary to define the position of the atomic planes in the crystal with respect to a fixed reference. The most well-established coordinate system of expressing orientation in 3-D space is the three Euler angles [82]. According to the definition made by Bunge, the three Euler angles are: φ_1 about the ND, transforming the TD into TD′ and RD into RD′; ϕ about the axis RD′; φ_2 about the ND′′ [85]. The schematic of Bunge's Euler angles is shown in Figure 2.10. Thus, any orientation can be expressed unequivocally as a point in Euler space, whose axes are spanned by the three Euler angles [82].

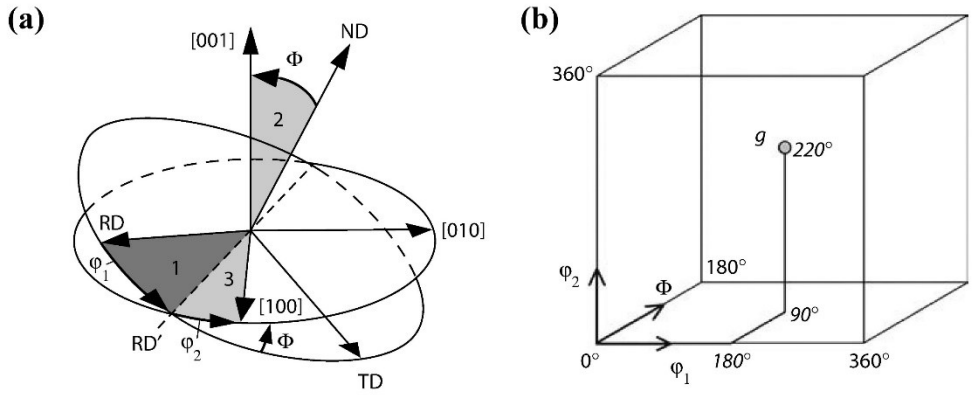

Figure 2.10 The (a) Euler angles defined by Bunge and (b) Euler space [82].

The probability density function of orientations in the Euler space, which precisely and quantitatively describes texture, is defined as the orientation distribution function (ODF) [86]. Normally, the ODF is demonstrated by a series of two-dimensional figures with different φ_2, as shown in Figure 2.11. However, the ODF is hard to measure directly.

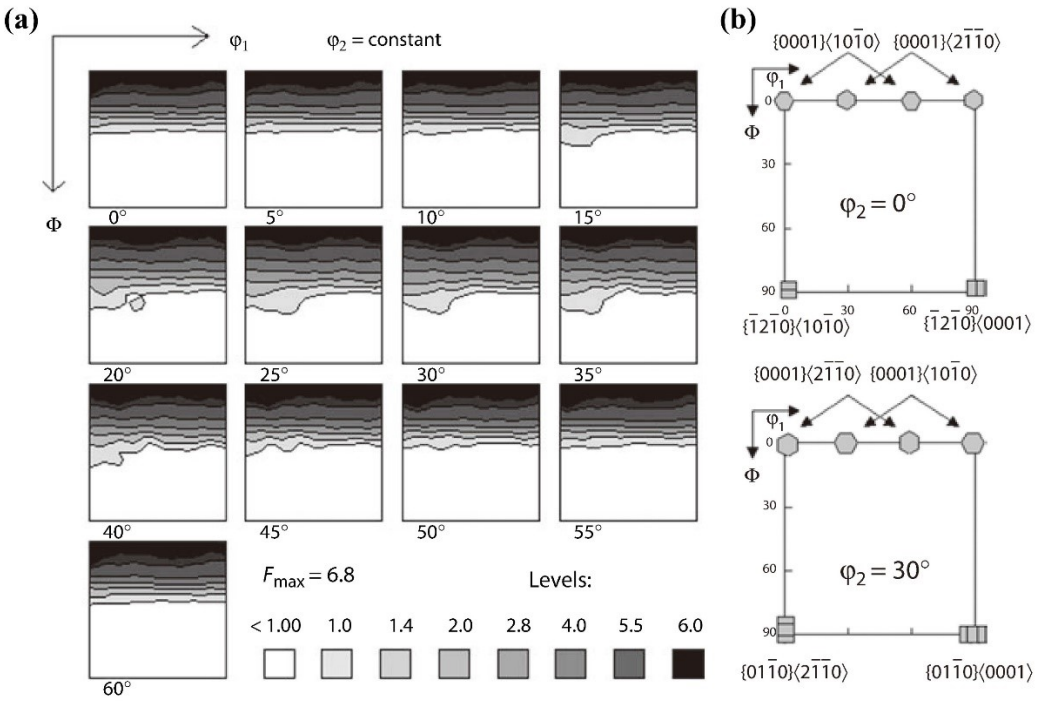

Figure 2.11 (a) example of ODF of Mg alloy and (b) the position of important orientations of hexagonal materials in Euler space [82].

A more commonly used orientation descriptor for Mg alloys, which is derived from the experimental measurement, is the pole figures. Poles, which represent the normal direction of various crystal planes, are projected onto the pole figure from the reference sphere to describe the variation of pole density with pole orientation [82,86]. The pole figures are stereographic projections, as shown in Figure 2.12(a). It is worth noting that pole figures, as the 2-D expression of 3-D information, suffer from limitations. For example, the position of (10-10) is needed to define the orientation of the crystal shown in Figure 2.12(b). Furthermore, the pole figures obtained from measurement are also incomplete owing to the nature of x-ray diffraction geometry [82]. Therefore, the ODF calculated from multiple pole figures is more precise although the pole figure is sufficient for most cases [86].

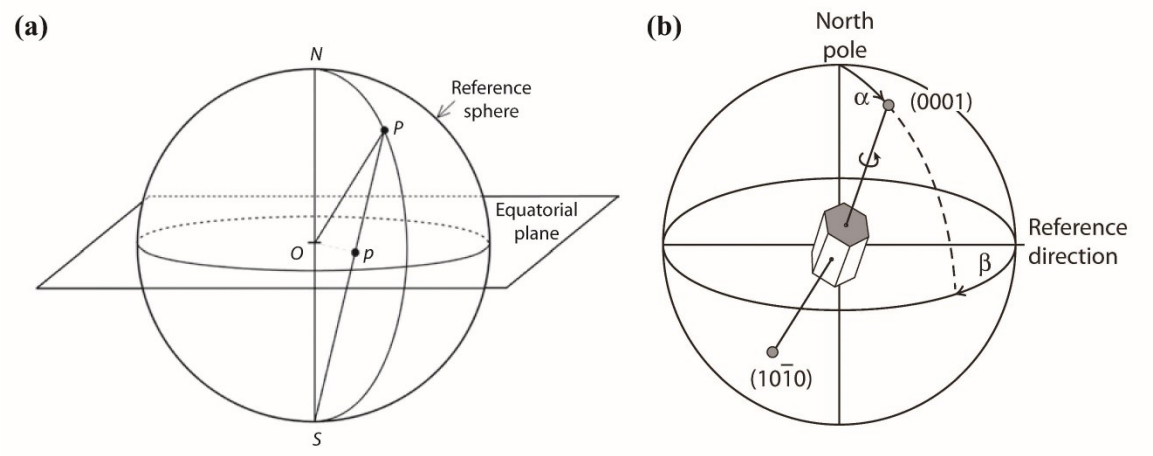

Figure 2.12 (a) schematic of stereographic projection and (b) orientation of the basal plane (0001) in a hexagonal crystal [82].

2.3.1.2.Measurement of texture

Based on the scale of the surveyed area and the consequent primary output data, the texture measurement can be divided as macro-texture and micro-texture. The former focuses on a large contiguous sample volume and acquires a profile of diffracted intensities through X-ray or neutron diffraction [82]. On the other hand, the complete crystallographic information is obtained through electron diffraction (usually electron backscattered diffraction (EBSD) in SEM) for the latter case [82]. Unlike the x-ray diffraction, which generates pole figures (schematics is shown in Figure 2.13(a)), the Kikuchi pattern originating from Bragg diffraction of electrons, as shown in Figure 2.13(b), can be interpreted as the crystal orientations [82].

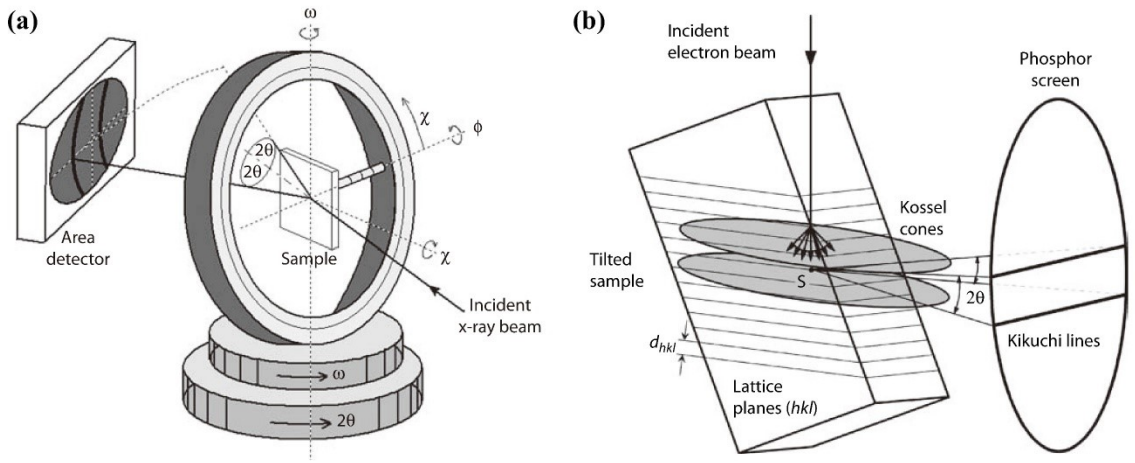

Figure 2.13 Schematics showing the (a) macro-texture measurement using XRD and (b) generation of Kikuchi pattern in SEM observation [82].

2.3.2.Basal texture

The basal texture is the most commonly observed texture in Mg alloy sheets, which is characterized as (0002) basal poles parallel to the ND of rolled sheets [8] (as demonstrated in Figure 2.14). The formation of basal texture is generally ascribed to the basal plane orienting rolling plane during deformation as the consequence of excessive basal slip activation [86]. In addition to that, it is also proposed by Jin et al. [87] and Jiang et al. [88] that the basal texture initiates through {10-12} twinning which reorients (0002) plan parallel to the RD. Then the basal texture is progressively developed during deformation through nucleation and growth of TDRX grains [87]. Finally, the basal texture is gradually strengthened owing to the better stability of basal grains on resisting recrystallization as well as the repetitive DRX process in subsequent deformation. For the former, the <c+a> slip is hard to be activated due to the high CRSS, and the <a> slip is geometrically suppressed owing to low resolved shear stress [87] thus, the lower dislocation density inhibits the recrystallization of basal grains. For the latter, DRX, especially CDRX, has been observed inheriting the orientation of parent basal grains and

contributing basal texture strengthening despite a minor fraction of DRXed grains with diverse orientations in the vicinity of grain boundaries [88]. Thus, during the multi-pass rolling, the new grains with non-basal orientations may easily be consumed by repeated DRX [87].

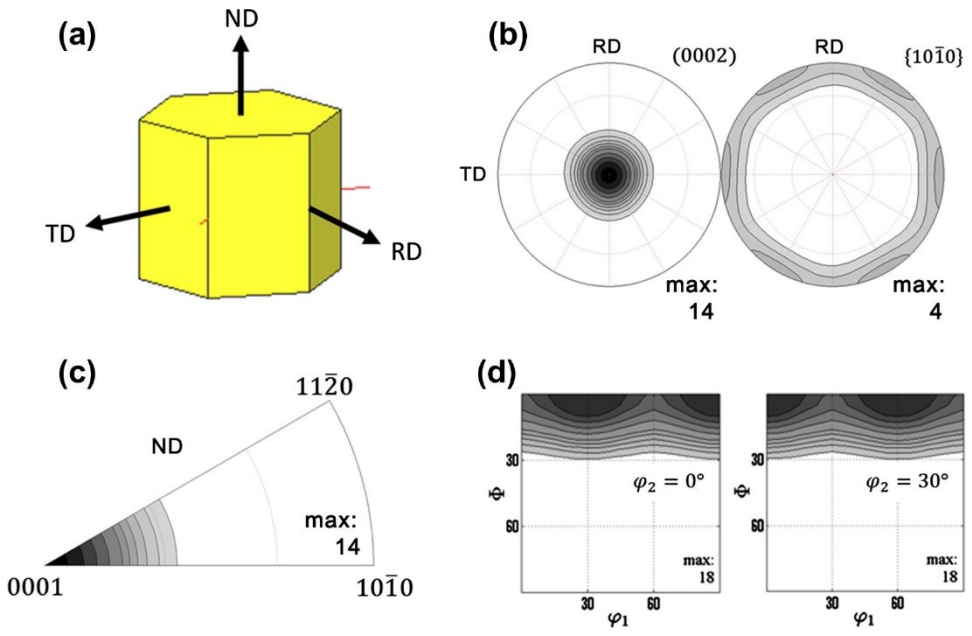

Figure 2.14 Example of a pure magnesium sheet texture obtained after hot rolling (400 °C/75% reduction) and annealing at 300 °C for 1 h represented schematically (a), using (b) recalculated (0 0 0 2) and pole figures, (c) inverse pole figure relative to ND, (d) ODF sections at $\varphi_2 = 0°$ and $\varphi_2 = 30°$ [89].

2.3.3.Non-basal textures

The two commonly observed non-basal patterns are the (0002) tilting towards the TD (TD-split texture) and the ND (ND-split texture) [8,90]. Their schematics and corresponding (0002) pole figures are shown in Figure 2.15.

The RD-split texture is widely reported in AZ31 [91,92], Mg-Li [93], Mg-Y [93,94], and Mg-Zn-Ca [95], Mg-Ce(-Zn) [90] and Mg-Gd(-Zn) [75] alloys subjecting to rolling or plane strain compression. The emergence of the RD-split component in deformed textures is attributed to the higher activity of <c+a> slip [92–94] and the promoted compression and

double twinning owing to the alloying element [37]. However, it has been observed that, upon annealing, the RD-split texture is transformed to the strong basal fiber [91] or a non-basal texture [75].

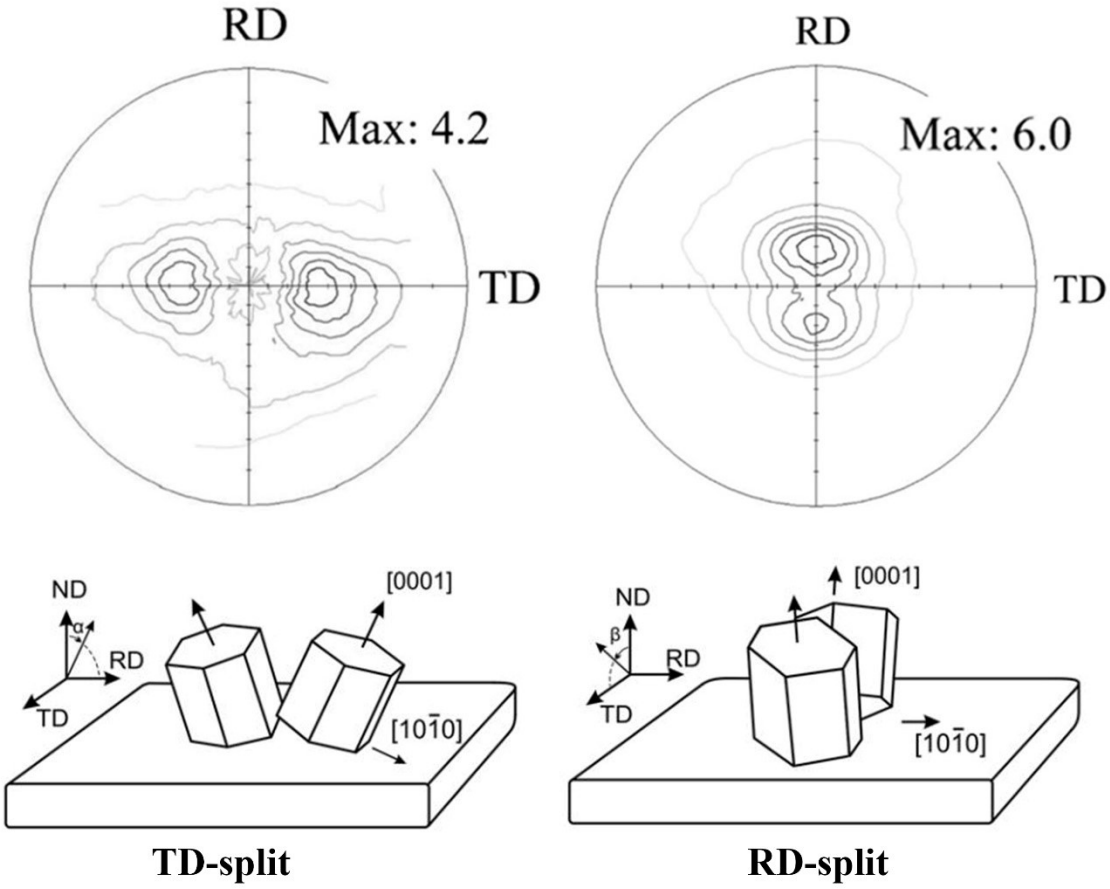

Figure 2.15 Schematics and (0002) pole figures showing the TD-split texture and RD-split texture. TD-split: rolled and subsequently annealed Mg–1.5Zn–0.2Ce. RD-split: rolled Mg–0.2Ce [8,90]

The TD-split texture, on the other hand, is commonly observed in RE-containing Mg alloys. It has been reported that Nd [49], Ce [96], Gd [97], and Ca [98] are capable of triggering the TD-split texture in Mg alloys. In addition, Zn is reported as an essential alloying element to amplify the effect of RE [75]. Jung et al. [99] have proposed that the usage of RE can be reduced in the Mg-Zn-RE system. However, the mechanism for the formation of TD-split texture upon annealing is still under debate. It has been proposed

that the PSN [75,90], bimodal structure [100], shear bands [77], twinning [101], solute drag effect brought by RE segregated along the grain boundaries (GBs) [102], the enhanced non-basal slip system activation [49,103], preferential nucleation of recrystallized grains [97], etc. are related to the TD-split texture formation. Moreover, since a considerable amount of RE (≥0.5 wt. % [84]) is commonly employed to guarantee the texture modification effect, the economical and sustainable alloying strategy is less considered.

2.3.4.Effect of texture on mechanical performance

In general, better ductility is expected in Mg alloys with weakened texture owing to the fact that plastic deformation can be achieved by the easy-activated basal slip, as discussed in 2.1.1. With the increased spread of grain orientations, there is good agreement of decreasing texture intensity correlating with maximum elongation to fracture [89,104]. In addition, the tension-compression yield asymmetry is also expected to be reduced due to the formation of non-basal texture, and the resulting enhanced formability has been validated by the Erichsen test [90,105], as seen in Figure 2.16.

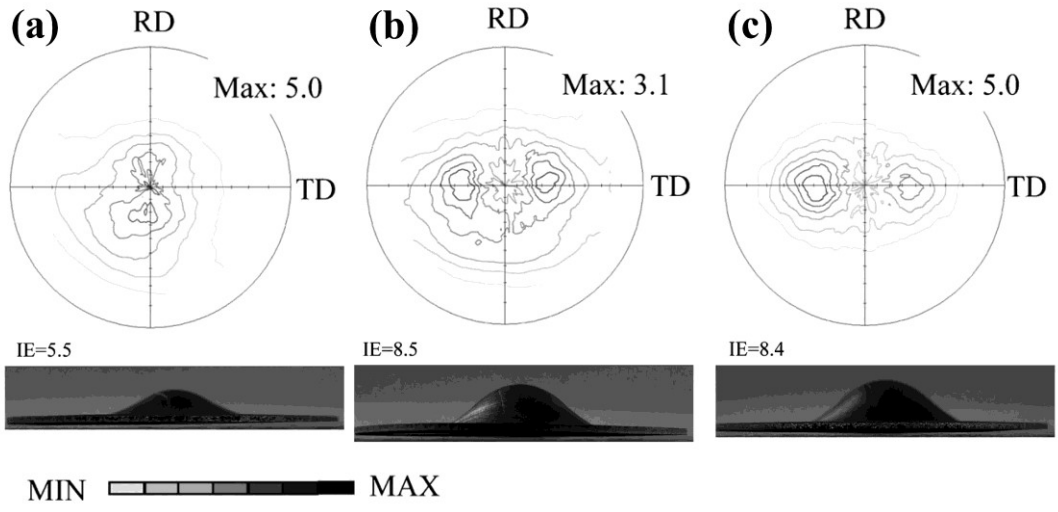

Figure 2.16 Modified sheet textures of rolled and subsequently annealed ZK10 magnesium alloys and the resulting tensile elongations to fracture at room temperature: (a) Mg–0.2Ce, (b) Mg–1.0Zn–0.2Ce, (c) Mg–2.0Zn–0.2Ce [90].

2.4. Texture modification of wrought Mg alloys

Given the detrimental effects brought by the strong basal texture on the formability of wrought Mg sheets, texture weakening (modification) is the prerequisite for the manufacture of Mg components. Two main routes have been focused on in studies dedicated to texture control: processing-oriented practices and alloying-related approaches [8]. Thus, in the following, texture weakening mechanisms and approaches for the wrought Mg sheet will be highlighted.

2.4.1.Texture modification mechanisms

Considerable efforts have been made by researchers to modify the strong basal texture of Mg alloys. However, the mechanism of the observed texture modification phenomenon has not been thoroughly explained due to the complexity of texture formation in magnesium alloys. This complexity stems from a complex deformation mechanism that combines slip and twinning and is further complicated by the texture evolution upon deformation and subsequent annealing. Here, the well-recognized mechanisms for various texture modifications are summarized.

Non-basal dislocation activation: Given the formation of basal texture in Mg alloys (section 2.3.2), the attenuation of the basal slip dominance needs to be considered. The activation of pyramidal <c+a> slip and the prismatic <a> slip has been associated with the texture modification in various Mg alloys. The formation of RD-split texture is explained as the consequence of promoted pyramidal <c+a> slip by experimental observation [91] and theoretical simulation [106]. This enhanced activation can be achieved by performing special processing procedures such as the HSR [107] that generates higher temperature, ECAR [108] that induces shear deformation. More commonly, the SFE and CRSS change

resulting from alloying element addition is accounted for by the motivated pyramidal <c+a> slip. The studies from Sandlobes et al. [109] and Yoo et al. [110] suggest that I_1 stacking faults act as heterogeneous nucleation sources for pyramidal <c+a> dislocations. Yuasa et al. [111] reported an increased γ_{us}(basal) in Mg-Zn-Ca alloy which leads to γ_{us}(basal)/γ_{us}(prism) close to 1. This ratio explains the basal texture weakening and the resulting formability improvement. Kim et al. [23] theoretically predicted that the activation of <c+a> slip system in Mg–Y alloys is related to the reduction of difference in the CRSSes between basal slip and non-basal <c+a> slip. Zhu et al. [22] found the connection between $CRSS_{prism}/CRSS_{basal}$ and the observed grain orientation rotation. In alloys exhibiting TD-split texture, prismatic <a> slip has been reported being the dominant deformation mechanism in TD-oriented grains upon deformation [49]. This phenomenon indicates that the TD-split texture is related to the promoted prismatic <a> slip, similar to the situation of titanium (Ti) alloys, which possesses a c/a less than Mg [86]. However, the mechanisms for the formation of TD-split texture as well as the activation of prismatic slip still need to be revealed by further investigation.

Deformation structure: Various deformation structures have been associated with the formation of weakened or non-basal texture, such as the contraction and secondary twinning [107,112]. However, their texture modification effect upon annealing needs to be investigated in detail. In addition, DRX also weakens the basal texture owing to grain refinement [88].

Solute segregation: The segregation of alloying elements, especially REs, has been related to the texture modification as described in 2.4.3. The beneficial effect on texture modification of alloying element is ascribed to the boundary mobility difference and the

consequent selective growth of basal and non-basal nuclei due to solute segregation [75], DRX suppression resulting from solute drag [113], and texture randomization related to reduced grain boundary energy [95]. On the other hand, precipitation contributes to the pinning of GBs and thus affects the recrystallization behavior and the related texture [84,114].

Recrystallization: Unlike DRX, which inherits orientation from the parent grain, the SRX affects the basal texture through the nucleation and growth of non-basal grains upon annealing. In the former case, PSN [81], DTIN [78], and SBIN [77] have been related to texture weakening as the consequence of orientation randomization. It is worth noting that those nucleation mechanisms only generate nuclei with broader angular distribution rather than forming a specific pattern since nucleation is not favoring a specific orientation. The preferential nucleation, although rarely observed, has been reported by Zhao [97] which leads to the TD-split texture of an Mg-Zn-Gd alloy. In addition, preferential grain growth has also been related to the formation of TD-split texture in Mg-Zn-Nd alloy [77]. Further study is crucial to understand the origin of preference of TD-split orientation upon recrystallization.

2.4.2.Texture weakening by processing

During deformation, the orientation of grains is rotated owing to the activation of various deformation mechanisms. Thus, to weaken or even alter the strong basal texture, shear deformation can be introduced to fabricate Mg alloys with weakened basal texture. Various special processing procedures have been performed by researchers [115]. Equal channel angular pressing (ECAP) has been applied to weaken the texture of the AZ31 bar [116]. Based on ECAP, equal channel angular rolling (ECAR) has been proposed to

fabricate large volumes of texture-controlled Mg alloy sheets [108]. Following the rolling, the shear strain is introduced by a customized ECAP die for sheet production. The texture weakening mechanism is similar to the ECAP, in which RD-split texture forms after deformation due to the promoted <c+a> slip and DRX [116]. The ECAR process and the resulting texture are shown in Figure 2.17(a).

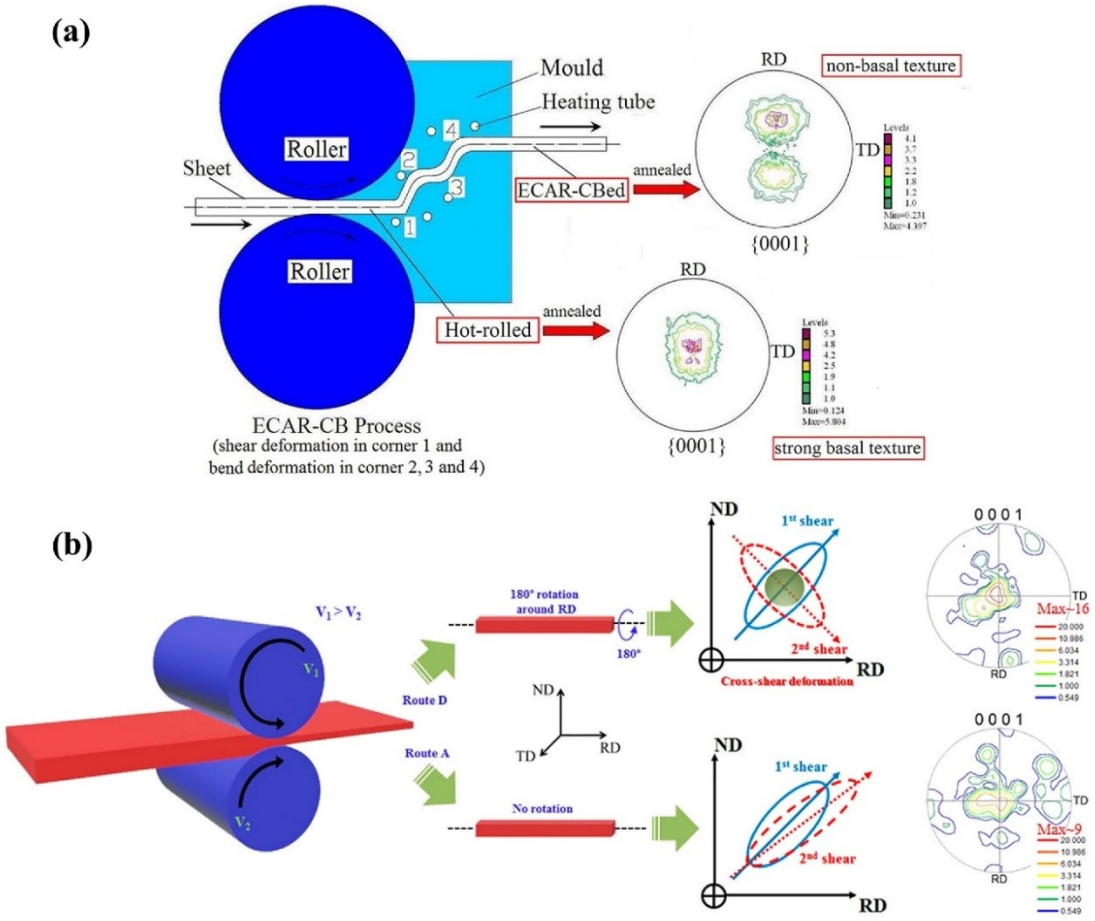

Figure 2.17 The schematic and resulting texture of (a) ECAR process [109] and (b) DSR process [108].

Another sheet fabrication procedure is the differential speed rolling (DSR), as shown in Figure 2.17(b). The asymmetric deformation due to the different rotational speeds between upper and lower rollers introduces shear deformation during rolling. In combination with the rotation of the sample between adjacent passes of DSR the basal

texture can be randomized and reach values of the ultimate tensile strength and elongation to failure 333MPa and 21%, respectively [116]. In addition, considerable efforts have been made on developing new processing techniques, such as the pre-twinning method [117], high-speed rolling (HSR) [107], wave-shaped die rolling [118], etc.

2.4.3.Texture weakening by alloying

Compared to the processing methods, which need complicated instruments or customized equipment, the alloying-oriented approaches are favored in Mg sheet production [84]. Both RE and non-RE elements have shown texture weakening effect, as mentioned in 2.3.3. The typical alloying elements are considered in the following.

2.4.3.1.RE elements

RE elements are well-known as the most effective solution to weaken, modify or even alter the strong basal texture of Mg alloys, the overall effect of commonly used RE is summarized in Figure 2.18.

Yttrium (Y): Y has a decent solubility limit of 12.4 wt. % in Mg alloys [119]. Thus, the texture modification brought by Y is closely related to the interaction of Y atoms with dislocations and GBs [120]. The critical content of Y to trigger noticeable texture weakening in the Mg-Y system is around 0.6 wt. % [120]. Higher Y addition (2.7 wt. %) can promote the activation of prismatic <a> slip [102]. It has been reported that the Y addition mainly contributes to the formation of RD-split texture [93,94,102] although a similar texture can also be acquired in AZ31 [91]. Compared to other RE elements, Y is less effective in terms of texture weakening. This is explained as the consequence of the weaker atomic interaction between Mg and Y [119].

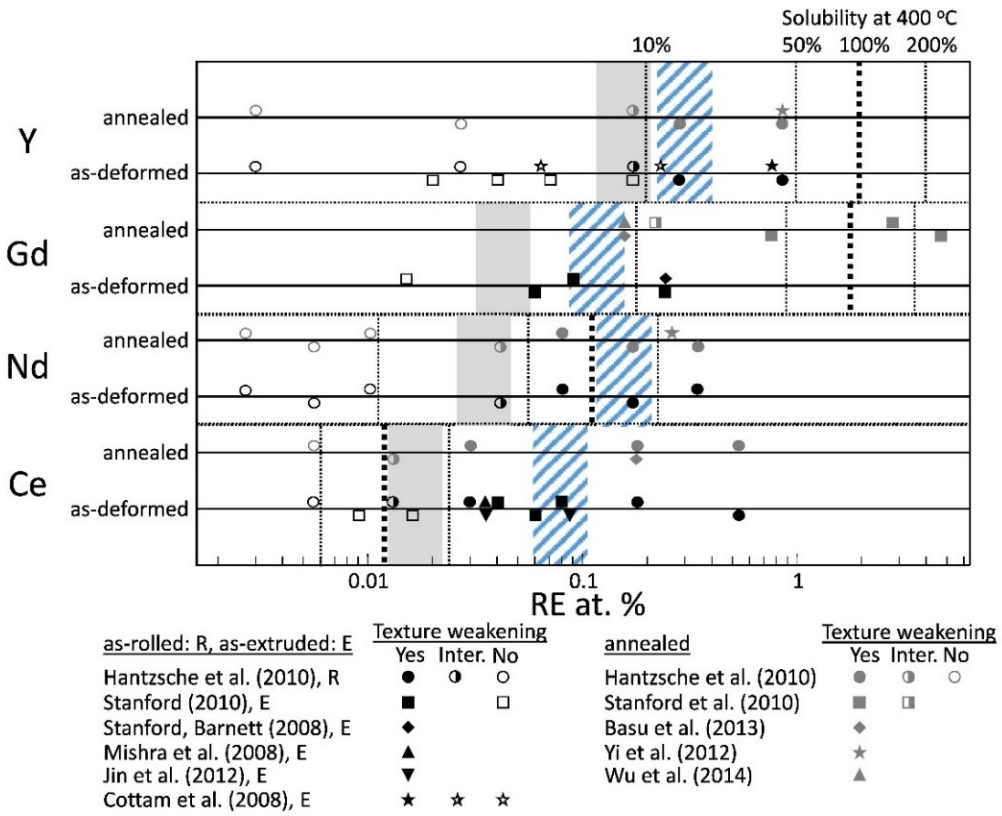

Figure 2.18 Critical amount of RE necessary for texture weakening in the Mg–RE system during deformation and post-annealing conditions at about 400 °C. Gray shaded: the critical overall amount of RE in Mg–RE alloys; blue shaded: segregation of RE at GBs estimated from calculations [100].

Cerium (Ce): Despite exhibiting the lowest solubility limit in Mg-Ce (0.5 wt. %), significant texture modification can be archived by diluted addition of Ce (around 0.2 wt.%) [25]. On the other hand, the Ce-containing precipitates could affect texture by PSN when particle size is higher than 1 μm or pinning effect when precipitates are fine and evenly distributed [84]. Non-basal textures develop upon annealing at a wide temperature range in Mg-Ce alloys (150 ~ 400 °C) [96,121]. However, the formability of Ce-containing Mg alloys is curtailed due to the low solubility of Ce and the resulting brittle precipitates [104]. In terms of texture pattern, the Ce generates both RD-split and TD-split texture. The former is attributed to the enhanced <c+a> slip yet the mechanism for the latter is still unclear [84].

Gadolinium (Gd): Gd is one of the most well-investigated elements in RE-containing Mg alloys [75,122]. The Gd is effective in solid solution due to the suppression of precipitation resulting from the high solubility of Gd in Mg [84]. The texture weakening initiates with 0.38 wt. % addition of Gd [120]. With increasing Gd content, various non-basal textures are observed [75,104]. For rolled sheets subjected to post-deformation annealing, an encouraging TD-split texture with reduced intensity is commonly identified [97,104]. However, no decisive mechanism has been widely acknowledged by researchers.

Neodymium (Nd): The critical content of Nd to trigger noticeable texture weakening is around 0.24 wt. % [112]. The Nd possesses moderate solubility and texture weakening effect according to T. Al-Samman et al.'s compression of Gd, Ce, La, Nd, and mischmetal [104]. It is noteworthy that a shift in dislocation dynamics has been observed in Nd-containing alloys, i.e., from a basal <a> dominance to a prismatic <a> dominance [49,80]. This phenomenon is explained as the consequence of inhibition of basal <a> and cross-slip promotion of prismatic <a> [80].

2.4.3.2.Non-RE elements

Recently, the texture modification brought by non-RE element addition has attracted researchers' attention for the potential cost reduction. Except for the conventional AZ31, a new alloying strategy has been proposed to produce wrought Mg alloy with modified texture by adding non-RE elements.

Zinc (Zn): Although separate Zn additions have been rarely investigated, Zn is crucial for the texture modification for the ternary and quaternary Mg alloys. It has been validated that the alloying Zn amplifies the effect of diluted RE [75]. The Zn/RE ratio can also affect the texture of Mg alloys [113,123].

Calcium (Ca): Ca, which has exhibited significant texture modification in Mg-Zn-Ca alloys [95], is a potential alternative to the expensive RE because of the similar atomic radius of Ca and RE [99]. Moreover, the plastic anisotropy and resultant basal texture weakening are ascribed to the stacking fault energy (SFE) modification in the Mg-Zn-Ca system. However, the ductility of Ca-containing Mg alloys suffers from the brittle precipitates along the GBs owing to the segregation and subsequent precipitation of Ca [124].

Lithium (Li): The addition of Lithium preserves the lightweight property of Mg alloys while achieving non-basal texture resulted from a reduced c/a ratio [125]. It is also reported by Al-Samman that the Mg-4Li exhibits remarkable ductility at ambient temperature with a total reduction of 86% upon cold rolling [126].

2.5. Summary

Based on the above literature survey, the production of Mg alloy sheets with better formability requires texture modification aiming at the formation of non-basal texture [8]. Meanwhile, for the practical application of texture-modified Mg sheets in the automobile industry, the complexity of fabrication process, as well as the consumption of energy and resources, should also be limited [3]. Due to the additional investment in customized equipment and the requirement of deformation at higher elevated temperature, the various texture weakening processing procedures mentioned in 2.4.2 are less attractive. On the other hand, the alloying approach suffers from a potential cost increase owing to the excessive addition of alloying elements, especially RE. A wide variety of RE with different concentration has been proposed by researchers, yet most studies were reported as “lean Mg alloy” with RE added more than 0.5 wt. % [127]. Therefore, better alloying strategies

featuring a further reduced level of RE or employment of alternative non-RE elements, based on an in-depth understanding of texture modification mechanism in lean Mg alloy, are essential for the development of formable Mg alloy sheets manufactured by conventional multi-pass rolling.

2.6. Reference

[1]C.J. Allegre, J.-P. Poirier, E. Humler, A.W. Hofmann, The chemical composition of the Earth, Earth Planet. Sci. Lett. 134 (1995) 515–526.

[2]B.L. Mordike, T. Ebert, Magnesium Properties - applications - potential, Mater. Sci. Eng. A. 302 (2001) 37–45. https://doi.org/10.1016/S0921-5093(00)01351-4.

[3]W.J. Joost, P.E. Krajewski, Towards magnesium alloys for high-volume automotive applications, Scr. Mater. 128 (2017) 107–112. https://doi.org/10.1016/j.scriptamat.2016.07.035.

[4]J.P. Weiler, A review of magnesium die-castings for closure applications, J. Magnes. Alloy. 7 (2019) 297–304. https://doi.org/10.1016/j.jma.2019.02.005.

[5]D. Hull, D.J. Bacon, Introduction to dislocations, Elsevier, 2011.

[6]B.L. Mordike, K.U. Kainer, Magnesium Alloys and their application, Weinheim: Wiley-VCH, 2000.

[7]M. Gupta, N.M.L. Sharon, Magnesium, magnesium alloys and magnesium composites, 2011.

[8]J.F. Nie, K.S. Shin, Z.R. Zeng, Microstructure, Deformation, and Property of Wrought Magnesium Alloys, Springer US, 2020. https://doi.org/10.1007/s11661-020-05974-z.

[9]H. Conrad, W.D. Robertson, Effect of temperature on the flow stress and strain-hardening coefficient of magnesium single crystals, Jom. 9 (1957) 503–512.

[10]P.W. Bakarian, C.H. Mathewson, Slip Arid Twinning In Magnesium Single Crystals At Elevated Temperatures, (1943).

[11]E. Schmid, Beiträge zur physik und metallographie des magnesiums, Zeitschrift Für Elektrochemie Und Angew. Phys. Chemie. 37 (1931) 447–459.

[12]R.E. Reed-Hill, W.D. Robertson, Deformation of magnesium single crystals by nonbasal slip, Jom. 9 (1957) 496–502.

[13]P.W. Flynn, J. Mote, J.E. Dorn, On the thermally activated mechanism of prismatic slip in magnesium single crystals, Trans. Metall. Soc. AIME. 221 (1961) 1148–1154.

[14]C.M. Byer, B. Li, B. Cao, K.T. Ramesh, Microcompression of single-crystal magnesium, Scr. Mater. 62 (2010) 536–539. https://doi.org/10.1016/j.scriptamat.2009.12.017.

[15]K.Y. Xie, Z. Alam, A. Caffee, K.J. Hemker, Pyramidal i slip in c-axis compressed Mg single crystals, Scr. Mater. 112 (2016) 75–78. https://doi.org/10.1016/j.scriptamat.2015.09.016.

[16]H. Tonda, K. Nakamura, K. Takashima, {1122}〈1123〉 slip in magnesium single crystal, J. Japan Inst. Light Met. 42 (1992) 765–771. https://doi.org/10.2464/jilm.42.765.

[17]R. Von Mises, Mechanics of the ductile form changes of crystals, Zeitschrift Fur Angew. Math. Und Mech. 8 (1928) 161–185.

[18]J.F.W. Bishop, R. Hill, XLVI. A theory of the plastic distortion of a polycrystalline aggregate under combined stresses., London, Edinburgh, Dublin Philos. Mag. J. Sci. 42 (1951) 414–427. https://doi.org/10.1080/14786445108561065.

[19]Y.B. Chun, C.H.J. Davies, Investigation of prism 〈a〉 slip in warm-rolled AZ31 alloy, Metall. Mater. Trans. A Phys. Metall. Mater. Sci. 42 (2011) 4113–4125. https://doi.org/10.1007/s11661-011-0800-2.

[20]A. Akhtar, E. Teghtsoonian, Solid solution strengthening of magnesium single crystals-I alloying behaviour in basal slip, Acta Metall. 17 (1969) 1339–1349. https://doi.org/10.1016/0001-6160(69)90151-5.

[21]A. Akhtar, E. Teghtsoonian, Solid solution strengthening of magnesium single crystals-ii the effect of solute on the ease of prismatic slip, Acta Metall. 17 (1969) 1351–1356. https://doi.org/10.1016/0001-6160(69)90152-7.

[22]G. Zhu, L. Wang, H. Zhou, J. Wang, Y. Shen, P. Tu, H. Zhu, W. Liu, P. Jin, X. Zeng, Improving ductility of a Mg alloy via non-basal <a> slip induced by Ca addition, Int. J. Plast. 120 (2019) 164–179. https://doi.org/10.1016/j.ijplas.2019.04.020.

[23]K.H. Kim, J.B. Jeon, N.J. Kim, B.J. Lee, Role of yttrium in activation of “c + a” slip in magnesium: An atomistic approach, Scr. Mater. 108 (2015) 104–108. https://doi.org/10.1016/j.scriptamat.2015.06.028.

[24]N. Stanford, M.R. Barnett, Solute strengthening of prismatic slip, basal slip and {10$\bar{1}$2} twinning in Mg and Mg-Zn binary alloys, Int. J. Plast. 47 (2013) 165–181. https://doi.org/10.1016/j.ijplas.2013.01.012.

[25]Y. Chino, M. Kado, M. Mabuchi, Enhancement of tensile ductility and stretch formability of magnesium by addition of 0.2 wt%(0.035 at%)Ce, Mater. Sci. Eng. A. 494 (2008) 343–349. https://doi.org/10.1016/j.msea.2008.04.059.

[26]M.R. Barnett, Twinning and its role in wrought magnesium alloys, (2012) 105–143. https://doi.org/10.1533/9780857093844.1.105.

[27]J.W. Christian, S. Mahajan, Deformation twinning, Prog. Mater. Sci. 39 (1995) 1–157.

[28]M.R. Barnett, Twinning and the ductility of magnesium alloys. Part I: “Tension” twins, Mater. Sci. Eng. A. 464 (2007) 1–7. https://doi.org/10.1016/j.msea.2006.12.037.

[29]M.R. Barnett, Twinning and the ductility of magnesium alloys. Part II. “Contraction” twins, Mater. Sci. Eng. A. 464 (2007) 8–16. https://doi.org/10.1016/j.msea.2007.02.109.

[30]P. Cizek, M.R. Barnett, Characteristics of the contraction twins formed close to the fracture surface in Mg-3Al-1Zn alloy deformed in tension, Scr. Mater. 59 (2008) 959–962. https://doi.org/10.1016/j.scriptamat.2008.06.041.

[31]E. Roberts, P.G. Partridge, The accommodation around $\{10\bar{1}2\}$ $\langle\bar{1}011\rangle$ twins in magnesium, Acta Metall. 14 (1966) 513–527. https://doi.org/10.1016/0001-6160(66)90319-1.

[32]M.D. Nave, M.R. Barnett, Microstructures and textures of pure magnesium deformed in plane-strain compression, Scr. Mater. 51 (2004) 881–885. https://doi.org/10.1016/j.scriptamat.2004.07.002.

[33]J. Koike, Enhanced deformation mechanisms by anisotropic plasticity in polycrystalline Mg alloys at room temperature, Metall. Mater. Trans. A Phys. Metall. Mater. Sci. 36 (2005) 1689–1696. https://doi.org/10.1007/s11661-005-0032-4.

[34] tienne Martin, R. K., J. J., Deformation Structures and Recrystallization in Magnesium Alloys, Magnes. Alloy. - Des. Process. Prop. (2011). https://doi.org/10.5772/13023.

[35]I. Basu, T. Al-Samman, Twin recrystallization mechanisms in magnesium-rare earth alloys, Acta Mater. 96 (2015) 111–132. https://doi.org/10.1016/j.actamat.2015.05.044.

[36]A. Rollett, F.J. Humphreys, G.S. Rohrer, M. Hatherly, Recrystallization and related annealing phenomena, Elsevier, 2004.

[37]S. Sandlöbes, S. Zaefferer, I. Schestakow, S. Yi, R. Gonzalez-Martinez, On the role of non-basal deformation mechanisms for the ductility of Mg and Mg-Y alloys, Acta Mater. 59 (2011) 429–439. https://doi.org/10.1016/j.actamat.2010.08.031.

[38]K. Hazeli, J. Cuadra, P.A. Vanniamparambil, A. Kontsos, In situ identification of twin-related bands near yielding in a magnesium alloy, Scr. Mater. 68 (2013) 83–86. https://doi.org/10.1016/j.scriptamat.2012.09.009.

[39]M.R. Barnett, M.D. Nave, C.J. Bettles, Deformation microstructures and textures of some cold rolled Mg alloys, Mater. Sci. Eng. A. 386 (2004) 205–211. https://doi.org/10.1016/j.msea.2004.07.030.

[40]A. KELLY, K.M. KNOWLES, Crystallography and Crystal Defects, 1997. https://doi.org/10.1002/9783527644131.ch10.

[41]J.R. Luo, A. Godfrey, W. Liu, Q. Liu, Twinning behavior of a strongly basal textured AZ31 Mg alloy during warm rolling, Acta Mater. 60 (2012) 1986–1998. https://doi.org/10.1016/j.actamat.2011.12.017.

[42]M.R. Barnett, Z. Keshavarz, M.D. Nave, Microstructural features of rolled Mg-3Al-1Zn, Metall. Mater. Trans. A Phys. Metall. Mater. Sci. 36 (2005) 1697–1704. https://doi.org/10.1007/s11661-005-0033-3.

[43]K.D. Molodov, T. Al-Samman, D.A. Molodov, G. Gottstein, On the role of anomalous twinning in the plasticity of magnesium, Acta Mater. 103 (2016) 711–723. https://doi.org/10.1016/j.actamat.2015.10.043.

[44]S. Wang, C. Schuman, L. Bao, J.S. Lecomte, Y. Zhang, J.M. Raulot, M.J. Philippe, X. Zhao, C. Esling, Variant selection criterion for twin variants in titanium alloys deformed by rolling, Acta Mater. 60 (2012) 3912–3919. https://doi.org/10.1016/j.actamat.2012.03.046.

[45]C. Guo, Y. Xiao, R. Xin, Evaluation of Twinning Behavior in Rolling of Mg Alloys with Three Kinds of Textures by a Generalized Schmid Factor, Met. Mater. Int. 26 (2019) 1366–1372. https://doi.org/10.1007/s12540-019-00378-0.

[46]M. Meyers, A. Engineering, S. Diego, E. Conferences, H. Senior, S. Award, T.M.S.D. Scientist, E. Awards, L.H. Award, K. Chawla, M. Science, Mechanical behavior of materials, 2009. https://doi.org/10.5860/choice.46-6830.

[47]R. Xin, M. Wang, X. Huang, C. Guo, Q. Liu, Observation and Schmid factor analysis of multiple twins in a warm-rolled Mg-3Al-1Zn alloy, Mater. Sci. Eng. A. 596 (2014) 41–44. https://doi.org/10.1016/j.msea.2013.12.030.

[48]Y.B. Chun, M. Battaini, C.H.J. Davies, S.K. Hwang, Distribution characteristics of in-grain misorientation axes in cold-rolled commercially pure titanium and their correlation with active slip modes, Metall. Mater. Trans. A Phys. Metall. Mater. Sci. 41 (2010) 3473–3487. https://doi.org/10.1007/s11661-010-0410-4.

[49]X. Zeng, P. Minárik, P. Dobroň, D. Letzig, K.U. Kainer, S. Yi, Role of deformation mechanisms and grain growth in microstructure evolution during recrystallization of Mg-Nd based alloys, Scr. Mater. 166 (2019) 53–57. https://doi.org/10.1016/j.scriptamat.2019.02.045.

[50]A. Khosravani, D.T. Fullwood, B.L. Adams, T.M. Rampton, M.P. Miles, R.K. Mishra, Nucleation and propagation of { 1 0 1 ¯ 2 } twins in AZ31 magnesium alloy, Acta Mater. 100 (2015) 202–214. https://doi.org/10.1016/j.actamat.2015.08.024.

[51]J.F. Nye, Some geometrical relations in dislocated crystals, Acta Metall. 1 (1953) 153–162. https://doi.org/10.1016/0001-6160(53)90054-6.

[52]C.J. Gardner, B.L. Adams, J. Basinger, D.T. Fullwood, EBSD-based continuum dislocation microscopy, Int. J. Plast. 26 (2010) 1234–1247. https://doi.org/10.1016/j.ijplas.2010.05.008.

[53]W. Pantleon, Resolving the geometrically necessary dislocation content by conventional electron backscattering diffraction, Scr. Mater. 58 (2008) 994–997. https://doi.org/10.1016/j.scriptamat.2008.01.050.

[54]A. Arsenlis, D.M. Parks, Crystallographic aspects of geometrically-necessary and statistically-stored dislocation density, Acta Mater. 47 (1999) 1597–1611. https://doi.org/10.1016/S1359-6454(99)00020-8.

[55]P.D. Littlewood, T.B. Britton, A.J. Wilkinson, Geometrically necessary dislocation density distributions in Ti-6Al-4V deformed in tension, Acta Mater. 59 (2011) 6489–6500. https://doi.org/10.1016/j.actamat.2011.07.016.

[56]T. Ben Britton, S. Birosca, M. Preuss, A.J. Wilkinson, Electron backscatter diffraction study of dislocation content of a macrozone in hot-rolled Ti-6Al-4V alloy, Scr. Mater. 62 (2010) 639–642. https://doi.org/10.1016/j.scriptamat.2010.01.010.

[57]C. Zhu, T. Harrington, G.T. Gray, K.S. Vecchio, Dislocation-type evolution in quasi-statically compressed polycrystalline nickel, Acta Mater. 155 (2018) 104–116. https://doi.org/10.1016/j.actamat.2018.05.022.

[58]M.B. Bever, D.L. Holt, A.L. Titchener, The stored energy of cold work, Prog. Mater. Sci. 17 (1973) 5–177.

[59]M.O. Pekguleryuz, Current developments in wrought magnesium alloys, in: M. Barnett (Ed.), Adv. Wrought Magnes. Alloy., Woodhead Publishing, 2012: pp. 3–62. https://doi.org/http://dx.doi.org/10.1533/9780857093844.1.3.

[60]R. Kaibyshev, Dynamic recrystallization in magnesium alloys, Woodhead Publishing Limited, 2012. https://doi.org/10.1533/9780857093844.1.186.

[61]K. Xia, J.T. Wang, X. Wu, G. Chen, M. Gurvan, Equal channel angular pressing of magnesium alloy AZ31, Mater. Sci. Eng. A. 410–411 (2005) 324–327. https://doi.org/10.1016/j.msea.2005.08.123.

[62]A.G. Beer, M.R. Barnett, Microstructural development during hot working of Mg-3Al-1Zn, Metall. Mater. Trans. A Phys. Metall. Mater. Sci. 38 (2007) 1856–1867. https://doi.org/10.1007/s11661-007-9207-5.

[63]O. Sitdikov, R. Kaibyshev, Dislocation glide and dynamic recrystallization in LiF single crystals, Mater. Sci. Eng. A. 328 (2002) 147–155. https://doi.org/10.1016/S0921-5093(01)01691-4.

[64]É. Martin, J.J. Jonas, Evolution of microstructure and microtexture during the hot deformation of Mg-3% Al, Acta Mater. 58 (2010) 4253–4266. https://doi.org/10.1016/j.actamat.2010.04.017.

[65]A. Galiyev, R. Kaibyshev, G. Gottstein, Correlation of plastic deformation and dynamic recrystallization in magnesium alloy ZK60, Acta Mater. 49 (2001) 1199–1207. https://doi.org/10.1016/S1359-6454(01)00020-9.

[66]R. Kaibyshev, K. Shipilova, F. Musin, Y. Motohashi, Continuous dynamic recrystallization in an Al-Li-Mg-Sc alloy during equal-channel angular extrusion, Mater. Sci. Eng. A. 396 (2005) 341–351. https://doi.org/10.1016/j.msea.2005.01.053.

[67]A.S.H. Kabir, M. Sanjari, J. Su, I.H. Jung, S. Yue, Effect of strain-induced precipitation on dynamic recrystallization in Mg-Al-Sn alloys, Mater. Sci. Eng. A. 616 (2014) 252–259. https://doi.org/10.1016/j.msea.2014.08.032.

[68]J. Su, S. Kaboli, A.S.H. Kabir, I.-H.H. Jung, S. Yue, Effect of dynamic precipitation and twinning on dynamic recrystallization of micro-alloyed Mg-Al-Ca alloys, Mater. Sci. Eng. A. 587 (2013) 27–35. https://doi.org/10.1016/j.msea.2013.08.019.

[69]X. Yang, H. Miura, T. Sakai, Dynamic evolution of new grains in magnesium alloy AZ31 during hot deformation, Mater. Trans. 44 (2003) 197–203. https://doi.org/10.2320/matertrans.44.197.

[70]D.K. Sun, C.P. Chang, P.W. Kao, Microstructural aspects of grain boundary bulge in a dynamically recrystallized Mg-Al-Zn alloy, Metall. Mater. Trans. A Phys. Metall. Mater. Sci. 41 (2010) 1864–1870. https://doi.org/10.1007/s11661-010-0220-8.

[71]S. Yi, I. Schestakow, S. Zaefferer, Twinning-related microstructural evolution during hot rolling and subsequent annealing of pure magnesium, Mater. Sci. Eng. A. 516 (2009) 58–64. https://doi.org/10.1016/j.msea.2009.03.015.

[72]O. Sitdikov, Dynamic recrystallization based on twinning in coarse-grained Mg, in: Inst. Met. Superplast. Probl. Khalturina//Materials Sci. Forum, 2003: p. 422.

[73]J. Victoria-Hernández, S. Yi, D. Klaumünzer, D. Letzig, Recrystallization behavior and its relationship with deformation mechanisms of a hot rolled Mg-Zn-Ca-Zr alloy, Mater. Sci. Eng. A. 761 (2019). https://doi.org/10.1016/j.msea.2019.138054.

[74]T. Sakai, A. Belyakov, R. Kaibyshev, H. Miura, J.J. Jonas, Dynamic and post-dynamic recrystallization under hot, cold and severe plastic deformation conditions, Prog. Mater. Sci. 60 (2014) 130–207. https://doi.org/10.1016/j.pmatsci.2013.09.002.

[75]I. Basu, T. Al-Samman, Triggering rare earth texture modification in magnesium alloys by addition of zinc and zirconium, Acta Mater. 67 (2014) 116–133. https://doi.org/10.1016/j.actamat.2013.12.015.

[76]K.Y. Zhu, D. Chaubet, B. Bacroix, F. Brisset, A study of recovery and primary recrystallization mechanisms in a Zr-2Hf alloy, Acta Mater. 53 (2005) 5131–5140. https://doi.org/10.1016/j.actamat.2005.07.034.

[77]D. Guan, W.M. Rainforth, J. Gao, L. Ma, B. Wynne, Individual effect of recrystallisation nucleation sites on texture weakening in a magnesium alloy: Part 2- shear bands, Acta Mater. 145 (2018) 399–412. https://doi.org/10.1016/j.actamat.2017.12.019.

[78]D. Guan, W.M. Rainforth, J. Gao, J. Sharp, B. Wynne, L. Ma, Individual effect of recrystallisation nucleation sites on texture weakening in a magnesium alloy: Part 1- double twins, Acta Mater. 135 (2017) 14–24. https://doi.org/10.1016/j.actamat.2017.06.015.

[79]É. Martin, R.K. Mishra, J.J. Jonas, Effect of twinning on recrystallisation textures in deformed magnesium alloy AZ31, Philos. Mag. 91 (2011) 3613–3626. https://doi.org/10.1080/14786435.2011.588613.

[80]J.P. Hadorn, K. Hantzsche, S. Yi, J. Bohlen, D. Letzig, S.R. Agnew, Effects of solute and second-phase particles on the texture of Nd-containing Mg alloys, Metall. Mater. Trans. A Phys. Metall. Mater. Sci. 43 (2012) 1363–1375. https://doi.org/10.1007/s11661-011-1018-z.

[81]J.D. Robson, D.T. Henry, B. Davis, Particle effects on recrystallization in magnesium-manganese alloys: Particle-stimulated nucleation, Acta Mater. 57 (2009) 2739–2747. https://doi.org/10.1016/j.actamat.2009.02.032.

[82]O. Engler, V. Randle, O. Engler, Introduction to Texture Analysis,Macrotexture,Microtexture,and Orientation Mapping, CRC press, 2000.

[83]Q. Wang, B. Jiang, D. Chen, Z. Jin, L. Zhao, Q. Yang, G. Huang, F. Pan, Strategies for enhancing the room-temperature stretch formability of magnesium alloy sheets: a review, J. Mater. Sci. (2021). https://doi.org/10.1007/s10853-021-06067-x.

[84]A. Imandoust, C.D. Barrett, T. Al-Samman, K.A. Inal, H. El Kadiri, A review on the effect of rare-earth elements on texture evolution during processing of magnesium alloys, J. Mater. Sci. 52 (2017) 1–29. https://doi.org/10.1007/s10853-016-0371-0.

[85]H.J. Bunge, Three-dimensional texture analysis, Int. Mater. Rev. 32 (1987) 265–291.

[86]Y.N. Wang, J.C. Huang, Texture analysis in hexagonal materials, Mater. Chem. Phys. 81 (2003) 11–26. https://doi.org/10.1016/s0254-0584(03)00168-8.

[87]Q. Jin, S.-Y. Shim, S.-G. Lim, Correlation of microstructural evolution and formation of basal texture in a coarse grained Mg–Al alloy during hot rolling, Scr. Mater. 55 (2006) 843–846. https://doi.org/10.1016/j.scriptamat.2006.05.040.

[88]M.G. Jiang, C. Xu, H. Yan, G.H. Fan, T. Nakata, C.S. Lao, R.S. Chen, S. Kamado, E.H. Han, B.H. Lu, Unveiling the formation of basal texture variations based on twinning and dynamic recrystallization in AZ31 magnesium alloy during extrusion, Acta Mater. 157 (2018) 53–71. https://doi.org/10.1016/j.actamat.2018.07.014.

[89]J. Hirsch, T. Al-Samman, Superior light metals by texture engineering: Optimized aluminum and magnesium alloys for automotive applications, Acta Mater. 61 (2013) 818–843. https://doi.org/10.1016/j.actamat.2012.10.044.

[90]Y. Chino, X. Huang, K. Suzuki, K. Sassa, M. Mabuchi, Influence of Zn concentration on stretch formability at room temperature of Mg-Zn-Ce alloy, Mater. Sci. Eng. A. 528 (2010) 566–572. https://doi.org/10.1016/j.msea.2010.09.081.

[91]S.R. Agnew, Ö. Duygulu, Plastic anisotropy and the role of non-basal slip in magnesium alloy AZ31B, Int. J. Plast. 21 (2005) 1161–1193. https://doi.org/http://dx.doi.org/10.1016/j.ijplas.2004.05.018.

[92]J. Victoria-Hernandez, S. Yi, J. Bohlen, G. Kurz, D. Letzig, The influence of the recrystallization mechanisms and grain growth on the texture of a hot rolled AZ31 sheet during subsequent isochronal annealing, J. Alloys Compd. 616 (2014) 189–197. https://doi.org/10.1016/j.jallcom.2014.07.083.

[93]S.R. Agnew, M.H. Yoo, C.N. Tomé, Application of texture simulation to understanding mechanical behavior of Mg and solid solution alloys containing Li or Y, Acta Mater. 49 (2001) 4277–4289. https://doi.org/http://dx.doi.org/10.1016/S1359-6454(01)00297-X.

[94]Y.M. Kim, C. Mendis, T. Sasaski, D. Letzig, F. Pyczak, K. Hono, S. Yi, Static recrystallization behaviour of cold rolled Mg-Zn-Y alloy and role of solute segregation in microstructure evolution, Scr. Mater. 136 (2017) 41–45. https://doi.org/10.1016/j.scriptamat.2017.04.001.

[95]Z.R. Zeng, Y.M. Zhu, S.W. Xu, M.Z. Bian, C.H.J.J. Davies, N. Birbilis, J.F. Nie, Texture evolution during static recrystallization of cold-rolled magnesium alloys, Acta Mater. 105 (2016) 479–494. https://doi.org/10.1016/j.actamat.2015.12.045.

[96]L.W.F. Mackenzie, M.O. Pekguleryuz, The recrystallization and texture of magnesium-zinc-cerium alloys, Scr. Mater. 59 (2008) 665–668. https://doi.org/10.1016/j.scriptamat.2008.05.021.

[97]L.Y. Zhao, H. Yan, R.S. Chen, E.H. Han, Oriented nucleation causing unusual texture transition during static recrystallization annealing in cold-rolled Mg–Zn–Gd alloys, Scr. Mater. 188 (2020) 200–205. https://doi.org/10.1016/j.scriptamat.2020.07.037.

[98]C. Ha, J. Bohlen, X. Zhou, H.G. Brokmeier, K.U. Kainer, N. Schell, D. Letzig, S. Yi, Texture development and dislocation activities in Mg-Nd and Mg-Ca alloy sheets, Mater. Charact. 175 (2021). https://doi.org/10.1016/j.matchar.2021.111044.

[99]I.-H. Jung, M. Sanjari, J. Kim, S. Yue, Role of RE in the deformation and recrystallization of Mg alloy and a new alloy design concept for Mg–RE alloys, Scr. Mater. 102 (2015) 1–6. https://doi.org/10.1016/j.scriptamat.2014.12.010.

[100]S. Asqardoust, A.Z. Hanzaki, H.R. Abedi, T. Krajnak, P. Minárik, Enhancing the strength and ductility in accumulative back extruded WE43 magnesium alloy through achieving bimodal grain size distribution and texture weakening, Mater. Sci. Eng. A. 698 (2017) 218–229.

[101]I. Basu, T. Al-Samman, Hierarchical Twinning Induced Texture Weakening in Lean Magnesium Alloys, Front. Mater. 6 (2019) 1–15. https://doi.org/10.3389/fmats.2019.00187.

[102]J.P. Hadorn, K. Hantzsche, S. Yi, J. Bohlen, D. Letzig, J.A. Wollmershauser, S.R. Agnew, Role of solute in the texture modification during hot deformation of Mg-rare earth alloys, Metall. Mater. Trans. A Phys. Metall. Mater. Sci. 43 (2012) 1347–1362. https://doi.org/10.1007/s11661-011-0923-5.

[103]Y. Liu, J. Su, R. Gao, H. Geng, A. Javaid, T. Skszek, S. Yue, Effect of Cooling Path on Precipitation Behavior, Microstructure, and Texture Evolution of Micro-alloyed Magnesium Alloy, J. Mater. Eng. Perform. (2020) 1–8. https://doi.org/10.1007/s11665-020-04718-9.

[104]T. Al-Samman, X. Li, Sheet texture modification in magnesium-based alloys by selective rare earth alloying, Mater. Sci. Eng. A. 528 (2011) 3809–3822. https://doi.org/10.1016/j.msea.2011.01.080.

[105]D. Wu, R.S. Chen, E.H. Han, Excellent room-temperature ductility and formability of rolled Mg-Gd-Zn alloy sheets, J. Alloys Compd. 509 (2011) 2856–2863. https://doi.org/10.1016/j.jallcom.2010.11.141.

[106]Y. Onuki, K. Hara, H. Utsunomiya, J.A. Szpunar, High-Speed Rolling of AZ31 Magnesium Alloy Having Different Initial Textures, J. Mater. Eng. Perform. 24 (2015) 972–985. https://doi.org/10.1007/s11665-014-1318-8.

[107]J. Su, M. Sanjari, A.S.H. Kabir, I.H. Jung, J.J. Jonas, S. Yue, H. Utsunomiya, Characteristics of magnesium AZ31 alloys subjected to high speed rolling, Mater. Sci. Eng. A. 636 (2015) 582–592. https://doi.org/10.1016/j.msea.2015.03.083.

[108]D. Song, T. Zhou, J. Tu, L. Shi, B. Song, L. Hu, M. Yang, Q. Chen, L. Lu, Improved stretch formability of AZ31 sheet via texture control by introducing a continuous bending channel into equal channel angular rolling, J. Mater. Process. Technol. 259 (2018) 380–386.

[109]S. Sandlöbes, M. Friák, S. Zaefferer, A. Dick, S. Yi, D. Letzig, Z. Pei, L.F. Zhu, J. Neugebauer, D. Raabe, The relation between ductility and stacking fault energies in Mg and Mg-Y alloys, Acta Mater. 60 (2012) 3011–3021. https://doi.org/10.1016/j.actamat.2012.02.006.

[110]M.H. Yoo, J.R. Morris, K.M. Ho, S.R. Agnew, Nonbasal deformation modes of HCP metals and alloys: Role of dislocation source and mobility, Metall. Mater. Trans. A Phys. Metall. Mater. Sci. 33 (2002) 813–822. https://doi.org/10.1007/s11661-002-0150-1.

[111]M. Yuasa, M. Hayashi, M. Mabuchi, Y. Chino, Improved plastic anisotropy of Mg-Zn-Ca alloys exhibiting high-stretch formability: A first-principles study, Acta Mater. 65 (2014) 207–214. https://doi.org/10.1016/j.actamat.2013.10.063.

[112]K. Hantzsche, J. Bohlen, J. Wendt, K.U. Kainer, S.B. Yi, D. Letzig, Effect of rare earth additions on microstructure and texture development of magnesium alloy sheets, Scr. Mater. 63 (2010) 725–730. https://doi.org/10.1016/j.scriptamat.2009.12.033.

[113]M. Sanjari, A.S.H. Kabir, A. Farzadfar, H. Utsunomiya, R. Petrov, L. Kestens, S. Yue, A.S.H. Kabir, H. Utsunomiya, I.H. Jung, R. Petrov, L. Kestens, S. Yue, Promotion of texture weakening in magnesium by alloying and thermomechanical processing: (I) alloying, J. Mater. Sci. 49 (2014) 1408–1425. https://doi.org/10.1007/s10853-013-7826-3.

[114]M.G. Jiang, C. Xu, T. Nakata, H. Yan, R.S. Chen, S. Kamado, Rare earth texture and improved ductility in a Mg-Zn-Gd alloy after high-speed extrusion, Mater. Sci. Eng. A. 667 (2016) 233–239. https://doi.org/10.1016/j.msea.2016.04.093.

[115]L. Wang, Y. Li, H. Zhang, Z. Zhang, Q. Yang, Q. Zhang, H. Wang, W. Cheng, K.S. Shin, M. Vedani, Review: Achieving enhanced plasticity of magnesium alloys below recrystallization temperature through various texture control methods, J. Mater. Res. Technol. 9 (2020) 12604–12625. https://doi.org/10.1016/j.jmrt.2020.09.002.

[116]K. Hamad, Y.G. Ko, A cross-shear deformation for optimizing the strength and ductility of AZ31 magnesium alloys, Sci. Rep. 6 (2016) 1–8. https://doi.org/10.1038/srep29954.

[117]H. Zhang, Y. Liu, J. Fan, H. Jørgen, W. Cheng, B. Xu, Microstructure evolution and mechanical properties of twinned AZ31 alloy plates at lower elevated temperature, J. Alloys Compd. 615 (2014) 687–692. https://doi.org/10.1016/j.jallcom.2014.07.045.

[118]H.-Y. Wang, T.-T. Feng, L. Zhang, C.-G. Liu, Y. Pan, M. Zha, X.-L. Nan, C. Wang, Q.-C. Jiang, Achieving a weak basal texture in a Mg–6Al–3Sn alloy by wave-shaped die rolling, Mater. Des. 88 (2015) 157–161. https://doi.org/10.1016/j.matdes.2015.08.154.

[119]L.L. Rokhlin, Magnesium Alloys Containing Rare Earth Metals, Crc Press, 2003. https://doi.org/10.1201/9781482265163.

[120]N. Stanford, Micro-alloying Mg with Y, Ce, Gd and La for texture modification-A comparative study, Mater. Sci. Eng. A. 527 (2010) 2669–2677. https://doi.org/10.1016/j.msea.2009.12.036.

[121]J. Bohlen, M.R. Nürnberg, J.W. Senn, D. Letzig, S.R. Agnew, The texture and anisotropy of magnesium-zinc-rare earth alloy sheets, Acta Mater. 55 (2007) 2101–2112. https://doi.org/10.1016/j.actamat.2006.11.013.

[122]L.Y. Zhao, H. Yan, R.S. Chen, E.H. Han, Study on the evolution pattern of grain orientation and misorientation during the static recrystallization of cold-rolled Mg-Zn-Gd alloy, Mater. Charact. 150 (2019) 252–266. https://doi.org/10.1016/j.matchar.2019.02.023.

[123]M. Sanjari, A.R. Farkoosh, B. Shalchi Amirkhiz, Y. He, A. Javaid, A.S. Kabir, J. Su, I.H. Jung, S. Yue, The role of the Zn/Nd ratio in the microstructural evolution of the Mg-Zn-Nd system during static recrystallization: Grain boundary partitioning of solutes, Scr. Mater. 134 (2017) 1–5. https://doi.org/10.1016/j.scriptamat.2017.01.033.

[124]Z.R. Zeng, M.Z. Bian, S.W. Xu, C.H.J. Davies, N. Birbilis, J.F. Nie, Effects of dilute additions of Zn and Ca on ductility of magnesium alloy sheet, Mater. Sci. Eng. A. 674 (2016) 459–471. https://doi.org/10.1016/j.msea.2016.07.049.

[125]R. Li, F. Pan, B. Jiang, H. Dong, Q. Yang, Effect of Li addition on the mechanical behavior and texture of the as-extruded AZ31 magnesium alloy, Mater. Sci. Eng. A. 562 (2013) 33–38. https://doi.org/10.1016/j.msea.2012.11.032.

[126]T. Al-Samman, Comparative study of the deformation behavior of hexagonal magnesium-lithium alloys and a conventional magnesium AZ31 alloy, Acta Mater. 57 (2009) 2229–2242. https://doi.org/10.1016/j.actamat.2009.01.031.

[127]N.P. Papenberg, S. Gneiger, P.J. Uggowitzer, S. Pogatscher, Lean wrought magnesium alloys, Materials (Basel). 14 (2021) 1–30. https://doi.org/10.3390/ma14154282.

Chapter 3.Effect of cooling rate on precipitation behavior, microstructure, and texture evolution of micro-alloyed magnesium alloy

To expand the findings of the literature review regarding developing Mg sheets with better formability through texture modification with lean alloying elements addition, this chapter aims on initiating texture modification by dilute Nd addition through conventional multi-pass rolling. Three micro-alloyed Mg-1Zn-xNd alloys (x= 0.1, 0.2 and 0.5) were homogenized and cooled differently before subjecting rolling and post-deformation annealing. The microstructure and texture evolution during this procedure were then investigated.

This chapter has been published as:

Y. Liu, J. Su, R. Gao, H. Geng, A. Javaid, T. Skszek, S. Yue, Effect of Cooling Path on Precipitation Behavior, Microstructure, and Texture Evolution of Micro-alloyed Magnesium Alloy, J. Mater. Eng. Perform. (2020) 1–8. https://doi.org/10.1007/s11665-020-04718-9.

3.1. Abstract

Alloying with rare-earth (RE) elements enhance the formability of magnesium (Mg) alloys, especially for the lower-elevated temperatures. The beneficial effect brought by RE addition is related to texture modification. However, the complexity of the precipitation behavior in RE-containing alloy and the often excessive RE additions has impeded the understanding of the mechanism for RE texture modification. The current study is based on three micro-alloyed Mg-1Zn-xNd (wt.%) alloys with reduced levels of Nd, i.e., x= 0.1, 0.2, and 0.5 wt.%. Two different cooling paths were employed after solutionizing to achieve different precipitation conditions. The alloys were then subjected to hot rolling at 450°C to a total reduction of 45% in two passes, and post-deformation annealing was also conducted. The precipitation behavior of the current alloy was discussed based on experimental observations and thermodynamic simulations. It was found that 'dilute' Nd in solid solution is more effective in suppressing both dynamic and static recrystallization compared to Nd in the form of precipitates. Ultimately, a non-basal texture with basal poles splitting towards rolling direction and transverse direction was obtained for the Mg-1Zn-0.5Nd alloy after annealing. The mechanism of texture weakening effect was attributed to the presence of Nd in solid solution.

3.2. Introduction

As a structural material candidate for weight reduction in the transportation and aerospace industry, wrought Mg alloys have been receiving increasing attention [1]. Apart from having a high specific strength, Mg alloys have excellent recyclability [2-4]. However, the application of the Mg alloy sheets suffers from the limited formability [5] at lower elevated temperatures mainly due to the preferred crystallographic texture [6]. This can be

attributed to the hexagonal-close-packed (HCP) structure of Mg alloys being unable to provide sufficient numbers of independent slip systems to accommodate uniform plastic deformation [7,8] and the formation of strong basal texture upon various deformation processes [9]. The precipitation behavior is another critical factor that needs to be considered. The mechanical properties and deformation mechanisms are affected by the particle volume fraction, shape and the orientation relationship of precipitates and matrix [10,11].

Alloying with rear-earth (RE) elements to enhance the formability of Mg alloys [6], has been widely reported in the literature aiming to expand the range of applications of wrought Mg alloys [12,13]. The beneficial effects of the RE additions on promoting the formability of Mg alloys are found to be related to several mechanisms activated during thermomechanical processing, i) the activation of the non-basal slip systems [14], ii) texture weakening accompanied by particle stimulated nucleation (PSN) upon recrystallization [15], iii) grain refinement as a result of the suppression of dynamic and static recrystallization during deformation and subsequent annealing [16]. Sanjari et al. [17] investigated the effect of Zn/Nd ratio on microstructural evolution, precipitation behavior and the consequent grain boundary pinning effect in an Mg-Zn-RE alloy system. The results revealed that the combination of Zn and Nd could slow the kinetics of grain growth, and the texture was also modified during annealing. Bohlen et al. [18] found that RE and Y containing Mg alloys presented a broader angular distribution of the basal poles, which leads to the reversed anisotropy of the yield and flow strengths and reduced planar anisotropy. Hence, the mechanical performance of RE added alloys was improved by decreasing the gauge of Mg alloy sheets. However, in the literature, RE elemental additions

are commonly at least 1 wt. % [6,19,20], leading to secondary phase formation. Thus, the role of RE in the form of precipitates or in solid solution has been difficult to separate.

It has been reported that neodymium (Nd) shows an effective texture weakening effect in Mg alloys [21], and it has moderate solubility in Mg-Zn alloys [22]. Thus, in the current study, Nd was added at relatively low concentrations to an Mg-1Zn base alloy to explore the effectiveness of reducing RE addition and, at the same time, to clarify the roles of Nd in the form of precipitates and Nd in solid solution on texture weakening. Therefore, the aims of this study are to investigate the precipitation behavior in micro-alloyed Nd-containing Mg-Zn ternary alloys, and to understand the microstructural evolution and texture modification brought by the diluted Nd by performing different post-solutionizing cooling methods.

3.3. Methodology

Three micro-alloyed Mg alloy sheets were used in the current research. They were cast in a water-cooled copper mold at CametMATERIALS (CMAT) and identified, based on Nd content, as ZE-01, ZE-02, and ZE-05 (Table 3.3.1).

Table 3.3.1 The composition of alloys (wt. %) enrolled in current research.

Alloys	Zn	Nd	Mg
ZE-01	1	0.1	
ZE-02	1	0.2	balance
ZE-05	1	0.5	

In order to homogenize the as-casted alloy, all ingots were solutionized at 500°C for 12 hours, while different cooling rates were applied during the subsequent cooling stage.

Alloys were divided into WQ (water quenched) and FC (Furnace cooled) regarding the cooling method used. Then, both groups were subjected to hot rolling under 450°C for two passes with a 20% reduction for each pass. Intermediate annealing under 450°C for 10 minutes was performed to avoid heat loss between individual passes. To preserve the as-rolled microstructure, all specimens were water quenched after performing the second rolling pass. Specimens were cut from the as-rolled alloy sheet to investigate the microstructure and texture. In addition, post-deformation annealing was conducted to ZE-01 and ZE-05 alloy samples at various temperatures for 10 minutes. The specimens prepared for structure and texture analysis were ground and polished conventionally with SiC and colloidal silica suspension.

A Hitachi SU3500 scanning electron microscopy (SEM) equipped with a Backscattered electron detector (BSE) and Energy-dispersive detector (EDS) was used to identify the morphology, distribution, and composition of the precipitates. The volume fraction of precipitates was measured using the mean section area fractions on BSE images. The precipitation behavior was also studied by thermodynamic FactSage simulations based on the CALPHAD method using FTlite database.

Optical microscopy (OM) with CLEMEX image processing system was used to acquire microstructure images for the as-rolled and annealed samples. An acetic picral solution, which consisted of 4.2 g picric acid, 10 ml acetic acid, 10 ml water, and 70 ml ethanol, was employed to reveal the microstructure.

The macro-texture evolution of various specimens during rolling and subsequent annealing was quantified with a Brucker D8 Discovery x-ray diffractometer with Co Kα radiation operated at 35KV and 45mA. The orientation distribution function (ODF) was

calculated with TexTools, a texture analysis software, by combining three incomplete pole figures acquired through the X-ray diffraction (XRD) technique.

3.4. Results and discussion

3.4.1.Precipitation behavior

The phase evolution (wt. %) during equilibrium cooling for ZE alloys was simulated through FactSage calculation, and the results are shown in Figure 3.1. The general sequence of precipitation in ZE alloys is that the Tao3 phase with a composition of NdMg(Zn, Mg)2 appears first after cooling starts.

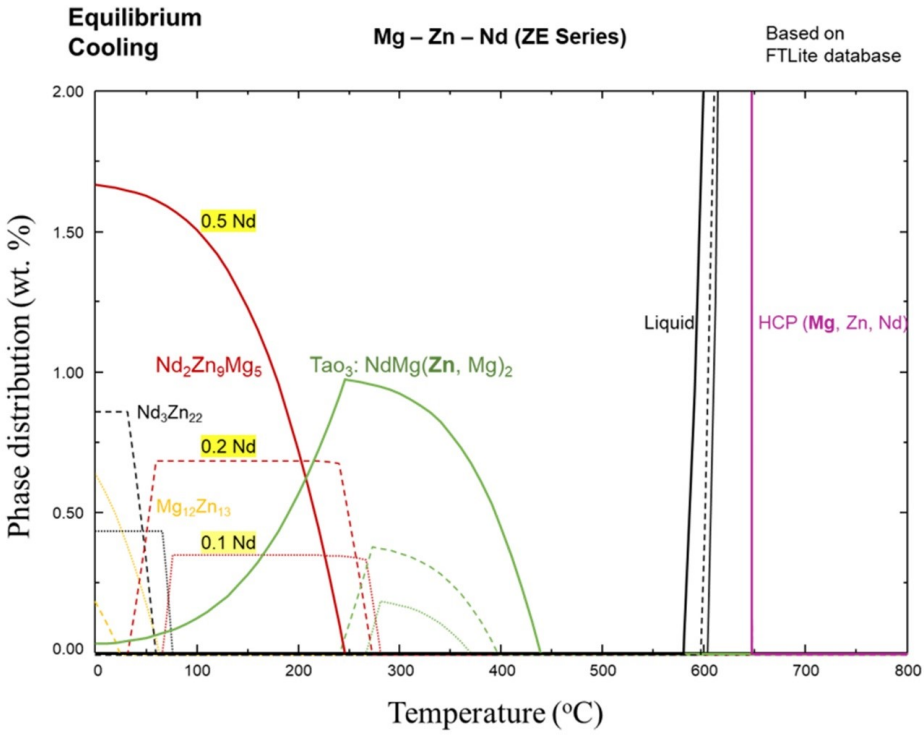

Figure 3.1 The phase distribution diagrams during equilibrium cooling for the ZE series alloys.

Then Tao3 phase reaches a maximum at 250°C to 300°C with a fraction between 0.3wt. % to 0.9 wt. %, the peak temperature is inversely proportional to the Nd content. Then Nd2Zn9Mg5 phase consumes the alloying element by depriving the Nd of Tao3

phase. With decreasing temperature, Nd2Zn9Mg5 dominates precipitation with 1.7 wt. % in ZE05 alloy. On the other hand, for ZE-01 and ZE-02 alloy, precipitates evolve from Nd2Zn9Mg5 to a combination of Nd3Zn22 and Mg12Zn13 at a temperature below 100°C.

In the current research, following the solutionizing treatment at 500°C, different cooling paths were used before the hot rolling processes. In contrast to the WQ samples, which aim to preserve the solutionized structure, the FC samples are closer to the equilibrium condition. The precipitates of three ZE alloys were characterized through the SEM-BSE technique. The morphology of precipitates is shown in Figure 3.2, and the mean volume fraction for precipitation is shown in Figure 3.3 (a). The measured volume fraction of precipitates is less than 0.9 vol. % for all alloys under each condition due to the limited addition of alloying elements. Furthermore, even lower (0.3 - 0.6 vol. %) volume fractions were attained after the hot rolling process was performed. The cooling rate considerably influenced the precipitation behavior of ZE alloys. Fewer precipitates with smaller size were found in the WQ samples both before and after hot rolling for all alloys. The precipitates were generally refined by hot rolling, while precipitation along the grain boundaries was found in FC samples with high Nd additions (Figure 3.2 (g), (k), and (l)). After solutionizing, the precipitates with star shape can be observed in ZE-01 and ZE-02 alloy (Figure 3.2 (a), (c), (e), and (g)), while more spherical precipitates dominated ZE-05. EDS analysis revealed that the star shape precipitates contain lower Zn content compared with other precipitates (Mg-Nd phase was observed in ZE-01 alloy), which indicates this phase could be the “Tao3: NdMg(Zn, Mg)2” phase forms during the initial cooling after casting. The appearance of the initial Tao3 phase demonstrates that the kinetics of the “dissolved” Tao3 phase plays an important role during solutionizing.

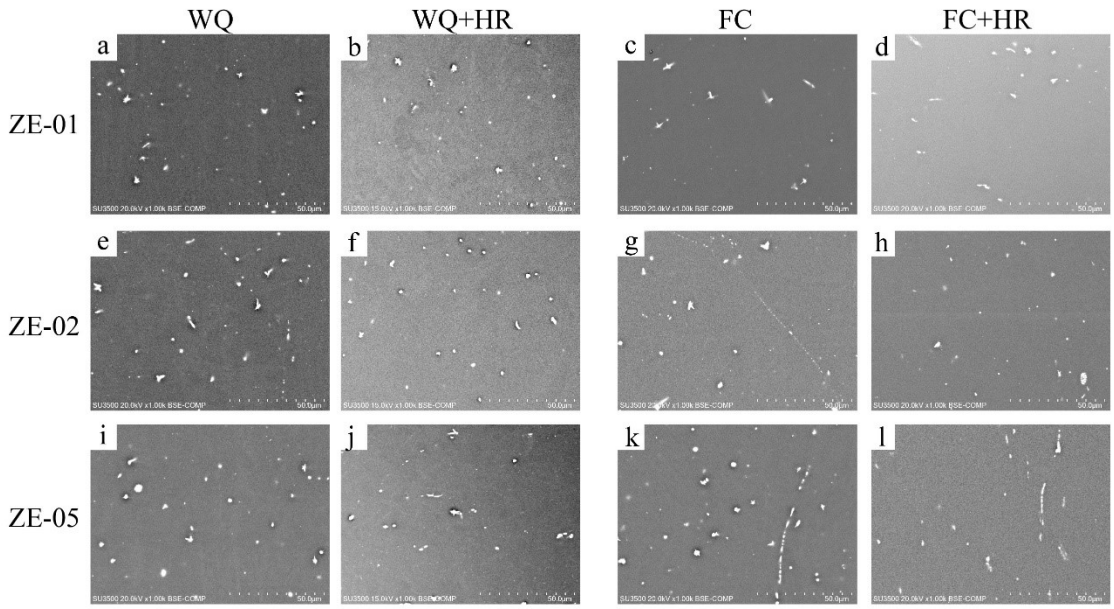

Figure 3.2 The morphology of precipitates for ZE alloys under different treatment.

The evolution of alloying element content solutionized in the matrix of ZE alloys can also be followed from the development of precipitation volume fraction combined with FactSage simulations. In general, fewer precipitates were observed in WQ ZE alloys, revealing a higher content of the alloying elements in the solid solution compared with FC ZE alloys. For FC ZE alloys, the volume fraction of precipitates doubled with increased Nd addition when FC ZE-01 and FC ZE-02 alloy samples were furnace cooled after solutionizing. FactSage simulations also indicate that the composition of secondary phases for ZE-01 and ZE-02 alloy under equilibrium cooling shares similarities. It can be inferred from the proportional relation between alloying element content and precipitation fraction, as well as the slow cooling rate after solutionizing, that almost all Nd added in FC ZE-01 and FC ZE-02 exists in the form of precipitates rather than in matrix. While the FC ZE-05 exhibited an inconsistent trend of precipitation volume fraction increment with elevated alloying element content. Less precipitation than predicted was observed for FC ZE-05

despite it having the highest Nd addition, which is revealed as a gentle slope of the graph in Figure 3.3 (a). According to the phase distribution analysis given by FactSage simulation, the inconsistency of precipitation behavior of FC ZE-05 is related to the absence of the formation of low-temperature precipitates, such as Nd3Zn22 and Mg12Zn13. This trend also leads to the increase of the alloying elements, especially Nd, in the matrix of ZE-05 alloy. As a result of the faster cooling rate, higher Nd addition, and formation of fewer precipitates, the WQ+HR ZE-05 sample had the highest Nd content in the matrix with low precipitation volume fraction among all specimens. Based on the discussion mentioned above, the cooling rate difference in this current research leads to an Nd difference in solid solution. Thus, as inferred from the precipitation behavior, the levels of Nd in solid solution in the hot-rolled specimens can be listed in descending order as WQ+HR ZE-05, FC+HR ZE-05, WQ+HR ZE-02, WQ+HR ZE-01, FC+HR ZE-02, and FC+HR ZE-01.

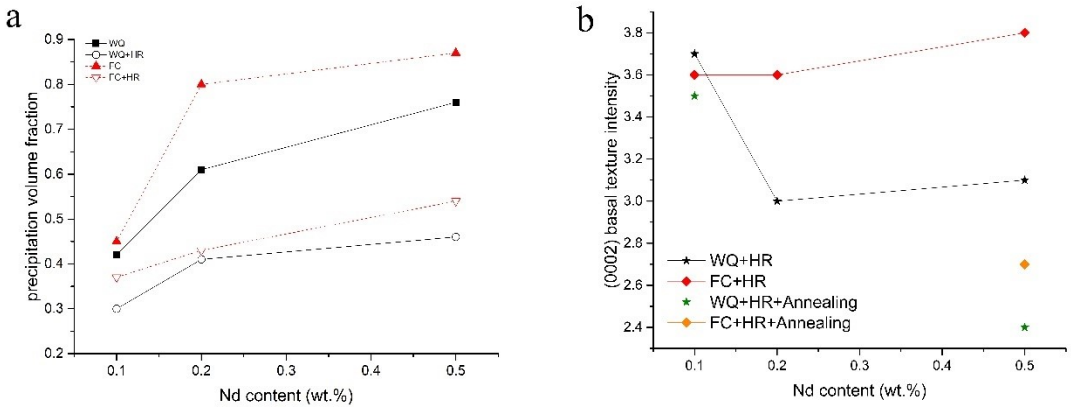

Figure 3.3 (a) the mean precipitation volume fraction of ZE alloys under different heat treatment procedure, and (b) the (0002) basal texture intensity of hot rolled ZE alloys.

3.4.2.Microstructure evolution upon hot rolling

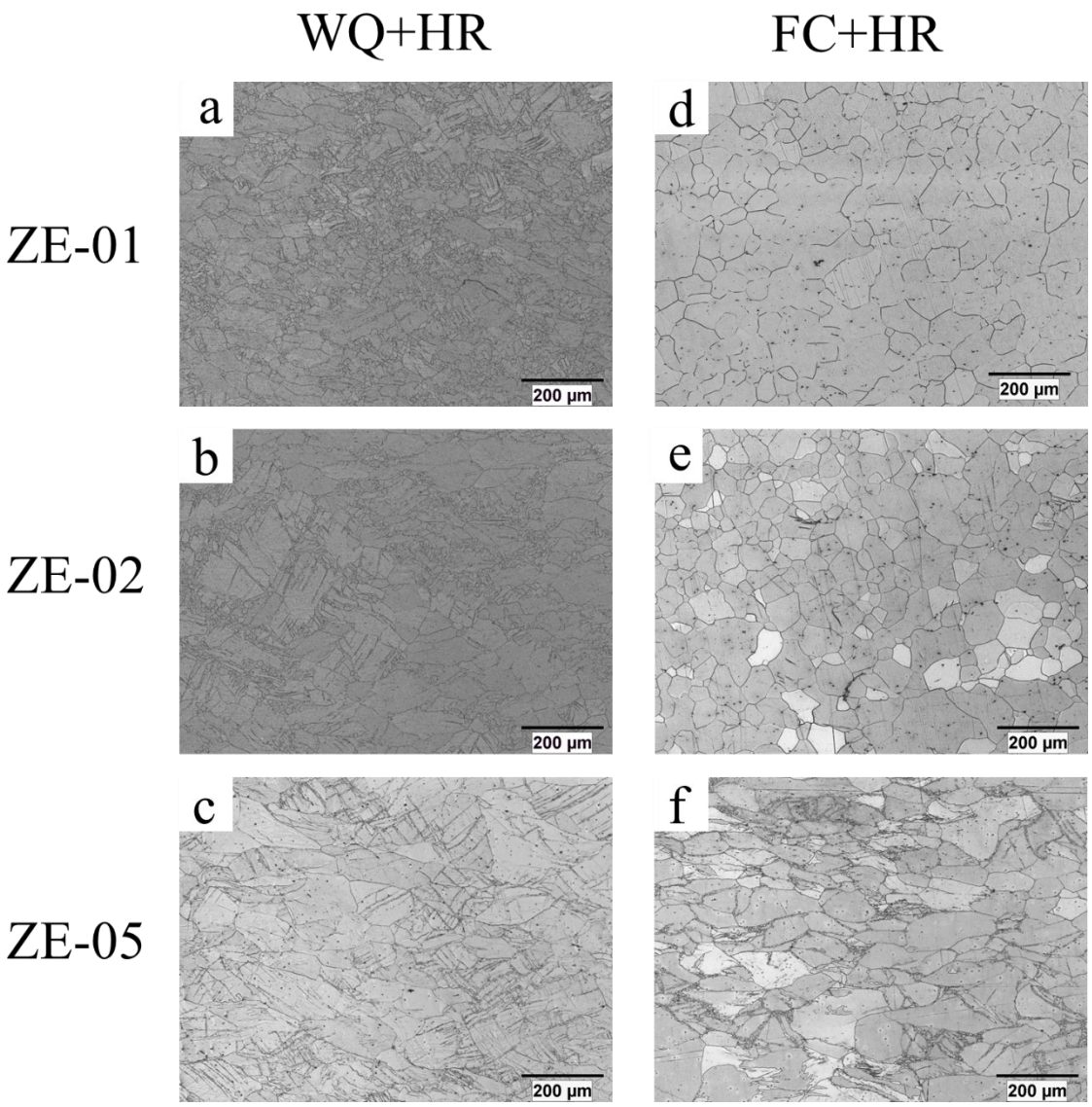

Figure 3.4 The microstructure evolution of water quenched and furnace cooled ZE alloy specimens after two passes of hot rolling.

The optical microstructures of the as-rolled ZE alloys are shown in Figure 3.4. For the WQ ZE-01 and ZE-02, the microstructures were similar and exhibited a typical hot-rolled structure, where grains were elongated along the rolling direction (RD) with dynamic recrystallization (DRX) occurred in deformation twins and near grain boundaries [23]. A higher volume fraction of DRX grains can be found in the WQ+HR ZE-01 compared to

FC+HR ZE-01 sample. However, in the WQ+HR ZE-05, a heavily deformed microstructure with twins observed in elongated grains and no obvious DRX was evident after hot rolling. The suppressed DRX phenomenon with RE additions in Mg alloys has been reported in previous studies [16,24]. The mechanism of DRX suppression was attributed to the RE solute segregation at GBs [25] or the precipitation along GBs [25], both mechanisms are expected to hinder the motion of GBs and hence to suppress the DRX process. In addition, the segregated RE may also contribute the DRX suppression by pinning the twin boundaries (TBs) [26]. Given the fact that the volume fraction of precipitates for WQ+HR ZE-02 and ZE-05 was around 0.4 wt. %. It can be assumed that the influence of precipitation on the different microstructures is negligible. Thus, the formation of the twinned structure was attributed to the suppression effect on DRX brought by solid solution alloying elements in ZE-05 [27].

In contrast to the WQ ZE alloys, an equiaxed grain structure was found in the FC+HR ZE-01 and ZE-02 alloys, which indicates the occurrence of static recrystallization. Based on the previous discussion on the precipitation behavior of ZE alloys, the volume fraction of precipitates for ZE alloys was insufficient to pin the movement of grain boundaries[28]due to the limited addition of micro-alloyed Nd. Also, the kinetics for grain growth was promoted by the high rolling temperature at 450°C. Thus, a recrystallized structure resulted in the FC+HR ZE-01 and ZE-02. Nevertheless, a deformed structure with an apparent “necklace” structure [23] in the vicinity of twins and grain boundaries of elongated primary grains was observed for the FC+HR ZE-05 alloy. Similar to the WQ+HR ZE-05 specimen, the evidence of fine DRXed grains also resulted from the increased Nd addition in the alloy. From the evolution of the microstructure of ZE alloys

subjected to different cooling pathes, it appears that the nucleation and growth of DRXed grains are positively correlated to the Nd content in matrix. The FC+HR ZE-01 showed a fully recrystallized structure, while DRX was totally suppressed in the WQ+HR ZE-05 specimen.

3.4.3.Texture evolution upon hot rolling

The macro-texture evolution of ZE alloys after hot rolling is shown in Figure 3.5. The macro-textures were expressed regarding the basal (0002) and prismatic (10-10) pole figures recalculated from the original XRD data by using Textools [29]. After rolling, despite the difference in cooling rate, both ZE-01 and ZE-02 alloy exhibited a typical basal texture pattern where the orientation distribution of basal poles is close to the sheet normal direction (ND) [30], as can be seen in Figure 3.6 (a), (b), (d) and (e). The macro-texture for ZE-05 alloy is denoted as a modified basal texture with a broader angular distribution of basal poles. For the WQ+HR ZE-05 sample, the wide scattered basal poles were found expanding along both rolling direction (RD) and transverse direction (TD), while the FC+HR ZE-05 basal poles only tilted away from ND along RD of the sheet, as shown in Figure 3.5 (c) and (f), respectively. As an indication of the activation of other non-basal deformation mechanisms, especially the pyramidal <c+a> slip system, textures with the RD-splitting pattern has been reported in other RE-containing Mg alloys as well as AZ31 after hot rolling [5,31]. The TD-splitting pattern, even though the machnism for this unique texture component is still under debate, is also inevetabley related to the promoted formability. Shi et al. [32] explained the reorientation of basal pole towarding TD as the result of the activation of {10-12} tension twinning. The study made by I. Basu et al. [33] concluded the TD-splitting pattern in Gd-containing Mg alloy as a result of segregated RE

and the consequenced solute drag effect. In current study, it is clear that the modified texture after hot rolling with basal poles splitted along TD was resulted from the Nd addition. WQ+HR ZE-05, as the sample holds highest solutionized Nd, exhibited visible TD-splitting texture pattern.

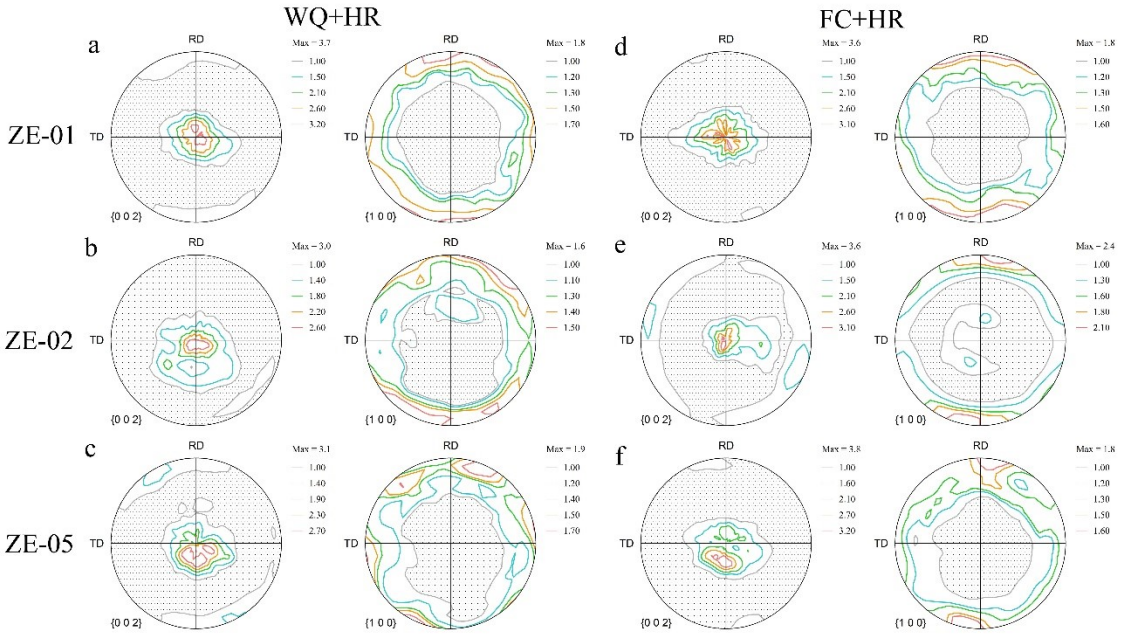

Figure 3.5 Macro-texture of as-rolled ZE alloys: (a) WQ ZE-01[34]; (b) WQ ZE-02; (c) WQ ZE-05 [34]; (d) FC ZE-01; (e) FC ZE-02; (f) FC ZE-05.

The texture intensities of basal poles for ZE alloys subjected to different cooling treatments after solutionizing are shown in Figure 3.3 (b); accordingly, a more randomized texture would have a lower texture intensity closer to 1 mrd. The basal texture was significantly weakened in WQ+HR ZE specimens by over 16% when more than 0.1 wt. % Nd was added. The weakest basal texture of as-rolled ZE alloy, with an intensity of 3.0 mrd, was achieved by WQ+HR ZE-02, which related to the high fraction of fine DRXed grains and an amplified texture modification effect brought by increased Nd addition. In addition, the work-hardened structure of the WQ+HR ZE-05 sample shows the possibility

of further randomization of basal pole distribution through SRX. However, an opposite trend was observed in FC+HR ZE samples, with no pronounced texture weakening effect, which was found in FC+HR ZE-01 and FC+HR ZE-02; as well the basal intensity of FC+HR ZE-05 was slightly raised even with 0.5 wt. % Nd was added. Therefore, it can be inferred that lower Nd content in solid solution is responsible for this trend. For FC+HR ZE-05, the increased texture intensity was also attributed to a partially DRXed microstructure with large deformed grains being predominant. In contrast to the WQ samples, the recrystallized structure of FC+HR ZE-01 and ZE-02 narrows the potential possibility to further weaken the texture.

3.4.4.Role of post-deformation annealing on microstructure and texture

In order to further investigate the influence of cooling path on texture modification, the as-rolled ZE-01 and ZE-05 samples with a partially recrystallized microstructures (WQ+HR ZE-01, WQ+HR ZE-05, and FC+HR ZE-05) were annealed under various temperatures. The annealing temperatures were chosen to unify the average grain size of different samples, hence the texture intensity variation brought by grain size difference would be minimized. The annealed microstructures and textures of ZE-01 and ZE-05 alloy are shown in Figure 3.6, and the annealed (0002) basal texture intensity is also shown in Figure 3.3 (b). For the ZE-01 alloy, the deformed structure in WQ+HR ZE-01 fully recrystallized statically after annealing under 350°C for 10 minutes, and the texture intensity dropped from 3.7 to 3.0 after annealing, although the basal poles were still parallel to ND of the sheet. The FC+HR ZE-01 appeared to be recrystallized without annealing with a strong basal texture at an intensity of 3.6 mrd. With higher Nd addition, the texture of the ZE alloy sheet developed a unique feature with weakened intensity during annealing.

During annealing of the WQ+HR ZE-0.5 and FC+HR ZE-05 specimens, the basal poles were split away from the ND of the sheet, which leads to a non-basal texture pattern. For the FC+HR ZE-05, the RD-splitting pattern indicates the activation of pyramidal <c+a> slip system resulting from hot rolling under 450°C [34] and the intensity of basal poles dropped nearly 30% to 2.7 after annealing. Meanwhile, the texture intensity of annealed WQ+HR ZE-05 was reduced to 2.4, which is the lowest basal pole intensity among all conditions, and the texture exhibited a pronounced modification with a broader angular distribution of the basal poles towards both the TD and RD via static recrystallization. The noticeable texture modification effect for WQ+HR ZE-05 alloys was attained through SRX during annealing.

Similar to the microstructure evolution during hot rolling, the SRX process was suppressed in higher Nd containing specimens during annealing. In the current study, DRX is less efficient on texture weakening compared to SRX. The DRXed microstructure generally preserves a strong basal deformation texture. This can be related to two reasons, i) the continous DRX nuclei would inherit orientations from parent grains, ii) dynmamically recrystallized grains continuously deformed via predominant basal slip system upon hot rolling, although the discontinuous DRX grains and twinning induced DRX grains possess high misorientation angles with respect to the matrix. On the contrary, during SRX process, the strong basal texture could be weakend by introducing non-basal texture components, as well as, by avoiding unfavorable grain growth via precipitation pinning and/or solute segregation through controlling annealing conditions. Previous work has shown that the decrease in SRX kinetics is essential for texture modification in ZE alloys [34]. In other studies, the mechanism for texture weakening during SRX has been

explained as a consequence of particle stimulated nucleation (PSN) [15]. However, this mechanism could not be employed in the current experiment due to the smaller precipitate size and very small volume fraction of precipitates as well as the newly formed grains mainly located in the vicinity of twins and grain boundaries.

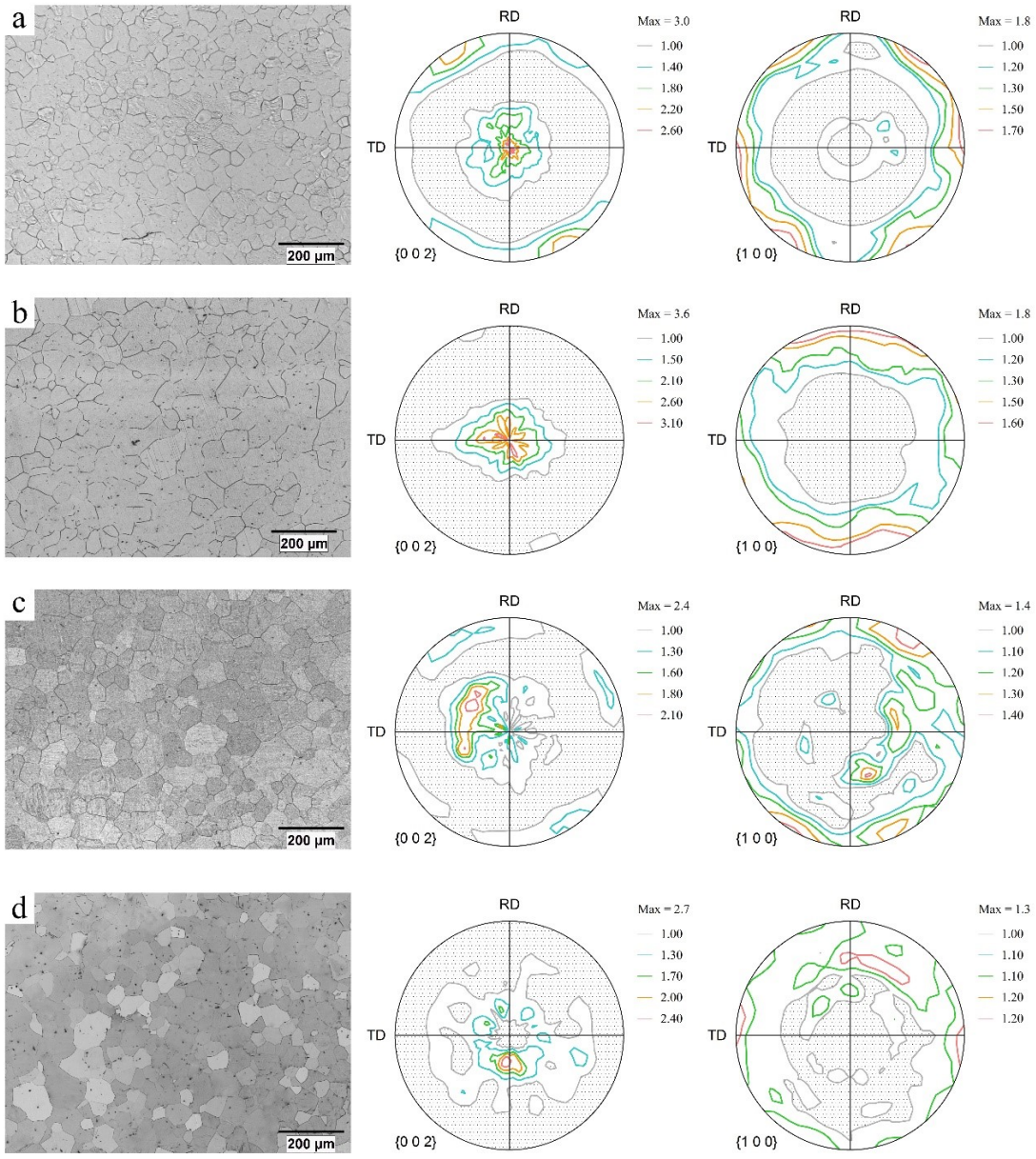

Figure 3.6 Comparison between fully recrystallized ZE alloys on microstructure and macro-texture: (a) ZE-01 WQ+HR annealed under 350℃ for 10 minutes [34]; (b) ZE-01 FC+HR; (c) ZE-05 WQ+HR annealed under 450℃ for 10 minutes [34]; (d) ZE-05 FC+HR annealed under 450℃ for 10 minutes.

The FC+HR ZE-01 and WQ+HR ZE-05 have similar size and volume fraction regarding precipitates, but the macro-texture exhibits distinctive features after annealing. Hence, the texture randomization can be explained by the micro-alloyed Nd in solid solution based on the correlation between (0002) basal texture intensity and precipitation behavior shown in Figure 3.3 (b). Annealed Gd-containing Mg alloys also exhibited a non-basal texture with the combination of TD and RD splitting, and the mechanism was attributed to the effect of RE element on grain boundary migration resulting from preferential segregation of solute atoms [21]. It is known that, during the thermomechanical processing of Mg alloy sheets, recrystallization inevitably occurs dynamically and/or statically. From the current study, SRX would be the better choice in terms of texture modification as well as microstructure control.

3.5. Conclusions

- The results indicate that the volume fraction of precipitates in current Mg-Zn-Nd alloy experiences a proportional increase with Nd addition raised from 0.1 wt. % to 0.2 wt.%, while fewer precipitates were observed by further increasing Nd to 0.5 wt. % due to the absence of low-temperature precipitation phases such as Nd3Zn22 and Mg12Zn13.
- Different cooling paths after solutionizing affect the microstructure and macro-texture evolution of ZE alloy by altering Nd content in the solid solution.
- Both DRX and SRX were suppressed due to the addition of Nd in micro-alloyed ZE alloys. The suppression of DRX and SRX was largely related to Nd content in solid solution, rather than the precipitates in the current ZE micro-alloys.

- The macro-texture of hot rolled ZE alloy revealed a reduced intensity of the basal texture with increasing Nd from 0.1 wt.% to 0.2 wt. %. Nonetheless, modified texture with broader angular distribution was achieved in the alloy with the Nd addition of 0.5 wt. %.
- The combination of the non-basal slip system activated by hot rolling, which was revealed as a basal pole split along RD, and the texture weakening effect brought by Nd in solid solution, revealed by TD-splitting on (0002) pole figure, leads to a unique weakened, non-basal texture in annealed WQ+HR ZE-05.

3.6. Reference

[1] B. L. Mordike and T. Ebert, "Magnesium Properties - applications - potential," *Mater. Sci. Eng. A*, vol. 302, no. 1, pp. 37–45, Apr. 2001.

[2] J. Su, S. Kaboli, A. S. H. Kabir, I.-H. H. Jung, and S. Yue, "Effect of dynamic precipitation and twinning on dynamic recrystallization of micro-alloyed Mg-Al-Ca alloys," *Mater. Sci. Eng. A*, vol. 587, pp. 27–35, Dec. 2013.

[3] M. O. Pekguleryuz, "Current developments in wrought magnesium alloys," in *Advances in Wrought Magnesium Alloys*, M. Barnett, Ed. Woodhead Publishing, 2012, pp. 3–62.

[4] A. S. H. Kabir, M. Sanjari, J. Su, I. H. Jung, and S. Yue, "Effect of strain-induced precipitation on dynamic recrystallization in Mg-Al-Sn alloys," *Mater. Sci. Eng. A*, vol. 616, pp. 252–259, 2014.

[5] D. Wu, R. S. Chen, and E. H. Han, "Excellent room-temperature ductility and formability of rolled Mg-Gd-Zn alloy sheets," *J. Alloys Compd.*, vol. 509, no. 6, pp. 2856–2863, 2011.

[6] A. Imandoust, C. D. Barrett, T. Al-Samman, K. A. Inal, and H. El Kadiri, "A review on the effect of rare-earth elements on texture evolution during processing of magnesium alloys," *J. Mater. Sci.*, vol. 52, no. 1, pp. 1–29, 2017.

[7] M. H. Yoo, "Slip, twinning, and fracture in hexagonal close-packed metals," *Metall. Trans. A*, vol. 12, no. 3, pp. 409–418, 1981.

[8] S. R. Agnew, "Deformation mechanisms of magnesium alloys," in *Advances in Wrought Magnesium Alloys*, Elsevier, 2012, pp. 63–104.

[9] A. Jäger, P. Lukáč, V. Gärtnerová, J. Haloda, and M. Dopita, "Influence of annealing on the microstructure of commercial Mg alloy AZ31 after mechanical forming,"

Mater. Sci. Eng. A, vol. 432, no. 1–2, pp. 20–25, 2006.

[10] J. F. Nie, "Effects of precipitate shape and orientation on dispersion strengthening in magnesium alloys," *Scr. Mater.*, vol. 48, no. 8, pp. 1009–1015, Apr. 2003.

[11] N. Stanford, J. Geng, Y. B. Chun, C. H. J. Davies, J. F. Nie, and M. R. Barnett, "Effect of plate-shaped particle distributions on the deformation behaviour of magnesium alloy AZ91 in tension and compression," *Acta Mater.*, vol. 60, no. 1, pp. 218–228, Jan. 2012.

[12] A. Hadadzadeh, M. A. Wells, and A. Javaid, "Warm and Hot Deformation Behavior of As-Cast ZEK100 Magnesium Alloy," *Exp. Mech.*, vol. 56, no. 2, pp. 259–271, 2016.

[13] Y. Xin, M. Wang, Z. Zeng, G. Huang, and Q. Liu, "Tailoring the texture of magnesium alloy by twinning deformation to improve the rolling capability," *Scr. Mater.*, vol. 64, no. 10, pp. 986–989, 2011.

[14] K. Hantzsche, J. Bohlen, J. Wendt, K. U. Kainer, S. B. Yi, and D. Letzig, "Effect of rare earth additions on microstructure and texture development of magnesium alloy sheets," *Scr. Mater.*, vol. 63, no. 7, pp. 725–730, 2010.

[15] E. A. Ball and P. B. Prangnell, "Tensile-compressive yield asymmetries in high strength wrought magnesium alloys," *Scr. Metall. Mater.*, vol. 31, no. 2, pp. 111–116, Jul. 1994.

[16] S. A. Farzadfar, E. Martin, M. Sanjari, E. Essadiqi, and S. Yue, "Texture weakening and static recrystallization in rolled Mg-2.9Y and Mg-2.9Zn solid solution alloys," *J. Mater. Sci.*, vol. 47, no. 14, pp. 5488–5500, 2012.

[17] M. Sanjari *et al.*, "The role of the Zn/Nd ratio in the microstructural evolution of the Mg-Zn-Nd system during static recrystallization: Grain boundary partitioning of solutes," *Scr. Mater.*, vol. 134, pp. 1–5, Jun. 2017.

[18] J. Bohlen, M. R. Nürnberg, J. W. Senn, D. Letzig, and S. R. Agnew, "The texture and anisotropy of magnesium-zinc-rare earth alloy sheets," *Acta Mater.*, vol. 55, no. 6, pp. 2101–2112, 2007.

[19] Y. M. Kim *et al.*, "Static recrystallization behaviour of cold rolled Mg-Zn-Y alloy and role of solute segregation in microstructure evolution," *Scr. Mater.*, vol. 136, pp. 41–45, 2017.

[20] S. Tekumalla, S. Seetharaman, A. Almajid, and M. Gupta, *Mechanical Properties of Magnesium-Rare Earth Alloy Systems: A Review*, vol. 5, no. 1. 2014.

[21] T. Al-Samman and X. Li, "Sheet texture modification in magnesium-based alloys by selective rare earth alloying," *Mater. Sci. Eng. A*, vol. 528, no. 10–11, pp. 3809–3822, 2011.

[22] I.-H. Jung, M. Sanjari, J. Kim, and S. Yue, "Role of RE in the deformation and recrystallization of Mg alloy and a new alloy design concept for Mg–RE alloys," *Scr. Mater.*, vol. 102, pp. 1–6, 2015.

[23] Y. Liu, J. Fan, H. Zhang, W. Jin, H. Dong, and B. Xu, "Recrystallization and microstructure evolution of the rolled Mg–3Al–1Zn alloy strips under electropulsing treatment," *J. Alloys Compd.*, vol. 622, pp. 229–235, 2015.

[24] J. D. Robson, "Effect of Rare-Earth Additions on the Texture of Wrought Magnesium Alloys: The Role of Grain Boundary Segregation," *Metall. Mater. Trans. A Phys. Metall. Mater. Sci.*, vol. 45, no. 8, pp. 3205–3212, 2014.

[25] M. G. Jiang *et al.*, "Correlation between dynamic recrystallization and formation of rare earth texture in a Mg-Zn-Gd magnesium alloy during extrusion," *Sci. Rep.*, vol. 8, no. 1, pp. 1–11, 2018.

[26] J. F. Nie, Y. M. Zhu, J. Z. Liu, and X. Y. Fang, "Periodic segregation of solute atoms in fully coherent twin boundaries," *Science (80-.).*, vol. 340, no. 6135, pp. 957–960, 2013.

[27] X. Y. Fang, D. Q. Yi, J. F. Nie, X. J. Zhang, B. Wang, and L. R. Xiao, "Effect of Zr, Mn and Sc additions on the grain size of Mg–Gd alloy," *J. Alloys Compd.*, vol. 470, no. 1, pp. 311–316, 2009.

[28] Y. Zhang *et al.*, "Effects of yttrium on microstructure and mechanical properties of hot-extruded Mg-Zn-Y-Zr alloys," *Mater. Sci. Eng. A*, vol. 373, no. 1–2, pp. 320–327, May 2004.

[29] H. Li, "TexTools software version 3.0," *Resmat Corp. Montr. Quebec, Canada*, 2009.

[30] M. Wang, R. Xin, B. Wang, and Q. Liu, "Effect of initial texture on dynamic recrystallization of AZ31 Mg alloy during hot rolling," *Mater. Sci. Eng. A*, vol. 528, no. 6, pp. 2941–2951, Mar. 2011.

[31] S. Yi, J. Bohlen, F. Heinemann, and D. Letzig, "Mechanical anisotropy and deep drawing behaviour of AZ31 and ZE10 magnesium alloy sheets," *Acta Mater.*, vol. 58, no. 2, pp. 592–605, Jan. 2010.

[32] B. Q. Shi, R. S. Chen, and W. Ke, "Effects of yttrium and zinc on the texture, microstructure and tensile properties of hot-rolled magnesium plates," *Mater. Sci. Eng. A*, vol. 560, pp. 62–70, 2013.

[33] I. Basu, K. G. Pradeep, C. Mießen, L. A. Barrales-Mora, and T. Al-Samman, "The role of atomic scale segregation in designing highly ductile magnesium alloys," *Acta Mater.*, vol. 116, pp. 77–94, 2016.

[34] Y. Liu, J. Su, A. Javaid, T. Skszek, and S. Yue, "Microstructure and Texture Evolution of Micro-Alloyed Magnesium-Zinc-Neodymium Alloys," in *Contributed Papers from MS&T17*, 2017, vol. 2017, no. Ml, pp. 185–192.

Chapter 4.The underlying deformation mechanisms and texture evolution in micro-alloyed Mg-Zn-Nd alloys

In the previous chapter, non-basal texture featuring noticeable TD-split component has been observed in micro-alloyed Mg-Zn-Nd (ZE) alloy system. Although the faster cooling rate after homogenization leads to a higher content of alloying elements in the matrix, especially Nd, has been shown to promote the evolution of the texture, the mechanism for this phenomenon is not clear. Therefore, this chapter focuses on exploring the correlation between Nd solute and texture modification by tracking the TD-split texture formation upon annealing in three micro-alloyed ZE alloys subjecting to various solutionizing and subsequent thermal processing schedules.

This chapter is ready for submission and will be credited to the following authors:

Y. Liu, J. Su, H. Chen, Q. Qiu, R. Gao, N. Brodusch, A, Javaid, T. Skszek, J. Song, S. Yue, The underlying deformation mechanisms and texture evolution in micro-alloyed Mg-Zn-Nd alloys.

4.1. Abstract

In this study, texture transition from concentrated basal to weakened non-basal texture featuring (0002) poles tilting toward the transverse direction (TD) is tracked by quasi-in-situ EBSD observations in micro-alloyed magnesium-zinc-neodymium (ZE) alloys. The mechanism of this transition upon hot rolling and subsequent annealing was investigated systematically by comparing three micro-alloyed ZE alloys with dilute Nd additions (0.1, 0.2, 0.5 wt.%). Scanning transmission electron microscopy (STEM) reveals that the formation of TD-split texture is triggered by Nd in solid solution, which is controlled through various solutionizing procedures. By using intragranular misorientation axis (IGMA) and Generalized Schmid Factor (GSF) evaluation, the prismatic slip was promoted owing to the increase in Nd solute at elevated temperature. First-principle calculations and molecular dynamic simulations indicated the Nd solute promotes non-basal slip activation by lowering the stacking fault energy (SFE) and critical resolved shear stress (CRSS). To quantify the contribution of different deformation modes to the microstructure and texture evolution, a parameter based on the ratio of prismatic to basal geometrically necessary dislocation densities ($rGND_{p/b}$) was originally proposed. The shear-band induced nucleation introduced nuclei with various orientations and the TD-split texture was obtained through preferential grain growth of the TD-split oriented grains, which can be explained through the $rGND_{p/b}$ evolution. Consequently, the alloys containing ≥0.2% Nd with the TD-split texture exhibited enhanced ductility (23%) compared to that with 0.1% Nd. However, the improvement in ductility was limited to increases in Nd from 0.2 to 0.5%.

4.2. Introduction

Despite the encouraging potential for weight reduction in the automobile industry, the use of wrought magnesium (Mg) alloy sheets has been curtailed by insufficient lower temperature formability [1,2]. This correlates with the strong crystallographic texture of basal poles parallel to the normal direction (ND) of the rolled Mg sheets [3]. In order to enhance the formability of Mg sheets, numerous efforts have been devoted to weakening the strong basal texture, which originates from the predominant activation of basal slip [4,5]. Owing to pyramidal <c+a> slip, texture with double peaks splitting along the rolling direction (RD-split) has been widely observed in Mg alloy subjecting to plastic deformation at higher temperatures [6–8]. However, the RD-split texture is sensitive to recrystallization since attenuation [9] or disappearance [10] of the RD-split texture components upon annealing have been reported. On the contrary, non-basal texture with basal poles tilting towards the transverse direction (TD), which is referred to as the "TD-split" texture, has been observed in Mg alloyed with rare earth (RE) elements subjected to post-deformation annealing [11–15]. Moreover, formability has been enhanced in Mg alloys featuring TD-split texture. Basu et al. [13] reported an excellent 38.8% elongation to failure in annealed Mg-1Zn-1Gd-0.6Zr alloy with the TD-split texture. Chino et al.[14] achieved TD-split texture and enhanced room temperature formability in an annealed Mg–1.5Zn–0.2Ce alloy with an Erichsen value of 9.0, which is similar to that of commercial aluminum (Al) alloys. Wu et al. [16] reached ~50% elongation to failure accompanied with high Erichsen values (nearly 8) at room temperature.

Although zinc (Zn) has been enrolled to reduce the usage of RE [17], researchers still commonly use excessive amounts of RE. The TD-split texture has been obtained in

various Mg-Zn-RE alloys with RE contents ranging from 0.2 wt.% to 3 wt.% [13,14,16,18,19]. This alloying strategy is related to the fact that the mechanism of TD-split texture formation brought about by RE addition remains a matter of debate. Several mechanisms have been proposed to explain the texture evolution. Nuclei with randomized orientation could be generated through particle stimulated nucleation (PSN) mechanism [13,14]. A solute drag effect brought by RE segregated along the grain boundaries (GBs) could suppress dynamic recrystallization (DRX) [20], which rarely introduces new orientations. The grain growth rate and GB mobility, which affect the microstructure and texture, are retarded due to RE segregation [21]. The enhanced non-basal slip system activation resulted from RE addition contributes to the texture weakening [19,22]. Various structural features, such as bimodal structure [23], shear bands [24], and twinning [11], also influence the texture by providing non-basal orientations. Therefore, the thorough investigation of formation mechanism of TD-split texture in the micro-alloyed Mg-Zn-Nd alloys (RE content 0.5 wt. %) is of interest.

In the current study, three micro-alloyed Mg-Zn-xNd alloys (x = 0.1, 0.2, 0.5 wt. %) are examined. Thermomechanical processing is designed to produce Mg alloy sheets while manipulating the Nd contents in the solid solution based on thermodynamic simulations (FactSage) [25]. A modified texture featuring a TD-split pattern and weakened intensity is revealed in the fully annealed ZE alloy with 0.2 and 0.5% Nd, which contributes to enhanced ductility compared to that with 0.1% Nd. The goals of this work are i) to investigate the influence of Nd solute on the deformation mechanisms and the corresponding texture formation during hot rolling and ii) to determine the recrystallization mechanisms responsible for the texture evolution during annealing. First-principle

calculations and molecular dynamic (MD) simulation are applied to evaluate the effect of Nd on stacking fault energy (SFE) and critical resolved shear stress (CRSS).

4.3. Experimental methods

4.3.1.Alloy design and thermodynamics calculation

Three micro-alloyed Mg-1Zn-xNd (x=0.1, 0.2, 0.5 wt.%) alloys, denoted as ZE-01, ZE-02, and ZE-05, were cast and rolled at CanmetMATERIALS. The nominal compositions are listed in Table 4.3.1.

Table 4.3.1 Nominal chemical compositions of ZE alloys (wt. %).

Alloys	Zn	Nd	Mg
ZE-01	1	0.1	
ZE-02	1	0.2	balance
ZE-05	1	0.5	

4.3.2.Thermomechanical processing design

The equilibrium phase diagram of three proposed alloys was calculated through thermodynamic simulations based on the CALPHAD method using FactSage [25]. The temperature versus Nd content of an Mg- 1wt.% Zn system is shown in Figure 4.1(a).

Based on the phase diagram, all alloying elements would dissolve in the matrix at temperatures above 450°C, while various Nd-containing precipitates start forming with the decreasing temperature. Besides the equilibrium solid solution temperature, kinetics also affects the solutionizing process. To achieve sufficient Nd dissolution, the as-received 5 mm thick sheets were solutionized at 450°C and 500°C for 72 hours, followed by water quenching. Subsequently, the solutionized sheets were hot rolled in two passes at 350°C for a total reduction of 36%. Intermediate annealing at 350°C for 10 minutes was applied between each pass. Post-deformation annealing was executed at 350°C and 450 °C to achieve a fully recrystallized structure. Quasi-in-situ microstructure characterization was

applied to study the static recrystallization (SRX) evolution of the as-rolled structures during interrupted annealing at $450°C$, as shown in Figure 4.1(b).

4.3.3.Microstructure characterization

Optical microstructures (OM) were recorded by a CLEMEX image system. Macro-textures were characterized by X-ray diffraction (XRD) using a Bruker D8 x-ray diffractometer with Co Kα radiation. TexTools [26], a texture analysis software, was used to analyze the XRD data. For the quasi-in-situ specimens, EBSD was performed by a Hitachi SU3500 scanning electron microscopy (SEM). The step size was set to 0.4 μm for deformed specimens and increased to 1 μm for specimens with SRX fraction higher than 90%. Channel 5, Aztec Crystal, and MTEX Toolbox [27] were employed to process the EBSD data. Backscattered-Electron (BSE) images that showed the distribution of various precipitates were captured by the BSE detector attached to the SU3500 SEM. A Hitachi SU9000 scanning transmission electron microscopy (STEM) microscope was used to characterize the distribution of alloying elements.

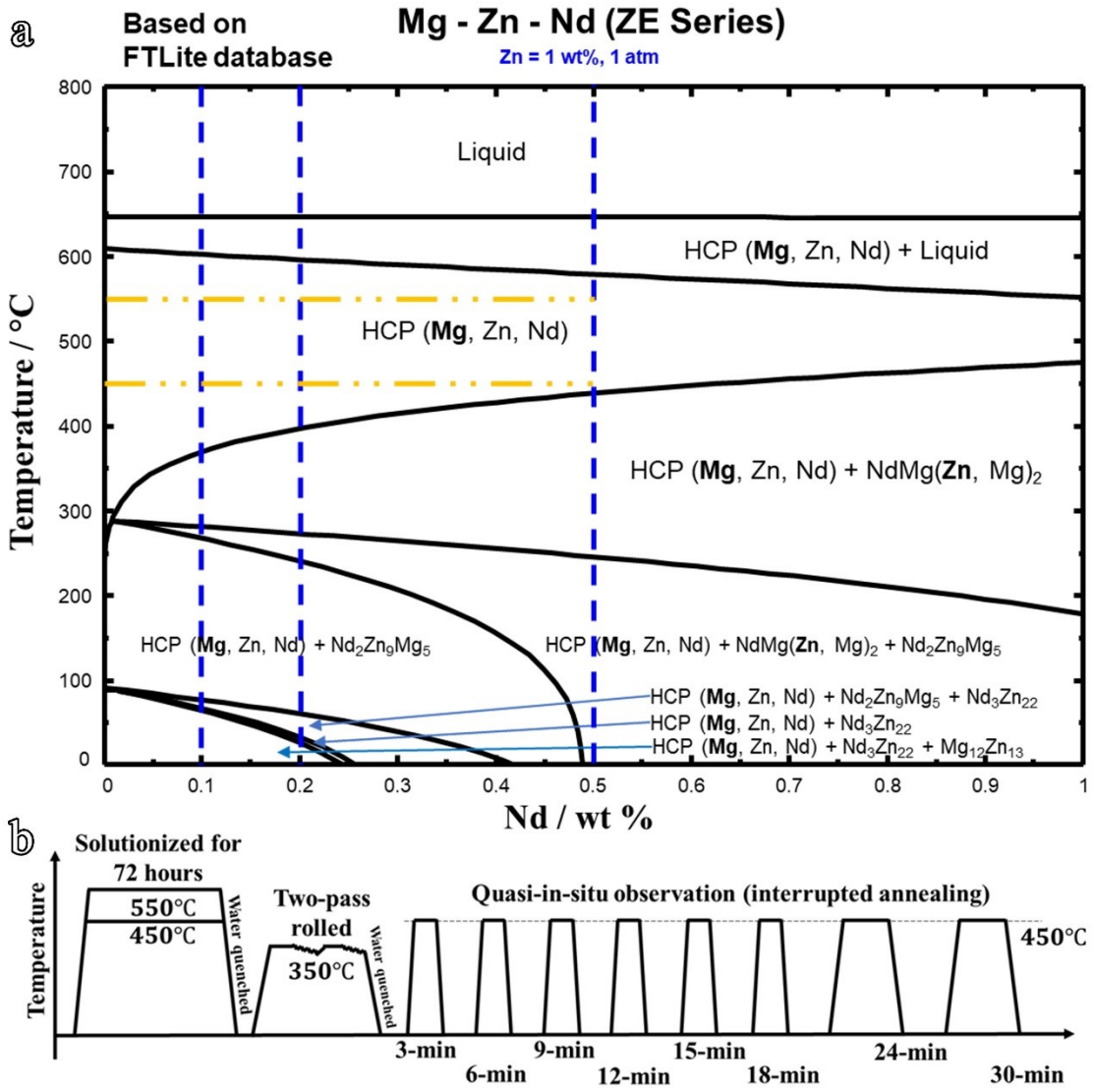

Figure 4.1 (a) Equilibrium phase diagram and (b) thermomechanical processing procedures of micro-alloyed ZE-01, ZE-02, and ZE-05 alloys.

4.3.4.Theoretical simulations

Density functional theory (DFT) calculations were introduced to investigate the influence of alloying elements on SFEs among various slip systems. All the DFT calculations were performed using Vienna Ab-initio Simulation Package (VASP) [28,29] with projector-augmented plane-wave (PAW) method [30]. For the exchange-correlation functional, the generalized gradient approximation (GGA-PBE) [31] is used. Molecular

dynamics (MD)Atomistic simulations are performed using LAMMPS package [32] considering three common slip systems in Mg, and the evolution of Peierls stress was simulated.

4.3.5.Mechanical property testing

To examine the effect of texture weakening on ductility, tensile tests were conducted on annealed specimens using an MTS testing system equipped with an extensometer. Bone shape specimens with a gauge length of 25mm and thickness of 2mm were machined along the RD according to ASTM standards [33]. The tensile tests were performed at room temperature with an engineering strain rate of $1 \times 10^{-3}\ s^{-1}$.

4.4. Results

4.4.1.Nd dissolution upon solutionizing

The as-received plates of three alloys all presented a large number of Nd-related precipitates (Figure 4.20). To achieve significant Nd dissolution, two solutionizing temperatures of $450°C$ and $550°C$, according to the thermodynamic calculation, have been examined. The Nd solute can be further divided as the solutionized Nd in the matrix and the segregated Nd along grain boundaries. Figure 4.2 shows the STEM images after solutionizing at 450℃ and 550℃ of the ZE-02 specimen as an example. The bright field (BF) images reveal Nd-related precipitates and high-angle annular dark-field (HAADF) images show grain boundary segregation. The corresponding EDS mapping of Mg, Zn, and Nd are also shown in Figure 4.2. At 450℃, Nd and Zn were co-segregated along the grain boundaries (Figure 4.2 (a)) and a large number of precipitates containing Nd and Zn were observed (Figure 4.2 (b)). By contrast, in the 550℃-solutionized specimen, only a few

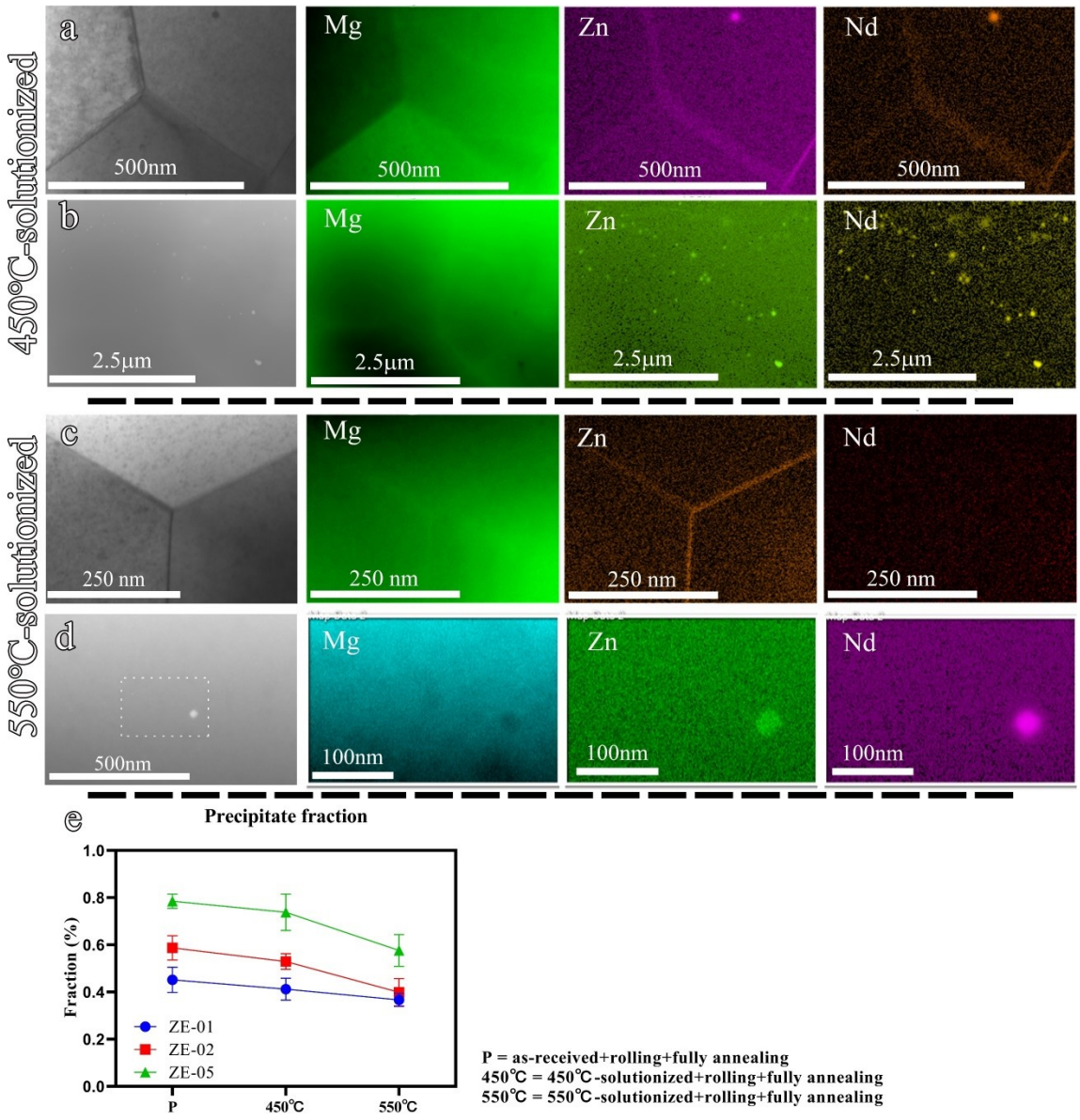

Figure 4.2 (a, c) STEM-HAADF images and corresponding EDS maps showing grain boundary segregation, (b, d) STEM-BF images and corresponding EDS maps showing precipitates of 450 ℃ and 550 ℃-solutionized ZE-02, and (e) the volume fraction of precipitate of ZE-01, -02, -05 alloys at initial, 450 ℃ and 550 ℃-solutionized conditions.

fine precipitates (~30 nm) containing Nd were observed (Figure 4.2 (d)) and the grain boundary segregation vanished (Figure 4.2 (c)). This suggests that more Nd was dissolved in the Mg matrix at 550℃ as predicted in the Langmuir and McLean mode [34]. The volume fractions of precipitates of the three ZE alloys at the as-received, 450℃-solutionized, 550℃-solutionized conditions have been measured based on BSE images

(Figure 4.2 (e)). Fewer precipitates were observed in the three ZE alloys with increasing the solutionizing temperature. Hence, it can be inferred that more Nd dissolution was achieved after 550℃ solutionizing.

4.4.2.Microstructure and texture of solutionized ZE alloys

The solutionized materials at both $450°C$ and $550°C$ were subjected to hot rolling and post-deformation annealing to understand the effect of Nd solute on the microstructure and texture evolution.

4.4.2.1.ZE alloys solutionized at $450°C$

The as-rolled microstructures of three ZE alloys solutionized at $450°C$ are shown in Figure 4.3.

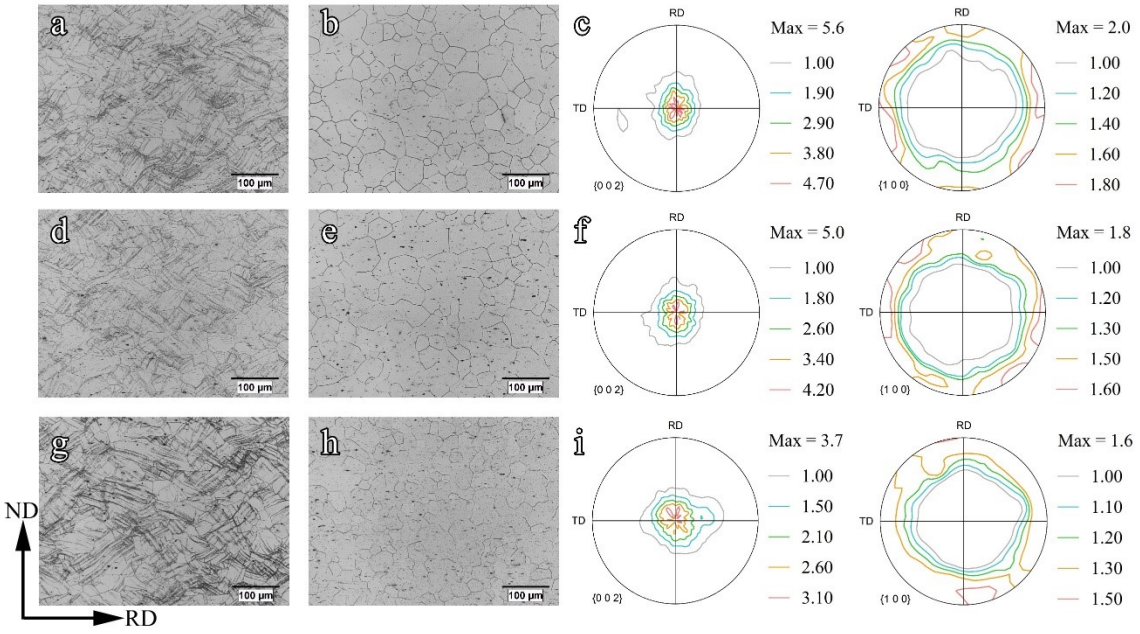

Figure 4.3 The optical microstructures and the (0002) and (10-10) pole figures of 450℃-solutionized ZE alloys subjecting to rolling and subsequent annealing: (a) rolled ZE-01, (b) annealed ZE-01, (c) macro-texture of annealed ZE-01, (d) rolled ZE-02, (e) annealed ZE-02, (f) macro-texture of annealed ZE-02, (g) rolled ZE-05, (h) annealed ZE-05, and (i) macro-texture of annealed ZE-05.

The three alloys reveal heavily twinned microstructures and DRX is suppressed. After post-deformation annealing at 350°C for 10 minutes, refined equiaxed grains were obtained in all specimens indicating the completion of SRX. The average SRXed grain sizes (GS) of the ZE-01, -02, and -05 alloys were 36 μm, 32 μm, and 24 μm, respectively (Figure 4.3 (b), (e) and (h)). After annealing, the macro-textures remained basal for ZE-01 and ZE-02, while their texture intensities were slightly weakened compared to their corresponding as-received counterparts (Figure 4.3 (c) and (f), Figure 4.21 (c) and (f)). However, the macro-texture of ZE-05 exhibited a noticeable basal pole split along the TD. The texture intensity dropped to a much weaker level at 3.7 (Figure 4.3 (i)).

4.4.2.2.ZE alloys solutionized at 550°C

4.4.2.2.1.Microstructure and texture as-hot rolled

The Inverse pole figure (IPF) maps of the as-rolled specimens are shown in Figure 4.4. The high angle grain boundaries (HAGBs, >10°) are marked as black and low angle grain boundaries (LAGBs, 2°~10°) are marked as grey. A deformed microstructure with grains containing deformation twins is observed in ZE-01 after rolling (Figure 4.4 (a)). Limited texture randomization is observed with the basal poles mainly being scattered along the RD. Meanwhile, a secondary TD-split texture component is also detected. The microstructure of as-hot rolled ZE-02 was roughly divided as the basal grains occupied area and the heavily deformed area. The former was dominated by very large basal grains (red grains in Figure 4.4 (b)), which lead to the concentrated basal texture at an intensity of 49.3 mrd. The latter was characterized as a mixture of non-basal grains, shear bands, and deformation twins. The ZE-05 specimen revealed a heavily twinned structure along

with evident shear bands. The texture of deformed ZE-05 was intensified at 42.95 due to the occurrence of non-basal parent grain (Figure 4.4 (c)).

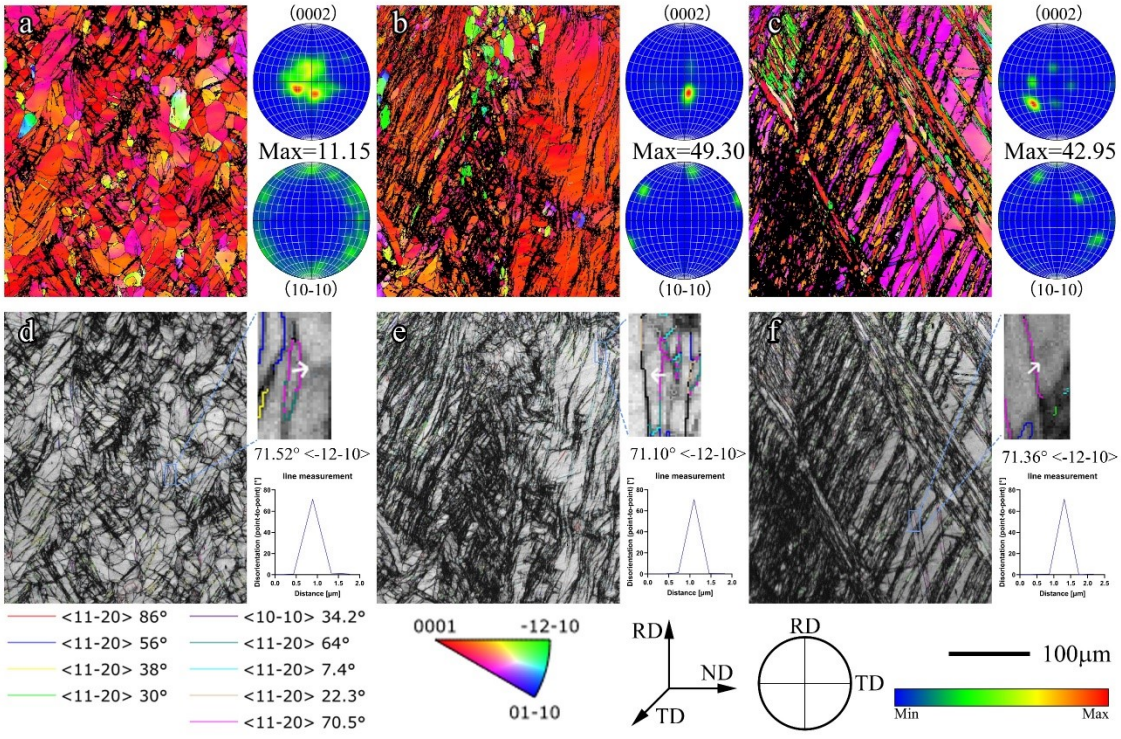

Figure 4.4 The as-rolled microstructures, micro-textures, twin distributions of 550 ℃-solutionized ZE alloys : (a, d) ZE-01, (b, e) ZE-02, (c, f) ZE-05.

Deformation twins were characterized by EBSD in as-rolled ZE alloys despite the non-indexed region due to severe plastic deformation, as shown in Figure 4.4 (d), (e), and (f). The commonly reported twinning modes and the corresponding twin boundary fractions are listed in Table 4.4.1. The twin boundaries in the as-rolled ZE-01 alloy were dominated by the $\{10\bar{1}1\} - \{10\bar{1}2\}$ compression-tension double twin (CTDT), which was characterized as a misorientation angle of $38 \pm 5°$ about the $\langle 11\bar{2}0\rangle$axis. For the ZE-02 alloy, the $\{10\bar{1}2\} - \{10\bar{1}2\}$ tension-tension double twin (TTDT) occupied almost a quarter of the total indexed boundaries, which was validated by the predominance of a $7.4 \pm 3°$ misorientation rotating about the $\langle 11\bar{2}0\rangle$ axis. Moreover, the TTDTs were found mainly in

the giant basal grains rather than in the non-basal grains. Also, it is noted that a considerable number of compression twins and CTDT were detected in the ZE-02, as shown in the band contrast (BC) map in Figure 4.4 (e). In the as-rolled ZE-05 specimen, the $\{10\bar{1}1\} - \{10\bar{1}2\}$ CTDT was characterized as the main twinning mechanism.

Table 4.4.1 Twin modes, possible CSL boundaries, the corresponding crystallographic information, and the twin boundary fraction in EBSD characterized as-rolled 550℃-solutionized ZE-01, ZE-02, and ZE-05.

		Twin plane	Twin shear direction	Theoretical Misorientation	Twin Characterization	Twin boundary fraction (%)		
						ZE-01	ZE-02	ZE-05
Tension – I [32]		$\{10\bar{1}2\}$	$\langle\bar{1}011\rangle$	$86.3°\langle11\bar{2}0\rangle$	$86 \pm 5°\langle11\bar{2}0\rangle$	4.25	3.47	11.00
Compression – I [32]		$\{10\bar{1}1\}$	$\langle10\bar{1}\bar{2}\rangle$	$56.2°\langle11\bar{2}0\rangle$	$56 \pm 5°\langle11\bar{2}0\rangle$	5.54	9.87	7.01
Compression – II [32]		$\{10\bar{1}3\}$	$\langle30\bar{3}\bar{2}\rangle$	$64°\langle11\bar{2}0\rangle$	$64 \pm 5°\langle11\bar{2}0\rangle$	3.60	4.98	1.46
Tension – II [33]		$\{11\bar{2}1\}$	$\langle11\bar{2}\bar{6}\rangle$	$34.2°\langle10\bar{1}0\rangle$	$34.2 \pm 5°\langle10\bar{1}0\rangle$	0.15	0.03	0
Compression-tension – I [32]	**Variant-I**	$\{10\bar{1}1\} - \{10\bar{1}2\}$		$37.5°\langle11\bar{2}0\rangle$	$38 \pm 5°\langle11\bar{2}0\rangle$	22.0	9.16	15.90
	Variant-II			$30.1°\langle11\bar{2}0\rangle$	$30 \pm 5°\langle11\bar{2}0\rangle$	7.40	9.36	13.30
Compression-tension – II [32]	**Variant-II**	$\{10\bar{1}3\} - \{10\bar{1}2\}$		$29.7°\langle11\bar{2}0\rangle$				
	Variant-I			$22.3°\langle11\bar{2}0\rangle$	$22.3 \pm 5°\langle11\bar{2}0\rangle$	1.72	12.1	0.96
Tension-tension [34]		$\{10\bar{1}2\} - \{10\bar{1}2\}$		$7.4°\langle11\bar{2}0\rangle$	$7.4 \pm 3°\langle11\bar{2}0\rangle$	7.46	24.4	4.59
Near-CSL boundary [31]				$70.5°\langle11\bar{2}0\rangle$	$70.5 \pm 5°\langle11\bar{2}0\rangle$	2.71	2.33	2.67

Besides the various twins reported in other Mg alloys, a new type of twinning, which exhibited a characteristic misorientation angle of $70.5 \pm 5°$ about the $\langle11\bar{2}0\rangle$ axis, was also observed. Evidence of this was seen in the rolled $550°C$-solutionized ZE alloys (the line measurement results in Figure 4.4 (d), (e), and (f)). This special boundary was theoretically predicted as one of the possible coincidence site lattice (CSL) boundaries in Bonnet's work [35]. To the authors' knowledge, this is the first time that this near-CSL boundary was experimentally observed as the form of a twin boundary in Mg alloys. Since this twinning mechanism barely affect the overall texture evolution, the detailed works

focusing on revealing the crystallographic information for this specific twinning mode is not executed in the current study.

4.4.2.2.2.Microstructure and texture evolution during post-deformation annealing

Post-deformation annealing of the as-rolled ZE alloys subjected to 550 °C solutionizing was performed at 450°C for 9 minutes. Full SRX was accomplished in the ZE-01, -02, and -05 alloys with average grain sizes of 39 μm (Figure 4.5 (a)), 19 μm (Figure 4.5 (c)), and 29 μm (Figure 4.5 (e)), respectively.

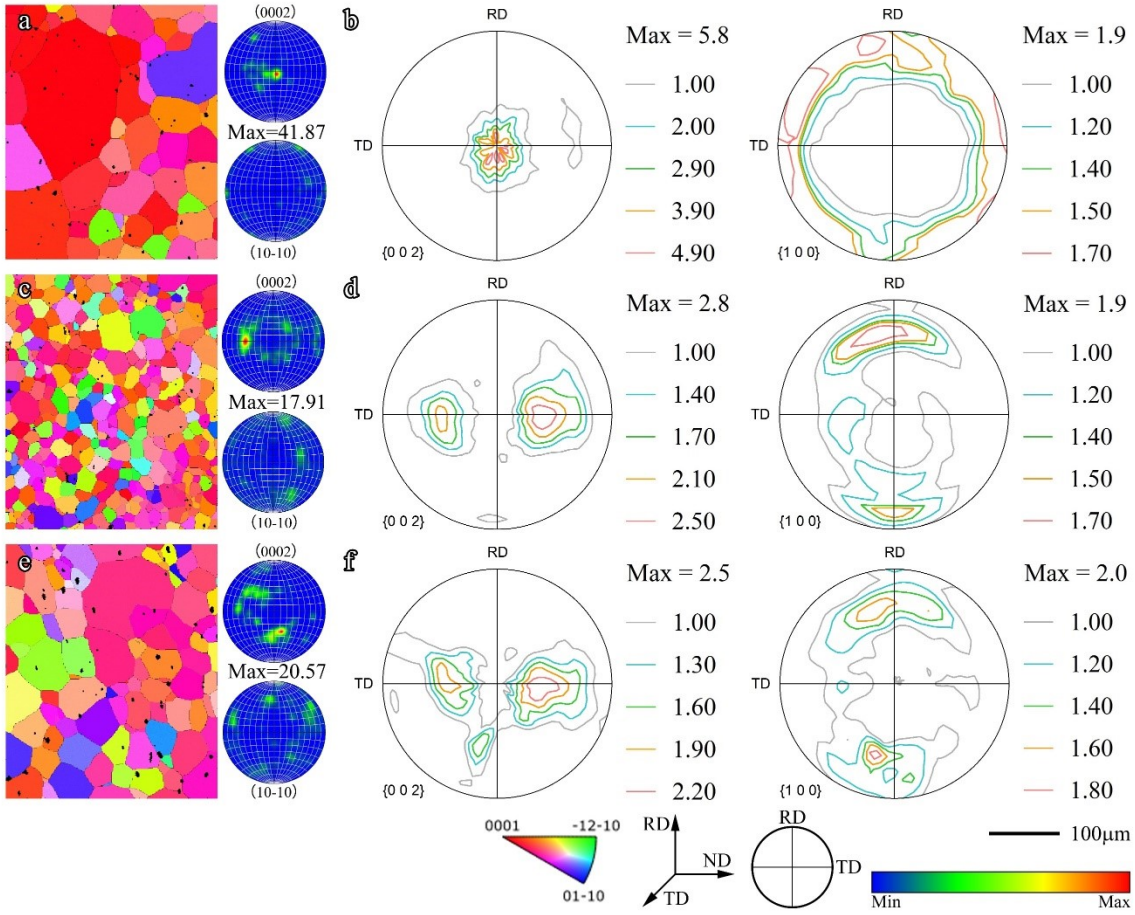

Figure 4.5 The EBSD IPF maps and corresponding micro-textures and macro-textures of 9-minutes continuously annealed ZE alloys: (a, b) ZE-01, (c, d) ZE-02, (e, f) ZE-05.

The as-annealed ZE-01 showed a basal texture and its intensity was higher than that of the 450°C-solutionized counterpart due to the slight grain coarsening caused by higher

annealing temperature (Figure 4.5 (b)). However, pronounced texture difference occurred in ZE-02 and ZE-05. The concentrated basal textures were altered to a weakened macro-texture with basal poles tilted $\pm 40\sim60°$ away from the ND toward the TD, as shown in Figure 4.5 (d) and (f). This TD-split texture was indexed closing to $\{01\bar{1}2\}\langle 0\bar{1}11\rangle$ and $\{11\bar{2}3\}\langle\bar{1}\bar{1}22\rangle$.

To understand the role of different deformation substructures, such as twins and shear bands, on SRX nucleation and grain growth, the SRX process of the $550°C$-solutionized ZE alloys was tracked by quasi-in-situ EBSD. After annealing ZE-01 for 3 minutes at $450°C$, 98.7% of the surveyed area recrystallized with an average GS of 10.9 μm. Meanwhile, a weaker basal texture with intensity at 8.5 mrd and basal poles dispersed along the RD was observed (Figure 4.6 (a)). With increasing annealing time to 30 minutes, the SRXed grains were gradually coarsened to an average GS of 26.5 μm. The texture randomization brought by SRS also lightly retarded due to the grain growth. Eventually, the basal texture was strengthened with a final intensity at 9.8 mrd (Figure 4.6 (a) to (h)). This phenomenon indicated that the grain growth of non-basal grains was less favored.

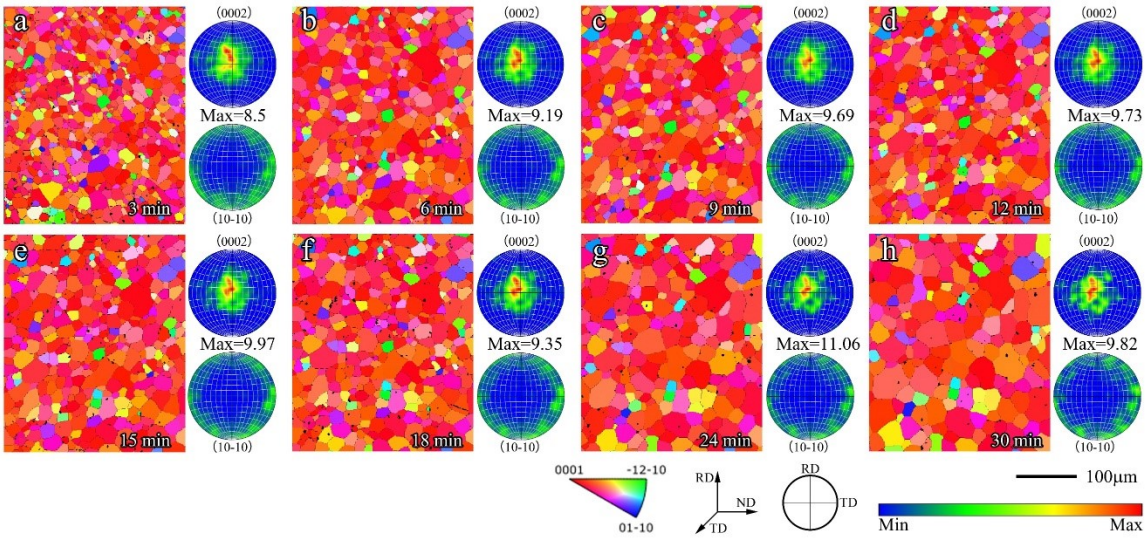

Figure 4.6 The IPF maps and the corresponding micro-textures of hot rolled 550℃-solutionized ZE-01 during 450℃ annealing intervals of (a) 3 minutes, (b) 6 minutes, (c) 9 minutes, (d) 12 minutes, (e) 15 minutes, (f) 18 minutes, (g) 24 minutes, and (h) 30 minutes.

The SRX kinetics was significantly retarded for ZE-02 compared to that of ZE-01. After annealing at $450°C$ for 3 minutes, 5.6% recrystallization was achieved. Over 60% of the microstructure was dominated by giant basal grain that originated from the solutionizing (Figure 4.7 (a)), which lead to a strong basal texture. Recrystallized grains were mainly observed in the vicinity of the shear bands and deformation twins. The SRX fraction leaped to 47.6% (Figure 4.7 (b)) after 6-minutes annealing, while the residual of basal grain with TTDT twins was reluctant to nucleate. Meanwhile, a weak TD-split texture component featuring the basal poles tilting toward TD about 40~60 degrees emerged (Figure 4.7 (b)). This TD-split texture component resulted from the new orientation introduced by the SRXed grains. The SRX fraction linearly climbed to 99.5% after 30-minutes annealing in companied with the recrystallization of deformed structures and the enhancement of the TD-split texture component (Figure 4.7 (c) to (h)). As demonstrated by Su et al. [51], the deformation temperature has a profound effect on the CRSS of different slip systems in Mg alloys.

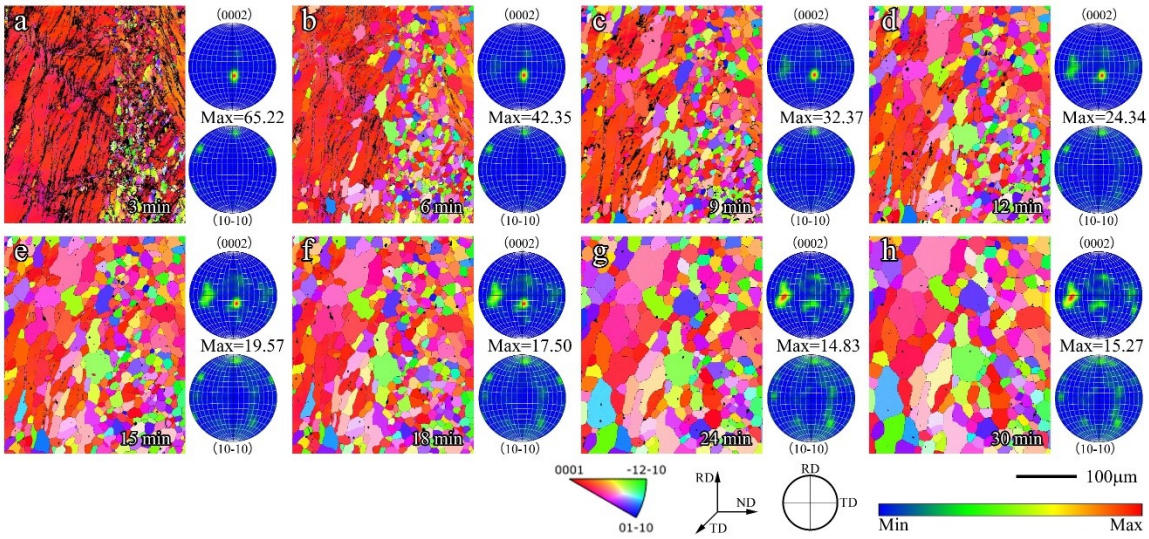

Figure 4.7 The IPF maps and the corresponding micro-textures of hot rolled 550℃-solutionized ZE-02 during 450℃ annealing intervals of (a) 3 minutes, (b) 6 minutes, (c) 9 minutes, (d) 12 minutes, (e) 15 minutes, (f) 18 minutes, (g) 24 minutes, and (h) 30 minutes.

The microstructural evolution of the 550°C-solutionized ZE-05 is similar to that of ZE-02. SRX kinetics was further reduced due to higher RE addition and solutionizing. The recrystallization initiated after 9-minutes annealing with SRX nucleated preferentially in the areas more deformed, such as shear bands and twins (Figure 4.8 (a) to (c)). The SRX fraction reached 30%, relatively slowly, after 18-minutes annealing. This increment in SRX fraction was gained mainly due to the grain growth. The deformed microstructure was maintained featuring a mixture of giant grains along with twinning (Figure 4.8 (d) to (f)). Eventually, the SRX fraction reached 82.2% and 90.1% after 24-minutes and 30-minutes, respectively (Figure 4.8 (g) and (h)). It is worth mentioning that there was still part of the residual deformed grain that failed to recrystallize, which was indicated by arrows in Figure 4.8 (h). Texture weakening was also observed during the annealing of the ZE-05 alloy. In general, the texture intensity descanted from 44.5 mrd to 22.8 mrd, while the primary non-basal texture resulting from rolling was reformed to a TD-split texture.

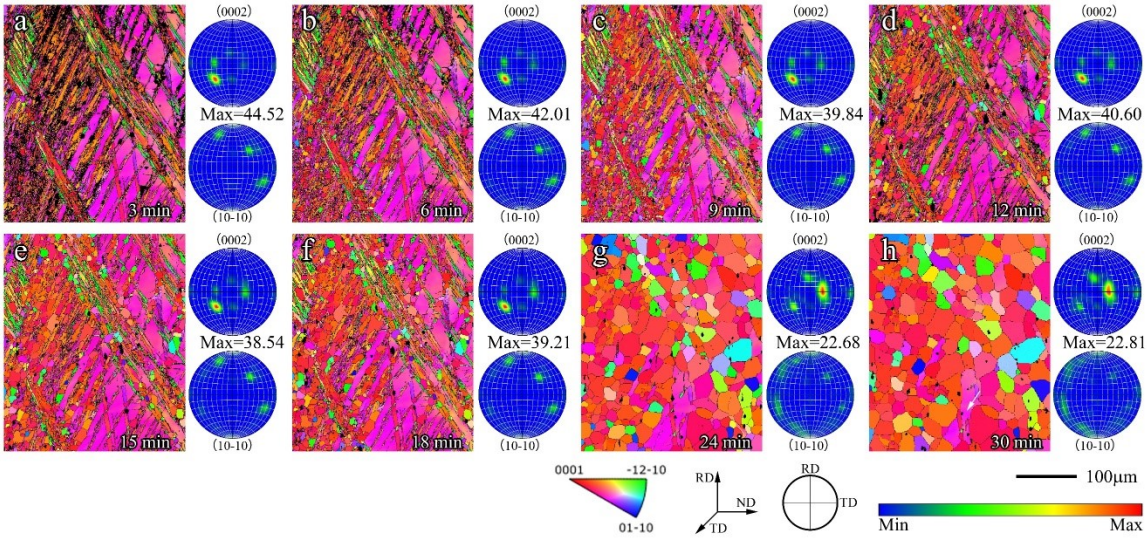

Figure 4.8 The IPF maps and the corresponding micro-textures of hot rolled 550℃-solutionized ZE-05 during 450℃ annealing intervals of (a) 3 minutes, (b) 6 minutes, (c) 9 minutes, (d) 12 minutes, (e) 15 minutes, (f) 18 minutes, (g) 24 minutes, and (h) 30 minutes.

4.4.3.Room temperature tensile test

Room temperature tensile tests were executed to assess the influence of texture modification on ductility for $550°C$-solutionized ZE alloys. The stress-strain curves, macro-textures, and microstructures are shown in Figure 4.9. The ZE-01 specimen, annealed at $350°C$ for 10 minutes, exhibited a refined grain structure (average GS 26 μm) and maximum texture intensity of 4.6 mrd. Despite this being the lowest texture intensity of this series of annealed ZE-01 structures, the elongation to failure of the annealed ZE-01 specimen was only 12.3%. To achieve the fully SRXed structure, the ZE-02 and ZE-05 specimens were annealed at $450°C$ for 9 minutes. The elongation to failure of annealed ZE-02 and ZE-05 reached 23.0% and 23.7%, and the corresponding average grain sizes were 19 μm and 29 μm, respectively. Obviously, grain refinement was not the reason for the doubled elongation in ZE-02 and ZE-05 since annealed ZE-05 held the largest GS. Given the distinctive texture weakening performance of ZE-02 and ZE-05 have shown. The

ductility enhancement was mainly brought by the non-basal texture with low intensity and TD-split feature.

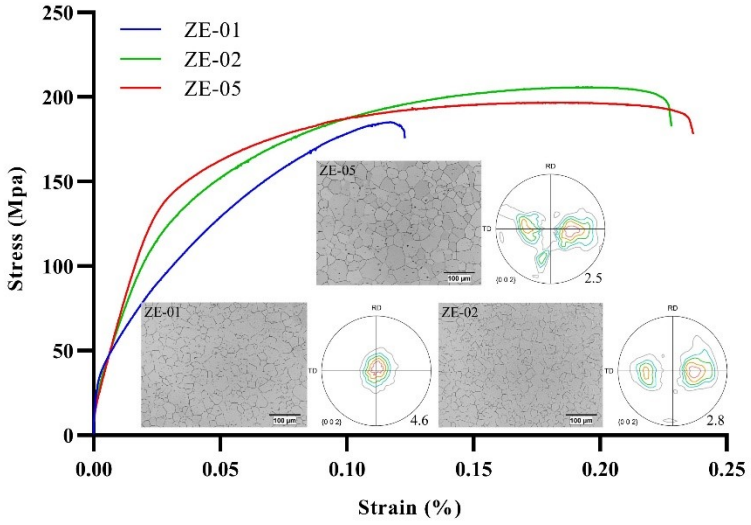

Figure 4.9 The stress-strain curve, the corresponding microstructures, and (0002) pole figures of annealed ZE alloys subjected to room temperature tensile test.

4.5. Discussion

4.5.1.Effect of Nd on macro-texture evolution

The ZE-01, -02, and -05 alloys with three different initial conditions, i.e., as-received, $450°C$-solutionized, and $550°C$-solutionized, were subjected to the same hot rolling processes followed by full static recrystallization upon post-deformation annealing. Figure 4.10 shows the comparison of the maximum macro-texture intensities of the annealed ZE alloys with three different initial conditions. In general, texture was weakened for ZE alloys with increasing Nd content from 0.1 wt.% to 0.5 wt.%. Meanwhile, lower texture intensity and wider basal pole distribution resulting from higher solutionizing temperature. The most weakened textures were found in ZE-02 and ZE-05 specimens solutionized at $550°C$. One of the popular theories to explain the texture weakening in RE-

containing Mg alloy is the PSN effect brought by RE addition [13]. However, the average precipitate fraction for all three micro-alloyed ZE alloys was less than 0.8% (Figure 4.2 (e)). Moreover, PSN was reported contributing to texture weakening by randomizing the SRXed grains rather than forming a specific texture pattern. Finally, in this current work, texture weakening/change increased with increasing solutionizing temperature, almost certainly reducing the precipitate volume fraction. Thus, PSN is not considered to be the reason for the formation of TD-split texture. Given the fact that more Nd was dissolved in the matrix at 550°C owing to the accelerated kinetics (as proven by the STEM observations (Figure 4.2)), it can be concluded that Nd in solution is crucial for texture modifications in these micro-alloyed Mg-Zn-Nd alloys [22]. The results indicate that there is little change in texture in the as-deformed state, with the significant changes occurring during static recrystallization. Therefore, the next section discusses the effect of Nd on recrystallization behaviour.

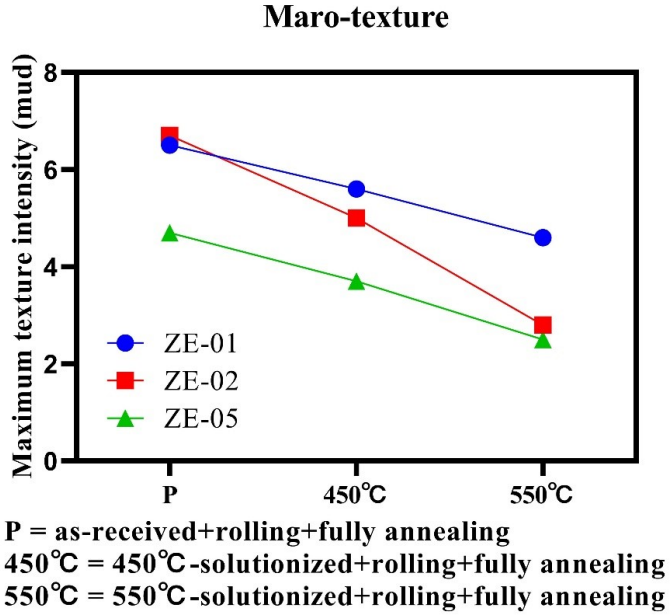

Figure 4.10 Macro-texture of ZE alloys subjecting to different solutionizing treatment (the 550℃-solutionized ZE-02 and ZE-05 were annealed at 450℃ for 9 minutes, and the rest of samples were annealed at 350℃ for 10 minutes).

4.5.2.Role of Nd in solution on the formation of TD-split texture during recrystallization

In the three ZE alloys, nucleation initiated in the vicinity of deformation twins and shear bands, which possess higher stored energy and thus provide a higher driving force for recrystallization [36] (Figure 4.6, 4.7, and 4.8). The former is known as deformation twin induced nucleation (DTIN) [37] and the latter has been reported as shear band induced nucleation (SBIN) [38].

The deformed ZE-01 showed a twinned structure with the CTDT being the dominant twinning mode (Figure 4.4 (d)). The predominant existence of CTDT was attributed to the Nd addition; a similar phenomenon was reported in Mg-Nd binary alloys subjecting to hot rolling [39]. Guan et al. [40] reported that the TD-split texture component in an Mg-Y-Nd-Zr alloy was associated with the nucleation taking place within CTDT. The CTDTs were also observed exhibiting an overall non-basal texture with noticeable TD-split distribution in the current ZE-01 specimen (Figure 4.11 (a)). The TD-split component originated from CTDT was demonstrated by the parent gains and their twins in Figure 4.11 (b). However, the fully recrystallized specimen merely showed concentrated poles along the TD (Figure 4.11 (c)). This indicates the TD-split orientation failed to be preserved during the subsequent grain growth. The absence of TD-split texture was explained as the consequence of the inferior grain growth rate of DTIN grains [41]. The TD-split orientated grains within the individual CTDT were constrained and consumed by the other recrystallized grains [40]. Thus, the contribution of DTIN was limited in ZE-01 alloy in terms of texture optimization and the macro-texture remained basal pattern after annealing (Figure 4.5 (b)).

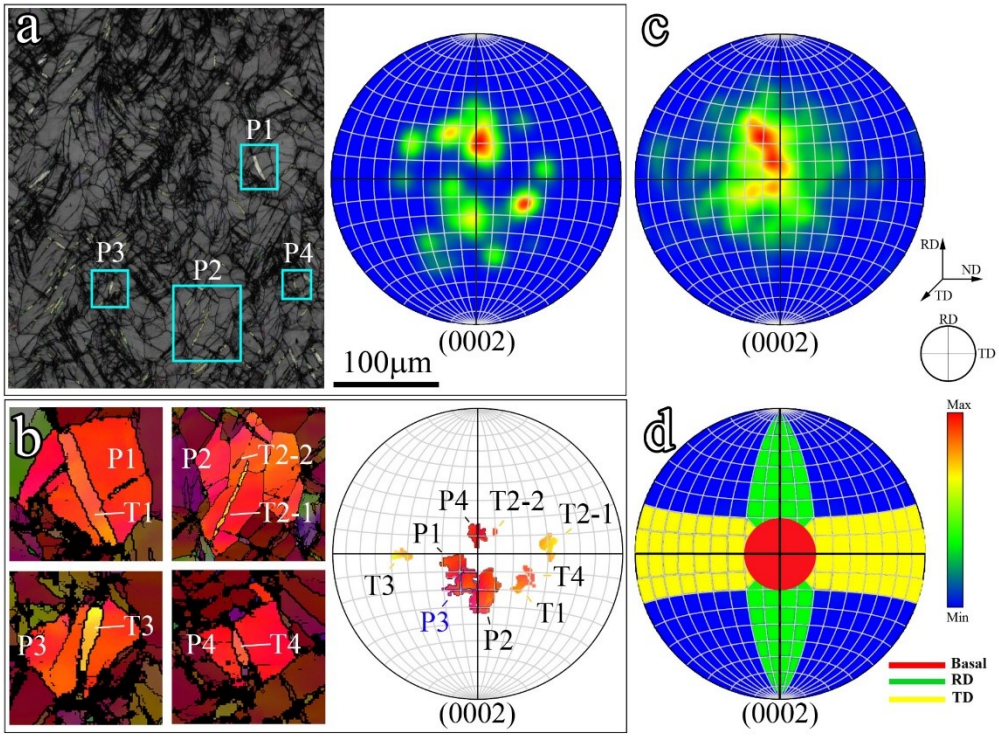

Figure 4.11 Texture modification brought by DTIN: (a) all CTDTs and the corresponding (0002) pole figure, (b) CTDTs providing TD-split orientation, (c) the (0002) pole figure of fully SRXed 550 ℃-solutionized ZE-01, (d) a schematic showing various texture components.

For the ZE-02 alloy, the nuclei and fine recrystallized grains with a Grain Orientation Spread (GOS) up to 1°are highlighted in the GOS map (Figure 4.12 (a)). Two individual zones associated with shear bands and deformation twins were selected to track the recrystallization process, as shown in Figure 4.12 (b) and (c). Recrystallized grains that contributed to the TD-split texture were highlighted in the corresponding IPF maps and pole figures. It is evident that the shear bands served as preferred nucleation site in both non-basal (Figure 4.12 (b)) and basal (Figure 4.12 (c)) oriented parent grains. The recrystallized grains with TD-split orientation mainly originated in the shear bands (marked with yellow arrows). On the contrary, deformation twin-related nucleation contributed less to TD splitting. Yet, the recrystallized grains associated with CTDTs were gradually replaced by the shear band recrystallized TD-split grains (Figure 4.12 (b)). Another major twinning mechanism is the TTDT that existed in the basal grains. The nucleation was less

favorable in TTDTs since the twins were still visible after 18-minutes annealing (Figure 4.12 (c)). This might be related to the 7.4° misorientation of the TTDT, which failed to provide enough stored energy. Therefore, these results further support that the formation of TD-split texture is less associated with DTIN. The (0002) pole figures of recrystallized grains (GOS≤1°) of ZE-02 were shown in Figure 4.12 (d). When recrystallization initiated (3 min), the SRXed grains were observed concentrating along the RD, combined with weak scattering along the TD in (0002) pole figures. The orientation was predominantly inherited from the deformed matrix (Figure 4.4 (b) and Figure 4.7(a)). Hence, the TD-split orientation is not favored during nucleation. As recrystallization proceeds, the TD-split component was gradually enhanced after 9-minutes annealing. This trend indicated the preferential grain growth during annealing favoring TD-split orientation. Thus, the main difference between ZE-01 and ZE-02 is that the TD split grains either do not nucleate or do not grow in the shear bands in ZE-01.

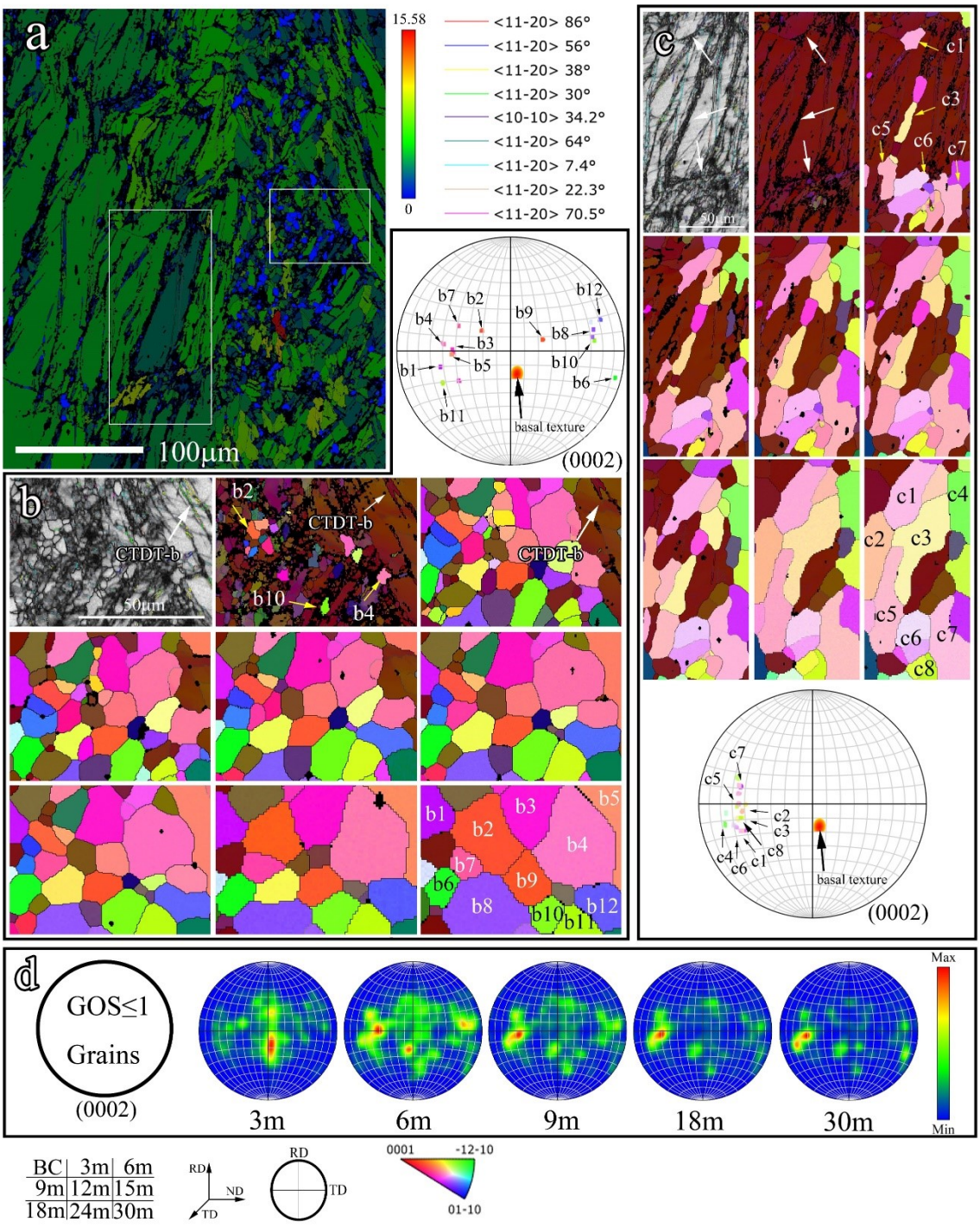

Figure 4.12 Quasi-in-situ EBSD observations of ZE-02 alloy: (a) GOS map of 3-minutes annealed ZE-02, (b, c) BC maps and IPF maps presenting the nucleation and grain growth in selected rectangular areas, (d) micro-textures of GOS⩽1 grains.

The quasi-in-situ observation of 550°C-solutionized ZE-05 provides an example of the microstructural and textural evolution in non-basal grains. The orientations that resulted

from recrystallization were divided into three categories: SB related, parent grain and DT related, as demonstrated in Figure 4.13. The SB-related orientation, which tilted the parent orientation toward the RD and TD about $50\sim60°$, was the main contributor to the SRXed texture (Figure 4.13 (b)). The SBIN played the major role in this transformation. In addition, the novel $70.5° \langle 11\bar{2}0 \rangle$ twinning also contributed to the TD-split orientation yet failed to recrystallize during the annealing. In the parent grain, the recrystallized grain orientation was the same as the as- deformed grain, and there are some unrecrystallized regions (arrowed in Figure 4.8(h)). The DT-related orientations were originated from CTDT, which exhibited a misorientation angle of $30\sim38°$ with respect to the parent grain. However, the recrystallized grains formed in CTDT were constrained within the twin lamellae and negligibly contributes to the final texture (Figure 4.13 (d)). A similar phenomenon has been reported [40], as well as proven in the observation of ZE-01. The (0002) pole figures of recrystallized grains (GOS≤1°) of ZE-05 are shown in Figure 4.13 (e). The nucleation in ZE-05 exhibits a strong dependency on the deformed structure rather than showing a preference for the TD-split orientation. The 3-min. annealed specimen simultaneously showed SB-related, parent, and DT-related orientations. After 9-minutes of annealing, the intense TD-split texture component (SB-1, black arrows in Figure 4.13 (e)) governed the micro-texture, which indicated the occurrence of preferential grain growth.

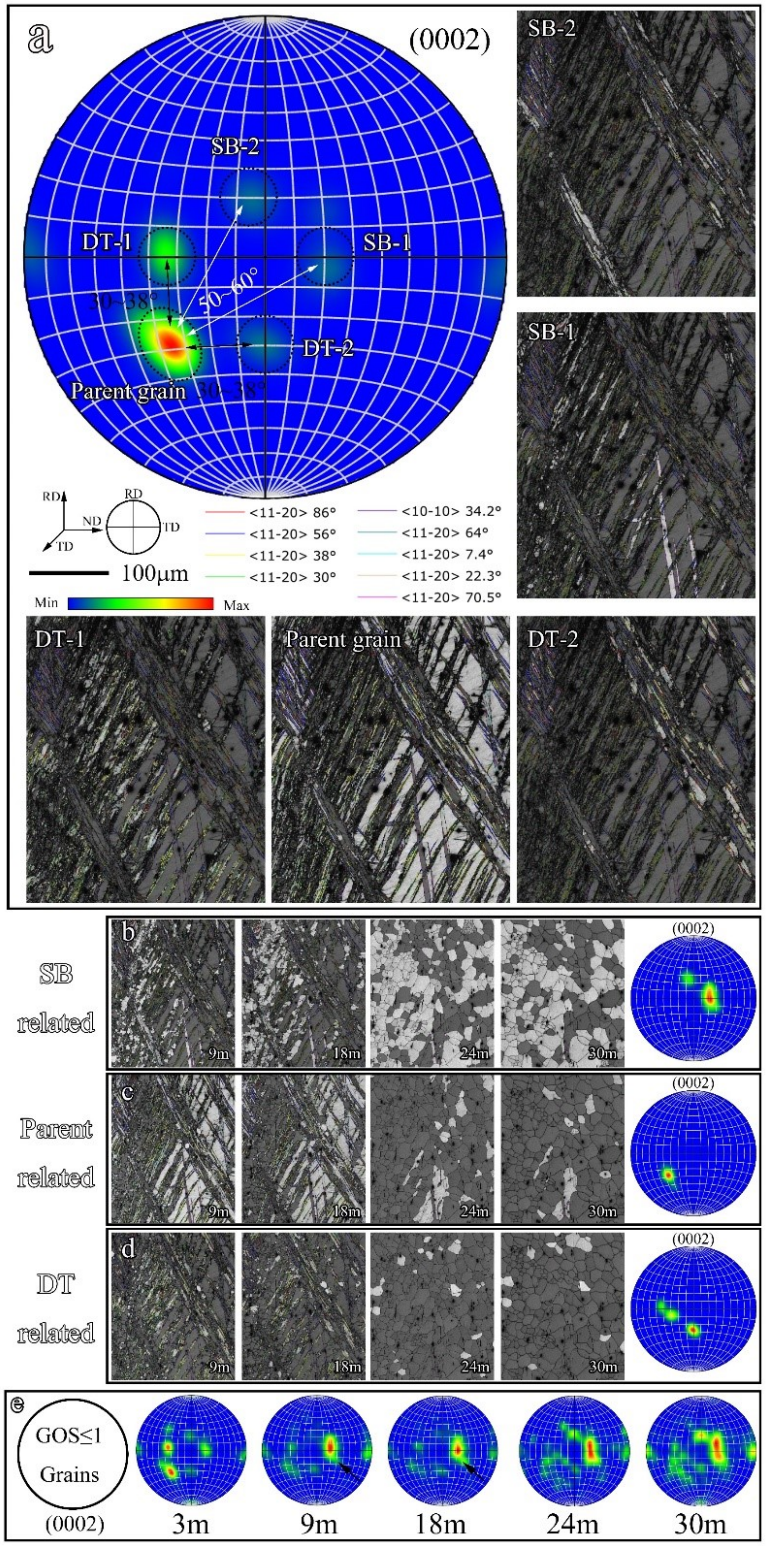

Figure 4.13 Quasi-in-situ EBSD observations of ZE-05 alloy: (a) texture components of 3-minutes annealed ZE-05, (b), (c), and (d) microstructure evolution of various texture components during annealing, (e) micro-textures of GOS ⩽1 grains.

It is known that the SBIN and DTIN serve as the mechanism that facilitates nucleation by providing heterogeneous nucleation sites. The SBIN and DTIN mechanisms were also triggered in other RE-free Mg alloys, such as AZ31 [6,42] and Mg–1wt%Zn alloy [43], but these alloys still exhibited a strong basal texture after recrystallization. This indicates that these two mechanisms alone are not an effective approach to alter the texture.

Thus, the formation of TD-split texture requires preferential grain growth upon annealing owing to the Nd-addition [19]. This has been previously observed yet has not been adequately explained. One obvious approach is to consider solute drag–like mechanisms affecting growth characteristics. However, because of the very low concentrations of Nd in solid solution, it is reasonable to expect to see segregation of Nd to grain boundaries to affect drag; this is not observed (Figure 4.2 (c)). Therefore, attention is turned to the effect of Nd on deformation mechanisms to see if this can furnish an explanation.

4.5.3.Dislocation modes and correlated recrystallization phenomena

Normally, the crystallographic texture is related to the mechanisms that accommodate deformation [8,41]. In this case, there seems to be no effect of Nd on texture of the as-deformed sheet (Figure 4.3). However, it has to be noted that texture only gives an ‘average’ picture of deformation mechanisms. Therefore, another approach is required to characterize the effect of Nd. One of the main concepts used here is to consider the formation of TD-split texture is the activation of prismatic slip [19]. Thus, in the following, the effect of Nd on the prismatic slip will be highlighted.

4.5.3.1.Intragranular misorientation axis (IGMA) evaluation

To experimentally validate the activation of the prismatic slip system, the intragranular misorientation axis (IGMA) of deformed ZE-02 was examined. The IGMA distribution was developed to analyze the influence of prismatic slip system in HCP metals [20,45,46]. The concentration around "⟨0001⟩ Taylor axis" was considered as evidence of prismatic slip system activation [45,46]. In Mg alloys, the misorientation angle within 1~3° was evaluated [19] and a maximum intensity higher than 2 mrd indicates slip system activation [45]. The three main texture components, i.e., basal, RD-split, and TD-split (Figure 4.14 (a) to (c)), were evaluated individually. The prismatic slip system dominated the TD-split grains with an IGMA intensity of 2.05 mrd around the ⟨0001⟩ Taylor axis.

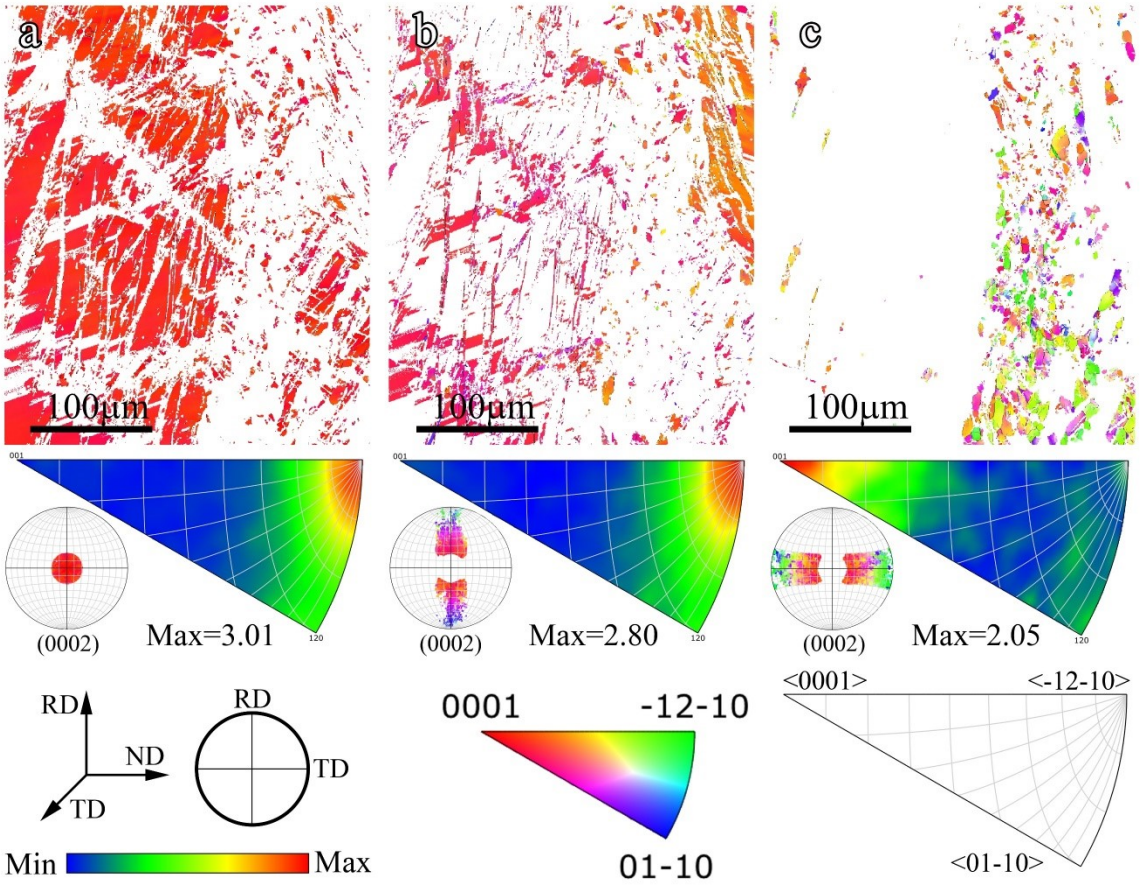

Figure 4.14 Microstructures and corresponding IGMA distribution of the (a) Basal, (b) RD-split, (c) TD-split texture components of 550℃-solutionized ZE-02 subjected to hot rolling and 3-minutes annealing.

4.5.3.2.Generalized Schmid Factor (GSF) evaluation

The correlation between TD-split texture and promoted prismatic dislocation can further be evaluated by the Generalized Schmid Factor (GSF). The GSF was proposed and developed by Luo [47] and Xin [48], who introduced the criteria of Schmid Factor evaluation into rolled Mg alloys. The GSF distribution of prismatic and basal slip systems of early (3-minutes) annealed ZE-02 are plotted in (b) and (c), respectively. In addition, slip system activation is visualized by evaluating the largest GSF among all possible slip modes. The trace of the slip plane is represented by the blue line and the slip direction was demonstrated as the red arrow. Moreover, slip traces of basal (red arrow) and prismatic (yellow arrow) slip activation are observed in deformed basal grains in ZE-02 (Figure 4.15 (a)). The slip traces indicate the activation of prismatic dislocation, especially in basal grains. Thus, combined with the IGMA analysis, the basal and prismatic slip system are the main mechanism that accommodate deformation. Apparently, the promoted prismatic slip system is crucial for the formation of TD-split texture, as reported in other RE-containing Mg alloys [19,49]. The TD-split texture failed to be observed in common Mg alloys, which have basal slip as the predominant deformation mechanism. However, the existence of basal slip should not be neglected, as revealed by the IGMA and GSF evaluation. Therefore, the TD-split texture is closely related to the promoted prismatic slip as well as the existence of basal slip.

In addition, the theoretical GSF distribution of basal and prismatic slip systems is calculated and interpreted in the (0002) pole figure (Figure 4.15 (d) and (e)). The TD-split texture of annealed ZE-02 ($\{01\bar{1}2\}\langle 0\bar{1}11\rangle$ and $\{11\bar{2}3\}\langle\bar{1}\bar{1}22\rangle$, Figure 4.15 (f)) was shown with the dashed cycles. This orientation was found to have high prismatic GSF ($GSF \geq$

0.3) as well as moderate basal GSF ($GSF \geq 0.25$). Therefore, the unique $\pm 40 \sim 60°$ TD-split texture in the current $550°C$-solutionized ZE alloys can accommodate both basal and prismatic slip during rolling.

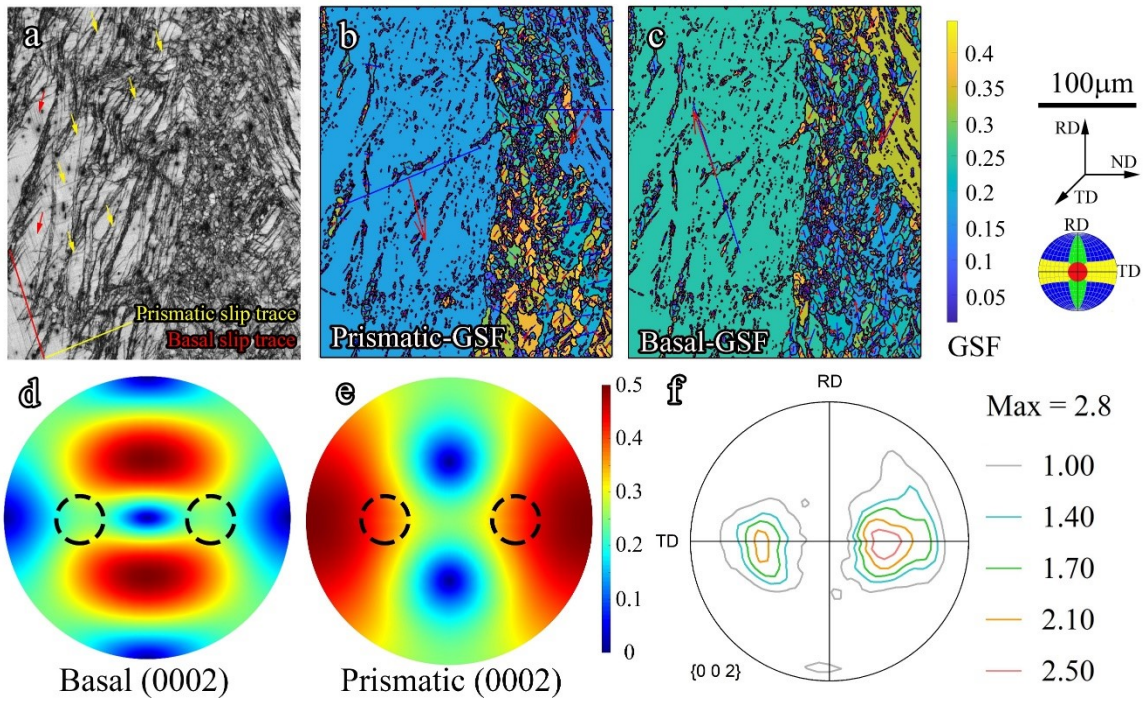

Figure 4.15 (a) BC map showing slip traces, GSF distribution maps of (b) prismatic slip system and (c) basal slip system of 550 ℃-solutionized ZE-02 subjected to hot rolling and 3-minutes annealing; Theoretical GSF distribution of (h) basal slip system and (i) prismatic slip system interpreted in (0002) pole figure; (j) macro-texture of fully annealed 550 ℃-solutionized ZE-02.

4.5.3.3.Mechanism of solute Nd in promoting prismatic slip

The IGMA and GSF analyses indicated the crucial role of the prismatic slip system in the formation of TD-split texture. Meanwhile, as described earlier, Nd addition was found to trigger the texture transition from basal to TD-split. These findings suggest a strong correlation between enhanced activity of the prismatic slip and Nd content in the current micro-alloyed ZE-alloys. To understand the mechanistic origin of such correlation, we examined how the Nd solute affects two key characteristics of dislocations, namely the SFE and Peierls stress, as elaborated in detail below.

SFE is a critical parameter that not only prescribes the dislocation core structure, but also governs activation and thermodynamic preference of different slip systems [50]. The generalized stacking fault energy (GSFE) curves were calculated for Mg with and without different alloying elements, from which the unstable SFE and stable SFE, respectively denoted as γ_{usf} and γ_{sf}, can be obtained (see 4.8.2 for details).

The calculated SFE for pure Mg and its alloys on different slip planes are shown in Figure 4.16(a). Pronounced prismatic γ_{usf} weakening was only observed with Nd addition. Moreover, it is worth noting that stable SFE does not exist for the prismatic slip (Figure 4.23), indicating the absence of dislocation dissociation into partials. The prismatic γ_{usf} values of different systems at the planar solute concentration of 50 at.% (2.08 at.% overall solute concentration for the whole system) were showed in Figure 4.16 (b). A linear relationship between the concentration of solutes and the γ_{usf} can be observed, which is also reported in Yin's work [51]. Nd has a reducing effect in prismatic γ_{usf} according to the negative slope. The lowered prismatic γ_{usf} is essential for activating the prismatic slip. The parameter χ from from Moitra's work [52] was also introduced. Higher the χ means more prismatic slip activation. The calculated results for Al, Zn and Nd are 0.80, 0.78 and 1.76, respectively. Therefore, with γ_{usf} being a critical parameter affecting dislocation nucleation and activation [53], prismatic slips are more likely to be activated in Nd-containing Mg alloys than in Al- or Zn-containing Mg alloys.

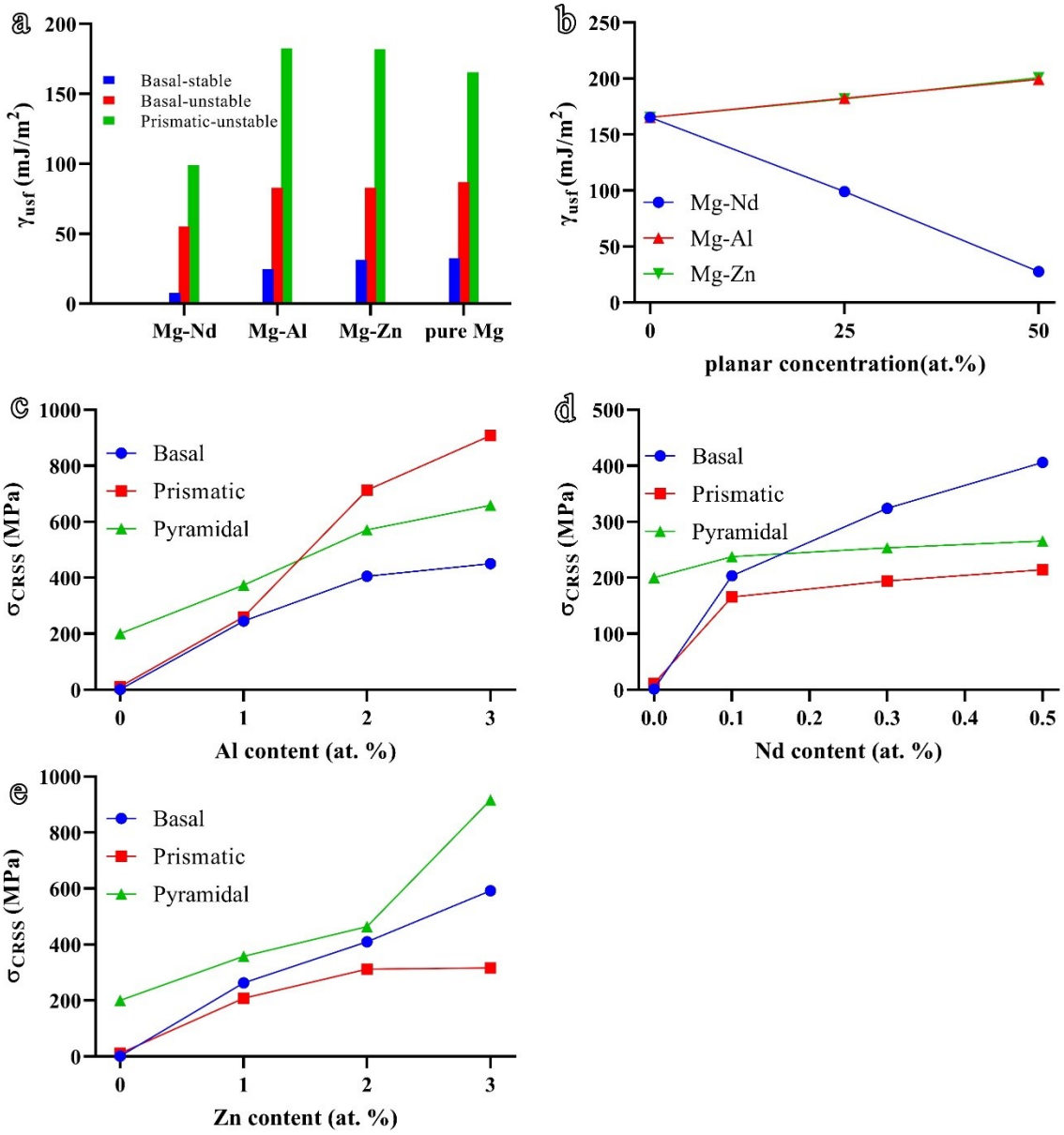

Figure 4.16 The SFE and Peierls stress (σ_{CRSS}) values obtained from simulations: (a) the calculated SFE on basal and prismatic slip plane with a planar solute concentration of 25 at. % (b) evolution of prismatic γ_{usf} with respect to planar solute concentration; The evolution of σ_{CRSS} as a function of the planar solute concentration in (c) Mg-Al system, (d) Mg-Nd system, (e) Mg-Zn system.

Besides the SFE, the Peierls stresses for different slip systems in Mg with and without different solute elements were studied. Different from the SFE calculations where solute elements were only introduced on different stacking fault planes, in simulations of Peierls stresses, solute elements were randomly introduced into the different dislocation structures (see 4.8.2 for details). The Peierls stress, which is the minimum shear stress

required to move a single straight dislocation, is directly related to the macroscopic yield stress, and thus can be regarded as an effective metric reflecting the critical resolved stress (CRSS) observed experimentally. For ease of representation, hereafter we denote the Peierls stress as σ_{CRSS}. For pure Mg, the σ_{CRSS} values obtained from simulations were 1.5Mpa, 11.5Mpa, and 200Mpa for the basal, prismatic, and pyramidal slip systems, respectively (Figure 4.25). This significant difference in σ_{CRSS} values for these slip systems is well expected and also part of the root cause of limited activation of different deformation modes beyond basal slip and thus low ductility and poor formability of pure Mg [1]. With alloying elements present, the flow stress was considerably affected, as demonstrated in Figure 4.26. The evolution of σ_{CRSS} as a function of solute concentration for the basal, prismatic, and pyramidal slip systems was shown in Figure 4.16(c), (d) and (e) for Al, Nd and Zn addition respectively. As can be seen in , though alloying element addition generally results in increase in σ_{CRSS} regardless of the slip system. However, quantitatively the effect of alloying on σ_{CRSS} can be quite different depending on the slip system and type of alloying element. For instance, in the case of Al alloying, the solute presence has strongest effect on the prismatic slip system, making the prismatic slip system the one with the highest σ_{CRSS} for Al content beyond 2 at% (Figure 4.16 (c)), and thus more difficult to be activated than basal and pyramidal slip systems. On the contrary, Nd and Zn alloying renders the prismatic slip system the one with the lowest σ_{CRSS}, and thus favors its activation over the other two slip systems. Particularly for the case of Nd alloying, the pyramidal slip system also exhibits lower σ_{CRSS} than the basal slip system for Nd content beyond 0.15 at%. It is worth noting that in the above discussion, the σ_{CRSS} values were obtained at 0K. In reality, temperature is another important factor affecting the activation

of different slip systems. As summarized by Nie et al. [3], the deformation temperature has a profound effect on the CRSS of different slip systems in Mg alloys. In particular, activation of prismatic and pyramidal slips at temperatures above 250°C was found to be greatly facilitated, attributing to a substantial reduction in their CRSS values, while in contrast, the CRSS of the basal slip is rather insensitive to temperature [52]. As described in 4.4.2.2, the as-rolled ZE-02 and ZE-05, with more Nd content, showed obvious TD tilted texture components compared to ZE-01. This indicates enhanced activation of prismatic slip in ZE-02 and ZE-05 and correlation of such activation with Nd content in the matrix. Moreover, interestingly, the unique TD-splitting texture was promoted during static recrystallization, suggesting that the prismatic dislocation structure plays an important role in preserving and enhancing TD splitting oriented grains upon recrystallization.

4.5.3.4.Geometrically necessary dislocations (GND) evaluation and preferential grain growth

To quantify the influence of various slip systems on texture evolution during recrystallization, the density of geometrically necessary dislocations (GNDs) was calculated. The GNDs derived from plastic strain is commonly employed to understand the effect of dislocation behavior on strengthening [55] and texture weakening [20]. In the current research, the EBSD data was post-processed by using Pantleon's method [56]. Given the above discussion, a relative GND ($rGND_{p/b}$) was originally proposed. The $rGND_{p/b}$ is defined as the GND density ratio between the prismatic slip system and basal slip system:

$$rGND_{p/b} = \rho_{GND-prismatic}/\rho_{GND-basal} \qquad \text{Equation 4.5.1}$$

Where the $\rho_{GND-prismatic}$ and $\rho_{GND-basal}$ are the corresponding GND densities. For $rGND_{p/b}$, the prismatic slip system and the basal slip system were simultaneously considered. The former is associated with TD-split texture and the latter is the principal slip system in Mg alloys. In addition, the $rGND_{p/b}$ eliminated the GND density difference between high GND region (deformed grains, substructures, LABs and slip traces) and low GND region (recrystallized grains). Thus, a global criterion was established to evaluate various structures in deformed, semi-recrystallized, and fully recrystallized specimens. The calculated $rGND_{p/b}$ data was illustrated in Figure 4.17, along with the evolution of the TD texture component and the SRX fraction.

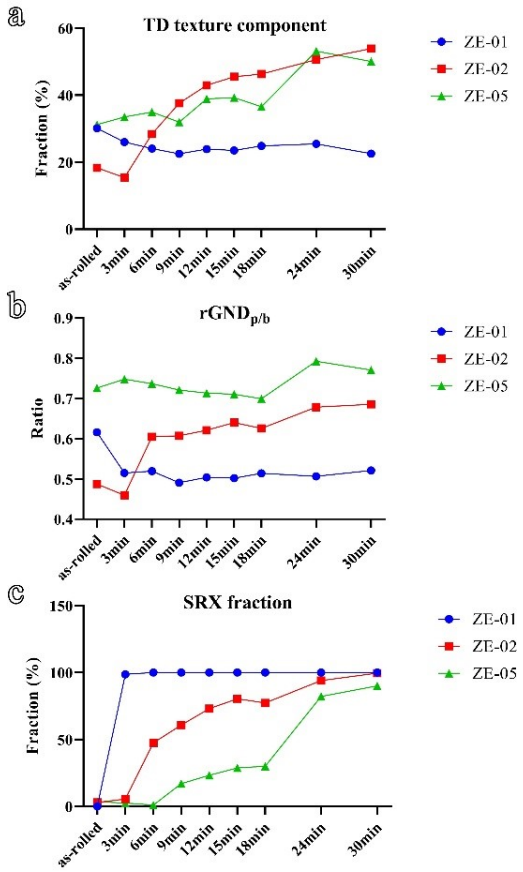

Figure 4.17 The evolution of TD-split texture component, the $rGND_{p/b}$, and the SRX fraction in current 550°C-solutionized ZE alloys during the quasi-in-situ observation.

In general, the tendency of TD texture component coincides well with that of $rGND_{p/b}$ for the $550°C$-solutionized ZE alloys with diluted Nd addition. The ZE-01 served as the reference baseline since its macro-texture is basal type upon annealing (Figure 4.5 (b)). The TD texture component gradually decreased with the annealing taking place, and the $rGND_{p/b}$ fell to about 0.5 after the SRX was accomplished. Compared to the ZE-01, the $rGNDp_{/b}$ increased to over 0.6 when SRX initiated in ZE-02 after 6-minutes annealing. Meanwhile, the TD texture component of ZE-02 surpassed that of ZE-01. Eventually, the $rGND_{p/b}$ gradually climbed to a final value of about 0.69 and the TD texture component reached its maximum at 53.9%. The positively correlated TD texture component and $rGND_{p/b}$ were also found in the ZE-05 alloy. However, its $rGND_{p/b}$ was fluctuating above 0.7, which is the highest among the three alloys. This promoted prismatic activation could be attributed to the initial non-basal texture. Overall, the $rGND_{p/b}$ is validated as an excellent tool that reflects the evolution of TD texture while circumventing the major constraints of conventional GND analysis.

Furthermore, the $rGND_{p/b}$ distributions for ZE alloys during annealing were calculated and plotted. In general, higher GND densities over 10^{16} were expected in the unrecrystallized grains as the result of residual deformation. Yet, the GND densities of basal and prismatic slip significantly dropped to about 10^{14} in recrystallized grains owing to dislocation annihilation (see Figure 4.27 for details). Thus, the $rGND_{p/b}$ distributions were interpreted differently for deformed and recrystallized grains. In the former case, a higher $rGND_{p/b}$ value (colored green to red) indicates promoted prismatic slip owing to the Nd solute, as explained in the previous part. For the latter, it was found that a lower $rGND_{p/b}$ value (colored blue) resulted from a higher basal GND density which is around 10^{15},

whereas recrystallized grains exhibited high $rGND_{p/b}$ values (around 1) due to similar GND densities for basal and prismatic slip (around 10^{14}).

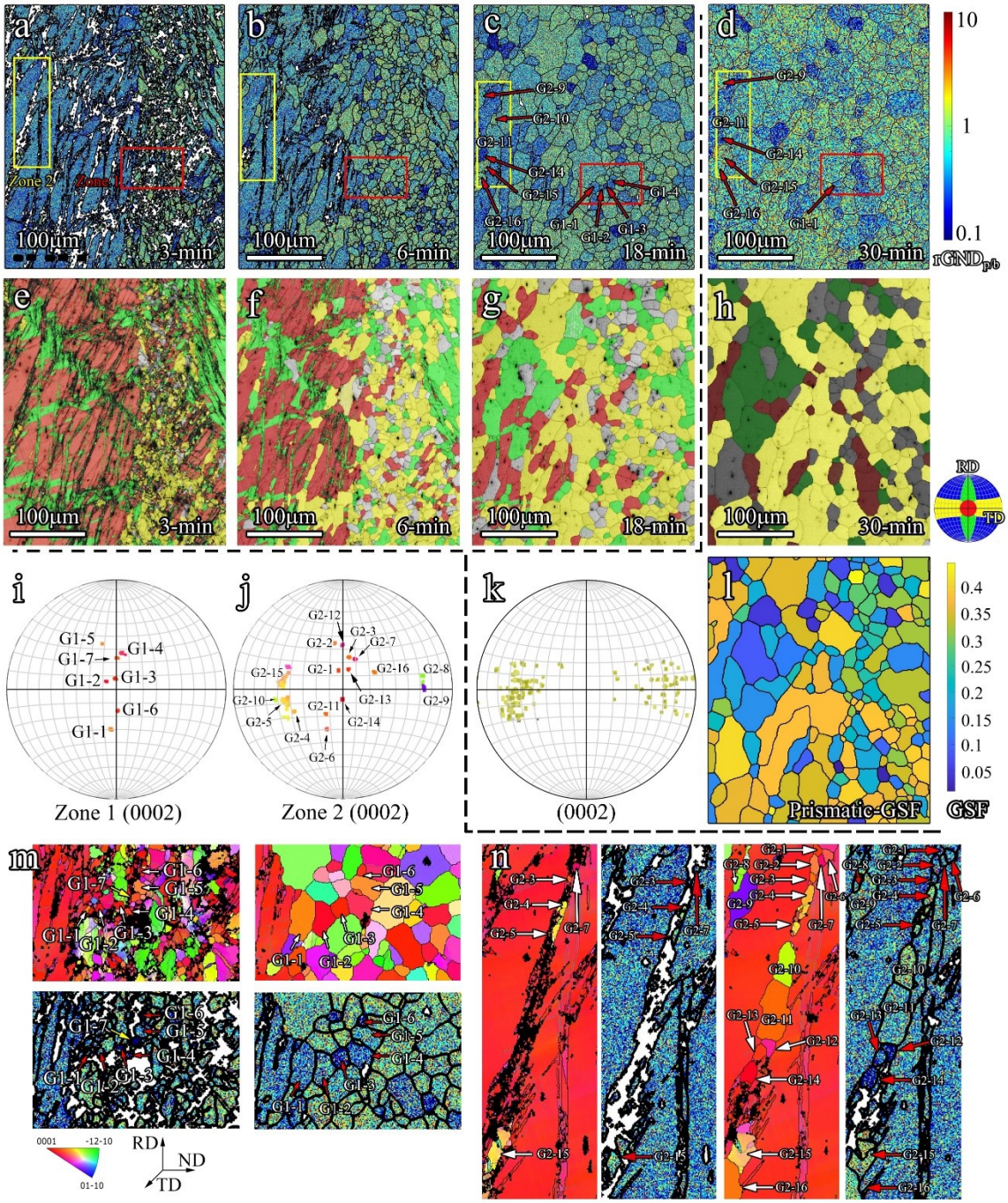

Figure 4.18 (a) to (d) the $rGND_{p/b}$ distribution and (e) to (h) texture components of ZE-02 during Quasi-in-situ EBSD; orientation of selected grains in (i) Zone 1 and (j) Zone 2; (k) orientation of highlighted grains and GSF distribution for 30-minutes annealed ZE-02; microstructure and GND distribution in (m) Zone 1 and (n) Zone 2.

Four $rGND_{p/b}$ distribution and the corresponding texture component maps are shown in Figure 4.18(a) to (d) and (e) to (h), respectively. Initially, the prismatic slip was observed significantly promoted within the deformed non-basal grains (Figure 4.18 (a)). The microstructure is dominated by the low $rGND_{p/b}$ basal grains (Figure 4.18(e)). After 6-minutes of annealing, the majority of SRXed grains feature high $rGND_{p/b}$ value and TD-split orientation (Figure 4.18 (b) and (f)). As recrystallization proceeds, those grains gradually grow (Figure 4.18 (c) and (g)) and eventually dominate the microstructure (Figure 4.18 (d) and (h)). It is worth mentioning that the TD-split grains in a fully annealed specimen display a high prismatic GSF ($GSF \geq 0.3$) (Figure 4.18 (k) and (l)). Furthermore, two individual zones were selected to trace the recrystallization process. Zone 1 focused on the deformed non-basal grains (Figure 4.18 (m)). Seven low $rGND_{p/b}$ nuclei are labeled on the IPF and $rGND_{p/b}$ distribution maps. The G1-7, which basal slip preserved the most (lowest $rGND_{p/b}$), failed to survive after 6-minutes of annealing. The other low $rGND_{p/b}$ grains exhibit a basal or RD-split orientation with lower $rGND_{p/b}$ values (Figure 4.18 (i)). Eventually, only G1-1 survives when SRX is completed (Figure 4.18 (d)). Zone 2 targets the SRX process within shear bands in the deformed basal grain (Figure 4.18 (n)). The recrystallized grains originating from the shear bands with high $rGND_{p/b}$ value are characterized as TD-split grains (Figure 4.18 (j)). Also, the grains formed through the recovery of deformed structures exhibit a lower $rGND_{p/b}$ value. As discussed in 4.5.2, the formation of TD-split texture was accomplished through preferential grain growth. Based on the evaluation of $rGND_{p/b}$ values of recrystallized grains, it can be concluded that the grains with high $rGND_{p/b}$ values, mainly TD-split grains, possessing lower GND densities, thereby growth of these grains is preferred. The grain growth of low $rGND_{p/b}$ grains,

represented by basal and RD-split grains, was less favored due to a higher basal slip GND density. Therefore, the $rGND_{p/b}$, which integrates deformation and recrystallization, serves as the indicator for TD-split texture formation.

Thus, the SRX process can be interpreted by the evolution of $rGND_{p/b}$ distribution: the prismatic slip system is promoted during deformation; nuclei with various $rGND_{p/b}$ values form mainly through SBIN; the growth of high $rGND_{p/b}$ grains is favored upon annealing. The resulting microstructure is occupied by high $rGND_{p/b}$ grains orientating TD and the overall $rGND_{p/b}$ is higher than 0.6. In addition, the $rGND_{p/b}$ reveals the criteria of TD-split texture: both prismatic and basal slip systems contribute to the TD-split texture and the former is the crucial factor.

Based on the above discussion, the mechanism of texture weakening in the current micro-alloyed ZE alloys is summarized in Figure 4.19. For the ZE alloy showing a conventional basal texture, the texture modification starts with enhanced activation of prismatic slip brought about by the solute Nd. During the intermediate annealing after the initial rolling pass, nucleation occurs in the shear bands. Meanwhile, the grain growth of nuclei with TD-split orientation is accelerated. Consequently, TD-split grains are formed in the vicinity of previous shear bands and TD-split texture component is introduced into the basal grains. Moreover, the prismatic slip would be further motivated due to the TD-split grains possessing higher GSF and $rGND_{p/b}$. Thus, a positive feedback route is established. Basal grains are gradually replaced by TD-split grains, while the TD-grains do not degrade into basal grains. Eventually, the basal texture is completely replaced with a TD-split texture after annealing. Thus, the complicated processing procedure applied to the micro-alloyed ZE alloy sheets is aimed to manipulate the Nd content in solid solution. For

the production of dilute Nd-containing Mg alloy sheet with TD-split texture and good mechanical properties, the beneficial effect brought by solutionized Nd could be facilitated by refined fabrication practice and advanced alloy design.

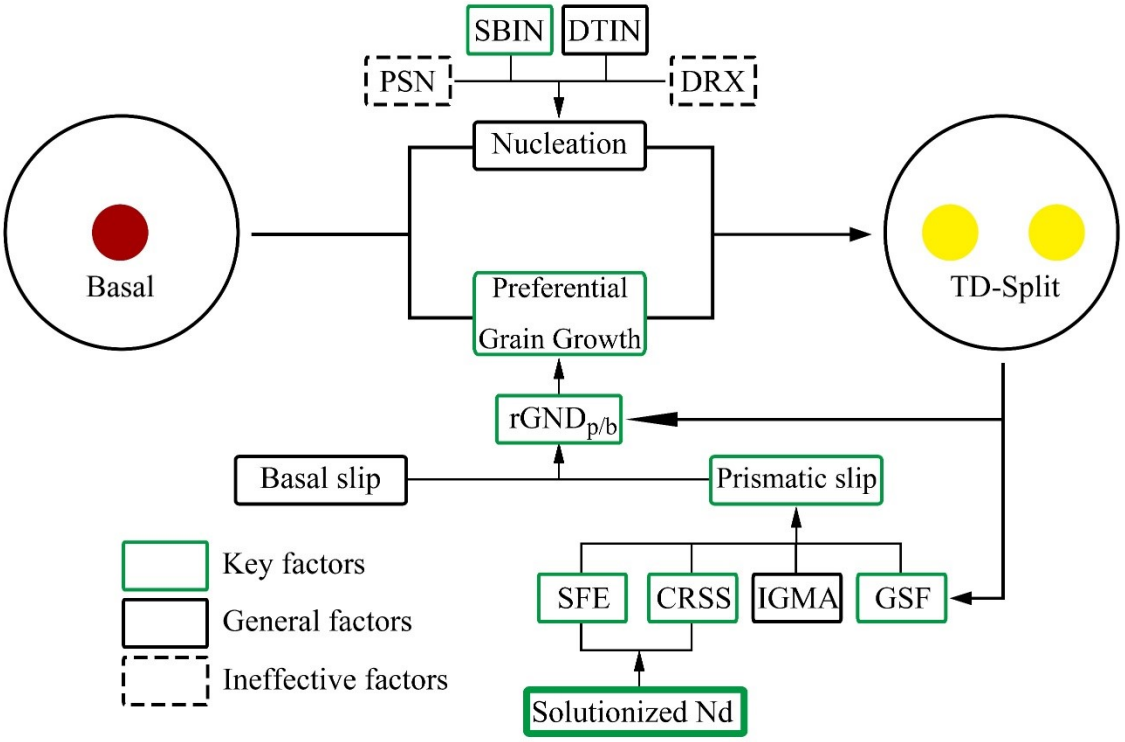

Figure 4.19 The schematic diagram showing the mechanism of forming TD-split texture due to solutionized Nd.

4.6. Conclusions

The present study has thoroughly examined and explained the origin of TD-split texture formed in Mg alloys with diluted (≤ 0.5 wt. %) Nd addition. The following conclusions can be drawn:

1) The recrystallized ZE-02 and ZE-05 alloys subjected to solutionizing at 550°C exhibited a distinctive TD-split texture (close to $\{01\bar{1}2\}\langle 0\bar{1}11\rangle$ and $\{11\bar{2}3\}\langle\bar{1}\bar{1}22\rangle$). As a comparison, the basal texture was presented in their counterparts with 450°C solutionizing. It suggested that the Nd in the solid solution is the most important factor for the formation of TD-split texture.

2) The texture transformation from concentrated basal to weakened TD-split texture upon recrystallization was precisely tracked by using the quasi-in-situ EBSD method. Nucleation was accomplished mainly through the SBIN mechanism; the formation of TD-split texture was attributed to the preferential grain growth of SRXed grains tilting toward the TD.
3) The enhanced activation of the prismatic slip system upon deformation was validated by evaluating the IGMA and GSF distribution.
4) The enhanced activation of the prismatic slip system resulted from the solute Nd. DFT and MD simulation revealed that the dilute Nd solute could easily improve the activation of the prismatic slip by modifying the SFE and CRSS of different deformation modes, which agrees with our experimental observation.
5) The evolution of $rGND_{p/b}$ values was originally proposed to provide a better understanding of the formation of TD-split texture upon recrystallization. The $rGND_{p/b}$ distribution revealed that both prismatic and the basal slip contributed to the TD-split texture, while the prismatic dislocations are the key factor to promote preferential grain growth.
6) The ZE-02 alloy showed enhanced ductility (23%) compared to the ZE-01. However, the beneficial effect was limited when Nd addition exceeded 0.2 wt.%. It provides a new pathway to economizing RE usage for the production of Mg alloy sheets with improved formability.
7) However, the 0.2 wt.% Nd gave a pronounced texture modification that is comparable to 0.5 wt.% Nd, i.e., the texture weakening effect levels off at 0.2 wt.%

Nd addition. This may be a consequence of the kinetics of Nd precipitate dissolution.

4.7. Reference

[1] M.O. Pekguleryuz, Current developments in wrought magnesium alloys, in: M. Barnett (Ed.), Adv. Wrought Magnes. Alloy., Woodhead Publishing, 2012: pp. 3–62. https://doi.org/http://dx.doi.org/10.1533/9780857093844.1.3.

[2] S.R. Agnew, J.F. Nie, Preface to the viewpoint set on: The current state of magnesium alloy science and technology, Scr. Mater. 63 (2010) 671–673. https://doi.org/10.1016/j.scriptamat.2010.06.029.

[3] J.F. Nie, K.S. Shin, Z.R. Zeng, Microstructure, Deformation, and Property of Wrought Magnesium Alloys, Springer US, 2020. https://doi.org/10.1007/s11661-020-05974-z.

[4] Y.N. Wang, J.C. Huang, Texture analysis in hexagonal materials, Mater. Chem. Phys. 81 (2003) 11–26. https://doi.org/10.1016/s0254-0584(03)00168-8.

[5] M.G. Jiang, C. Xu, H. Yan, G.H. Fan, T. Nakata, C.S. Lao, R.S. Chen, S. Kamado, E.H. Han, B.H. Lu, Unveiling the formation of basal texture variations based on twinning and dynamic recrystallization in AZ31 magnesium alloy during extrusion, Acta Mater. 157 (2018) 53–71. https://doi.org/10.1016/j.actamat.2018.07.014.

[6] J. Su, A.S. Abu, M. Sanjari, S. Yue, Correlation of static recrystallization and texture weakening of AZ31 magnesium alloy sheets subjected to high speed rolling, Mater. Sci. Eng. A. 674 (2016) 343–360. https://doi.org/10.1016/j.msea.2016.07.107.

[7] S.R. Agnew, Ö. Duygulu, Plastic anisotropy and the role of non-basal slip in magnesium alloy AZ31B, Int. J. Plast. 21 (2005) 1161–1193. https://doi.org/http://dx.doi.org/10.1016/j.ijplas.2004.05.018.

[8] J. Victoria-Hernandez, S. Yi, J. Bohlen, G. Kurz, D. Letzig, The influence of the recrystallization mechanisms and grain growth on the texture of a hot rolled AZ31 sheet during subsequent isochronal annealing, J. Alloys Compd. 616 (2014) 189–197. https://doi.org/10.1016/j.jallcom.2014.07.083.

[9] F. Guo, R. Pei, L. Jiang, D. Zhang, S. Korte-Kerzel, T. Al-Samman, The role of recrystallization and grain growth in optimizing the sheet texture of magnesium alloys with calcium addition during annealing, J. Magnes. Alloy. 8 (2020) 252–268. https://doi.org/10.1016/j.jma.2019.07.010.

[10] L.Y. Zhao, H. Yan, R.S. Chen, E.H. Han, Oriented nucleation causing unusual texture transition during static recrystallization annealing in cold-rolled Mg–Zn–Gd alloys, Scr. Mater. 188 (2020) 200–205. https://doi.org/10.1016/j.scriptamat.2020.07.037.

[11] I. Basu, T. Al-Samman, Hierarchical Twinning Induced Texture Weakening in Lean

Magnesium Alloys, Front. Mater. 6 (2019) 1–15. https://doi.org/10.3389/fmats.2019.00187.

[12] J. Min, J. Lin, Anelastic behavior and phenomenological modeling of Mg ZEK100-O alloy sheet under cyclic tensile loading-unloading, Mater. Sci. Eng. A. 561 (2013) 174–182. https://doi.org/10.1016/j.msea.2012.11.009.

[13] I. Basu, T. Al-Samman, Triggering rare earth texture modification in magnesium alloys by addition of zinc and zirconium, Acta Mater. 67 (2014) 116–133. https://doi.org/10.1016/j.actamat.2013.12.015.

[14] Y. Chino, X. Huang, K. Suzuki, K. Sassa, M. Mabuchi, Influence of Zn concentration on stretch formability at room temperature of Mg-Zn-Ce alloy, Mater. Sci. Eng. A. 528 (2010) 566–572. https://doi.org/10.1016/j.msea.2010.09.081.

[15] M. Boba, C. Butcher, N. Panahi, M.J. Worswick, R.K. Mishra, J.T. Carter, Warm forming limits of rare earth-magnesium alloy ZEK100 sheet, Int. J. Mater. Form. 10 (2015) 181–191. https://doi.org/10.1007/s12289-015-1267-2.

[16] D. Wu, R.S. Chen, E.H. Han, Excellent room-temperature ductility and formability of rolled Mg-Gd-Zn alloy sheets, J. Alloys Compd. 509 (2011) 2856–2863. https://doi.org/10.1016/j.jallcom.2010.11.141.

[17] I.-H. Jung, M. Sanjari, J. Kim, S. Yue, Role of RE in the deformation and recrystallization of Mg alloy and a new alloy design concept for Mg–RE alloys, Scr. Mater. 102 (2015) 1–6. https://doi.org/10.1016/j.scriptamat.2014.12.010.

[18] L.Y. Zhao, H. Yan, R.S. Chen, E.H. Han, Study on the evolution pattern of grain orientation and misorientation during the static recrystallization of cold-rolled Mg-Zn-Gd alloy, Mater. Charact. 150 (2019) 252–266. https://doi.org/10.1016/j.matchar.2019.02.023.

[19] X. Zeng, P. Minárik, P. Dobroň, D. Letzig, K.U. Kainer, S. Yi, Role of deformation mechanisms and grain growth in microstructure evolution during recrystallization of Mg-Nd based alloys, Scr. Mater. 166 (2019) 53–57. https://doi.org/10.1016/j.scriptamat.2019.02.045.

[20] J.P. Hadorn, K. Hantzsche, S. Yi, J. Bohlen, D. Letzig, J.A. Wollmershauser, S.R. Agnew, Role of solute in the texture modification during hot deformation of Mg-rare earth alloys, Metall. Mater. Trans. A Phys. Metall. Mater. Sci. 43 (2012) 1347–1362. https://doi.org/10.1007/s11661-011-0923-5.

[21] M. Sanjari, A.R. Farkoosh, B. Shalchi Amirkhiz, Y. He, A. Javaid, A.S. Kabir, J. Su, I.H. Jung, S. Yue, The role of the Zn/Nd ratio in the microstructural evolution of the Mg-Zn-Nd system during static recrystallization: Grain boundary partitioning of solutes, Scr. Mater. 134 (2017) 1–5. https://doi.org/10.1016/j.scriptamat.2017.01.033.

[22] Y. Liu, J. Su, R. Gao, H. Geng, A. Javaid, T. Skszek, S. Yue, Effect of Cooling Path on Precipitation Behavior, Microstructure, and Texture Evolution of Micro-alloyed Magnesium Alloy, J. Mater. Eng. Perform. (2020) 1–8.

https://doi.org/10.1007/s11665-020-04718-9.

[23] S. Asqardoust, A.Z. Hanzaki, H.R. Abedi, T. Krajnak, P. Minárik, Enhancing the strength and ductility in accumulative back extruded WE43 magnesium alloy through achieving bimodal grain size distribution and texture weakening, Mater. Sci. Eng. A. 698 (2017) 218–229.

[24] D. Guan, W.M. Rainforth, J. Gao, L. Ma, B. Wynne, Individual effect of recrystallisation nucleation sites on texture weakening in a magnesium alloy: Part 2- shear bands, Acta Mater. 145 (2018) 399–412. https://doi.org/10.1016/j.actamat.2017.12.019.

[25] C.W. Bale, P. Chartrand, S.A. Degterov, G. Eriksson, K. Hack, R. Ben Mahfoud, J. Melançon, A.D. Pelton, S. Petersen, FactSage thermochemical software and databases, Calphad. 26 (2002) 189–228. https://doi.org/https://doi.org/10.1016/S0364-5916(02)00035-4.

[26] H. Li, TexTools software version 3.0, Resmat Corp. Montr. Quebec, Canada. (2009).

[27] G. Nolze, R. Hielscher, Orientations - perfectly colored, J. Appl. Crystallogr. 49 (2016) 1786–1802. https://doi.org/10.1107/S1600576716012942.

[28] G. Kresse, J. Hafner, Ab initio molecular dynamics for liquid metals, Phys. Rev. B. 47 (1993) 558.

[29] G. Kresse, J. Furthmüller, Efficient iterative schemes for ab initio total-energy calculations using a plane-wave basis set, Phys. Rev. B. 54 (1996) 11169.

[30] P.E. Blöchl, Projector augmented-wave method, Phys. Rev. B. 50 (1994) 17953.

[31] J.P. Perdew, K. Burke, M. Ernzerhof, Generalized gradient approximation made simple, Phys. Rev. Lett. 77 (1996) 3865.

[32] S. Plimpton, Fast parallel algorithms for short-range molecular dynamics, J. Comput. Phys. 117 (1995) 1–19.

[33] A. Standard, E8, 2008, Stand. Test Methods Tens. Test. Met. Mater. ASTM Int. Pennsylvania, USA.[Doi 10.1520/E0008_E0008M-08]. (2008).

[34] J.D. Robson, Effect of Rare-Earth Additions on the Texture of Wrought Magnesium Alloys: The Role of Grain Boundary Segregation, Metall. Mater. Trans. A Phys. Metall. Mater. Sci. 45 (2014) 3205–3212. https://doi.org/10.1007/s11661-013-1950-1.

[35] R. Bonnet, E. Cousineau, D.H. Warrington, Determination of near-coincident cells for hexagonal crystals. Related DSC lattices, Acta Crystallogr. Sect. A. 37 (1981) 184–189. https://doi.org/10.1107/S0567739481000466.

[36] A. Rollett, F.J. Humphreys, G.S. Rohrer, M. Hatherly, Recrystallization and related annealing phenomena, Elsevier, 2004.

[37] K.D. Molodov, T. Al-Samman, D.A. Molodov, G. Gottstein, Mechanisms of

exceptional ductility of magnesium single crystal during deformation at room temperature: Multiple twinning and dynamic recrystallization, Acta Mater. 76 (2014) 314–330. https://doi.org/10.1016/j.actamat.2014.04.066.

[38] I. Basu, T. Al-Samman, G. Gottstein, Shear band-related recrystallization and grain growth in two rolled magnesium-rare earth alloys, Mater. Sci. Eng. A. 579 (2013) 50–56. https://doi.org/10.1016/j.msea.2013.04.076.

[39] K. Hantzsche, J. Bohlen, J. Wendt, K.U. Kainer, S.B. Yi, D. Letzig, Effect of rare earth additions on microstructure and texture development of magnesium alloy sheets, Scr. Mater. 63 (2010) 725–730. https://doi.org/10.1016/j.scriptamat.2009.12.033.

[40] D. Guan, W.M. Rainforth, J. Gao, J. Sharp, B. Wynne, L. Ma, Individual effect of recrystallisation nucleation sites on texture weakening in a magnesium alloy: Part 1- double twins, Acta Mater. 135 (2017) 14–24. https://doi.org/10.1016/j.actamat.2017.06.015.

[41] D. Guan, W.M. Rainforth, L. Ma, B. Wynne, J. Gao, Twin recrystallization mechanisms and exceptional contribution to texture evolution during annealing in a magnesium alloy, Acta Mater. 126 (2017) 132–144. https://doi.org/10.1016/j.actamat.2016.12.058.

[42] J. Su, M. Sanjari, A.S.H. Kabir, J.J. Jonas, S. Yue, Static recrystallization behavior of magnesium AZ31 alloy subjected to high speed rolling, Mater. Sci. Eng. A. 662 (2016) 412–425. https://doi.org/10.1016/j.msea.2016.03.047.

[43] L.W.F. Mackenzie, M.O. Pekguleryuz, The recrystallization and texture of magnesium-zinc-cerium alloys, Scr. Mater. 59 (2008) 665–668. https://doi.org/10.1016/j.scriptamat.2008.05.021.

[44] S.R. Agnew, M.H. Yoo, C.N. Tomé, Application of texture simulation to understanding mechanical behavior of Mg and solid solution alloys containing Li or Y, Acta Mater. 49 (2001) 4277–4289. https://doi.org/http://dx.doi.org/10.1016/S1359-6454(01)00297-X.

[45] Y.B. Chun, M. Battaini, C.H.J. Davies, S.K. Hwang, Distribution characteristics of in-grain misorientation axes in cold-rolled commercially pure titanium and their correlation with active slip modes, Metall. Mater. Trans. A Phys. Metall. Mater. Sci. 41 (2010) 3473–3487. https://doi.org/10.1007/s11661-010-0410-4.

[46] Y.B. Chun, C.H.J. Davies, Investigation of prism ⟨a⟩ slip in warm-rolled AZ31 alloy, Metall. Mater. Trans. A Phys. Metall. Mater. Sci. 42 (2011) 4113–4125. https://doi.org/10.1007/s11661-011-0800-2.

[47] J.R. Luo, A. Godfrey, W. Liu, Q. Liu, Twinning behavior of a strongly basal textured AZ31 Mg alloy during warm rolling, Acta Mater. 60 (2012) 1986–1998. https://doi.org/10.1016/j.actamat.2011.12.017.

[48] C. Guo, Y. Xiao, R. Xin, Evaluation of Twinning Behavior in Rolling of Mg Alloys with Three Kinds of Textures by a Generalized Schmid Factor, Met. Mater. Int. 26

(2019) 1366–1372. https://doi.org/10.1007/s12540-019-00378-0.

[49] J.P. Hadorn, K. Hantzsche, S. Yi, J. Bohlen, D. Letzig, S.R. Agnew, Effects of solute and second-phase particles on the texture of Nd-containing Mg alloys, Metall. Mater. Trans. A Phys. Metall. Mater. Sci. 43 (2012) 1363–1375. https://doi.org/10.1007/s11661-011-1018-z.

[50] D. Hull, D.J. Bacon, Introduction to dislocations, Elsevier, 2011.

[51] B. Yin, Z. Wu, W.A. Curtin, First-principles calculations of stacking fault energies in Mg-Y, Mg-Al and Mg-Zn alloys and implications for< c+ a> activity, Acta Mater. 136 (2017) 249–261.

[52] Y.N. Osetsky, D.J. Bacon, An atomic-level model for studying the dynamics of edge dislocations in metals, Model. Simul. Mater. Sci. Eng. 11 (2003) 427.

[53] J.R. Rice, Dislocation nucleation from a crack tip: an analysis based on the Peierls concept, J. Mech. Phys. Solids. 40 (1992) 239–271.

[54] A. Jain, S.R. Agnew, Modeling the temperature dependent effect of twinning on the behavior of magnesium alloy AZ31B sheet, Mater. Sci. Eng. A. 462 (2007) 29–36. https://doi.org/10.1016/j.msea.2006.03.160.

[55] C. Zhu, T. Harrington, G.T. Gray, K.S. Vecchio, Dislocation-type evolution in quasi-statically compressed polycrystalline nickel, Acta Mater. 155 (2018) 104–116. https://doi.org/10.1016/j.actamat.2018.05.022.

[56] W. Pantleon, Resolving the geometrically necessary dislocation content by conventional electron backscattering diffraction, Scr. Mater. 58 (2008) 994–997. https://doi.org/10.1016/j.scriptamat.2008.01.050.

4.8. Appendices

4.8.1.Microstructure and texture of as-received ZE alloys

The precipitation distribution of as-received ZE alloys were characterized by using a Backscattered Electron (BSE) detector, as seen in Figure 4.20. The existence of precipitates indicating the alloying elements were less solutionized in the matrix.

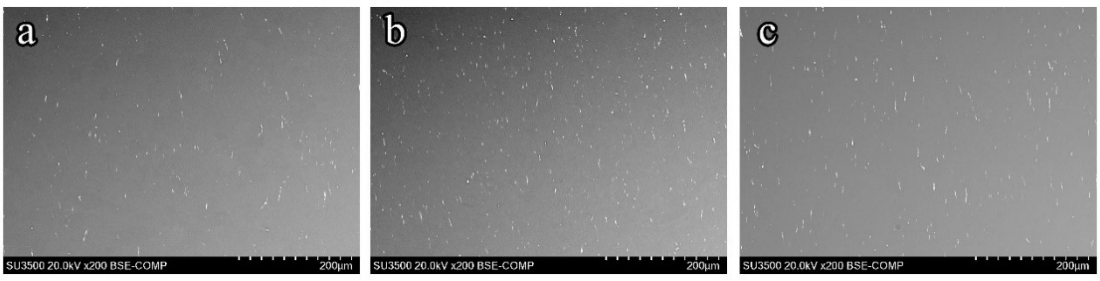

Figure 4.20 The precipitation distribution of as-received ZE alloys: (a) ZE-01, (b) ZE-02, (c) ZE-05.

The microstructures during hot rolling and subsequently annealing of as-received alloys were shown in Figure 4.21. The ZE-01 alloy with the lowest amount of Nd showed the highest DRX fraction, around 49%. The ZE-02 alloy displayed the mediate DRX fraction at 12.4% with 0.2 wt.% Nd addition. In addition, the equiaxed DRXed grains were found within deformation twins and in the vicinity of grain boundaries forming a necklace structure [1], as shown in Figure 4.21 (a) and (d). However, DRXed grains were barely observed in ZE-05 which has the highest Nd content, as seen in Figure 4.21 (g).

After post-deformation annealing at 350℃ for 10 minutes, equiaxed structures were observed in all three alloys. The average grain sizes of the annealed specimens were 45 μm, 46 μm and 29 μm respectively, as shown in Figure 4.21 (b), (e), and (h). Despite the minor difference in grain size, all as-received ZE alloys exhibited a typical strong basal texture after annealing. A weakened texture with intensity at 4.7 mrd was observed in precipitated ZE-05 which is resulted from the refined grains, as shown in Figure 4.21 (i). While the other two alloys showed a similar concentrated basal texture with texture intensity around 6.5 mrd (Figure 4.21 (c) and (f)). It is worth mentioning that a minor dispersion of (0002) poles was also observed in the precipitated ZE alloys after annealing which is shown as the gray contour lines on the (0002) pole figure in Figure 4.21 (c), (f), and (i). However, the effect of those texture components was limited since their intensity was too low to influence the mechanical performance.

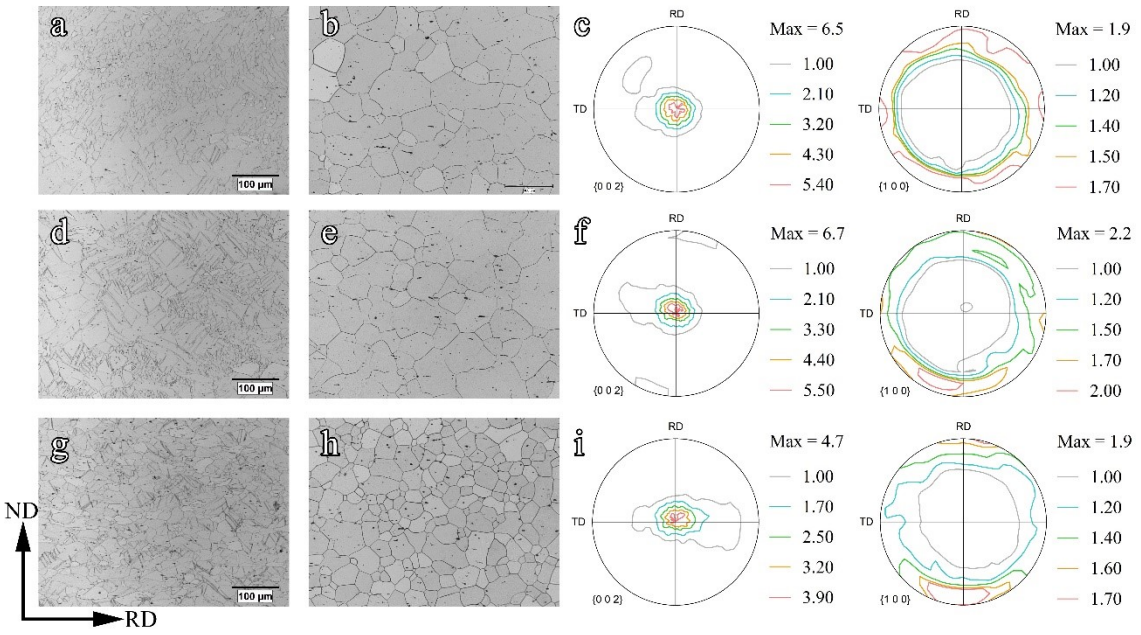

Figure 4.21 The microstructures and the (0002) *and (10-10) pole figures of as-received ZE alloys subjecting to rolling and subsequent annealing: (a) rolled ZE-01, (b) annealed ZE-01, (c) macro-texture of annealed ZE-01, (d) rolled ZE-02, (e) annealed ZE-02, (f) macro-texture of annealed ZE-02, (h) rolled ZE-05, (h) annealed ZE-05, and (i) macro-texture of annealed ZE-05.*

4.8.2.Computational procedure

4.8.2.1.First-principles density functional theory (DFT) calculations

DFT calculations were performed to obtain the GSFE curves of Mg with or without alloying elements. All calculations were performed using Vienna Ab-initio Simulation Package (VASP) [2] with projector-augmented plane-wave (PAW) method [2,3]. For the exchange-correlation functional, the generalized gradient approximation (GGA-PBE) was chosen [4]. Periodic supercells of dimensions 2×2×12and containing 96 atoms were used, as illustrated in Figure 4.22. A vacuum gap of 15 Å exists along Z direction (see Figure 4.22) to eliminate interactions between periodic images along Z direction. Additional benchmark calculations were also performed to confirm that the supercell dimensions were sufficient and that the results were not size dependent. The effect of alloying was considered by substituting Mg atoms with solute atoms in the plane that would become the

fault plane after slip (see further details in the procedure of SFE calculation). The cut off energy was set to 400 eV and the 7×7×1 Monkhorst-Pack k-point mesh was used. The convergence criteria for energy and force during relaxation were 10-5 eV and 10-2 eV/Å respectively.

To obtain the GSFE curve, the supercell was partitioned into two regions along the slip plane. The bottom region, i.e., the one below the slip plane was held fixed, while the top region, i.e., the one above the slip plane was displaced along the fault vector. The SFE was then obtained using the following equation:

$$\gamma = \frac{E_f - E_0}{S} \qquad \text{Equation 4.8.1}$$

where E_f and E_0 denote the total energies of the faulted supercell and original supercell respectively, and S is the area of the fault plane in the supercell. Some sample prismatic GSFE curves of pure Mg and Mg alloys were shown in Figure 4.23figure .

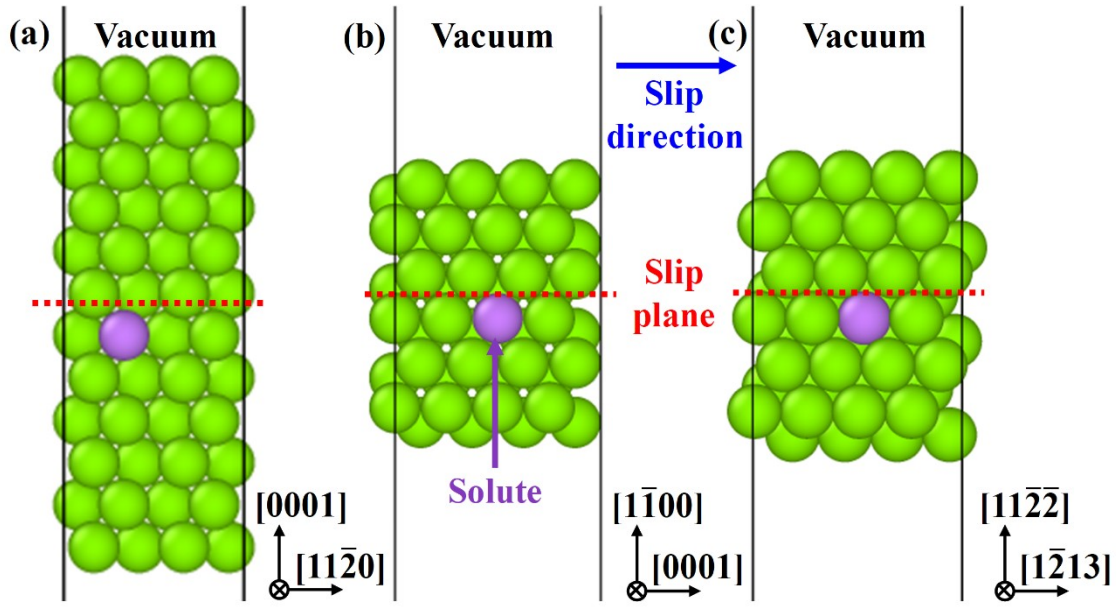

Figure 4.22 Illustration of a representative supercell used to calculate the GSFE curve of (a) basal; (b)prismatic; (c) pyramidal II; slip plane.

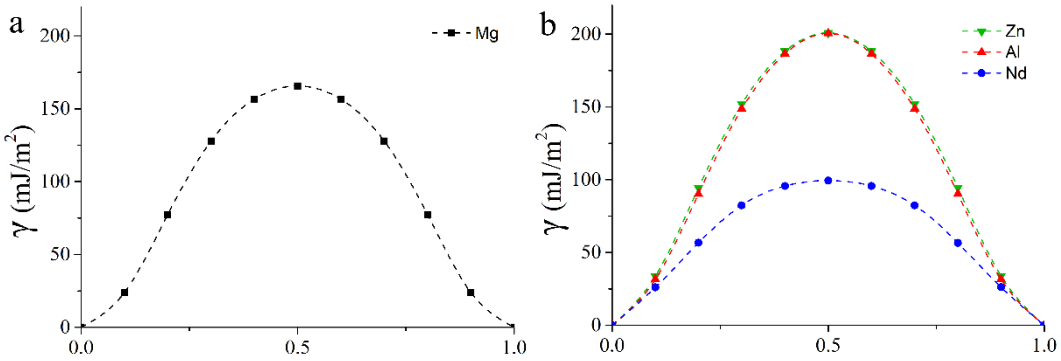

Figure 4.23 Sample DFT-calculated prismatic GSFE curves of (a) pure Mg and (b) Mg alloys at a planar solute concentration of 25 at. %.

4.8.2.2.Atomistic simulations

Molecular dynamics (MD) simulations were performed to examine the Peierls stress (i.e., effectively the CRSS for a single straight dislocation). The simulations were carried out using the Large-scale Atomic/Molecular Massively Parallel Simulator (LAMMPS) package [5]. The second nearest neighbor modified embedded-atom method (2NN MEAM) interatomic potentials were employed to describe interatomic interactions for pure Mg [6], Mg-Al [6], Mg-Zn [7], and Mg-Nd [8] systems.

Current simulations consider three common slip systems in Mg, the basal <a> slip, prismatic <a> slip and second-order pyramidal II <c+a> slip. All dislocations were created at the center of the simulation cell by displacing all atoms according to the Volterra fields [9] with the *y*-axis being normal to the slip plane, and x-axis being along the dislocation line direction. Periodic boundary conditions were imposed along the dislocation line and glide directions, while the free boundary condition was imposed along the third orthogonal direction. The simulation cells have dimensions ($l_x \times l_y \times l_z$) of 31.6 nm × 52 nm × 1.1 nm, 3.16 nm × 52 nm × 1.6 nm and 30 nm × 32.9 nm × 2.2 nm for supercells enclosing the basal, prismatic and pyramidal II slips respectively. Following the initial dislocation creation, the system was relaxed using energy minimization. The core structures after

relaxation for pure Mg [3] was illustrated in Figure 4.24 (a). The alloy system was created on base of the pure Mg system, and alloying was done by randomly substituting Mg atoms by solute atoms throughout the system, followed by relaxation.

After the relaxation, the simulation box was then deformed to drive dislocation motions. Rigid strain-controlled loading method [10] was used to apply a shear displacement, as schematically illustrated in Figure 4.24 (b). The simulation boxes were partitioned into three regions, as seen in Figure 4.24 (b), where the center region located free atoms while atoms in the bottom and top regions were held rigid and not allowed to relax. In performing the deformation, the top block was displaced incrementally, each time by a small distance $\Delta\mu$, along *x* direction, to induce shear deformation and thus drive gliding of the dislocation. Here, $\Delta\mu = \delta\varepsilon \times l_y$, where $\delta\varepsilon$ (=6× 10^{-6}) is the corresponding strain increment and l_y is dimension of the simulation box along *y* direction. Conjugate gradient minimization [11] was applied to relax the system after each incremental displacement. The corresponding stress at each strain was computed from the internal force per unit area [10],

$$\sigma^{xy} = \frac{\sum_{i\in Top} F_i^x}{A} = \frac{N^{Top} F^{Top}}{A} \qquad \text{Equation 4.8.2}$$

where N^{Top} and F^{Top} are the number of atoms and the average force for each atom in top layer, respectively. *A* is the cross-section area normal to the *y* direction. The instant shear strain ε^{xy} was calculated by the displacement of the center-of-mass position of atoms in the top layer from its reference configuration, i.e., the relaxed structure prior to loading. Thus, we have:

$$\varepsilon^{xy} = \frac{1}{l_y}(u_i^x - u_0^x) \qquad \text{Equation 4.8.3}$$

where u_i^x is the center-of-mass position of atoms from the top layer after the ith strain loading and u_0^x is the initial position. The Peierls stress σ_{CRSS} was taken to be the average of flow stresses (in Figure 4.26) after the dislocation starts gliding at a critical stress of σ_j^{xy}, i.e.,

$$\sigma_{CRSS} = \frac{\sum_{i \geq j} \sigma_i^{xy}}{N_{yield}} \qquad \text{Equation 4.8.4}$$

where σ_i^{xy} is the stress after yielding and N_{yield} is the number of stresses after yielding.

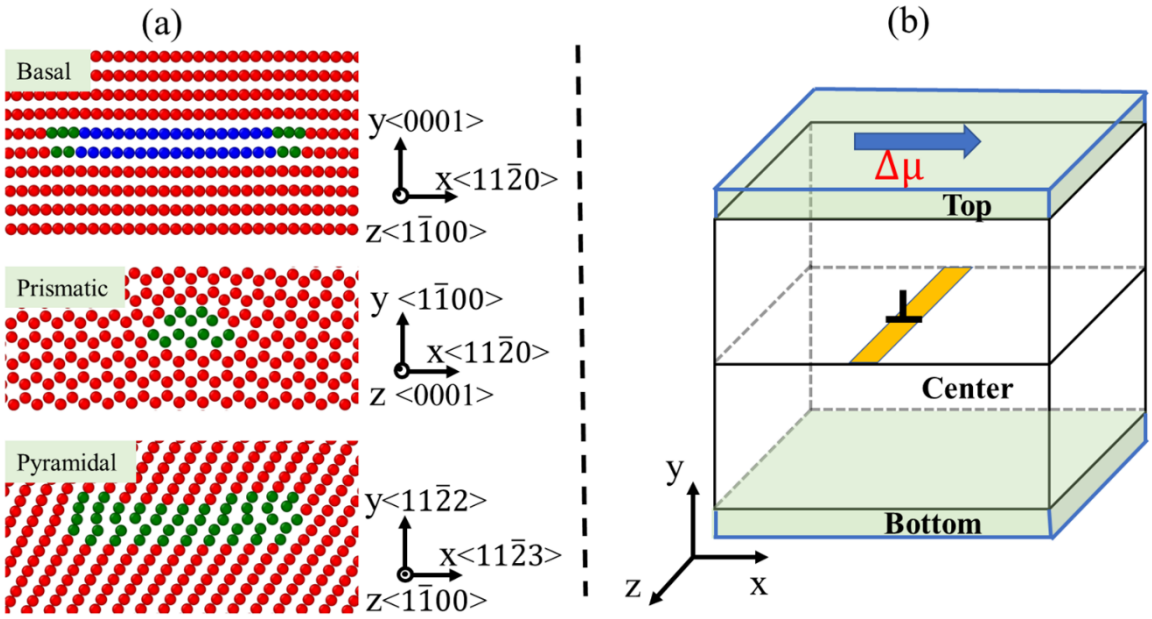

Figure 4.24 (a) Relaxed core structures of edge dislocations in basal, prismatic and pyramidal II slips as predicted by the presently used MEAM [6] interatomic potential for pure Mg. Red, green and blue atoms denote atoms within the HCP, FCC and other lattice environments respectively, as identified from common-neighbor analysis [12]; (b) Schematic illustration of the simulated cell partitioned into three regions, with free atoms in the center-region, while rigid atoms in the top and bottom regions. The shear deformation was realized by rigidly displacing the top block along x direction.

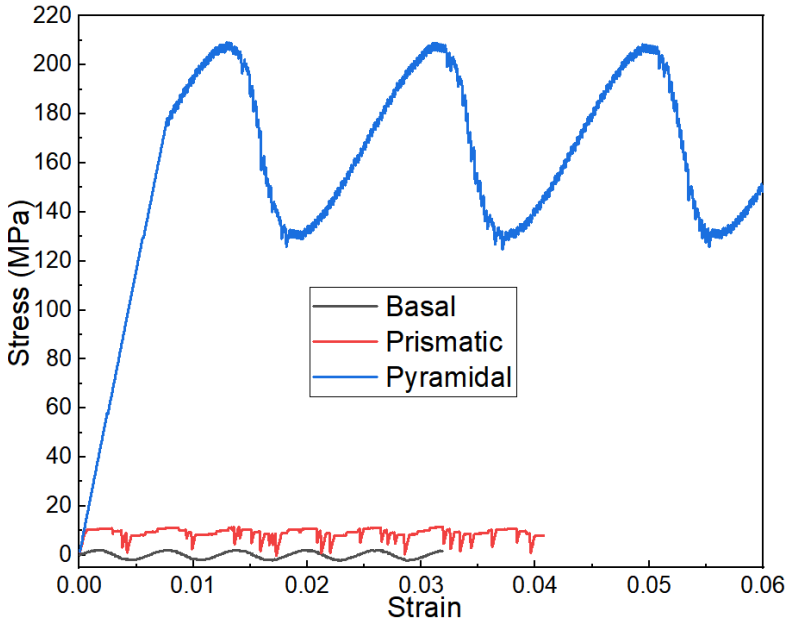

Figure 4.25 Simulated stress–strain curves for pure Mg on the basal, prismatic, and pyramidal II planes, at 0 K.

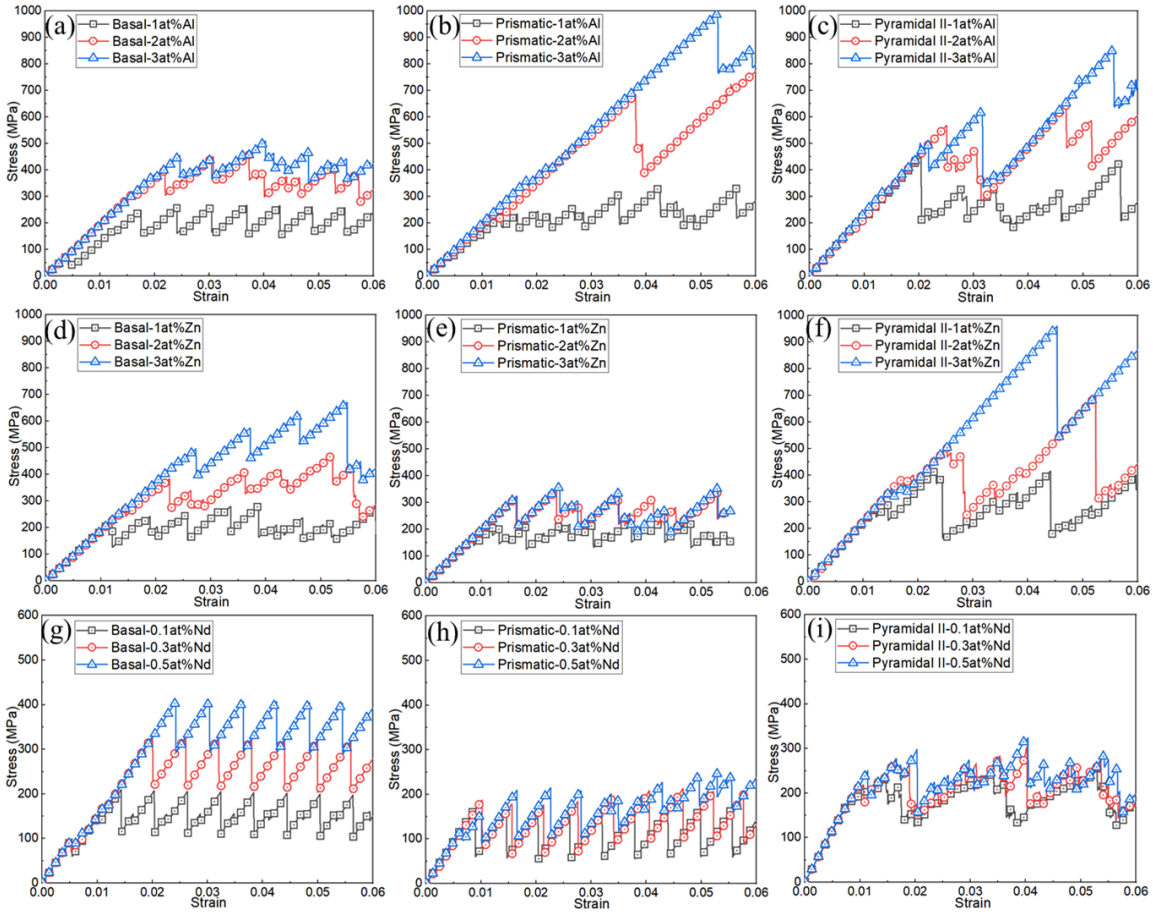

Figure 4.26 Simulated stress-strain curves: (a, b and c) Mg-Al, (d, e, and f) Mg-Zn and (g, h and i) Mg-Nd on basal, prismatic and pyramidal II planes, at 0 K. Different symbols correspond to different solute concentrations.

4.8.3.Geometrically necessary dislocations (GND) evaluation

The relative GND ($rGND_{p/b}$) was originally proposed in the current study. An example was demonstrated in Figure 4.27. The GND distribution maps of basal and prismatic slip are shown in Figure 4.27 (a) and (b). The GND density experienced a noticeable decrease in recrystallized grains. More importantly, the basal GND is observed relative higher (around 10^{15}) in certain recrystallized grains, especially the basal and RD-split grains. It indicates the more basal dislocation was preserved after recrystallization, which lead to a lower $rGND_{p/b}$ value. On the other hand, a lower $rGND_{p/b}$ value in deformed grains proves more basal dislocations were activated owing to the principal position of basal slip in Mg alloys.

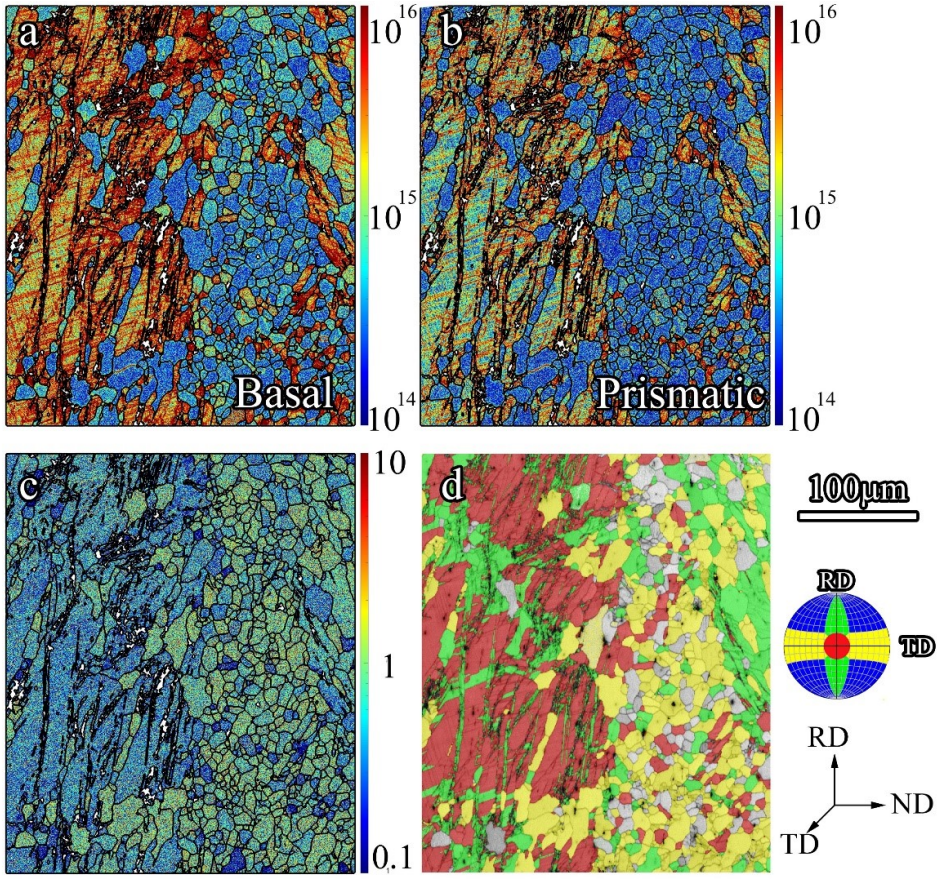

Figure 4.27 An example showing the GND and $rGND_{p/b}$ distribution map: GND distribution of (a) basal and (b) prismatic slip, the (c) $rGND_{p/b}$ distribution map and (d) texture component.

4.8.4.Reference

[1] K.D. Molodov, T. Al-Samman, D.A. Molodov, G. Gottstein, Mechanisms of exceptional ductility of magnesium single crystal during deformation at room temperature: Multiple twinning and dynamic recrystallization, Acta Mater. 76 (2014) 314–330. https://doi.org/10.1016/j.actamat.2014.04.066.

[2] G. Kresse, J. Furthmüller, Efficient iterative schemes for ab initio total-energy calculations using a plane-wave basis set, Phys. Rev. B. 54 (1996) 11169.

[3] G. Kresse, D. Joubert, From ultrasoft pseudopotentials to the projector augmented-wave method, Phys. Rev. B. 59 (1999) 1758.

[4] J.P. Perdew, K. Burke, M. Ernzerhof, Generalized gradient approximation made simple, Phys. Rev. Lett. 77 (1996) 3865.

[5] S. Plimpton, Fast parallel algorithms for short-range molecular dynamics, J. Comput. Phys. 117 (1995) 1–19.

[6] Y.-M. Kim, N.J. Kim, B.-J. Lee, Atomistic modeling of pure Mg and Mg–Al systems, Calphad. 33 (2009) 650–657.

[7] H.-S. Jang, K.-M. Kim, B.-J. Lee, Modified embedded-atom method interatomic potentials for pure Zn and Mg-Zn binary system, Calphad. 60 (2018) 200–207.

[8] K.-H. Kim, B.-J. Lee, Modified embedded-atom method interatomic potentials for Mg-Nd and Mg-Pb binary systems, Calphad. 57 (2017) 55–61.

[9] D. Hull, D.J. Bacon, Introduction to dislocations, Elsevier, 2011.

[10] Y.N. Osetsky, D.J. Bacon, An atomic-level model for studying the dynamics of edge dislocations in metals, Model. Simul. Mater. Sci. Eng. 11 (2003) 427.

[11] A. V Ivanov, V.M. Uzdin, H. Jónsson, Fast and robust algorithm for energy minimization of spin systems applied in an analysis of high temperature spin configurations in terms of skyrmion density, Comput. Phys. Commun. 260 (2021) 107749.

[12] J.D. Honeycutt, H.C. Andersen, Molecular dynamics study of melting and freezing of small Lennard-Jones clusters, J. Phys. Chem. 91 (1987) 4950–4963.

Chapter 5.Tailoring texture in micro-alloyed Mg-Zn alloys with diluted Nd and Ca

In the previous chapter, the mechanism for the formation of TD-split textures in micro-alloyed ZE alloy was proposed, which provided guidance for the development of texture-modified Mg alloys with further reduced RE levels. Based on this mechanism, a ternary Mg-1Zn-0.2Ca alloy and a quaternary Mg-1Zn-0.1Nd-0.2Ca alloy were designed and compared for texture modification in the following chapter.

This chapter is ready for submission and will be credited to the following authors:

Y. Liu, J. Su, H. Chen, Q. Qiu, R. Gao, A, Javaid, T. Skszek, J. Song, S. Yue, Tailoring texture in micro-alloyed Mg-Zn alloys with diluted Nd and Ca.

5.1. Abstract

We adopted a computational simulation-guided approach to design Mg-Zn-based micro-alloys by partially replacing the expensive rare-earth element, Nd, with Ca while maintaining the beneficial 'rare-earth' texture. The first principle and molecular dynamic calculations suggested that Nd and Ca solutes in Mg show similar effects on promoting prismatic slip in competition with basal slip. In coupled with thermodynamic simulation, Mg-1Zn-0.2Ca and Mg-1Zn-0.1Nd-0.2Ca alloys were designed in terms of maintaining Nd and Ca in solid solution at typical hot rolling temperatures. Upon multi-pass rolling and subsequent annealing, texture modification with (0002) poles tilting toward the transverse direction (TD) was achieved in Mg-1Zn-0.1Nd-0.2Ca, while Mg-1Zn-0.2Ca exhibited a basal texture with less prominent TD-splitting. This is attributed to the diluted Nd maintaining Ca in solid solution to promote prismatic slip. Quasi-in-situ electron backscatter diffraction observation revealed that the TD-split texture was originated from shear-bands induced nucleation and enhanced by preferential grain growth during annealing.

As the lightest structural material, magnesium (Mg) alloys attract attentions for its weight saving potential [1]. Yet, the application of Mg sheets in automotive manufacturing is restricted due to its low formability [1], which is related to the strong basal texture formed during thermomechanical processing, especially after the multi-pass rolling [2,3]. The basal texture is originated from the dominant basal slip which aligns the (0002) poles parallel to the normal direction (ND) of rolled sheets [4]. Owing to the high critical resolved shear stress (CRSS) for the pyramidal slip, which is the only slip system accommodate

deformation along c axis, the basal texture further amplifies the shortage of independent slip system in Mg alloys on accommodating deformation [5,6].

Non-basal textures with the (0002) poles tilting towards the rolling direction (RD-split) [7,8], or transverse direction (TD-split) [9,10] have been observed in Mg alloys. The formation of non-basal textures was commonly ascribed to the activation of non-basal slip systems [10–12] and twins [13] and/or the contribution of static recrystallization (SRX) [14–16]. Alloying rare earth (RE) elements in Mg has been realized as an efficient way to acquire non-basal textures. However, the limited resources, cost inflation and weight increase brought by RE addition eliminate their wide applications. Jung et al. [17] suggested that the critical amount of Nd required to trigger texture modification in Mg-Zn-Nd ternary alloy system is much less compared to the Mg-Nd binary system based on a solute drag/pinning effect model. This is related to the reduced solubility limit of Nd in Mg by adding Zn [17]. Our previous work [9] showed that the formation of non-basal textures in Mg-Zn-Nd alloys is owing to the amount of Nd in solid solution and 0.2 wt.% addition is sufficient to form a weakened TD-split texture that is comparable to the texture with 0.5 wt.% Nd [18]. To further reduce the RE usage, exploring non-RE alternatives that can partially or even completely replace RE while preserving advantages ‘rare-earth’ textures are of great interest not only to scientific research but also to engineering applications. For example, calcium (Ca) has been reported as a potential candidate for texture modification in Mg-Zn system [19]. Thus, the combined effect of dilute additions of Nd and Ca on texture modification and corresponding mechanisms need to be investigated.

In the current study, we used density function theory (DFT) calculations and molecular dynamic (MD) simulations to examine the effects of Nd and Ca on the activation

of non-basal slip systems. In coupled with thermodynamic calculation, two micro-alloys, denoted as ZEX-0102 and ZX-02 (nominal compositions listed in Table 5.1.1), were designed with the aim to preserve Nd and Ca in solid solution at typical hot deformation temperatures (350-500°C [20]). The texture weakening effect was experimentally validated by comparing the textural transition of the two alloys subjecting to the same process of solutionizing, multi-pass rolling and subsequent annealing. The origin of this TD-split texture was tracked by quasi-in-situ electron backscatter diffraction (EBSD) during annealing.

Table 5.1.1 Nominal chemical compositions of ZEX and ZX alloys (wt. %).

Alloys	Zn	Nd	Ca	Mg
ZEX-0102	1	0.1	0.2	balance
ZX-02	1	-	0.2	

For atomistic simulations, the first-principles DFT calculations were used to investigate the effect of Nd and Ca on stacking fault energy (SFE). MD simulations were utilized to examine the evolution of Peierls stress (σ_{CRSS} as the atomistic representative of CRSS of the main slip systems in Mg (see Appendix for details of DFT and MD simulation). The equilibrium phase diagrams of Mg-Zn-Ca and Mg-Zn-Ca-Nd systems were calculated using FactSage [21]. To dissolve the Nd and Ca content in the solid solution, the as-received sheets were solutionized at 550°C for 72 hours. Both as-received and solutionized alloys were subjected to 2-pass rolling at 450°C with 20% reduction per pass and a 10 mins intermediate annealing at 450°C. In addition, 6-pass rolling was performed for the solutionized ZEX-0102 and ZX-02 with the same per-pass reduction and intermediate annealing procedure. The post-deformation annealing was executed for the 2-pass and 6-

pass rolled specimens at 450°C for 10 minutes. Macro-textures were measured by using an X-ray diffractometer with Cu Kα radiation. Optical microstructures (OM) were captured by the CLEMEX image software. For the 2-pass schedule, quasi-in-situ EBSD was executed during annealing at 450°C after the 2nd pass.

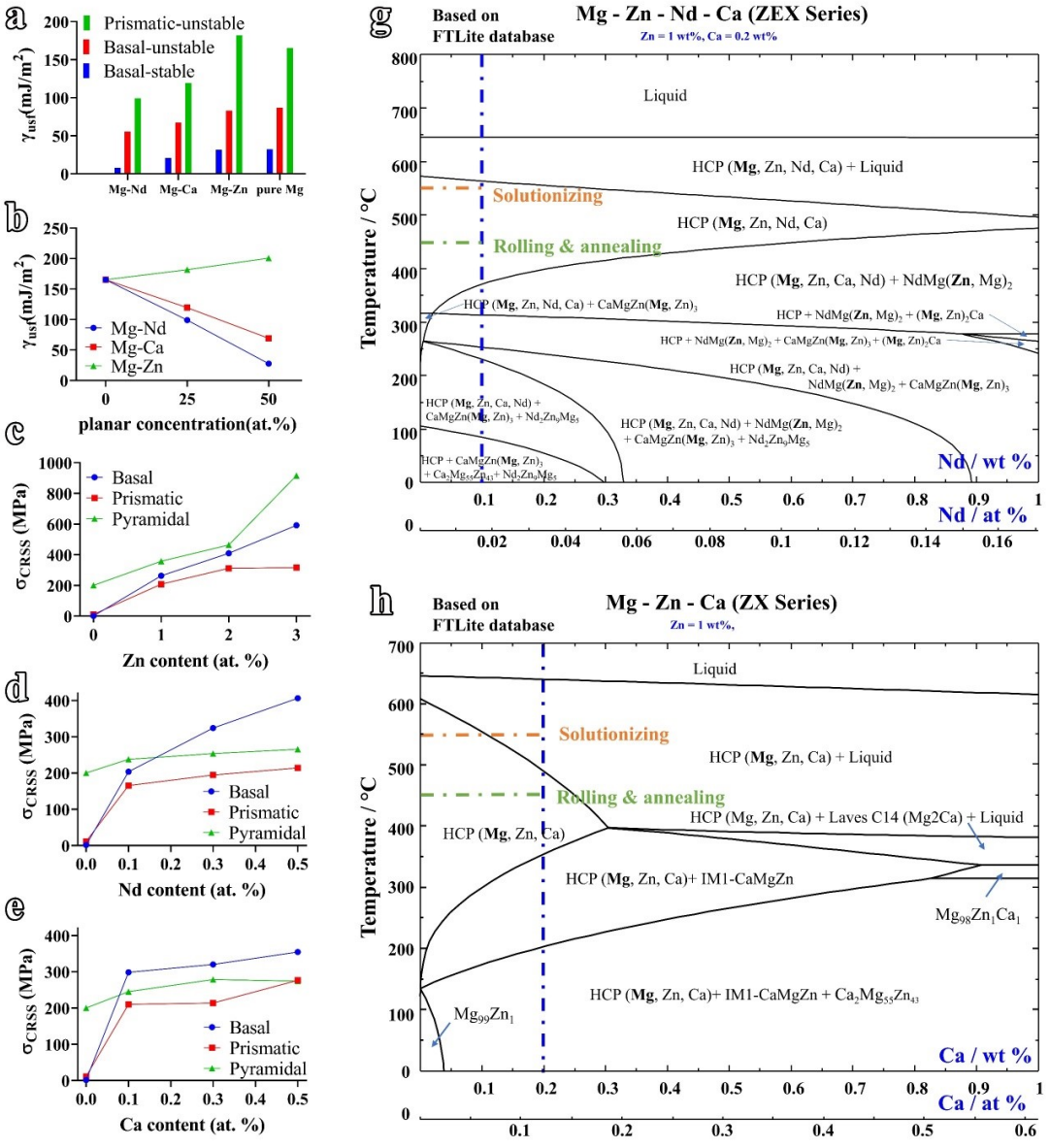

Figure 5.1 The (a) calculated SFE, (b) prismatic γusf evolution with respect to planar solute concentration; The σ_{CRSS} evolution in (c) Mg-Zn, (d)Mg-Nd and (e) Mg-Ca system; The equilibrium phase diagram of (g) ZEX and (h) ZX alloys.

The results of computational simulation are shown in Figure 5.1 (a) to (e). The SFE and Peierls stress under the influence of Nd and Ca were theoretically evaluated. SFE was known to be crucial for the governing core structures and mobility of dislocations [22]. The calculated stable stacking fault (γ_{sf})and unstable stacking fault (γ_{usf}) of Mg and its alloys were shown in Figure 5.1 (a). Note that only γ_{usf} exists on prismatic plane according to the GSFE curve (Figure 5.7). It is apparent that Nd presented a much stronger γ_{usf} weakening effect, while Ca is also a promising candidate regarding γ_{usf} reduction. The prismatic γ_{usf} values of different systems at the planar solute concentration of 25 at. % and 50 at. % was also calculated (Figure 5.1 (b)). The monotonic decreasing relationship between the concentration of alloying element solutes and corresponding γ_{usf} also validated the γ_{usf} reduction of Nd and Ca. As it is known that the γ_{usf} denotes the energy barrier of dislocation nucleation [23]. It can be inferred that the Nd and Ca solutes are beneficial for activating more slip systems, especially the prismatic slip system, to accommodate deformation. The Peierls stress evolution with increasing solute content at 0K for Mg-Nd, Mg-Ca and Mg-Zn system were calculated and plotted in Figure 5.1 (c) to (e). In general, the alloying elements would increase the σ_{CRSS} of various slip systems. However, the solute strengthening effect by Nd and Ca was limited compared with that in the Mg-Zn system. Furthermore, pronounced reduction of the σ_{CRSS} was achieved when Nd and Ca exist in matrix as solutes, which means the activation of prismatic dislocations would be promoted. It must be addressed that the current σ_{CRSS} evaluation was based on calculations at 0K. The CRSS of non-basal slip system in Mg alloys were reported dramatically reduced at elevated temperatures [24]. Nonetheless, it could be concluded that non-basal slips, especially the prismatic slips, would be promoted with increasing Nd and

Ca solute in matrix owing to the lowered SFE and CRSS. Also, the Nd was found to have a slightly better effect compared with Ca (Figure 5.1 (a) to (e)).

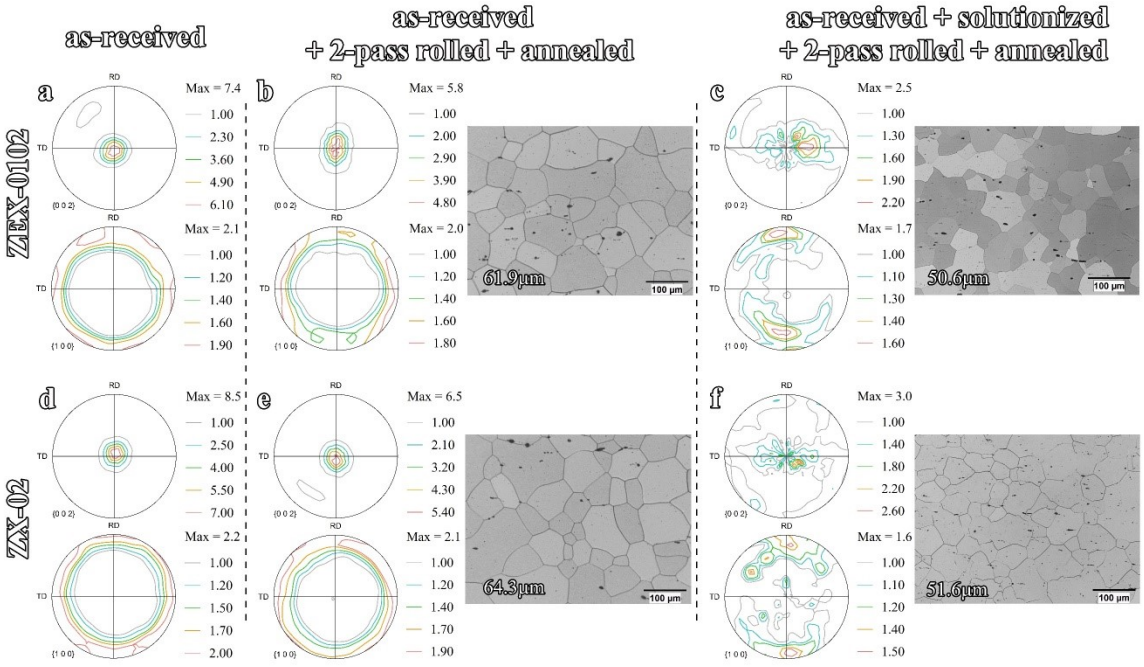

Figure 5.2 The macro-textures and microstructures of specimens subjecting to different treatment: (a to c) ZEX-0102, (d to f) ZX-02 (processing details were labeled accordingly).

The as-received ZEX-0102 and ZX-02 plates exhibit numerous precipitates (as shown in Figure 5.9 in appendix). According to the equilibrium phase diagrams (Figure 5.1 (g) and (h)), a single HCP phase solid solution is expected for both alloy systems at 550°C. Thus, more alloying elements were expected dissolving in the matrix after solutionizing at 550°C compared to the as-received state. The as-received ZEX-0102 and ZX-02 plates exhibit strong basal textures (Figure 5.2 (a) and (d)). After 2-pass rolling and subsequent annealing, a weaker basal texture is observed, accompanied by the equiaxed grain structure (Figure 5.2 (b) and (e)). It indicates that the deformation mechanism is basal slip dominated [4], while the lowered intensities are likely resulted from SRX. However, in the solutionized specimens subjected to 2-pass rolling, the initial strong basal texture

was altered to an “TD-split” texture with much weaker intensities in both alloys (Figure 5.2 (c) and (f)). Thus, it can be inferred that the formation of TD-split texture is related to the dissolution of Nd and Ca which activated non-basal slip mechanisms. Similar TD-split texture has been reported in alloys with higher RE content (commonly ≥1%) [10,14,15]. Thus, the texture transformation in current alloys, especially in the RE-free ZX-02, suggests that Ca behaves similarly to that of RE in terms of texture modification, as predicted by the atomistic simulations. It is also noted that the ZEX-0102 shows better texture modification than ZX-02 suggesting the beneficial effect of the additional 0.1 wt.% Nd on the enhancement of non-basal slip modes.

To understand the formation of TD-split texture in the current alloys, the SRX process of the solutionized alloys was tracked by the quasi-in-situ EBSD technique, as seen in Figure 5.2. In general, micro-textures of solutionized ZEX-0102 and ZX-02 evolved from concentrated basal texture to a weakened texture dominated by TD-split texture components accompanied by SRX. The SRX fraction evolution explicitly shows that the recrystallization kinetics was dramatically retarded by the additional 0.1 wt.% Nd. It takes ZEX-0102 specimen 4 minutes to initiated nucleation and SRX was not completed upon the 36-minutes annealing (Figure 5.3 (i)). Whereas pronounced recrystallization was observed in the ZX-02 after 3-minutes annealing and the SRX completed after 21-minutes annealing (Figure 5.3 (j)). The probable explanation for the recrystallization suppression in ZEX-0102 is the solute drag and dislocation pinning effect brought by the additional solute Nd [17,25].

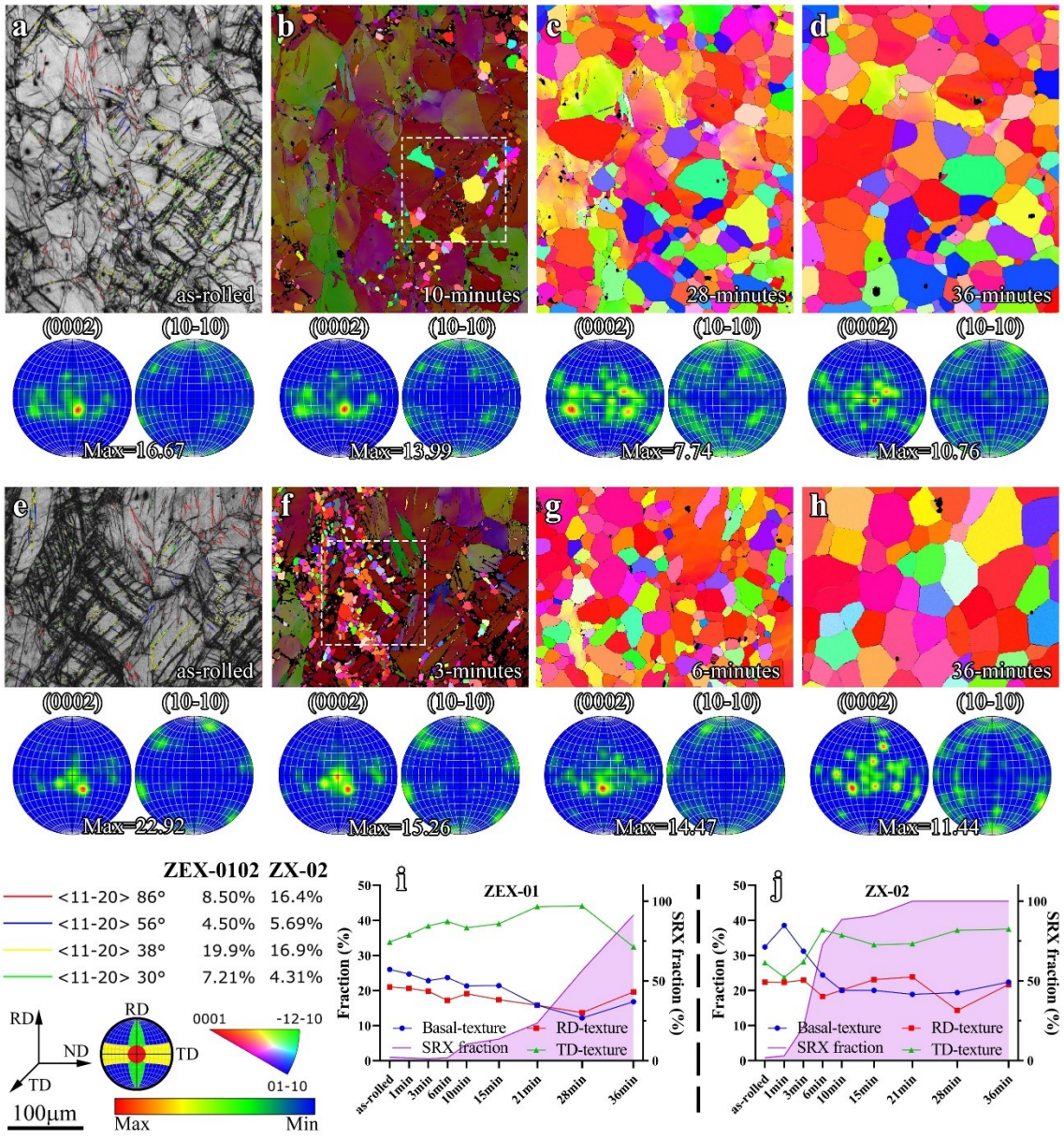

Figure 5.3 Quasi-in-situ EBSD observations of solutionized ZEX-0102 and ZX-02 subjecting to annealing: (a to d) ZEX-0102, (e to h) ZX-02, and the corresponding statistics of (i) ZEX-0102 and (j) ZX-02.

The as-rolled microstructures of the solutionized ZEX-0102 and ZX-02 specimens share many similarities, as seen in Figure 5.3 (a) and (e). Besides deformed grains elongated along the rolling direction (RD) and the noticeable shear bands, the $\{10\bar{1}1\} - \{10\bar{1}2\}$ compress-tension double twin (CTDT) dominates both alloys as the main twinning mechanism. The CTDT is characterized as misorientations with an angle of $38 \pm 5°$ about

the $\langle 11\bar{2}0\rangle$ axis (variant-I, marked with yellow) and $30 \pm 5°$ about the $\langle 11\bar{2}0\rangle$ axis (variant-II, marked with green) [26]. The recrystallized grains with grain orientation spread (GOS) less than 1° are highlighted (Figure 5.3 (b) and (f)). Evidently, the nucleation primarily initiated in the vicinity of shear bands, which is known as shear bands induced nucleation (SBIN) [27]. Although the dominance of CTDT in deformed Nd-containing Mg alloys has been previously reported [28] and observed here, the influence of CTDT on texture weakening in Nd-containing Mg alloys has been proven to be limited [13]. It is thus suggested that the occurrence of TD-split texture in basal grains relies on nucleation and subsequent grain growth.

To validate the effect of nucleation on the appearance of TD-split texture component, the pixel per grain pole figure was introduced, which was regenerated with the pixels representing the mean orientation of EBSD surveyed grains. By using pixel per grain pole figures, the grain area advantage of large grains in the texture measurements is neutralized. This means the contribution of individual grains to the micro-texture is equalized and the bias towards very large grains in texture evaluation is eliminated. At the early stage of SRX, the TD-split texture component has been observed, as seen in the comparison between the pole figures of as-rolled and recrystallized grains (GOS≤1°) (Figure 5.4 (c1) and (c2), (d1) and (d2)). This might create an illusion that the preferential nucleation favoring TD-split orientation leads to the final TD-split texture. However, this illusion can be easily overturned by comparison the pixel per grain pole figures (Figure 5.4 (c3) and (c4), (d3) and (d4)). The GOS≤1° pixel per grain pole figures indicate that the orientations of the deformed structure were predominantly inherited.

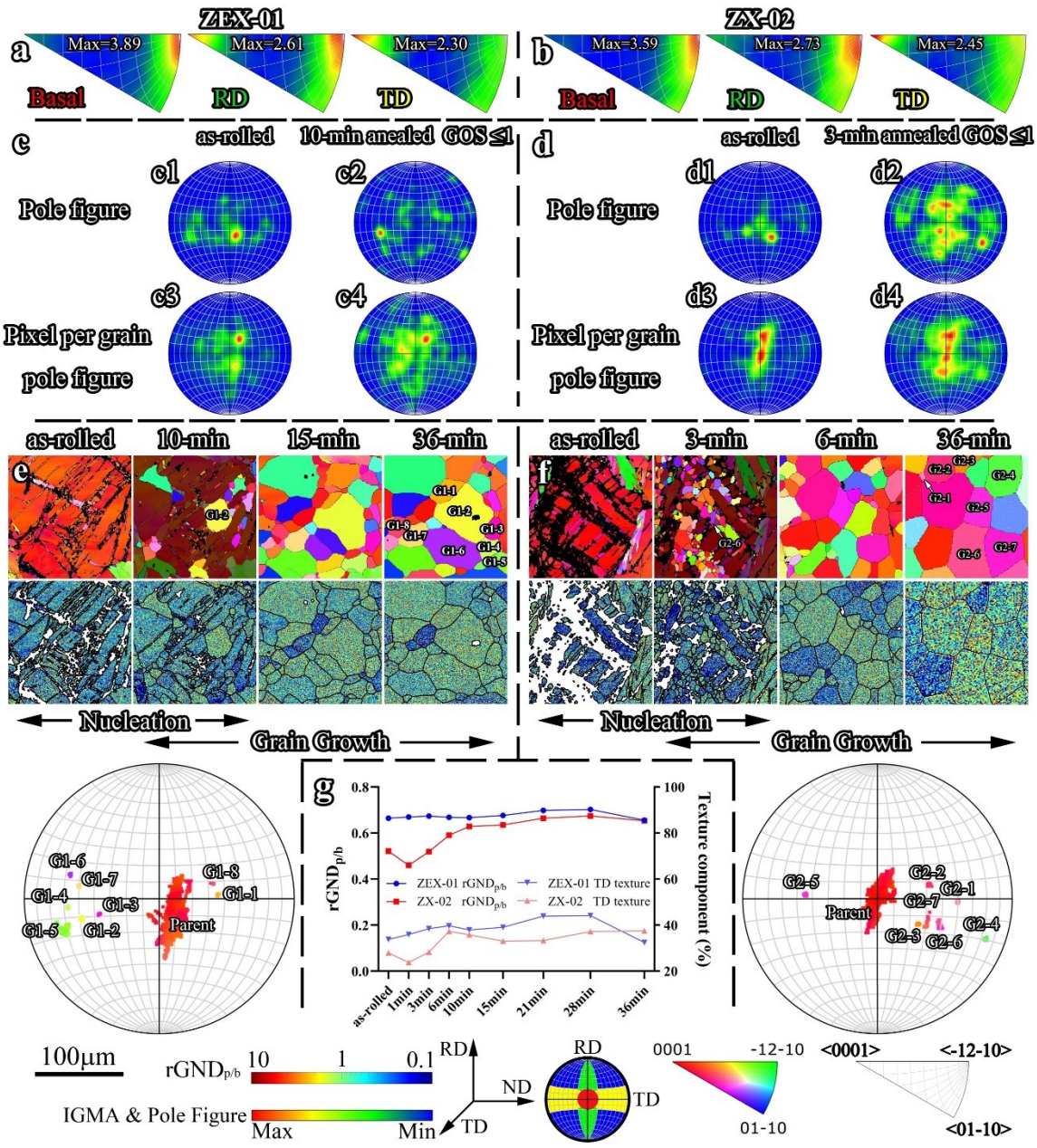

Figure 5.4 IGMA distribution of solutionized (a)ZEX-0102 and (b)ZX-02 upon rolling; (0002) pole figures, IPF maps and rGND$_{p/b}$ distributions presenting nucleation and grain growth of (c, e) ZEX-0102 and (d, f) ZX-02; (g) the evolution of TD texture component and the rGNDp/b during annealing.

Although TD-split orientations were observed, the orientations of recrystallized grains were mainly scattered along the RD. Meanwhile, the difference between pole figures and pixel per grain pole figures of recrystallized grains (Figure 5.4 (c2) and (c4), (d2) and (d4)) proves the existence of area advantage for TD-split grains. Therefore, it can be

inferred that the formation of TD-split texture is due to the preferential grain growth of TD-split grains.

It is well known that texture provides a general description of the deformation mechanism and recrystallization process. As aforementioned, twinning, represented by CTDTs, was found to be irrelevant to the formation of TD-split texture. Meanwhile, the prismatic <a> slip has been reported to tilt the basal pole towards the TD in Mg-Zn-Nd alloys [10]. For the solutionized alloys upon rolling, the intragranular misorientation axis (IGMA) map based on EBSD measurement [29,30] is introduced to evaluate the prismatic <a> slip in various texture components for the as-rolled state. A concentrated <0001> Taylor axis with an intensity higher than 2 mrd indicates that prismatic <a> slip dominates when misorientation angle falls between 1°~ 3° [29,30]. Prismatic slip dominates the TD-split texture component and is observable in the RD-split texture component for both solutionized alloys (Figure 5.4 (a) and (b)). This observation not only validates our theoretical predictions, but also reveals the connection between the activation of prismatic slip and the formation of TD-split texture component [10]. In addition, the basal slip as the principal slip system with the lowest CRSS also plays an important role in the formation of final texture [31]. To quantify the effect of various slip systems, the density of geometrically necessary dislocations (GNDs) was commonly used [32]. Here, the $rGND_{p/b}$ distribution is originally proposed to establish the connection between prismatic slip, the existence of basal slip and the occurrence of TD-split texture. It is defined as the GND density ratio between the prismatic slip system and basal slip system:

$$rGND_{p/b} = \rho_{GND-prismatic}/\rho_{GND-basal} \qquad \text{Equation 5.1.1}$$

Where the $\rho_{GND-prismatic}$ and $\rho_{GND-basal}$ are the corresponding GND densities calculated by using METX [33]. The evolution of $rGND_{p/b}$ and TD texture component of solutionized ZEX-0102 and ZX-02 is demonstrated in Figure 5.3(g). The tendency of the evolution of $rGND_{p/b}$ and corresponding TD texture component is well aligned. The transitions from deformed basal grains (delineated by the dashed rectangle in Figure 5.2) to recrystallized TD-split grains in solutionized ZEX-0102 and ZX-02 are shown in Figure 5.3 (e) and (f), respectively. The TD-split orientated grains with higher $rGND_{p/b}$ values are observed to have been nucleated through SBIN and eventually occupied the microstructure through preferential growth. The $rGND_{p/b}$ distribution revealed that the prismatic and basal grains are at the same magnitude in the TD-split grains. Hence, the $rGND_{p/b}$ can be considered as a growth factor; high $rGND_{p/b}$ grains are favored during growth and eventually contribute to the TD-split texture.

For the 2-pass rolling schedule, Ca performs as a slightly inferior substitute for Nd regarding the formation of TD-split texture. However, the macro-texture evolution of 6-pass rolled specimens exhibit entirely different characteristics for ZEX-0102 and ZX-02, as seen in Figure 5.5. During the multi-pass rolling, the TD-split texture component was preserved and enhanced for ZEX-0102 (Figure 5.5 (a) to (c)). Eventually, an ultra-weak texture with a pronounced TD-split feature was acquired (Figure 5.5 (d)). In comparison, the ZX-02 exhibited an exactly opposite trend. Despite the TD-split texture formation being triggered upon 2-pass rolling, the basal texture gradually dominates during the following deformation process (Figure 5.5 (e) to (g)). An intensified basal texture was acquired after annealing, which is similar to the as-received specimens. As discussed above, solute Nd and Ca trigger texture alternation from basal to TD-split. Therefore, the retarded texture in

solutionized ZX-02 is ascribed to the precipitation of Ca owing to the heat loss upon multi-pass rolling. On the other hand, the diluted Nd in ZEX-0102 not only promoted the prismatic slip as solute but also served as the stabilizer for Ca solute. It has been reported that solute–solute binding energy for Nd and Ca is -0.14 eV [34] and Ca has a higher diffusivity than Nd [35,36] in Mg alloys. Thus, stable texture modification is expected in solutionized ZEX-upon multi-pass rolling.

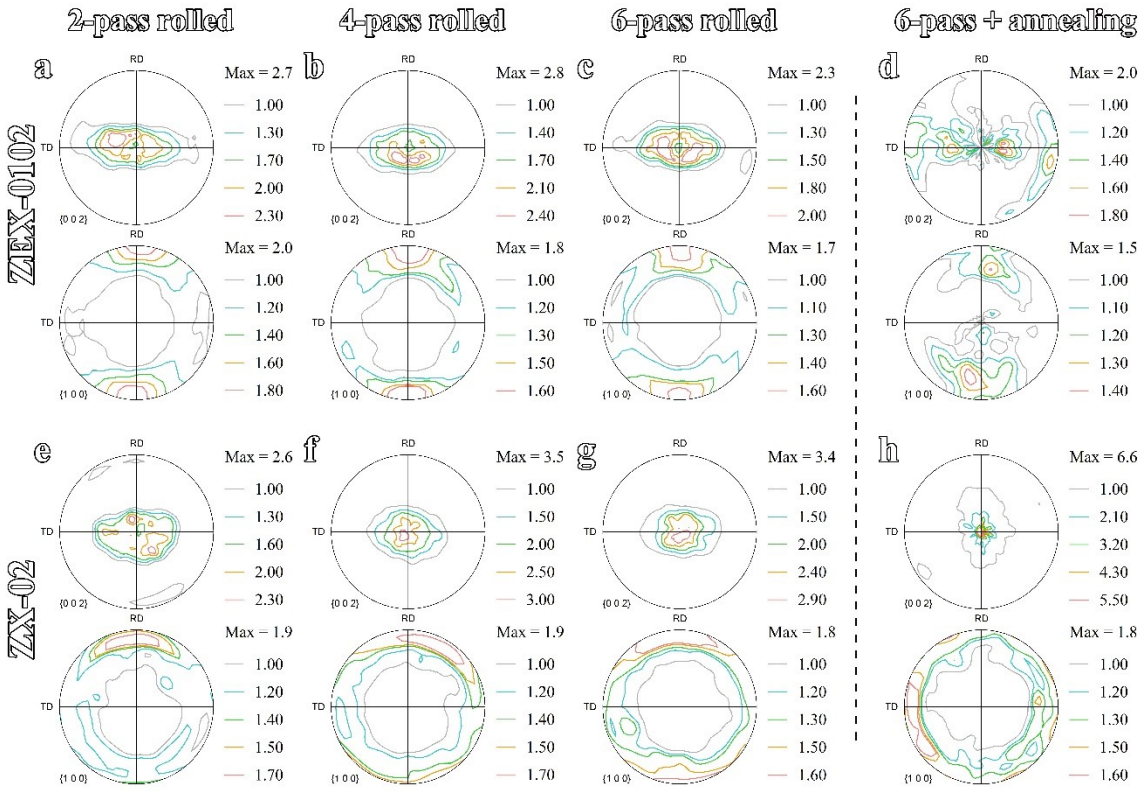

Figure 5.5 The macro-texture evolution of (a to d) ZEX-0102 and (e to h) ZX-02 upon multi-pass rolling and post-deformation annealing.

In summary, based on DFT and MD simulations that Ca performs similarly as Nd on promoting non-basal slip. We successfully designed a Mg-Zn-Nd-Ca alloy that achieved pronounced and consistent texture modification featuring TD-split texture during multi-pass hot rolling and annealing. The TD-split texture formation is attributed to the enhanced

activation of prismatic slip owing to both Nd and Ca in solid solution. This study thus provides a novel approach to design more economical Mg alloys by partially replacing the expensive rare-earth element, Nd, with Ca while maintaining the beneficial 'rare-earth' texture for improving the rollability and formability of Mg sheets.

5.2. Reference

[1] W.J. Joost, P.E. Krajewski, Scr. Mater. 128 (2017) 107–112.

[2] B.L. Mordike, K.U. Kainer, in: 2000.

[3] M.O. Pekguleryuz, in: M. Barnett (Ed.), Adv. Wrought Magnes. Alloy., Woodhead Publishing, 2012, pp. 3–62.

[4] Q. Jin, S.-Y. Shim, S.-G. Lim, Scr. Mater. 55 (2006) 843–846.

[5] Y. Liu, J. Fan, H. Zhang, W. Jin, H. Dong, B. Xu, J. Alloys Compd. 622 (2015) 229–235.

[6] J. Su, M. Sanjari, A.S.H. Kabir, I.H. Jung, S. Yue, Scr. Mater. 113 (2016) 198–201.

[7] J. Su, A.S. Abu, M. Sanjari, S. Yue, Mater. Sci. Eng. A 674 (2016) 343–360.

[8] Y.M. Kim, C. Mendis, T. Sasaski, D. Letzig, F. Pyczak, K. Hono, S. Yi, Scr. Mater. 136 (2017) 41–45.

[9] Y. Liu, J. Su, R. Gao, H. Geng, A. Javaid, T. Skszek, S. Yue, J. Mater. Eng. Perform. (2020) 1–8.

[10] X. Zeng, P. Minárik, P. Dobroň, D. Letzig, K.U. Kainer, S. Yi, Scr. Mater. 166 (2019) 53–57.

[11] Y. Onuki, K. Hara, H. Utsunomiya, J.A. Szpunar, J. Mater. Eng. Perform. 24 (2015) 972–985.

[12] S.R. Agnew, Ö. Duygulu, Int. J. Plast. 21 (2005) 1161–1193.

[13] D. Guan, W.M. Rainforth, J. Gao, J. Sharp, B. Wynne, L. Ma, Acta Mater. 135 (2017) 14–24.

[14] L.Y. Zhao, H. Yan, R.S. Chen, E.H. Han, Scr. Mater. 188 (2020) 200–205.

[15] I. Basu, T. Al-Samman, Acta Mater. 67 (2014) 116–133.

[16] D. Guan, W.M. Rainforth, J. Gao, L. Ma, B. Wynne, Acta Mater. 145 (2018) 399–412.

[17] I.-H. Jung, M. Sanjari, J. Kim, S. Yue, Scr. Mater. 102 (2015) 1–6.

[18] Y. Liu;, J. Su;, H. Chen, Q. Qiu;, R. Gao, A. Javaid, T. Skszek, J. Song;, S. Yue, J.

Mater. Sci. Technol. (n.d.).

[19] Z.R. Zeng, Y.M. Zhu, S.W. Xu, M.Z. Bian, C.H.J.J. Davies, N. Birbilis, J.F. Nie, Acta Mater. 105 (2016) 479–494.

[20] J.F. Nie, K.S. Shin, Z.R. Zeng, Microstructure, Deformation, and Property of Wrought Magnesium Alloys, Springer US, 2020.

[21] C.W. Bale, P. Chartrand, S.A. Degterov, G. Eriksson, K. Hack, R. Ben Mahfoud, J. Melançon, A.D. Pelton, S. Petersen, Calphad 26 (2002) 189–228.

[22] D. Hull, D.J. Bacon, Introduction to Dislocations, Elsevier, 2011.

[23] J.R. Rice, J. Mech. Phys. Solids 40 (1992) 239–271.

[24] J. Su, M. Sanjari, A.S.H. Kabir, I.H. Jung, J.J. Jonas, S. Yue, H. Utsunomiya, Mater. Sci. Eng. A 636 (2015) 582–592.

[25] J.P. Hadorn, K. Hantzsche, S. Yi, J. Bohlen, D. Letzig, J.A. Wollmershauser, S.R. Agnew, Metall. Mater. Trans. A Phys. Metall. Mater. Sci. 43 (2012) 1347–1362.

[26] J.W. Christian, S. Mahajan, Prog. Mater. Sci. 39 (1995) 1–157.

[27] I. Basu, T. Al-Samman, G. Gottstein, Mater. Sci. Eng. A 579 (2013) 50–56.

[28] K. Hantzsche, J. Bohlen, J. Wendt, K.U. Kainer, S.B. Yi, D. Letzig, Scr. Mater. 63 (2010) 725–730.

[29] Y.B. Chun, C.H.J. Davies, Metall. Mater. Trans. A Phys. Metall. Mater. Sci. 42 (2011) 4113–4125.

[30] Y.B. Chun, M. Battaini, C.H.J. Davies, S.K. Hwang, Metall. Mater. Trans. A Phys. Metall. Mater. Sci. 41 (2010) 3473–3487.

[31] Q. Wang, B. Jiang, D. Chen, Z. Jin, L. Zhao, Q. Yang, G. Huang, F. Pan, J. Mater. Sci. (2021).

[32] A. Khosravani, D.T. Fullwood, B.L. Adams, T.M. Rampton, M.P. Miles, R.K. Mishra, Acta Mater. 100 (2015) 202–214.

[33] W. Pantleon, Scr. Mater. 58 (2008) 994–997.

[34] G. Liu, J. Zhang, Y. Dou, Comput. Mater. Sci. 103 (2015) 97–104.

[35] R. Agarwal, D.R. Trinkle, Acta Mater. 150 (2018) 339–350.

[36] B.-C. Zhou, S.-L. Shang, Y. Wang, Z.-K. Liu, in: A. Singh, K. Solanki, M. V Manuel, N.R. Neelameggham (Eds.), Magnes. Technol. 2016, Springer International Publishing, Cham, 2016, pp. 97–101.

5.3. Appendix

DFT calculations were performed to obtain the GSFE curves of Mg with or without alloying elements. Vienna Ab-initio Simulation Package (VASP) [1] with projector-augmented plane-wave (PAW) method [2,3] was used. For the exchange-correlation functional, the generalized gradient approximation (GGA-PBE) was chosen [4]. The supercell is 2×2×12 with vacuum gap of 15 Å exists along Z direction (Figure 5.6 (a)). Additional benchmark calculations were also performed to confirm that the supercell dimensions were sufficient and that the results were not size dependent. The cut off energy was set to 400 eV and the 7×7×1 Monkhorst-Pack k-point mesh was used. The convergence criteria for energy and force during relaxation were 10-5 eV and 10-2 eV/Å respectively. For the SFE calculations, we employed the slab shearing method [5] to simulate the shearing process. Some sample prismatic GSFE curves of pure Mg and Mg alloys were shown in Figure 5.6 (b).

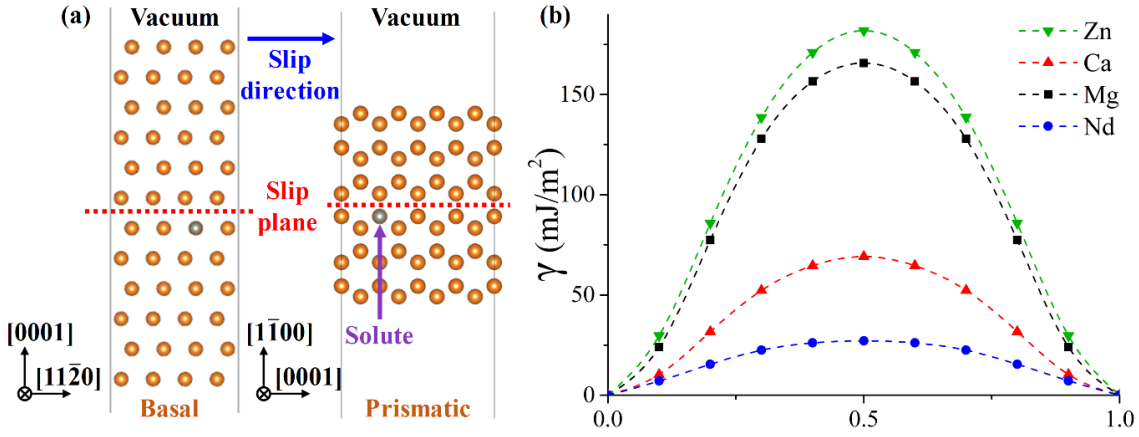

Figure 5.6 (a) Illustration of a representative supercell used to calculate the GSFE curve of basal and prismatic slip plane; (b)Sample DFT-calculated prismatic GSFE curves of pure Mg and Mg alloys at a planar solute concentration of 50 at. %.

MD simulations consider samples involving an edge dislocation on the three most common slip systems in Mg, the basal <a> slip, prismatic <a> slip and second-order pyramidal II <c+a> slip. All dislocations were created at the center of the simulation cell by displacing all atoms according to the Volterra fields [6] with the *y*-axis being normal to the slip plane, and x-axis being along the dislocation line direction. Periodic boundary conditions were imposed along the dislocation line and glide directions, while the free boundary condition was imposed along the third orthogonal direction. The simulation cells have dimensions ($l_x \times l_y \times l_z$) of 31.6 nm × 52 nm × 1.1 nm, 3.16 nm × 52 nm × 1.6 nm and 30 nm × 32.9 nm × 2.2 nm for supercells enclosing the basal, prismatic, and pyramidal II slips respectively. The core structures after relaxation for pure Mg was illustrated in Figure 5.7(a). Different from the SFE calculations where solute elements were only introduced on different stacking fault planes, in simulations of Peierls stresses, solute elements were randomly introduced into the different dislocation structures. The simulations were carried out using the Large-scale Atomic/Molecular Massively Parallel Simulator (LAMMPS) package [4]. The second nearest neighbor modified embedded-atom method (MEAM) interatomic potentials were employed to describe interatomic interactions for pure Mg [7], Mg-Zn [8], Mg-Ca [9] and Mg-Nd [10] systems. A rigid block with immobile atoms is assigned on the top and bottom few planes of the sample. Then rigid strain-controlled loading method [11] was used to apply a shear displacement to the top rigid block while fixing the bottom rigid block (see Figure 5.7(b).). The corresponding stresses were computed from the internal force per unit area [11],

$$\sigma^{xy} = \frac{\sum_{i \in Top} F_i^x}{A} = \frac{N^{Top} F^{Top}}{A}$$

where N^{Top} and F^{Top} are the number of atoms and the average force for each atom in top layer, respectively. A is the cross section area normal to the y direction. The instant shear strain ε^{xy} was calculated by the displacement of the center-of-mass position of atoms in the top layer from its reference configuration, i.e., the relaxed structure prior to loading. Thus, we have:

$$\varepsilon^{xy} = \frac{1}{l_y}(u_i^x - u_0^x)$$

where u_i^x is the center-of-mass position of atoms from the top layer after the ith strain loading and u_0^x is the initial position. The Peierls stress σ_{CRSS} was taken to be the average of flow stresses (in Figure 5.8) after the dislocation starts gliding at a critical stress of σ_j^{xy}, i.e.,

$$\sigma_{CRSS} = \frac{\sum_{i \geq j} \sigma_i^{xy}}{N_{yield}}$$

where σ_i^{xy} is the stress after yielding and N_{yield} is the number of stresses after yielding.

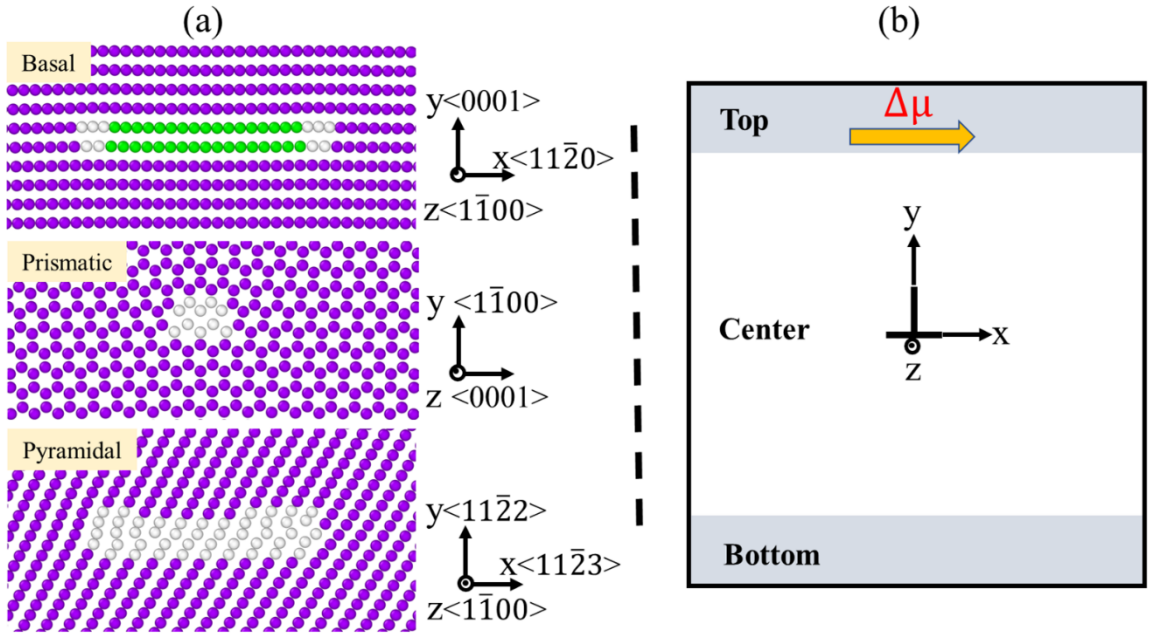

Figure 5.7 (a) Atomic structures of edge dislocations in basal, prismatic and pyramidal II slips after relaxation by the presently used MEAM *[7]* interatomic potential for pure Mg. Purple, green and white atoms denote atoms within the HCP, FCC and other lattice environments respectively, as identified from common-neighbor analysis *[12]*; (b)

Schematic illustration of the simulated cell partitioned into three regions, with free atoms in the center-region, while rigid atoms in the top and bottom regions. The shear deformation was realized by rigidly displacing the top block along x direction.

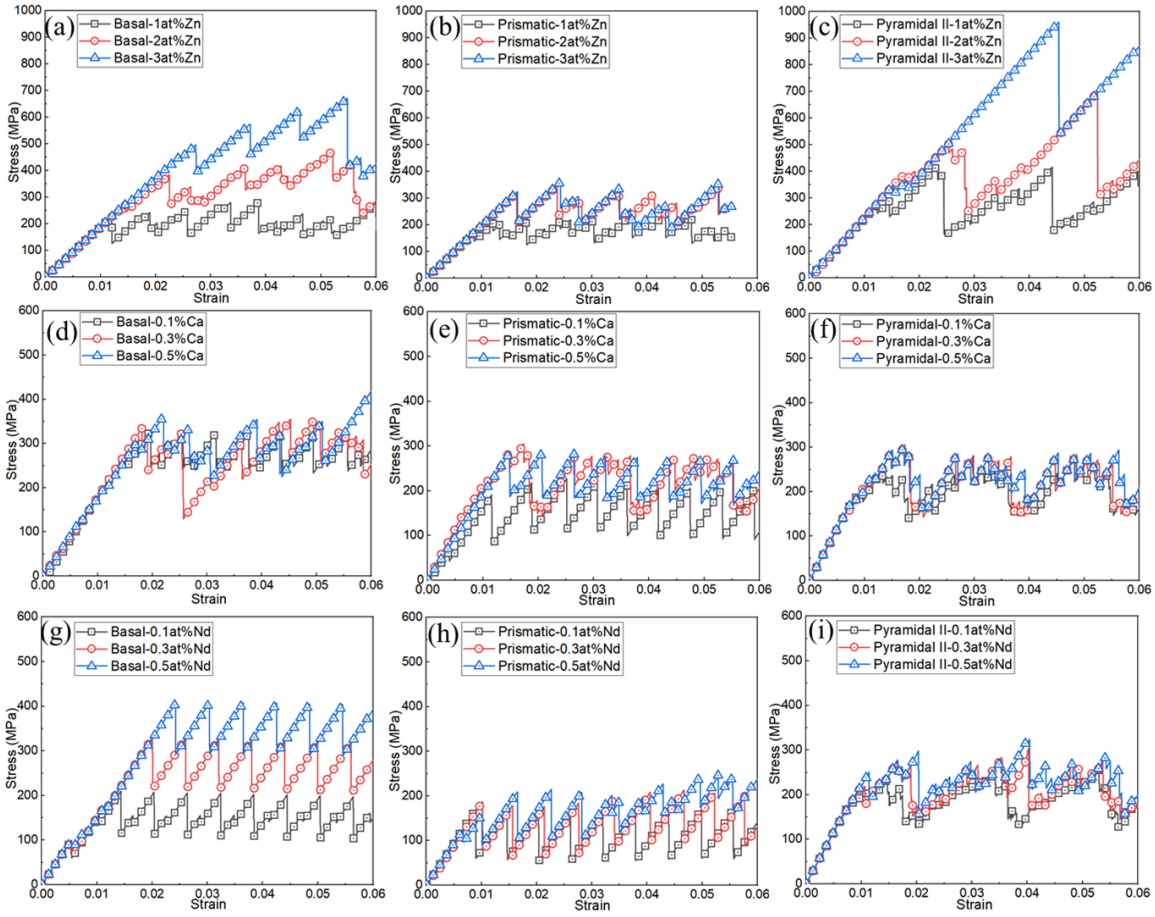

Figure 5.8 Simulated stress-strain curves: (a, b and c) Mg-Zn, (d, e, and f) Mg-Ca and (g, h and i) Mg-Nd on basal, prismatic and pyramidal II planes, at 0 K. Different symbols correspond to different solute concentrations.

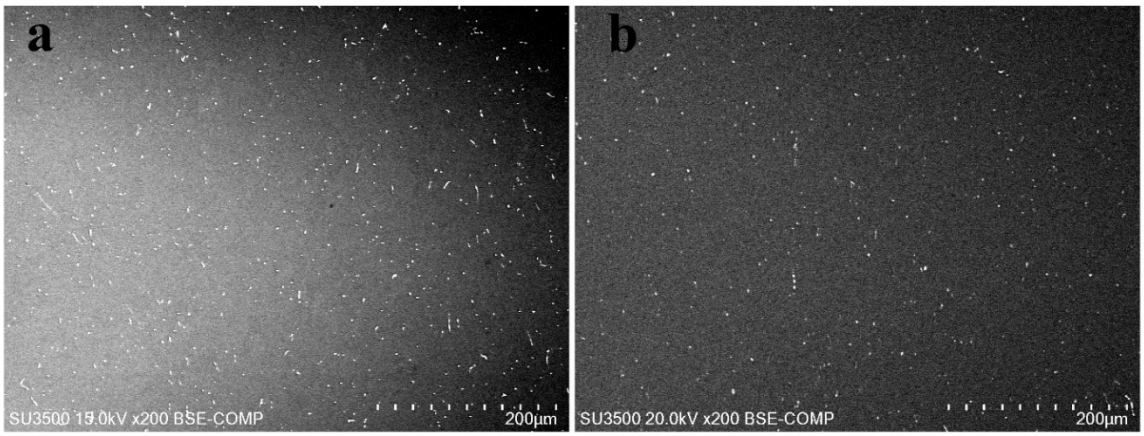

Figure 5.9 The precipitation distribution in as-received specimens: (a) ZEX-0102 and (b)ZX-02

5.3.1.Reference

[1] G. Kresse, J. Furthmüller, Phys. Rev. B 54 (1996) 11169.

[2] G. Kresse, D. Joubert, Phys. Rev. B 59 (1999) 1758.

[3] J.P. Perdew, K. Burke, M. Ernzerhof, Phys. Rev. Lett. 77 (1996) 3865.

[4] S. Plimpton, J. Comput. Phys. 117 (1995) 1–19.

[5] M. Muzyk, Z. and Pakiela, K.J. Kurzydlowski, Scr. Mater. 66 (2012) 219–222.

[6] D. Hull, D.J. Bacon, Introduction to Dislocations, Elsevier, 2011.

[7] Y.-M. Kim, N.J. Kim, B.-J. Lee, Calphad 33 (2009) 650–657.

[8] H.-S. Jang, K.-M. Kim, B.-J. Lee, Calphad 60 (2018) 200–207.

[9] K.-H. Kim, J.B. Jeon, B.-J. Lee, Calphad 48 (2015) 27–34.

[10] K.-H. Kim, B.-J. Lee, Calphad 57 (2017) 55–61.

[11] Y.N. Osetsky, D.J. Bacon, Model. Simul. Mater. Sci. Eng. 11 (2003) 427.

[12] J.D. Honeycutt, H.C. Andersen, J. Phys. Chem. 91 (1987) 4950–4963.

Chapter 6.The textural transition from basal to TD-split upon annealing in rolled micro-alloyed Mg-Zn-Nd-Ca alloy

From the previous chapter, it was shown that the quaternary Mg-1Zn-0.1Nd-0.2Ca (ZEX-0102) alloy is the favorable candidate for sheet production that stably triggers the formation of TD-split texture while minimizing the usage of Nd to 0.1 wt.%. To realize the manufacturing of texture-modified Mg sheets through the conventional multi-pass rolling process. The critical contents of Nd and Ca in solid solution for ZEX-0102 were determined and the texture and microstructure evolution subjected to multi-pass rolling at lower elevated temperatures (250°C~350°C) and subsequent recrystallization annealing was investigated.

This chapter is ready for submission and will be credited to the following authors:

Y. Liu, J. Su, B. Guo, R. Gao, N. Brodusch, A, Javaid, T. Skszek, S. Yue, The textural transition from basal to TD-split upon annealing in rolled micro-alloyed Mg-Zn-Nd-Ca alloy.

6.1. Abstract

A micro-alloyed Mg alloy sheet containing neodymium (Nd) and calcium (Ca) was subjected to different solutionizing treatments followed by multi-pass rolling and post-deformation annealing to understand the role of Nd and Ca solutes on texture modification. The initial strong basal texture was significantly modified with the (0002) basal poles tilting towards the transverse direction (TD) with a decreased intensity of more than 66%. The distribution and corresponding effects of Nd and Ca were examined via backscattered electron (BSE) imaging, scanning transmission electron microscope (STEM) and electron backscatter diffraction (EBSD). The critical contents of Nd and Ca solute to trigger TD-split texture formation were quantitatively characterized by electron probe micro-analysis (EPMA). In addition, a novel non-basal ring texture with both TD and RD splitting of (0002) poles was acquired through multi-pass rolling at 250°C, followed by recrystallization annealing. It was proposed that prismatic and pyramidal slip along with deformation twins contribute to the formation of this non-basal ring texture.

6.2. Introduction

The automotive industry's need for weight reduction, aimed at achieving higher fuel efficiency, lower CO2 emission and better cost-effectiveness, has heightened the application of magnesium (Mg) alloy sheets [1]. However, the insufficient formability, owing to the formation of strong basal texture after being subjected to thermomechanical treatments, limits the application of Mg alloy sheets [2,3]. Alloying with rare earth (RE) elements has been proven to be an effective approach to weaken or even alter the basal texture [4–6]. It has been reported that a weakened texture with (0002) basal poles tilting toward the transverse direction (TD) was acquired in RE-containing Mg alloys subjected

to rolling and subsequent annealing [7,8]. Different mechanisms were proposed to explain the formation of TD-split texture, including the occurrence of prismatic <a> slip by a reduced c/a ratio [9], oriented nucleation originating from preferential grain boundaries rotation [10], TD-split orientation introduced by secondary twins [11], etc. Although there is controversy of the TD-split texture formation mechanism, one common feature of these findings is that a considerable amount of RE ($\geqslant$ 0.5wt.%, much higher than the solid solubility) is used. This aggressive RE usage strategy is clearly inconsistent with the goal of weight reduction and cost control. It has been theoretically predicted [12] and experimentally validated [13] that significant texture modification can be achieved with 'diluted' RE levels in Mg-Zn alloys. Those observations indicate that RE is more effective in solid solution rather than in precipitates regarding texture modification.

In this current study, neodymium (Nd) was chosen due to the 'moderate' room temperature solid solubility limit in the Mg-Zn alloy system and a strong segregation effect [14]. In addition, calcium (Ca), was introduced to further reduce Nd usage based on its known effect on texture weakening [15,16]. Different solutionizing treatments were applied to control the Nd and Ca dissolution. The resulting textural evolution from basal to TD-split upon hot rolling and subsequent annealing was characterized. A proportional correlation between texture modification and alloying element solute was established through the measurement of Nd and Ca content in the matrix. The origin of TD-split texture was investigated through electron backscatter diffraction (EBSD) observation and ascribed to the enhanced activation of prismatic slip. In addition, the texture modification of solutionized alloys deformed at lower elevated temperatures (warm rolling) was validated.

6.3. Experimental procedure

A quaternary Mg-1Zn-0.1Nd-0.2Ca (wt.%) micro-alloy, denoted as ZEX-0102, was received from CanmetMATERIALS in the form of plates. The initial material showed a large number of precipitates. After some preliminary trials, several solutionizing treatments were performed at 550°C for 24, 48, and 72 hours to dissolve precipitates and quenched to prevent reprecipitation. The as-received and specimens solutionized for 24, 48 and 72 hours were denoted as S0, S1, S2, and S3, respectively. Hot rolling was performed on the as-received and three solutionized specimens at 450°C to investigate the role of solute contents in the microstructure and texture. To investigate the effect of the solutionizing treatments, hot rolling was performed in two passes with a per-pass reduction of 20% and an interpass anneal at 450°C for 10 minutes, followed by post-deformation annealing also at 450°C for 10 minutes. To investigate the effect of rolling temperature in the production of sheet, the S3 specimen was subjected to a 4-pass warm rolling schedules at 250°C, 300°C and 350°C with a per-pass 20% reduction and 10-minutes interpass annealing at the rolling temperature. Post-deformation annealing was then executed at 450° C for 10 minutes. Optical microscopy (OM) was utilized to reveal the microstructure evolution. The macro-texture evolution of rolled and annealed specimens was evaluated by X-ray diffraction (XRD). The precipitates and alloying element solute were characterized by a SU3500 scanning electron microscope (SEM) equipped with a backscattered electron (BSE) and energy-dispersive X-ray spectroscopy (EDX) detector, an SU8000 scanning transmission electron microscope (STEM) and a JAX-8600 electron probe X-ray microanalyzer (EPMA). Quasi-in-situ electron backscattered diffraction (EBSD) was

performed to analyze the texture modification mechanism. A 1μm step size was chosen for fully recrystallized specimens, while a 0.4μm step size was used for deformed specimens. Textools, HKL Channel 5, AZtecCrystal and MTEX [17] were used for the post-processing of various experimental data.

6.4. Results and discussion

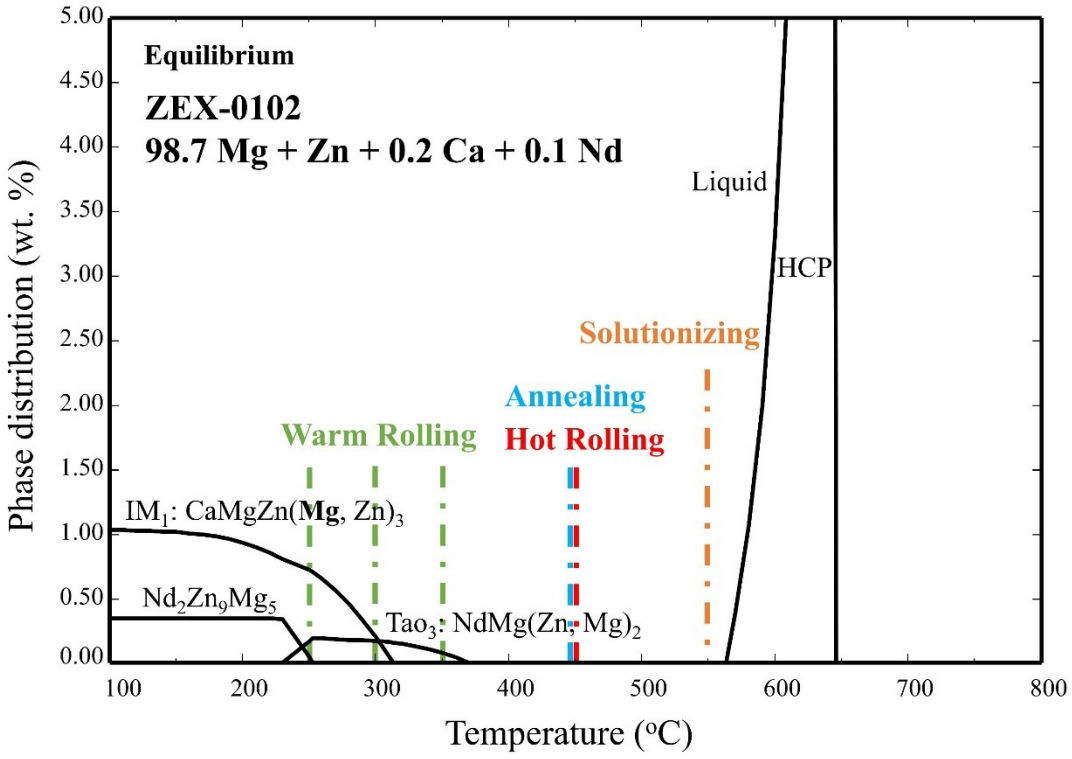

Figure 6.1 The equilibrium phase distribution and processing temperatures for ZEX-0102 alloy.

The equilibrium phase distribution of the ZEX-0102 alloy was calculated by FactSage [18], as shown in Figure 6.1, with various processing temperatures being labeled. It predicts that, at a temperature above 370°C, all the alloying elements would be in solid solution at equilibrium. Thus, the solutionizing temperature was chosen to be 550°C, close to the solidus line, to promote the kinetics of precipitate dissolution.

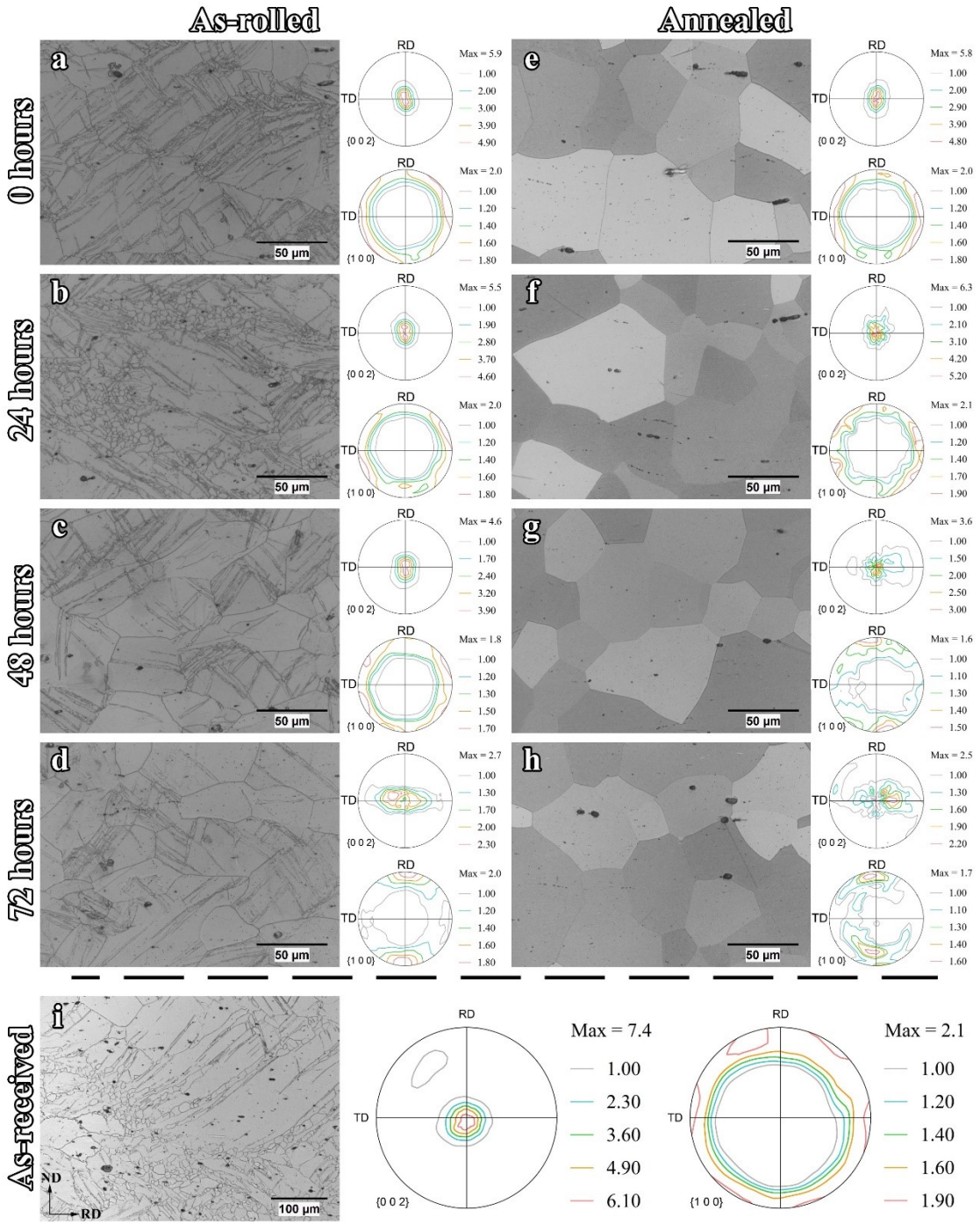

Figure 6.2 The microstructure and corresponding macro-textures of solutionized ZEX-0102 subjecting to 2-pass rolling: (a) to (d), subsequent annealing: (e) to (h) and the undeformed ZEX-0102 (i).

The hot rolling and post-deformation annealing were executed at 450°C to maintain Nd and Ca in solid solution. Therefore, for the S3 specimen, a higher amount of Nd and

Ca solutes is expected in solid solution after thermomechanical processing due to the prolonged solutionizing time. The as-received specimen exhibits a strong basal texture accompanied by a partially recrystallized microstructure (Figure 6.2 (i)). The DRX is observed in the vicinity of the twins and grain boundaries owing to the higher stored energy serving as the driving force for recrystallization.

6.4.1.Effect of solutionizing

The microstructure and macro-texture evolution of the 2-pass hot rolled and annealed specimens at different initial conditions are shown in Figure 6.2. Based on the macro-texture characteristics, the specimens are divided into two groups, i.e., basal texture and TD-split texture. The former includes the S0 and S1 specimens (Figure 6.2 (a) and (b)). Their as-rolled microstructures feature a mixture of elongated grains containing deformation twins and refined DRXed grains. Both specimens exhibit basal texture pattern upon hot rolling, which is similar to that of the as-received specimen. In contrast with the as-rolled S0 specimen, the as-rolled S1 showed a slightly weaker basal texture with intensity at 5.5 mrd due to the further DRXed structure. Upon post-deformation annealing, a fully statically recrystallized microstructure, as well as basal textures with intensities around 6.0, are obtained in S0 and S1 specimens. This suggests that the strong as-rolled basal texture can barely be weakened through static recrystallization.

The TD-slip texture group consists of the S2 and S3 specimens. In contrast to the first group, the as-rolled microstructures exhibit a combination of deformed grains and deformation twins. The DRX was significantly suppressed in the S2 and S3 after hot rolling owing to the higher solute dissolution. Yet, the static recrystallized microstructures of the second group are similar to those in the first group. On the other hand, the macro-textures

of the S2 and S3 were weakened and modified. The as-rolled texture of the S2 showed an intensity of 4.6 mrd, which is much weaker than those of the first group despite exhibiting a basal pattern (Figure 6.2 (c)). After annealing, the texture of the S2 was further weakened to an intensity of 3.6 mrd (Figure 6.2 (g)). More importantly, a weak, yet observable, TD-split texture component is observed. This indicates that the macro-texture transition from basal to TD-split was triggered upon annealing. For the S3 specimen, the texture modification is stronger. The as-rolled S3 specimen already featured a noticeable TD-split texture with a weak intensity of 2.7 mrd (Figure 6.2 (d)). Given that DRX is suppressed in the S3 specimens of the second pass rolling and deformation twinning occupies a limited area, this suggests that the source of TD-split orientation is related to the deformed parent grain. Therefore, it can be inferred that the concentrated TD-split texture existed prior to the second rolling. This means the SRX introduced the basal to TD-split texture transition during intermediate annealing. Eventually, a TD-split texture featuring basal poles tilting 45 degrees away from Nd, i.e., close to $\{01\bar{1}2\}\langle 0\bar{1}11\rangle$ and $\{11\bar{2}3\}\langle \bar{1}\bar{1}22\rangle$, with an intensity of 2.5 mrd is obtained in S3 upon annealing (Figure 6.2 (h)). Compared to the undeformed as-received specimen, the texture was significantly modified with a 66% reduction in intensity and a broader angular distribution of basal poles along with TD. The microstructure and texture evolution have proved that the TD-split texture, which formed during recrystallization, is closely related to the solutes that dissolved during solutionizing.

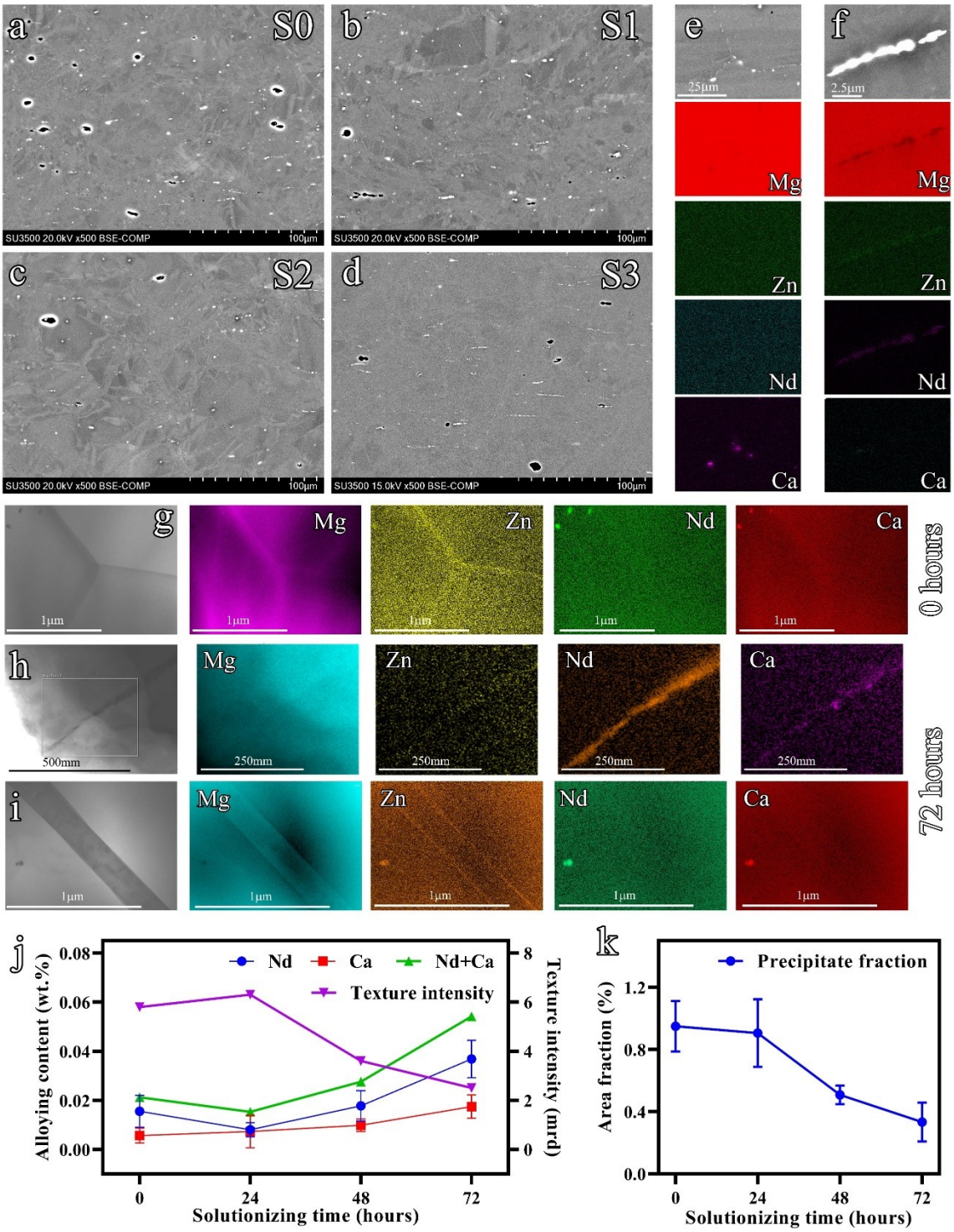

Figure 6.3 The BSE images (a) to (d), the EDS mapping (e) and (f), the STEM characterization (g) to (i), the EPMA measurements (j) and the precipitate fraction (k) showing the status of alloying Nd and Ca in ZEX-0102.

The precipitates of the S0 to S3 specimens were characterized by BSE (Figure 6.3 (a) to (d)) and EDS mapping (Figure 6.3 (e) and (f)). Two broad categories are classified based on the morphology of precipitates: the isolated spherical ones and short stick ones which consist of several fine precipitates. The former is characterized as Ca-rich precipitates (Figure 6.3 (e)), while the latter is dominated by fine Nd-rich particles (Figure 6.3 (f)). In general, the precipitate fraction, which is represented as the area fraction measured from BSE images, gradually drops with increasing annealing time (Figure 6.3 (k)). The distribution of alloying elements is characterized by STEM. By using the built-in BSE detector to avoid precipitates, the alloying element content in the matrix is determined through EPMA measurement. The high-angle annular dark-field (HAADF) images focus on the grain boundaries and deformation twin boundaries of S0 and S3 specimens subjected to hot rolling. The corresponding mappings show no visible segregation of Nd and Ca in the as-rolled S0 specimen (Figure 6.3 (g)). However, pronounced segregation of Nd and Ca along grain boundaries rather than twin boundaries is observed in as-rolled S3 specimen (Figure 6.3 (h) and (i)), which indicates that the segregation of Nd and Ca has resulted from solutionizing. Furthermore, it can be inferred that DRX suppression in S2 and S3 is due to grain boundary solute drag caused by Nd and Ca segregation. However, the solute drag effect serves only to weaken the strong basal texture but does not lead to the formation of TD-split texture [19,20]. On the other hand, there is consistency between the measured Nd and Ca solutes in the matrix and macro-texture intensities of annealed ZEX-0102 alloys, as observed in Figure 6.3 (j). These findings suggest a strong correlation between the Nd and Ca solutes and the formation of the TD-split texture. Furthermore, the texture modification process can be interpreted as the evolution of Nd and Ca solutes content. For

the S0 specimen, the total dissolved alloying elements are around 0.02 wt.%, which is insufficient to trigger texture modification. For S1 specimens, the alloying element content in the matrix, the precipitate fraction, and the macro-texture intensity fluctuated rather than showing a large difference compared to that of S0. This observation indicates that the time for precipitate dissolution is longer than 24 hours for the current as-received sheets. The 48-hours solutionized specimen, which showed traces of TD-split component, reveals the critical content to trigger TD-split texture formation is around 0.0276 wt.% (0.0178 wt.% Nd and 0.0098 wt.% Ca). Eventually, the overall solute content reaches 0.0542 wt.%, and a weak 45° TD-split texture formed upon hot rolling and subsequent annealing for the specimen subjecting to 72-hours solutionizing.

To understand the formation mechanism of TD-split texture, the hot-rolled S3 specimen was annealed at 350°C for 10 minutes and examined by EBSD. Figure 6.4 (a) shows the three main texture components distribution, i.e., basal (red), RD-split (green) and TD-split (yellow), as well as the micro-texture of the annealed sample. Distinctive TD-split texture is acquired accompanied by a partially recrystallized microstructure. The majority of the TD-split texture is ascribed to the residual deformed TD-split grains, which dominated the microstructure, as seen in the Kernel Average Misorientation (KAM) map (Figure 6.4 (e)). The SRXed grains, which exhibited a mean grain orientation spread (GOS) , were colored with corresponding texture components (Figure 6.4 (b)). The (0002) pole figure of recrystallized grains also exhibited a TD-split dominated texture. Moreover, for each texture component, the corresponding grain number and average grain area were measured and listed (Figure 6.4 (b)). From the statistics, the average number of GOS grains for a specific texture component (i.e., basal, RD, TD and the overall non-basal) is

about 73. Interestingly, the number of TD-split grains is 76, which failed to show a noticeable advantage in terms of grain number. Yet, the average area occupied by TD-split grains (35.8 μm^2) is significantly above the average (22.5 μm^2). In other words, the TD-split grains originated from preferential grain growth rather than preferential nucleation upon annealing.

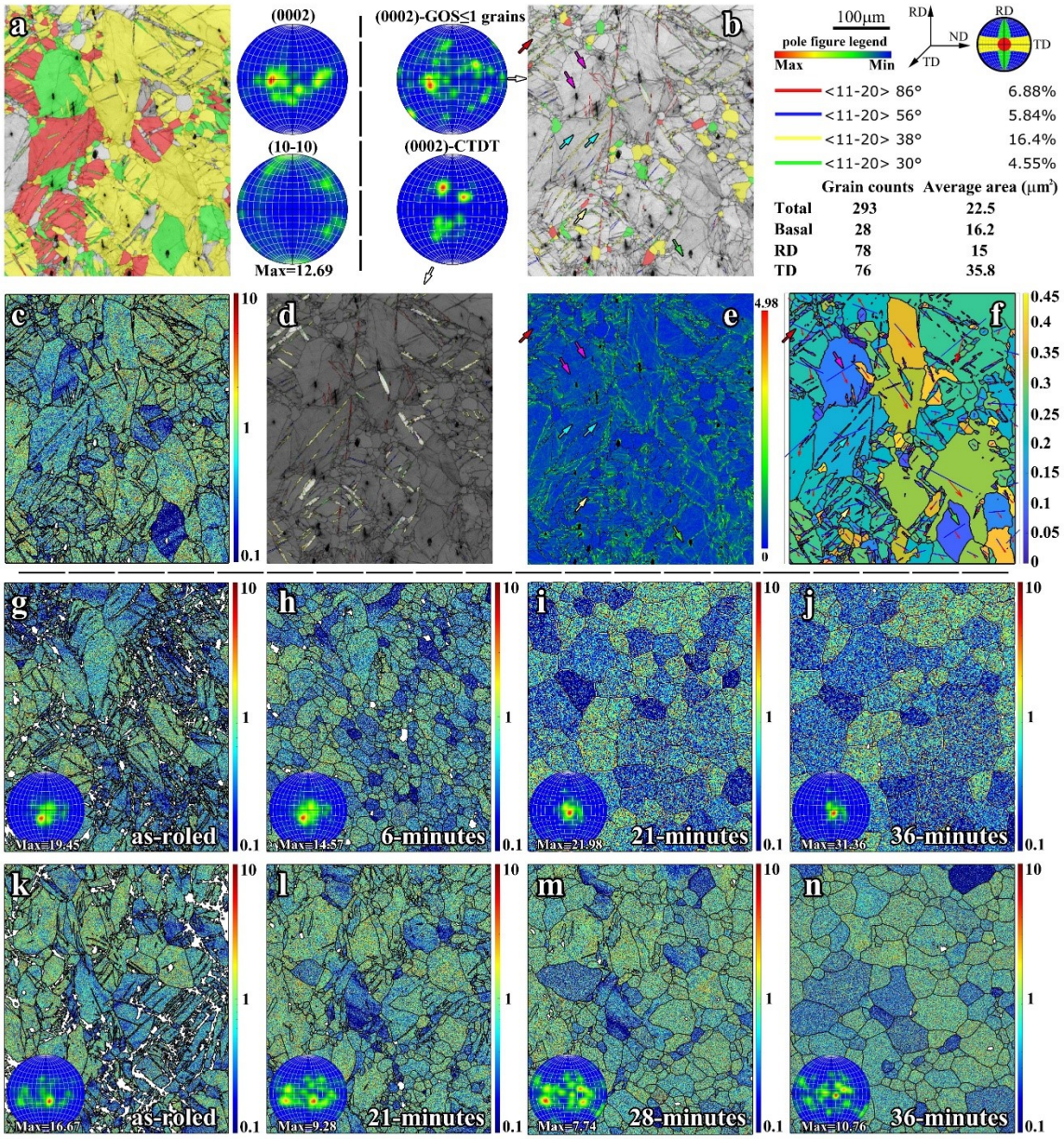

Figure 6.4 The texture component and micro-texture (a), the recrystallized grains and related status (b), the $rGND_{p/b}$ distribution (c), the CTDTs (d), the KAM distribution (e), and the GSF distribution of 350 ℃ annealed ZEX-0102; the $rGND_{p/b}$ distribution evolution of deformed as-received (g) to (j) and 72-hour solutionized (k) to (n) upon quasi-in-situ EBSD observation.

It is well known that the deformation twinning and dislocation movement accommodate plastic deformation in Mg alloys [21]. The commonly reported deformation twins and the corresponding twin boundary fractions were also shown in Figure 6.4 (b). The $\{10\bar{1}1\} - \{10\bar{1}2\}$ compression-tension double twin (CTDT), characterized as $38 \pm 5°$ about the $\langle 11\bar{2}0 \rangle$ for variant I and $30 \pm 5°$ about the $\langle 11\bar{2}0 \rangle$ for variant II [22], dominated the twin boundaries. However, the CTDTs negligibly contributed to the formation of TD-split texture since their (0002) pole figure featured a noticeable RD-split pattern (Figure 6.4 (d)). Zeng et al. [23] observed the enhanced activation of prismatic slip system in TD-slip orientated grains subjected to rolling in an Mg-Zn-Nd alloy. In this current research, the prismatic slip system activation is evaluated based on the criteria of the Generalized Schmid Factor (GSF) [24,25]. The most likely activated prismatic slip, which processes the highest GSF in each grain, is visualized in Figure 6.4 (f) as the combination of slip plane (blue line) and slip direction (red arrow) by MTEX. The theoretically predicted slip plane was observed in the band contrast (BC) map as slip traces and the KAM map with intensified traces (colored arrows in Figure 6.4 (d) and (e)). These observations validate the activation of prismatic slip, especially in basal and RD-split grains (as shown in the colored arrowed grains in Figure 6.4 (b)). It also has to be addressed that basal slip should always be considered as activated owing to its low critical resolved shear stress (CRSS) [26]. A geometrically necessary dislocation (GND) map was introduced and developed to describe dislocations that appeared in strain gradient fields due to lattice curvature and rotation resulting from deformation [27]. The GND density can

be used to evaluate the dislocation distribution on grain-scale [28]. To integrate the effect of prismatic and basal dislocation, an originally proposed parameter, namely $rGND_{p/b}$, is defined as the GND density ratio between prismatic and basal slip. The $rGND_{p/b}$ distribution of 350°C annealed S3 specimen is shown in Figure 6.4 (c). The high $rGND_{p/b}$ region ($rGND_{p/b} \geqslant 1$, colored green to red) represents an unusually increased prismatic GND density, which is comparable to that of basal slip for deformed grains. Interestingly, the basal and RD-split orientated grains exhibit an inferior activation of prismatic slip. The recrystallized (GOS $\leq 1°$) TD-split oriented grains also generally showed a higher $rGND_{p/b}$ value. These observations suggest a strong correlation between the existence of prismatic slip and TD-split texture in the current micro-alloyed ZEX-0102 alloy. The favored prismatic slip and the resultant TD-split texture were ascribed to the Nd and Ca addition as reported by Ha et al. [28] and Xun et al. [23]. Therefore, the $rGND_{p/b}$, as a general parameter integrating deformation and subsequent annealing, is related to the formation of TD-split texture. In the micro-alloyed ZEX-0102 alloy, the TD-split texture originated from the preferential growth of TD-split grains, which show high $rGND_{p/b}$ values. This tendency is further validated by the $rGND_{p/b}$ distribution evolution of deformed S0 and S3 specimens upon quasi-in-situ EBSD observation. For the S0 specimen, the basal texture is intensified upon annealing along with the progressive ascendancy of low $rGND_{p/b}$ grains (Figure 4(g) to (j)). However, for the S3 specimen, the microstructure is gradually occupied by high $rGND_{p/b}$ grains and the micro-texture is weakened with noticeable TD-split texture component (Figure 6.4 (k) to (n)).

6.4.2.Effect of rolling temperature

The microstructures and macro-texture evolution of the S3 specimen subjected to warm rolling at 250°C, 300°C and 350°C and subsequent annealing are shown in Figure 6.5. By decreasing rolling temperature from 350°C to 250°C, the as-rolled microstructure evolves from a twinned structure (Figure 6.5 (a)) to a recrystallization dominated structure (Figure 6.5 (c)) and eventually to a heavily deformed structure with a mixture of deformation twins, shear bands, and very fine recrystallized grains (Figure 6.5 (e)).

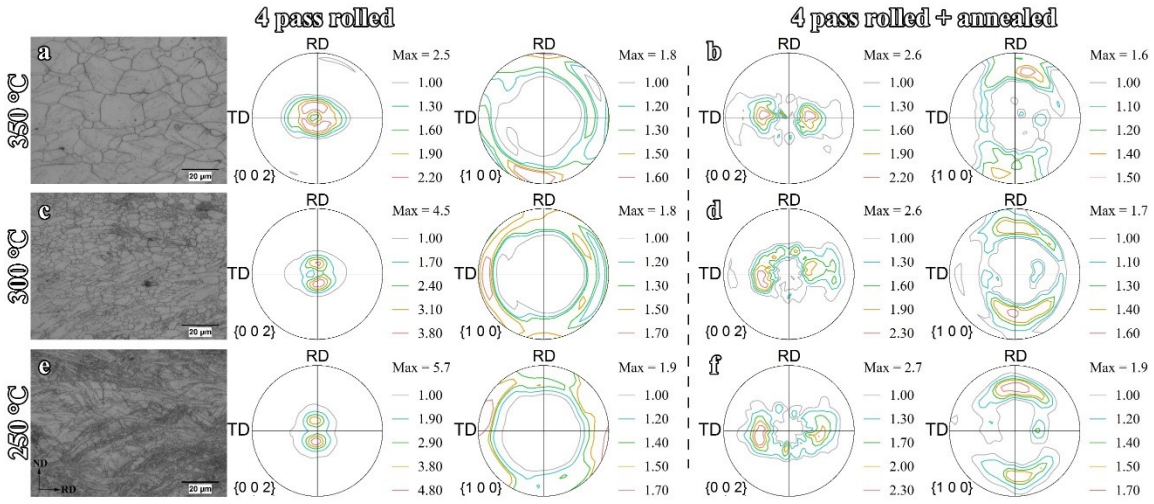

Figure 6.5 The deformed microstructures and macro-structures of solutionized ZEX-0102 subjecting to multi-pass rolling at different temperatures and the subsequent recrystallization annealing.

As proven by the annealed S3 specimen, annealing at 350°C for 10 minutes is insufficient to acquire a fully recrystallized structure owing to the drag effect brought by Nd and Ca solutes. Therefore, the TD-split texture component, which forms during SRX, is found gradually retarding with the decreasing rolling temperature from 350°C to 250°C. On the contrary, the RD-split texture components concentrate when dropping the rolling temperature, which is due to the activation of <c+a> pyramidal slip [29 – 31] and deformation twins [21] (Figure 6.5 (a), (c) and (e)). The activation of pyramidal slip is

likely caused by the strain localization owing to SRX suppression. Although the microstructures are refined due to recrystallization, the macro-textures are less affected since DRXed grains tend to inherit orientations from parent grains [19]. Despite the texture intensity increase owing to RD-split component enhancement as well as the TD-split component retardation with rolling temperature decreasing, a similar weakened texture is acquired after recrystallization annealing (Figure 6.5 (b), (d) and (f)). Especially for the 250 °C and 350 °C rolled specimens, a distinctive non-basal texture featuring a ring distribution of (0002) poles was observed. This ring texture consists of a slightly concentrated TD-split component and an RD-split component. The former, as previously discussed, results from prismatic slip activation owing to Nd and Ca addition. The latter, which is more obvious with the temperature decrease, is inherited from the as-rolled texture through the grain growth of DRXed grains and recrystallization of twins. The evident TD-split texture component in twinned, DRXed, and shear-banded structure indicates that the solutionized Nd and Ca and the resultant prismatic slip is the major contributor to the texture modification. More importantly, the occurrence of non-basal ring texture gives an insight into the development and processing of ductile Mg alloys with low RE addition at lower temperatures.

6.5. Conclusions

The current study proposes an economical approach to weaken the strong basal texture in Mg micro-alloys with minimizing Nb contents and substituting it with Ca. Pronounced texture modification, in which strong basal texture was altered to a weakened TD-split texture with a 66% reduction on texture intensity, was acquired upon multi-pass hot rolling and annealing. This texture modification effect was ascribed to the prismatic

slip brought by Nd and Ca in solution. The critical content for Nd and Ca solute was determined to be 0.0178 wt.% and 0.0098 wt.%, respectively. This implies that the usage of alloying elements could be further optimized. In addition, a unique non-basal ring texture with both RD and TD splitting was observed upon warm rolling from 250°C to 350° C and post-deformation annealing. This is related to the activation of multiple deformation modes at the lower elevated temperature range and utilizing their corresponding recrystallization mechanisms.

6.6. Reference

[1] M.O. Pekguleryuz, in: M. Barnett (Ed.), Adv. Wrought Magnes. Alloy., Woodhead Publishing, 2012, pp. 3–62.

[2] J. Su, M. Sanjari, A.S.H. Kabir, I.H. Jung, J.J. Jonas, S. Yue, H. Utsunomiya, Mater. Sci. Eng. A 636 (2015) 582–592.

[3] Y. Liu, J. Fan, H. Zhang, W. Jin, H. Dong, B. Xu, J. Alloys Compd. 622 (2015) 229–235.

[4] I. Basu, T. Al-Samman, Acta Mater. 67 (2014) 116–133.

[5] J.D. Robson, S.J. Haigh, B. Davis, D. Griffiths, Metall. Mater. Trans. A Phys. Metall. Mater. Sci. 47 (2016) 522–530.

[6] I. Basu, K.G. Pradeep, C. Mießen, L.A. Barrales-Mora, T. Al-Samman, Acta Mater. 116 (2016) 77–94.

[7] D. Guan, W.M. Rainforth, J. Gao, L. Ma, B. Wynne, Acta Mater. 145 (2018) 399–412.

[8] T. Al-Samman, X. Li, Mater. Sci. Eng. A 528 (2011) 3809–3822.

[9] T. Al-Samman, Acta Mater. 57 (2009) 2229–2242.

[10] L.Y. Zhao, H. Yan, R.S. Chen, E.H. Han, J. Mater. Sci. Technol. 60 (2021) 162–167.

[11] D. Guan, W.M. Rainforth, L. Ma, B. Wynne, J. Gao, Acta Mater. 126 (2017) 132–144.

[12] C. Ha, J. Bohlen, X. Zhou, H.G. Brokmeier, K.U. Kainer, N. Schell, D. Letzig, S. Yi, Mater. Charact. 175 (2021).

[13] Y. Liu, J. Su, R. Gao, H. Geng, A. Javaid, T. Skszek, S. Yue, J. Mater. Eng. Perform. (2020) 1–8.

[14] I.-H. Jung, M. Sanjari, J. Kim, S. Yue, Scr. Mater. 102 (2015) 1–6.

[15] D.W. Kim, B.C. Suh, M.S. Shim, J.H. Bae, D.H. Kim, N.J. Kim, Metall. Mater. Trans. A Phys. Metall. Mater. Sci. 44 (2013) 2950–2961.

[16] J. Victoria-Hernández, S. Yi, D. Klaumünzer, D. Letzig, Mater. Sci. Eng. A 761 (2019).

[17] G. Nolze, R. Hielscher, J. Appl. Crystallogr. 49 (2016) 1786–1802.

[18] C.W. Bale, P. Chartrand, S.A. Degterov, G. Eriksson, K. Hack, R. Ben Mahfoud, J. Melançon, A.D. Pelton, S. Petersen, Calphad 26 (2002) 189–228.

[19] J.P. Hadorn, K. Hantzsche, S. Yi, J. Bohlen, D. Letzig, J.A. Wollmershauser, S.R. Agnew, Metall. Mater. Trans. A Phys. Metall. Mater. Sci. 43 (2012) 1347–1362.

[20] J.P. Hadorn, K. Hantzsche, S. Yi, J. Bohlen, D. Letzig, S.R. Agnew, Metall. Mater. Trans. A Phys. Metall. Mater. Sci. 43 (2012) 1363–1375.

[21] J. Su, A.S. Abu, M. Sanjari, S. Yue, Mater. Sci. Eng. A 674 (2016) 343–360.

[22] S.R. Agnew, in: Adv. Wrought Magnes. Alloy., Elsevier, 2012, pp. 63–104.

[23] X. Zeng, P. Minárik, P. Dobroň, D. Letzig, K.U. Kainer, S. Yi, Scr. Mater. 166 (2019) 53–57.

[24] C. Guo, Y. Xiao, R. Xin, Met. Mater. Int. 26 (2019) 1366–1372.

[25] J.R. Luo, A. Godfrey, W. Liu, Q. Liu, Acta Mater. 60 (2012) 1986–1998.

[26] H. Zhang, Y. Liu, J. Fan, H. Jørgen, W. Cheng, B. Xu, J. Alloys Compd. 615 (2014) 687–692.

[27] A. Arsenlis, D.M. Parks, Acta Mater. 47 (1999) 1597–1611.

[28] A. Khosravani, D.T. Fullwood, B.L. Adams, T.M. Rampton, M.P. Miles, R.K. Mishra, Acta Mater. 100 (2015) 202–214.

[29] J. Su, M. Sanjari, A.S.H. Kabir, I.H. Jung, S. Yue, Scr. Mater. 113 (2016) 198–201.

[30] Y. Onuki, K. Hara, H. Utsunomiya, J.A. Szpunar, J. Mater. Eng. Perform. 24 (2015) 972–985.

[31] S.R. Agnew, M.H. Yoo, C.N. Tomé, Acta Mater. 49 (2001) 4277–4289.

Chapter 7.Conclusions

The formation of TD-split texture (close to $\{01\bar{1}2\}\langle 0\bar{1}11\rangle$ and $\{11\bar{2}3\}\langle\bar{1}\bar{1}22\rangle$) in Mg-Zn alloys through diluted Nd and Ca addition was thoroughly investigated in current research. Texture modification was achieved through the processing procedure of solutionizing, rolling, and post deformation annealing. The texture transition that transforms the strong basal texture into a weakened non-basal texture dominated by TD-split components has been tracked by quasi in-situ EBSD observations. To explain the texture modification phenomenon, the microstructure evolution was characterized, and the contribution of various deformation mechanisms was clarified. The main results are summarized as follows:

1. Enhanced texture modification, observed as lower texture intensity and broader angular distribution of (0002) basal poles, is related to the increased Nd and Ca content in the solid solution as the consequence of faster cooling rate after homogenization, higher solutionizing temperature, and longer solutionizing time.
2. In terms of texture modification, Ca acts as an inferior substitute of Nd. The combined addition of Nd and Ca can trigger the formation of TD-split texture and maintain cost reduction. Under the same condition, a similar TD-split texture has been observed in a ternary Mg-1Zn-0.2Nd alloy and a quaternary Mg-1Zn-0.1Nd-0.2Ca alloy.
3. In the Mg-Zn-Nd-Ca system, the critical contents of Nd and Ca solute to stimulate the basal to TD-split textural transition were measured as 0.0178 wt.% and 0.0098 wt.%, respectively.

4. Both DRX and SRX were suppressed in the texture-modified alloy owing to the solute drag and grain boundary stabilizing brought by increased Nd and Ca solute in the matrix.
5. For current alloys, the deformed structure was dominated by deformation twins and shear bands. The $\{10\bar{1}1\}-\{10\bar{1}2\}$ CTDT was characterized as the main twinning mechanism in current alloys exhibiting TD-split texture.
6. The activation of prismatic <a> slip in texture-modified alloys, which is closely related to the Nd and Ca solute, was revealed by the IGMA distribution analysis and slip trace analysis. DFT and MD simulation revealed that the dilute Nd and solute could improve the activation of the prismatic slip by modifying the SFE and CRSS of different deformation modes. Moreover, prismatic slip is geometrically favored in TD-split grains with higher GSF.
7. Nucleation of deformed micro-alloyed ZE and ZEX alloys was executed mainly through the SBIN mechanism without showing preference on TD-split orientation.
8. The $rGND_{p/b}$ distribution was originally proposed which revealed the relative contribution of basal and prismatic slip on the microstructure evolution upon recrystallization. It was found that both prismatic and basal slip contributed to the formation of TD-split texture, while the former is essential to promote preferential grain growth.
9. The development of TD-split texture is progressively developed during multi-pass rolling.
10. A TD-split texture featuring a TD-split pattern and an intensity of 2 mrd is achieved in an Mg-1Zn-0.1Nd-0.2Ca alloy upon multi-pass rolling and annealing at 450°C.

Furthermore, a unique non-basal ring texture featuring both RD and TD splitting was obtained upon warm rolling from 250°C to 350°C and post-deformation annealing. The RD-split component is inherited from the deformation texture while the TD-split component emerges with static recrystallization.

11. Ductility boost owing to the texture weakening has been observed in ZE alloys. The ZE-02 alloy showed enhanced ductility (23%) compared to the ZE-01. However, there was no significant further improvement in texture modification and ductility when Nd addition exceeded 0.2 wt.% for the ternary Mg-Zn-Nd system.

Chapter 8.Contributions to original knowledge

1. The formation of TD-split texture component was related to the Nd and Ca in the solid solution. The critical content of Nd and Ca for triggering texture modification was measured for the first time.
2. The texture transition from strong basal to weakened TD-split in Mg alloys with dilute addition of Nd and Ca was tracked by quasi-in-situ EBSD upon annealing for the first time. In terms of microstructure evolution, preferential grain growth was proposed as playing the crucial role in developing the TD-split orientation rather than preferred nucleation.
3. According to experimental observation and theoretical simulation, the activation of prismatic <a> is due to the increased Nd and Ca solute. The initiation and development of TD-split texture were attributed to the preferential grain growth originating from the combined contribution of basal and prismatic slip activation.
4. The $rGND_{p/b}$ distribution map, which integrated deformation mechanisms with microstructure evolution, was originally proposed. It provides an alternative approach to understand the relative contributions of basal and prismatic slip system and the resultant texture evolution upon annealing.

Chapter 9.Future work

1. The current study revealed that Nd addition can be further reduced since the non-basal texture was resulted from Nd and Ca in solid solution. Therefore, an investigation on element selection as well as the optimization on alloying element content are needed to economically produce texture modified sheets for automobile applications.
2. To avoid the time consuming and energy intensive solutionizing treatment of micro-alloyed Mg-Zn-Nd-Ca alloy (or similar alloy systems), twin roll cast material should be used as a better method for manufacturing texture modified sheets. Since rolling can be directly performed after casting at higher temperatures without formation of precipitates, more alloying elements are expected to be preserved in solid solution.
3. Given the strong recrystallization suppression brought by the RE solutes, further microstructure control approaches, in particular grain refinement, are suggested to enhance the mechanical performance of the final product.
4. A novel non-basal ring texture featuring both RD-split and TD-split texture components has been obtained at 250°C. Detailed investigations of deformation at lower temperatures (≤250°C) as well as the characterization of mechanical performance are suggested.
5. An investigation to clarify the crystallography of the newly observed twins is suggested.